School of Earth and Planetary Sciences

Improving Precise Point Positioning Performance Using Multi-Frequency Multi-Constellation GNSS

Manoj Nilesh Deo

This thesis is presented for the Degree of
Doctor of Philosophy
of
Curtin University

May 2019

DECLARATION

This thesis is based on refereed publications. To the best of my knowledge and belief this thesis contains no material previously published by any other person except where due acknowledgment has been made.

This thesis contains no material which has been accepted for the award of any other degree or diploma in any university.

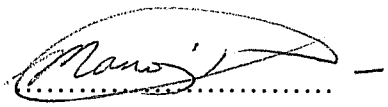

Manoj Nilesh Deo

15 May 2019

ABSTRACT

Precise Point Positioning (PPP) is a technique for determining the precise coordinates of a stand-alone Global Navigation Satellite System (GNSS) receiver without relying on simultaneous measurements from a network or nearby reference receiver. PPP can provide decimetre level accuracy for kinematic positioning and cm-level accuracy for static surveying, provided that long duration dual-frequency measurements are used with the most precise satellite orbit and clock products. However, its main drawback is a long convergence time of typically half an hour to reach cm-level accuracy with static data, and decimetre level accuracy with kinematic data. The ongoing modernisation of GPS and GLONASS, accompanied by the development of Galileo, Beidou and regional navigation satellite systems (RNSS) including Quazi Zenith Satellite System (QZSS) and the Indian Regional Navigation Satellite System (IRNSS), with an operational name NAVIC, provides opportunities for developing novel PPP models with improved performance compared to the present dual-frequency models. The availability of multi-frequency and multi-constellation (MFMC) systems brings benefits, but along with it comes challenges such as dealing with inter-frequency and inter-system biases, differences in coordinate frames and time systems. This thesis aims to integrate MFMC GNSS data to improve the PPP performance in comparison to conventional single-system models, by reducing the convergence time and improving or maintaining positional accuracy.

A number of contributions were made to reach this aim. Firstly, a thorough analysis of the biases that occur when integrating MFMC data was carried out to identify the individual biases and develop mathematical models to eliminate or reduce their detrimental effect on PPP performance.

Next, the conventional dual-frequency PPP model that includes float ambiguity estimation was investigated in detail by incorporating triple frequency measurements. This resulted in the development of three models, one of which included a novel mixed code-phase linear combination with ionosphere-free, geometry preserving and low noise propagation properties. The second model used a code- and phase-only triple frequency ionosphere-free, geometry preserving and noise minimisation linear combination, which was developed for the major GNSS constellations. The full mathematical derivations for these combinations were

presented for the first time, for easy implementation in navigation algorithms in the GNSS receiver. The third model used the additional frequency to estimate the ionosphere error, rather than forming combinations to eliminate it. The analysis of test data with these three models revealed that they all had similar performance in terms of convergence time and achievable accuracy. All the three models had significantly improved reduction in convergence time when compared to the conventional use of dual-frequency observations. The PPP model with the code- and phase-only triple frequency linear combination for a single system (such as GPS) was extended to the multi-constellation case. The validation revealed that use of multi-constellation data further improved PPP convergence time.

The PPP model with raw un-combined carrier phase and code measurements was augmented with a precise Regional Ionospheric Model (RIM) to constrain the ionosphere error. This model significantly improved the PPP convergence performance, particularly in the horizontal positioning component. Here, better than 5cm accuracy was achieved within five minutes for all the tested datasets with RIM precisions of standard derivation (std) from 0.1 to 1.0 Total Electron Content Unit (TECU). Such rapid PPP convergence is promising for real-time PPP users having access to triple frequency GNSS data and high precision ionospheric corrections.

The contribution of tropospheric delay estimates derived from Numerical Weather Model (NWM) to constrain the troposphere error was studied. For the first time, the Australian Bureau of Meteorology (BoM) NWM data was used to estimate the tropospheric delay estimates, which was compared to other empirical and NWM derived troposphere models. The BoM NWM was found to give the best accuracy in the Australian sites that were tested. Using the BoM NWM data to constrain the troposphere error was found to improve the PPP convergence performance, particularly in the vertical component during the first few minutes of initialisation.

A method was developed to maintain real-time PPP accuracy during a loss in data communication, when the precise clock and orbit corrections are not available to the user. The clocks were predicted based on time-series analysis of their properties, including their temporal behaviour and stability. The proposed method was found to give better than 0.5ns prediction accuracy for up to one hour after a loss of communication. Using the predicted clock corrections, it was shown that the PPP user can maintain decimetre level accuracy for up to two hours after a communication loss.

Some key contributions were made in PPP with integer Ambiguity Resolution (PPP-AR). A new triple frequency geometry-free and ionosphere-free (GIF) linear combination was developed for estimating the extra wide-lane (EWL) and wide-lane (WL) ambiguities, that had improved performance compared to the widely used Melbourne-Wübbena (MW) combination. A full rank triple frequency carrier phase only PPP model was proposed where the carrier phase equations were formulated in terms of an individual carrier phase ambiguity rather than a narrow-lane (NL) ambiguity used in present-day PPP-AR models. Analysis of the probability of AR success rate with the LAMBDA method showed that PPP-AR performance of the proposed model is greatly improved when using precise atmospheric models to constrain the ionosphere and troposphere errors. A method was also proposed for the direct estimation of the NL integer ambiguity by multi-epoch averaging of a newly proposed triple frequency linear combination. This is applied after the EWL and WL ambiguities are resolved with the proposed linear combinations, which takes 1-2 minutes. This approach gave comparable performance to the existing PPP-AR methods, and may be used as an alternative method for NL ambiguity resolution.

ACKNOWLEDGEMENTS

Firstly, I am sincerely grateful to my supervisor, Associate Professor Ahmed El-Mowafy for kindly accepting me as his PhD student and for providing relentless support and guidance throughout my studies. His valuable suggestions and insightful comments have greatly enhanced the quality of my work and increased my understanding of the subject matter.

Sadly, I lost my beloved father during the course of my study, who would have been very proud of my achievement. I would like to thank my wife, daughter and mother for their patience, sacrifices and encouragement over the years to help me reach my goal.

Special thanks go to the reviewers of my publications for their input in uplifting the quality of the work. Lastly, a big thanks to my employers for supporting my study through study assistance procedures.

LIST OF PUBLICATIONS

This PhD thesis is submitted as a series of published papers that include six first-author and two second author peer reviewed publications, as detailed below. Of these, the first five are journal papers, the sixth paper was accepted for the ION Pacific PNT conference based on an extended abstract, whereas the remaining two are peer-reviewed conference proceedings. Appendix A gives the copyright authorisation, Appendix B gives the signed declarations by fellow authors for co-authored publications, whereas Appendix C gives evidence that all papers are peer-reviewed and have been published.

1. **Deo MN**, El-Mowafy A (2019) A method for Precise Point Positioning with Integer Ambiguity Resolution with Triple-frequency GNSS Data, Measurement Science and Technology, 30(6): 065009, https://doi.org/10.1088/1361-6501/ab0945
2. **Deo MN**, El-Mowafy A (2018) Comparison of Advanced Troposphere Models for Aiding Reduction of PPP Convergence Time in Australia, Journal of Spatial Science, https://doi.org/10.1080/14498596.2018.1472046, published online 24 May 2018.
3. **Deo MN**, El-Mowafy A (2018) Triple Frequency GNSS Models for PPP with Float Ambiguity Estimation – Performance Comparison using GPS, Survey Review, 50(360): 249-261, doi: 10.1080/00396265.2016.1263179.
4. El-Mowafy A, **Deo MN**, Kubo N (2016) Maintaining real-time precise point positioning during outages of orbit and clock corrections. GPS Solutions, 21(3), 937-947. DOI:10.1007/s10291-016-0583-4.
5. El-Mowafy A, **Deo M**, Rizos C (2016) On Biases in Precise Point Positioning with Multi-Constellation and Multi-Frequency GNSS Data. Measurement Science and Technology, 27(3), 035102. DOI:/10.1088/0957-0233/27/3/035102.
6. **Deo MN**, El-Mowafy A (2017) Ionosphere Augmentation for accelerated convergence in Precise Point Positioning with multi-frequency and multi-constellation GNSS, paper presented at ION Pacific PNT 2017 Conference, Honolulu, Hawaii, May 1-4, 2017.
7. **Deo MN**, El-Mowafy A (2016) Triple Frequency precise point positioning with multi-constellation GNSS, IGNSS Conference, UNSW Australia, 6–8 December 2016.

8. **Deo MN**, El-Mowafy A (2015) Cycle Slip and Clock Jump Repair with Multi-Frequency Multi-Constellation GNSS data for Precise Point Positioning, IGNSS Conference, Surfers Paradise, Qld, Australia, 14-16 July 2015.

TABLE OF CONTENTS

LIST OF ABBREVIATIONS

ANTEX	Antenna Exchange Format
APC	Antenna Phase Centre
AR	Ambiguity Resolution
ARNS	Aeronautical Radio Navigation Services
ARP	Antenna Reference Point
BDS	Beidou Satellite Navigation System
BoM	Bureau of Meteorology
BSSD	Between Satellite Single Differenced
C/A	Coarse Acquisition
CDMA	Code Division Multiple Access
CODE	Centre for Orbit Determination
CoM	Centre of Mass
DCB	Differential Code Bias
DEM	Digital Elevation Model
DGPS	Differential GPS
DLR	German Aerospace Centre
DOP	Dilution of Position
ECEF	Earth-Centred Earth-Fixed
ECMWF	European Centre for Medium-Range Weather Forecasts
EOP	Earth Orientation Parameters
ERP	Earth Rotation Parameters
ESA	European Space Agency
EU	European Union
EWL	Extra Wide-Lane
FAA	Federal Aviation Administration
FDMA	Frequency Division Multiple Access
FOGM	First Order Gauss-Markov
GAGAN	GPS Aided GEO Augmented Navigation
GDAS	Global Data Assimilation System
GDOP	Geometric Dilution of Position
GEO	Geostationary Earth Orbit
GIF	Geometry-free and Ionosphere-free

GIM	Global Ionospheric Model
GIOVE	Galileo In Orbit Validation Experiment
GLONASS	Global'naya Nawigatsionnaya Sputnikowaya Sistema
GNSS	Global Navigation Satellite Systems
GPS	Global Positioning System
GPST	GPS Time
GPT	Global Pressure Temperature
GSO	Geosynchronous Orbit
HF	High Frequency
IAG	International Association of Geodesy
IAU	International Astronomical Union
ICD	Interface Control Document
IERS	International Earth Rotation Service
IF	Ionosphere-free
IGS	International GNSS Service
IGSO	Inclined Geosynchronous Orbit
IOV	In-Orbit Validation
IRNSS	Indian Regional Navigation Satellite System
ISRO	Indian Space Research Organisation
ISTB	Inter-System Time Bias
ITRF	International Terrestrial Reference Frame
ITU	International Telecommunication Union
JAXA	Japan Aerospace Exploration Agency
LAMBDA	Least Squares Ambiguity Decorrelation Adjustment
MEO	Medium Earth Orbit
MFMC	Multi-Frequency and Multi-Constellation
M-GEX	Multi-GNSS Experiment
MW	Melbourne-Wübbena
NL	Narrow-Lane
NOAA	National Oceanic and Atmospheric Administration
NWM	Numerical Weather Model
PCV	Phase Centre Variations
PDOP	Position Dilution of Position

PPP	Precise Point Positioning
PPP-AR	Precise Point Positioning with Ambiguity Resolution
PRN	Pseudo Random Noise
Ps	Probability of Ambiguity Resolution Success Rate
QZSS	Quazi Zenith Satellite System
RCP	Right Circularly Polarised
RIM	Regional Ionospheric Model
RINEX	Receiver Independent Exchange Format
RMS	Root Mean Square
RMS	Root Mean Square Error
RNSS	Regional Navigation Satellite Systems
RTCM	Radio Technical Commission for Maritime
RTK	Real Time Kinematic
RTS	Real Time Service
RW	Random Walk
SA	Selective Availability
SAIF	Sub-meter Class Augmentation with Integrity Function
SBAS	Space Based Augmentation System
SIS	Signal-in-Space
SPP	Single Point Positioning
SPS	Standard Positioning Service
std	Standard Deviation
SVN	Space Vehicle Number
TEC	Total Electron Content
TECU	Total Electron Content Unit
UPD	Uncalibrated Phase Delay
USNO	United States Naval Observatory
UT	Universal Time
VMF	Vienna Mapping Function
VTEC	Vertical Total Electron Content
WAAS	Wide Area Augmentation System
WGS84	World Geodetic System 1984
WL	Wide-Lane

ZHD	Zenith Hydrostatic Delay
ZPD	Zenith Path Delay
ZWD	Zenith Wet Delay

1. INTRODUCTION

1.1 Background

Precise Point Positioning (PPP) is a technique for determining the precise coordinates of a stand-alone Global Navigation Satellite System (GNSS) receiver without relying on simultaneous measurements from a network or nearby reference receiver. PPP is widely used in applications such as precision agriculture (Guo et al., 2018), precise positioning of ocean buoys (Kuo eta al., 2012), deformation monitoring (Bellone et al, 2014; Aydin et al, 2017), natural hazard monitoring systems, e.g. monitoring of tsunami and earthquakes (Bawden et al, 2016), volcanoes (Lee et al, 2015), landslides (Giovanni, 2012), vehicular navigation, e.g. lane determination (Knoop et al., 2017; de Bakker & Tiberius, 2017) and many more. PPP can provide decimetre level accuracy for kinematic positioning and cm-level accuracy for static surveying, provided that long duration dual-frequency measurements are used with the most precise satellite orbit and clock products (Ebner and Featherstone, 2008). It also offers several advantages over network or relative positioning in terms of operational flexibility and cost effectiveness; including (1) No corrections or simultaneous observations are required from a single or network of reference stations (2) It works globally, and (3) There are no user confusions arising from reference frame realisation (Bisnath and Gao, 2009; Abdel-salam, 2005). However, its main drawback is a long convergence time of typically half an hour required to reach an accuracy of a few cm with static data, and a decimetre with kinematic data. Thus, PPP is an intensively researched topic as researchers continue to work on improving its performance.

Since PPP models process data from a stand-alone receiver, it requires precise modelling of errors which are normally cancelled in relative positioning that include solid earth tide, atmospheric loading, ocean tide loading, Earth rotation effects, satellite phase wind-up error, Sagnac delay, relativistic effects, satellite/ receiver antenna phase centre offset and variation (Heroux and Kouba, 2001). These corrections are determined from a-priori models (IERS, 2010). The precise satellite coordinates and clock errors are also known a-priori from real-time or post-processed products. For real-time PPP, the real-time orbit and clock corrections may be sourced, for example, from the International GNSS Service (IGS) Real-Time Service (RTS), or other commercial providers. For post-processed PPP, the IGS final, rapid or ultra-rapid precise orbit and clock products may be used. The orbit and clock

accuracies of the IGS products for GPS are 2.5cm/ 75ps for the final version, 2.5cm/ 75ps for rapid version, 3cm/ 150ps for the ultra-rapid (observed half), and 5cm/ 1.5ns for the ultra-rapid (predicted half) (Dow et al., 2009).

The availability of GNSS signals from multi-frequency and multi-constellation (MFMC) satellites, and advances in development of precise troposphere (e.g. Lu et al. 2017; Zheng et al., 2017) and ionosphere products (e.g. Banville et al., 2018) gives additional motivation to do further research on their contribution to PPP. These developments present opportunities to develop innovative PPP models that reduce convergence time and improve accuracy compared to the conventional GPS case. However, such integration of data requires careful consideration of the differences between the constellations and signal tracking of the individual frequencies. There are two main categories of PPP models that may be enhanced, including (1) PPP with float ambiguity estimation and (2) PPP with integer Ambiguity Resolution (PPP-AR).

In addition to the availability of MFMC GNSS data, recently there has been an increased development in the availability of precise atmospheric products such as high precision Regional Ionospheric Models (RIM) and troposphere models derived from Numerical Weather Model (NWM) data. These models allow constraining the ionosphere and troposphere errors, instead of estimating these as unknown parameters. Since there are less unknowns to solve for, the geometry of the PPP model is strengthened and hence the solution convergence time may be potentially reduced.

1.2 Literature Review

This section presents an overview of existing GNSS and Regional Navigation Satellite Systems (RNSS), observation equations and the models for PPP with float ambiguity estimation and PPP-AR.

1.2.1 Overview of Existing GNSS and RNSS

Up until recently, PPP research was primarily focused on GPS, and GLONASS to some extent, but a suite of GNSS constellations are now available for civilian use. These include Galileo (European Union (EU) in cooperation with European Space Agency (ESA)) and BeiDou (China). Apart from these, two RNSS are also available including the Quazi-Zenith Satellite System (QZSS) (Japan) and the Indian Regional

Navigation Satellite System (IRNSS) (India) with an operational name NAVIC. GPS is currently going through a modernisation program to transmit new and improved signals. The Block IIF GPS satellites, twelve of which are in operation at present, are transmitting carrier signals on a new civil frequency, L5, centred at 1176.45MHz, in addition to the existing dual-frequency carriers, L1 (1575.42 MHz) and L2 (1227.60MHz) (Montenbruck et al., 2011). The Block IIR-M satellites, seven of which are in operation, are transmitting a civilian code on the L2 carrier, namely the L2C. The Block III satellites, the first of which was launched in December 2018, transmit a new civil code on the L1 carrier, namely L1C.

The GLONASS system regained full operational capability in November 2011 and is also undergoing modernisation to transmit triple-frequency signals using Code Division Multiple Access (CDMA), from Glonass-K1 and K2 satellites (Revnivykh, 2011). The first two of the GLONASS K1 satellites have been launched into operation and an additional 9 are planned for launch in future. These have a CDMA signal centred in the L3 band at 1205MHz. The future K2 satellites will have triple frequency CDMA signals, but this will only be available sometime in the next decade (Wanninger, 2012).

At the time of writing, the BeiDou-2 navigation satellite system has three Medium Earth Orbit (MEO) satellites, six Geostationary Earth Orbit (GEO) satellites and six inclined geosynchronous orbit (GSO) satellites, thus a total of fifteen satellites in operational orbit (http://en.beidou.gov.cn/; https://www.glonass-iac.ru/en/BEIDOU/). These satellites are transmitting signals on three frequencies, namely B1 (1561.098MHz), B3 (1,268.52 MHz) and B2 (1,207.14 MHz) (Lu and Yao, 2014). In addition to this, the Beidou-3 constellation has sixteen satellites in orbit and will eventually grow into a 35-satellite constellation providing global coverage. The BeiDou-3 satellites transmit signals on the three frequencies B1C (same as GPS L1), B2a (same as GPS L5) and B2b (same as Beidou-2 B2) (Lu and Yao, 2014).

The first Galileo satellite, GIOVE A (now inactive) was launched in December 2005 and at present, the Galileo constellation is nearing completion with 22 usable satellites. Galileo signals are transmitted on five frequency bands, namely E1 (same as GPS L1), E6 (same as QZSS LEX frequency), E5 (1191.795 MHz), E5a (same as GPS L5) and E5b (1207.14MHz). The E5a and E5b signals are part of the E5 signal, in its full bandwidth (European Union, 2010).

For the RNSS constellations, the first QZSS satellite (QZ1) was launched on 11 September 2010, and three subsequent satellites (QZ02, GE04 and QZ04) were launched in 2017 (http://qzss.go.jp/en). QZSS satellites transmit signals on the three GPS frequencies as well as a fourth carrier frequency (E6), LEX, on 1278.75MHz (JAXA, 2011). The LEX signal contains high precision corrections for GPS satellite clock and orbits errors as well as tropospheric and ionospheric errors (Hauschild et al., 2012). The IRNSS constellation, known as NAVIC, is fully operational in a defined region bounded by 30°S - 50°N, 30°E - 130°E, with five IGSO and three GEO satellites in orbit (https://www.isro.gov.in/irnss-programme). The NAVIC satellites transmit signals on two frequencies, namely L5 (same frequency as GPS L5) and a S-band frequency (2492.08MHz).

1.2.2 GNSS Observation Model

The observation equation of the carrier phase and pseudorange code measurements for satellite o from one GNSS constellation such as GPS (denoted as G) on frequency i in length units reads

$$P_i^{oG} = \rho^{oG} + c\left(dt_{\mathrm{G}} - dt^{oG} + d_{i_G} - d_i{}^{oG}\right) + T^{oG} + \mu_i I^{oG} + \varepsilon_{\mathrm{P}_i}^{oG} \quad (1)$$

$$\phi_i^{oG} = \rho^{oG} + c(dt_{\mathrm{G}} - dt^{oG}) + T^{oG} - \mu_i I^{oG} + \lambda_i\left(N_i^G + \delta_{i_G} - \delta_i{}^{oG}\right) + \varepsilon_{\phi_i}^{oG} \quad (2)$$

where

- ϕ_i^{oG} and P_i^{oG} are the carrier phase and code observables, in distance units, respectively,
- $\rho^{oG} = \sqrt{(X^o - x)^2 + (Y^o - y)^2 + (Z^o - z)^2}$ is the receiver-satellite geometric range, with X^o, Y^o, Z^o the satellite coordinates and x, y, z the receiver coordinates,
- c is the speed of light in vacuum,
- dt_{G} and dt^{oG} are the receiver and satellite clock errors,
- δ_{i_G} and $\delta_i{}^{oG}$ are the frequency-dependent receiver and satellite hardware phase delays,
- $d_{i_{\mathrm{G}}}$ and $d_i{}^{oG}$ are the frequency-dependent receiver and satellite hardware code delays,

- T^{o_G} the tropospheric delay which is expressed as a Zenith Path Delay (ZPD) scaled by a mapping function, to map the ZPD to the satellite's elevation-dependent slant delay. The ZPD can be further separated into hydrostatic (ZHD) and wet components (ZWD), where the hydrostatic part can be corrected with an a-priori model, e.g. the Saastamoinen model (Saastamoinen 1972), whereas the ZWD delay is estimated as a parameter in the PPP model,
- $\mu_i = \frac{f_1^2}{f_i^2}$ is a dispersive coefficient for conversion of the first-order estimated ionospheric delay on L1 to a chosen frequency $i = 1,2, \dots i_n$, where i_n is the number of frequencies,
- I^{o_G} the ionospheric slant delay for the L1 frequency, of which the impact on the code and phase has opposite signs. The first-order absolute ionospheric delay is typically in the order of several tens of meters, whereas the higher-order terms are in the order of a few cm (Kim & Tinin, 2011),
- N_i^G is the integer ambiguity and the combined term $M_i^G = N_i^G + \delta_{i_G} - \delta_i{}^{o_G}$ is the non-integer ambiguity due to the presence of initial phase delays for the receiver δ_{i_G} and satellite $\delta_i{}^{o_G}$ that originate from the frequency oscillators (Ge et al., 2008),
- λ_i the wavelength corresponding to frequency *i*,
- $\varepsilon_{\Phi_i}^{o_G}, \varepsilon_{\mathrm{P}_i}^{o_G}$ the carrier phase and pseudorange observation noise, including multipath, which is larger for the code observable compared to the phase observations. This is not modelled in the functional model, where its expectation is assumed equal to zero, but its impact is considered in the stochastic model.

For an additional constellation (e.g. Beidou denoted as C) with satellite p, the equations for carrier phase and pseudorange code measurement for frequency j

$$P_j^{p_C} = \rho^{p_C} + c\left(dt_G - dt^{p_C} + d_{j_C} - d_j{}^{p_C}\right) + T^{p_C} + \mu_j I^{p_C} + ISTB_{G-C} + \varepsilon_{P_j}^{p_C} \quad (3)$$

$$\phi_j^{p_C} = \rho^{p_C} + c(dt_G - dt^{p_C}) + T^{p_C} - \mu_j I^{p_C} + ISTB_{G-C} + \lambda_j\left(N_j^{p_C} + \delta_{j_G} - \delta_j{}^{p_C}\right) + \varepsilon_{\phi_j}^{p_C} \quad (4)$$

The terms are similar to the ones described for system G above. $ISTB_{G-C}$ is the inter-system time bias between systems G and C (i.e. GPS and Beidou), combined for the

receiver and the satellite. It includes the receiver clock offset, i.e. dt_{G-C} and the satellite clock offset dt^{G-C} assumed at the same level for all satellites from one system w.r.t GPS. Similar equations may be derived for other constellations such as Galileo denoted as E or QZSS, denoted as J.

1.2.3 PPP Models with Float Ambiguity Estimation

The traditional PPP model with float ambiguity estimation was firstly presented by Zumberge et al. (1997), where it was shown that cm-level repeatability can be achieved with dual-frequency, undifferenced GPS measurements from a network. The functional model, often known as the standard or traditional PPP model, consists of the dual-frequency ionosphere-free linear combinations for the pseudorange and carrier phase measurements. In the standard PPP model, the satellite and receiver hardware delays for the carrier and code measurements are lumped into the receiver clock and ambiguity terms, by assuming them to be constants over a short period, in order to remove the rank deficiency. The ionosphere-free equations as presented as

$$P_{if}^{o_G} = \rho^{o_G} + c(dt_{\mathrm{G}} - dt^{o_G}) + T^{o_G} + \varepsilon_{\mathrm{P}_{if}}^{o_G} \tag{5}$$

$$\phi_{if}^{o_G} = \rho^{o_G} + c(dt_{\mathrm{G}} - dt^{o_G}) + T^{o_G} + \lambda_{if} N_{if}^{G} + \varepsilon_{\phi_{if}}^{o_G} \tag{6}$$

Where the $'if'$ term denotes ionosphere-free combination. In this simplistic model, the receiver code hardware biases are included in the receiver clock offset term in the code observation, whereas the satellite code biases need correction if using the C1 code instead of P1 by applying a differential code bias (DCB) obtained from an external source such as IGS. In traditional dual-frequency PPP, the DCB correction is not required if using the P1 code in the IF combination. The DCB must be applied for single frequency PPP. The phase satellite and receiver hardware biases are absorbed into the non-integer ambiguity term. The first order ionospheric delay is eliminated in this combination, but the inherent noise is amplified by a factor of 2.978 for the GPS L1/ L2 case, due to the error propagation law. The precise satellite orbit and clock estimates are obtained from a regional or global network of GPS receivers such as the International GNSS Service (IGS) (Dow et al., 2009).

Considering the standard PPP model for dual-frequency observations from *n* tracked satellites from one system, e.g. GPS, there are *2n* measurements and *5+n* unknown parameters including the receiver position (x, y, z), receiver clock error

dt_{G}, tropospheric ZHD and the ionosphere-free float ambiguities for each individual satellite. A solution is possible with at least five satellites by using a sequential least squares or Kalman Filter. This model requires a long convergence time to stabilise the float ambiguities, taking approximately 30 minutes to achieve sub decimetre-level accuracy and few hours to achieve cm-level accuracy, which makes it impractical for most real-time precise applications. The main factors which cause the long convergence time include the high noise amplification of the code measurements, the number and geometry of satellites tracked, user environment, user dynamics and measurement quality (Bisnath and Gao, 2009).

Another approach to PPP includes the use of between satellite single differencing (BSSD) of the ionosphere-free code and phase measurements in addition to the use of precise satellite orbit and clock products (Colombo et al., 2004; Chen et al., 2005). Assuming that the receiver bias is the same for all satellites from the same constellation, the advantage of this model is that the receiver hardware biases are eliminated. From eqns. (1) and (2), the BSSD observation equations from one receiver to two satellites *o* and *p* reads:

$$P_{if}^{poG} = \rho^{poG} - c(dt^{poG} + d_i{}^{poG}) + T^{poG} + \varepsilon_{\mathrm{P}_{if}}^{poG} \tag{7}$$

$$\phi_{if}^{poG} = \rho^{poG} - cdt^{poG} + T^{poG} + \lambda_{if} N_i^{poG} + \varepsilon_{\phi_{if}}^{oG} \tag{8}$$

The receiver differential hardware delays are eliminated for the code and phase, and so is the initial fractional phase delay of the receiver, but the measurement noise is further increased by a factor of √2, in addition to the amplification due to the ionosphere-free amplification. The differential hardware phase delay at the satellite is lumped with the ionosphere-free ambiguity term. If the receiver uses the C/A code rather than P1 code, the satellite DCB corrections available from sources such as IGS are used to remove the satellite differential code delay. For *n* visible satellites using the BSSD model, there are *2n-2* measurements and *3+n* unknown parameters; the receiver position (x, y, z), the single differenced troposphere error and $n-1$ single differenced ionosphere-free float ambiguities. This model gives cm and decimetre-level accuracies for static and kinematic data, respectively with a typical convergence time of 30min, thus a similar performance to the traditional model (Chen et al., 2005).

Gao and Shen (2002) used an undifferenced mixed code-carrier ionosphere-free linear combination in their PPP model, which reduces the code noise by a factor of 0.5. Each mixed code-carrier combination is simply an average of the code and phase measurements from a single frequency, and two such equations are used in the functional model for frequencies i and j as follows:

$$\Theta_i^{oG} = \frac{P_i^{oG} + \phi_i^{oG}}{2} = \rho^{oG} + c(dt_G - dt^{oG}) + T^{oG} + \frac{\lambda_i N_i^G}{2} + \varepsilon_{\Theta_i}^{oG} \quad (9)$$

$$\Theta_j^{oG} = \frac{P_j^{oG} + \phi_j^{oG}}{2} = \rho^{oG} + c(dt_G - dt^{oG}) + T^{oG} + \frac{\lambda_j N_j^G}{2} + \varepsilon_{\Theta_j}^{oG} \quad (10)$$

These are together with the dual-frequency phase only ionosphere-free combination given in eqn. 5. Like the standard PPP model, the satellite and receiver hardware delays for the carrier phase measurements are lumped into the ambiguity terms, whereas the receiver code hardware bias is lumped with the receiver clock term. There is one mixed code-carrier combination for each frequency, i and j, with a reduction in the pseudorange noise by 50%. Compared to the traditional model, the author's of this approach reported that the solution is more stable, giving sub decimetre-level accuracy with just one hour of data. With long duration data, accuracy was at the same level as the traditional model, but an improvement of 13% reduction was achieved in convergence time (Gao and Shen, 2002).

At the commencement of this research, there were limited PPP models with float ambiguity estimation that took advantage of the triple frequency measurements. This was the motivation for further research into development of triple frequency PPP models to investigate the possibility of improving the convergence time and accuracy.

1.2.4 PPP with Integer Ambiguity Resolution

In order to achieve cm-level accuracy in near real-time, many researchers have attempted integer ambiguity resolution by estimating the satellite initial fractional phase biases using network data, and transferring these corrections to the user to resolve integer ambiguities. This approach is known as PPP-AR.

Ge et al. (2008) presented a BSSD model for estimating the single differenced satellite initial fractional phase bias using network GPS data to fix integer ambiguities. In this method, the fractional part of the satellite wide-lane (WL)

uncalibrated phase delay (UPD) is estimated by using data from a network of reference stations to estimate the receiver integer WL ambiguities, which are introduced into the ionosphere-free phase combination to estimate the narrow-lane (NL) UPD. If these biases are broadcast to real-time users, these may be applied to raw BSSD measurements to eliminate the receiver biases to isolate the integer ambiguities. The integer WL ambiguity is firstly estimated by multi-epoch averaging of Melbourne-Wübbena (MW) linear combination of measurements. This, along with the NL UPD is introduced in a carrier phase only ionosphere-free (IF) equation to fix the integer NL ambiguity. Ge et al. (2008) showed that the ambiguity fixed solutions with this method had an improvement of 27% in repeatability and 30% in the east component compared to the float solutions, with a probability of AR success rate of 80%. However, due to the short wavelength of the NL ambiguity ($\lambda_{NL} = 10.7\ cm$), it typically takes around 30 minutes to get a precise solution (Geng and Bock, 2013). Geng et al. (2009) modified this technique by using only one single-differenced NL UPD between a pair of satellites within each pass over a regional network to fix integer ambiguities. This method gave an accuracy of 5 mm, 5 mm and 14 mm in the East, North and Up components when using hourly data.

Laurichesse et al. (2009) presented a similar method for fixing undifferenced integer phase ambiguities, which estimates the undifferenced WL ambiguities and then fixes the L1 ambiguities over a network. The authors showed that the ambiguity fixing success rate was 90% for the network of 10 stations in Western Europe and accuracy was at the cm-level. Collins et al. (2010) presented a method for undifferenced ambiguity resolution based on decoupling the distinct oscillator parameters for the carrier phase and pseudorange measurements, allowing integer ambiguity estimation. This required estimation of satellite code and phase clock corrections from a GPS network to enable single user PPP. A significant improvement of convergence time was achieved with 90% of solutions converging to 2cm horizontal accuracy after 60min, compared to 10cm for standard PPP (Collins et al., 2010). Bertiger et al. (2010) presented an ambiguity resolution algorithm for single receiver phase ambiguity resolution, now implemented in the GIPSY-OASIS software. The algorithm also uses widelane phase bias estimates from a global network of GPS stations. The repeatability of daily coordinate estimates was improved by 30% in east compared to traditional solution. For static case, the repeatability was at the sub-cm level, whereas for the kinematic case, the

repeatability was slightly higher above 1 cm (Bertiger et al., 2010). Based on the PPP-RTK approach, a GNSS receiver manufacturer, Trimble, has developed a global real-time PPP infrastructure and service, known as CENTERPOINT RTX (Leandro et al., 2011). Although the authors reported real-time horizontal accuracies of 1-2cm (1-sigma), the claimed convergence time for RTX remains a problem at 10-45 minutes.

In addition to the dual-frequency models, Geng and Bock (2013) presented a PPP-AR approach for the triple-frequency GPS case, where the L2/L5 extra wide-lane (EWL) ambiguity was firstly resolved using the MW combination. This was then expressed in terms of L1/L2 WL carrier phase measurements to form a carrier phase only IF observable with $\lambda_{WL} = 3.4m$. This was used with the L1/L2 dual-frequency ionosphere-free pseudorange only linear combination to fix the L1/L2 WL ambiguity that was subsequently used to fix the NL ambiguity. Li et al. (2014) enhanced the step for estimating the WL ambiguity by using an ionosphere-free triple frequency linear combination of pseudorange measurements with measurement noise minimisation properties. However, these models could be further enhanced by enforcing ionosphere and troposphere constraints based on advanced Regional Ionosphere Models (RIM) and Numerical Weather Models (NWM), respectively. Furthermore, the triple frequency ionosphere-free carrier phase linear combinations used in Li et al (2014) are strongly affected by measurement noise and multipath, due to the significantly large coefficients used in the linear combinations, when applying the covariance propagation law. This was the motivation for conducting further research in this thesis to address this issue.

1.2.5 PPP with Combined GPS and GLONASS

An early GPS-GLONASS combined PPP model was presented in Cai and Gao (2007), where the traditional PPP model was adopted.

In integrating multi-system GNSS PPP, due consideration should be made to the GLONASS inter-frequency biases and the inter-system biases between the different systems and signals (Hegarty et al., 2005; Phelts 2007). Apart from having its own time and coordinate reference system, GLONASS signals are modulated by Frequency Division Multiple Access (FDMA). This means each GLONASS satellite has its own transmitting frequency, and due to this the signals from different GLONASS satellites take different paths through the high frequency (HF) part of the

receiver (Robach, 2000). This results in inter-frequency hardware biases in the receiver, which must be accounted for in high precision PPP. The inter-frequency biases can be estimated relative to one satellite, or relative to an average of all satellites. The common part (the reference satellite bias or the average bias) gets absorbed into the receiver clock term and the differential part is left to be accounted for. The inter-frequency biases may be regarded as linear functions of the signal frequency (Pratt et al., 1998), and the carrier phase biases can reach up to 0.2ns (>5cm) for adjacent frequencies and 2.4ns (73cm) for complete L1 or L2 frequency bands (Wanninger, 2012). The code inter-frequency biases for L1 and L2 frequency bands are typically at the metre level (Robach, 2000). When combining GPS with GLONASS, the inter-frequency biases are the same for all GPS satellite signals that have the same frequency, but the GLONASS biases are different for each satellite. Another consideration is that receivers have different realisations of the GLONASS and GPS system times, thus there is a system time offset between the two. The GLONASS observation equations for satellite p and frequency j are (Robach, 2000)

$$P_j^{p_R} = \rho^{p_R} + c\left(dt_R - dt^{p_R} + d_{j_R} - d_j{}^{p_R}\right) + T^{p_R} + \mu_j I^{p_R} + ISTB_{G-R} + \varepsilon_{P_j}^{p_R} \quad (11)$$

$$\phi_j^{p_R} = \rho^{p_R} + c(dt_R - dt^{p_R}) + T^{p_R} - \mu_j I^{p_R} + ISTB_{G-R} + \lambda_j\left(N_j^{p_R} + \delta_{j_R} - \delta_j{}^{p_R}\right) + \varepsilon_{\phi_j}^{p_R} \quad (12)$$

where the postscript ^{R} denotes a GLONASS satellite; $ISTB_{G-R}$ is the difference between the receiver clock offset between GPS and GLONASS, $ISTB_{G-R} = dt_R - dt_G$; d_{j_R} and $d_j{}^{p_R}$ contain the inter-frequency code biases in the receiver and satellites; δ_{j_R} and $\delta_j{}^{p_R}$ are the inter-frequency carrier phase biases for the receiver and satellite, respectively.

The inter-frequency biases for GLONASS are not eliminated by differencing across a reference satellite, because they are different for each satellite, thus need calibration by other means. The GLONASS K satellites use Code Division Multiple Access (CDMA) signals, where all satellites transmit on the same frequencies. Although the inter-frequency biases need not be considered when using GLONASS K satellites, the drawback is that only two such satellites are in operation. In the combined GPS-GLONASS PPP model of Cai and Gao (2007), the inter-frequency

biases were not considered and only the system time offsets were estimated. The GPS-GLONASS PPP model showed improvements in accuracy and solution convergence time, though results were not conclusive due to the partial completion of the GLONASS constellation at the time of study (Cai and Gao, 2007).

1.2.6 PPP with Multi-Frequency and Multi-Constellation GNSS

Integrating MFMC GNSS data provides improved satellite geometry for better PPP performance in challenging environments such as open-pit mines, urban canyons and forests. A combined GPS-Galileo model was attempted in Cao et al. (2010), based on the traditional PPP model. However, at this time two Galileo satellites, GIOVE-A and -B were in operation and the accuracy of their clocks was lower than GPS, resulting in degraded PPP performance with GPS+Galileo. At present, the precise orbit and clock products with comparable accuracy to GPS are available from several IGS analysis centres for post processed PPP. Cai et al. (2015) presented PPP results with four constellations, namely GPS, BeiDou, GLONASS and Galileo. For GPS-only PPP, the RMS of positioning errors after convergence was 3.9cm, 1.6cm and 5.7cm in the East, North and Up components, respectively. The GPS/Beidou PPP results improved the positioning accuracy by 28%, 6% and 7% and convergence time by 26%, 13% and 14% over GPS-only PPP. The GPS/Beidou /GLONASS PPP further improved positioning accuracy and decreased convergence time. However, adding Galileo did not result in a significant improvement in performance, due to the limited satellites available the time (Cai et al., 2015).

Rabbou and El-Rabbany (2017) also proposed a combined PPP model which integrated GPS, GLONASS, Galileo and Beidou. The BSSD model was developed based on ionosphere-free combination of the observations. The inter-system biases between GPS and other GNSS systems were estimated as unknown parameters. There were substantial benefits in PPP performance with GPS + Galileo + BeiDou + GLONASS as the accuracy after 15 minutes of initialisation improved by 8cm, 6cm and 11cm in the latitude, longitude and height components respectively, compared to the GPS only case (Rabbou and El-Rabbany, 2017). Additionally, the BSSD model was found to give superior performance than the traditional undifferenced model. Li et al. (2015) also presented a multi-constellation PPP model for GPS, GLONASS, Galileo and Beidou combined case. Here, the ionosphere constraints were used to estimate the ionospheric error as an unknown parameter rather than use of

ionosphere-free combinations. The inter-system and inter-frequency biases were calculated relative to GPS and were treated as constants over the observation period. The PPP convergence performance was much faster for the multi-constellation case compared to individual constellations. After 15 minutes of convergence, the position accuracy improved by 8.8cm, 3.8cm and 6.3cm in the East, North and Height components respectively, compared to the GPS only case (Li et al, 2015).

1.3 Thesis Objectives and Outline

PPP is an important technique that is widely used in several applications such as precision agriculture (Guo et al., 2018), precise positioning of ocean buoys and marine platforms (Kuo et al., 2012; Geng et al., 2010), deformation monitoring (Bellone et al., 2016; Aydin et al., 2017), natural hazard monitoring systems, e.g. tsunami and earthquakes (Bawden et al., 2016), volcanoes (Lee et al., 2015), landslides (Giovanni, 2012), lane determination in vehicular navigation (Knoop et al., 2017; de Bakker & Tiberius, 2017; Victor et al., 2017), high-rate structural vibration (Yigit and Gurlek, 2017), and many more. PPP is an actively researched topic and researchers continue to work on improving its performance by reducing solution time and improving or maintaining accuracy. The presence of multi-frequency signals from multi-constellations, along with advances in development of precise troposphere (e.g. Lu et al., 2017; Zheng et al., 2017) and ionosphere products (e.g. Banville, 2018) gives additional motivation to research this topic further.

1.3.1 Research Aim, Objectives and Hypotheses

The aim of this research is to develop approaches for improving the performance of PPP with MFMC data by addressing some of the challenging aspects of PPP. These challenging aspects include developing enhanced PPP models (both float ambiguity estimation and PPP-AR approaches) with triple frequency data, investigating the impact of constraining atmospheric parameters by using precise atmospheric products, and maintaining real-time accuracy during loss of precise orbit and clock corrections.

The six objectives that were identified in this research, with their respective hypotheses and testing are as follows:

1. Develop and validate methods that use triple frequency data to improve the data pre-processing steps of detection and repair of cycle slips and receiver clock jumps. Hypothesis: availability of triple frequency data

improves the likelihood of the detection and repair of cycle slips and clock jumps.

2. Identify the biases that occur when integrating MFMC data, and propose models for treating these biases in order to get the highest possible PPP accuracy. Hypothesis: the MFMC biases may be treated effectively by mathematical modelling of the measurements or though calibration from external sources.
3. Develop and validate novel triple frequency models with float ambiguity estimation that have superior performance than the present day dual-frequency model. Hypothesis: availability of triple frequency data enables development of enhanced PPP models with float ambiguity estimation that have superior performance than the standard dual-frequency model.
4. Extend the PPP with float ambiguity estimation model to constraint the atmospheric parameters through use of externally sourced precise atmospheric products. Investigate the required accuracy of these products to enable improved performance in terms of PPP convergence time and accuracy. Hypothesis: constraining the atmospheric parameters in the PPP model through use of precise atmospheric products improves the convergence time and maintains accuracy.
5. Develop and validate a method for maintaining real-time PPP accuracy during data communication outages, during which the real-time precise orbit and clock corrections are not available to a user. Investigate the period for which sub-decimetre PPP accuracy can be maintained after such loss of data communication. Hypothesis: real-time PPP accuracy can be maintained for a significant duration after loss of data communication.
6. Develop and validate an improved triple frequency PPP-AR method that uses atmospheric constraints. Hypothesis: an enhanced PPP-AR method with atmospheric constraints offers substantial benefits over the current triple frequency PPP-AR methods.

1.3.2 Innovative Contributions of Research

This research proposes innovative PPP models for both PPP with float ambiguity estimation and PPP with integer ambiguity resolution, since each approach is suitable for a range of applications. These models take advantage of the MFMC GNSS data, but address the challenges involved with integrating such data. When

integrating multi-constellation data, only the CDMA signals are considered in the modelling.

Ensuring data quality and assurance is a mandatary first step for any PPP software, prior to using the data for computing precise receiver position. If left unaccounted for, data quality issues such as cycle slips and clock jumps can adversely affect PPP convergence time, accuracy and precision. Therefore, the initial focus of this thesis is on pre-processing MFMC data with the aim of addressing data quality issues such as cycle slips and clock jumps. The benefit of the third frequency is investigated for detection and repair of cycle slips and clock jumps.

Integration of MFMC data results in various inter-system and inter-frequency biases (if using GLONASS) that must be dealt with in order to get the highest precision. Therefore, a detailed study is conducted on these biases and their sources. Methods are proposed for treatment of these biases when implementing the MFMC PPP model.

Following this, enhanced models are developed based on the existing float ambiguity estimation PPP dual-frequency models, including the undifferenced traditional model (Zumberge et al., 1997) and the mixed code-carrier model (Gao and Shen, 2002). The third frequency is utilised to improve the PPP performance in terms of convergence time and positional accuracy. A new PPP model is also developed and tested, which estimates the slant ionospheric error using the third additional frequency, rather than forming linear combinations to eliminate it. The proposed triple frequency models are inter-compared with each other as well as the standard dual-frequency model, in terms of solution convergence time and accuracy.

The float ambiguity estimation PPP models must deal with atmospheric errors including the troposphere and ionosphere, if not using the IF combination. This research found that instead of forming ionosphere-free linear combinations, constraining the ionospheric error with an external model results in a reduction of the overall number of parameters to solve for in the PPP model. This is because the ionosphere error affects each receiver to satellite signal and is not isotropic as is the case of the troposphere error, which can be projected onto a zenith direction by applying a mapping function. This reduction of parameters improves the measurement geometry and significantly reduces convergence time. Recent research has intensified on the development of high precision RIMs determined from a ground network of GNSS stations in a regional area. RIM accuracy better than 0.25 Total

Electron Content Unit (TECU) is attainable with inter-station separation distance of 100km (Rovira-Garcia et al, 2016). In this thesis, the float ambiguity estimation PPP model is tested by constraining the ionosphere errors with RIMs precisions in the range 0.1-1.0 TECU. The resulting convergence time and achievable accuracy is compared to the standard dual-frequency PPP model.

The application of high precision troposphere models derived from NWM data is next investigated for further improving the convergence time in float ambiguity estimation PPP models. The tropospheric Zenith Hydrostatic Delay (ZHD) from several troposphere models derived from empirical and NWM data are firstly compared to the IGS zenith troposphere delay product. For the first time, the NWM obtained from the Australian Bureau of Meteorology (BoM) is used in the analysis, which gave the highest accuracy with mean errors between -0.034m to 0.029m and standard deviation better than 0.045m. A troposphere constraint based on the BoM NWM data is then applied to the float ambiguity estimation PPP model, and the improvements in results are discussed.

The next focus of the research is on maintaining real-time PPP accuracy during communication outages, where the precise orbit and clock corrections become unavailable. This is a serious problem for real-time PPP users who as a result of these disruptions, face loss of productivity due to the additional time and costs incurred in waiting for the corrections to resume and the PPP solution to converge again. Thus, a detailed study is carried out on development of methods for forecasting the satellite orbit and clock corrections during data outages to maintain PPP accuracy.

Finally, the focus of the thesis changes from float PPP to improving PPP-AR models using triple frequency GNSS data and ionospheric constraint. Firstly, the development of an enhanced linear combination is investigated for rapid fixing of the EWL and WL ambiguities, building on the approach proposed by Ge et al. (2008). It is aimed to improve the performance of this linear combination compared to the MW linear combination used in many dual-frequency PPP-AR models. A full rank triple frequency carrier phase only PPP-AR model is investigated with atmospheric constraints for rapid integer ambiguity resolution. The carrier phase equations in this model are formulated in terms of individual carrier phase ambiguities, which is estimated using the Least Squares Ambiguity Decorrelation Adjustment (LAMBDA) method (Teunissen, 1995). This proposed approach was found to give superior

performance than the method given in Li et al. (2014) when a high precision RIM is used. The proposed method maintains high accuracy when the carrier phase measurements get noisier due to multipath or other effects, unlike the method of Li et al. (2014).

This thesis is structured by the chapters in the order given below, where the publications related to each chapter are given with specific objectives. The conclusion for each publication is contained within itself. The final chapter (9) gives an overall conclusion which summarises the findings of the whole thesis. Chapter 11 presents the references for Chapters 1 and 9. The additional references for Chapters 2-8 are listed at the end of the enclosed papers.

1.3.3 Outline of Thesis

This section gives an outline of the chapters forming the body of this thesis.

Chapter 2: Improved Cycle Slip and Clock Jump Detection and Repair with Triple Frequency Data for PPP

This chapter is covered by the following publication:

- Deo MN, El-Mowafy A (2015) Cycle Slip and Clock Jump Repair with Multi-Frequency Multi-Constellation GNSS data for Precise Point Positioning, IGNSS Conference, Surfers Paradise, Qld, Australia, 14-16 July 2015.

This paper presents algorithms for detecting and repairing cycle slips and clock jumps using MFMC GNSS data. It will be shown that availability of a third frequency enables reliable validation of detected cycle slips, because the third frequency enables identification of the frequency on which the cycle slip occurred. A clock jump detection and repair procedure is proposed for a receiver which shows jumps in both carrier phase and code measurements. The proposed method uses the average code and phase linear combination and applies to static data. A spline function is used to approximate the data for a pre-defined time window prior to each measuring epoch and a test is performed for detecting presence of a clock jump by comparing the interpolated value to measured value. The algorithm can effectively determine clock jumps for single frequency single constellation data as well as MFMC data. However, MFMC GNSS data adds redundancy, hence improves the reliability of the clock jump detection algorithm. It is recommended to detect and

repair clock jumps when using PPP to allow improved modelling of the receiver clock offset in the dynamic model.

Chapter 3: Dealing with biases in PPP with Multi-Frequency and Multi-Constellation Data

This chapter is covered by the following publication:

- El-Mowafy A, Deo M, Rizos C (2016) On Biases in Precise Point Positioning with Multi-Constellation and Multi-Frequency GNSS Data. Measurement Science and Technology, 27(3), 035102. DOI:/10.1088/0957-0233/27/3/035102

When integrating MFMC GNSS data to perform PPP, several measurement biases occur which must be correctly modelled and treated in order to achieve the highest positional accuracy, improve convergence time and allow for integer ambiguity resolution. This paper firstly reviews all these biases, including satellite and receiver hardware biases, differential code hardware biases, differential phase biases, initial fractional phase biases, inter-system receiver time biases, and system time scale offset. PPP models that take account of these biases are presented for two cases using ionosphere-free observations. The first case applies when the primary signals are used in the PPP model, i.e. signals that are used to generate precise orbits and clock corrections (such as L1 and L2 P(Y) for GPS, and E1 and E5a for Galileo). The second case applies when using signals in addition to the primary ones. In both cases, measurements from single and multiple constellations are addressed. It is suggested that the satellite-related code hardware biases be handled as calibrated quantities that are obtained externally from multi-GNSS experiment products, and the fractional phase cycle biases be obtained from a network to allow for integer ambiguity fixing. Some receiver-related biases are removed using between-satellite single differencing (BSSD), whereas other receiver biases such as inter-system biases need to be estimated. The test results show that the treatment of biases significantly improves PPP solution convergence in the float ambiguity mode, and leads to ambiguity-fixed PPP within a few minutes with a small improvement in solution precision. It is pointed out that the IGS can play a major role in supporting MFMC PPP users by producing precise orbit and clock corrections for each GNSS satellite and each individual frequency, rather than the IF combinations of the frequencies. This will enable PPP users to apply these corrections to raw measurements prior to forming any linear combination, thus avoiding further complications. Furthermore, the

calibration of satellite biases by external organizations would enable PPP users to perform integer ambiguity resolution resulting in a significantly reduced solution convergence time.

Chapter 4: Triple Frequency GNSS Models for PPP with Float Ambiguity Estimation

This chapter is covered by the following two publications:

- **Deo MN**, El-Mowafy A (2018) Triple Frequency GNSS Models for PPP with Float Ambiguity Estimation – Performance Comparison using GPS, Survey Review, 50(360): 249-261, doi: 10.1080/00396265.2016.1263179.
- **Deo MN**, El-Mowafy A (2016) Triple Frequency precise point positioning with multi-constellation GNSS, IGNSS Conference, UNSW Australia, 6–8 December 2016.

These papers present improved PPP models with float ambiguity estimation that utilise the triple frequency data from multi-constellation GNSS. The focus is on using the third frequency to improve the convergence time in the standard dual-frequency PPP model, where typically 30 minutes or more is required to reach an accuracy of a few centimetres.

In the first paper, the triple-frequency measurements from modernised GPS as well as other GNSS constellations are used to formulate new models that provide better performance than the widely used dual-frequency ionosphere-free PPP model. Two new PPP models are proposed that use triple-frequency data, which were designed to accelerate convergence of the carrier phase float ambiguities. The first model uses a triple-frequency ionosphere-free linear combination that has minimum noise propagation and geometry preserving properties. The second model uses a mixed code and carrier phase linear combination with the same properties. A third model is also implemented, which uses individual un-combined triple-frequency measurements.

The three models were validated using triple-frequency GPS data and their performance was compared to the traditional dual-frequency model in terms of the convergence time taken to achieve and maintain a uniform 3-dimensional accuracy of 5cm. Testing included PPP processing of 1-hour measurement blocks using 1-8 days of data from three locations in Australia. It was shown that all the three triple-frequency models had improved solution convergence time when compared to the

traditional PPP dual-frequency model. The convergence time when using the triple-frequency ionosphere-free model improved by 11% (3.1 min), the improvement was 9% (2.6 min) when using the mixed code-phase model, whereas the individual un-combined model resulted in 8% (2.4 min) improvement. The positional accuracy after convergence for all the triple-frequency algorithms was similar and showed marginal improvement at the 1 mm level, compared to the present dual-frequency model. These results demonstrate the significance of the triple frequency observations for future PPP applications. The analysis of the individual un-combined model revealed that use of externally provided ionosphere corrections can potentially improve the solution convergence time, which is investigated further in the next chapter.

The second paper extends the triple-frequency ionosphere-free model to the multi-constellation scenario, where additional biases must be considered to get the best accuracy. This paper firstly describes the various biases in multi-constellation PPP models and presents the equations for applying the satellite DCB products available from the IGS Multi-GNSS Experiment (MGEX) for each constellation and transmission signal. Following this, the triple frequency ionosphere-free PPP model was tested with hourly blocks of multi-constellation data from GPS, Beidou and Galileo at four sites covering the Australian continent. Improvements in both positioning accuracy by up to 5mm RMSE and convergence times by up to 11.5 minutes were noted at the four sites, when using the MFMC data compared to the GPS-only dual-frequency PPP case. Overall, the triple frequency solution for GPS + Beidou + Galileo gave the best performance with a substantial overall improvement in convergence time of 7.6 minutes, and improvements of 2mm in RMSE East and Up components. These results demonstrate the benefits of MFMC data for improving PPP performance, which is especially significant for real-time users.

Chapter 5: Use of Precise Ionosphere Corrections for Accelerated PPP Convergence with Multi-Frequency and Multi-Constellation GNSS

This paper is covered by the following publication:

- **Deo MN**, El-Mowafy A (2017) Ionosphere Augmentation for accelerated convergence in Precise Point Positioning with multi-frequency and multi-constellation GNSS, paper presented at ION Pacific PNT 2017 Conference, Honolulu, Hawaii, May 1-4, 2017.

This paper presents a PPP approach with float ambiguity estimation that uses the individual un-combined triple-frequency measurements with externally provided precise regional ionospheric model (RIM). The proposed method has two characteristics. Firstly, there is no noise amplification since raw un-combined carrier phase and code measurements are used. This reduces the solution convergence time, when compared to the ionosphere-free linear combination that is used in the traditional dual-frequency PPP model, where the noise is amplified by a factor of 2.978. Secondly, the ionosphere delay remaining in the un-combined measurement is corrected using externally provided RIM, hence reducing the number of parameters to be estimated. This improves the geometry of the model and hence reduces the solution convergence time.

The proposed model was validated with simulated data assuming a fully operational GPS constellation with three transmitting frequencies at four sites in Australia for one-week duration. The performance of 2-hourly PPP solutions was compared for three cases including: (1) the proposed triple frequency raw un-combined model with correction of the ionosphere delay using an externally provided model (2) triple frequency raw un-combined model where the ionosphere error is estimated (i.e. without RIM) and (3) the traditional dual-frequency PPP model. The three cases were compared in terms of solution convergence time taken to achieve and maintain 3-dimensional (3D), horizontal and vertical positional accuracies of 1 decimetre and 5cm, respectively. The tests for the first case considered the use of varying precisions of the externally provided RIM with standard deviations (std) of 0.1, 0.25, 0.5 and 1.0 Total Electron Content Unit (TECU).

Results from the comparison show that the best improvement was achieved with the proposed raw un-combined model with a high precision RIM of std = 0.1 TECU. Here, the convergence time to achieve sub-decimetre accuracy was reduced by 37%, 86% and 33% in the 3D, horizontal and vertical components respectively. The most significant improvement was in the horizontal component since the ionospheric error mostly occurs in the height component. A RIM with std = 0.1 TECU gave sub-decimetre accuracy in under 2 minutes for horizontal and 11 minutes for 3D component; whereas to achieve sub 5cm accuracy required 4.25 minutes for horizontal and 27 minutes for 3D components. All the RIM precisions between 0.1 to 1.0 TECU that were tested are capable of providing horizontal

positioning accuracy of 5cm within 5 minutes. These performance indicators are promising for real-time PPP users of triple frequency GPS data who require horizontal positioning accuracy, and have access to a high precision RIM generated from a nearby regional GNSS network.

The raw un-combined model with estimation of the ionospheric error also outperformed the standard dual-frequency model, but had less improvement in convergence time, compared to the case of correcting the error using a precise RIM. The improvements were by 13%, 3% and 21% in the 3D, horizontal and vertical components.

Chapter 6: Comparison of advanced troposphere models for aiding reduction of PPP convergence time

This chapter is covered by the following publication:

- **Deo MN**, El-Mowafy A (2018) Comparison of Advanced Troposphere Models for Aiding Reduction of PPP Convergence Time in Australia, Journal of Spatial Science, https://doi.org/10.1080/14498596.2018.1472046, first published online: 24 May 2018.

This paper focuses on use of empirical troposphere models and widely available Numerical Weather Model (NWM) data to aid in the reduction of PPP convergence time. Firstly, comparisons are made on the precision of tropospheric zenith total delay (ZTD) values obtained from the empirical models Global Pressure and Temperature-2 (GPT2) and GPT2w, and the NWM data from the Australian Bureau of Meteorology (BoM) and European Centre for Medium-Range Weather Forecasts (ECMWF). These ZTD values were compared with reference values used from the IGS ZTD product at four sites. Results showed that the ZTDs from NWM datasets were more precise than the empirical models. Overall, the ZTD from BoM data was found to give the best results, with mean errors between -0.034m to 0.029m and standard deviations better than 0.045m. The GPT2w empirical model was more precise and accurate than its predecessor GPT2. Comparison of the ZTD values obtained from ECMWF to the IGS ZTD values showed that the accuracy of the ECMWF model may be affected by the resolution of digital elevation model (DEM) heights used in this model.

The second part of the paper compares the PPP convergence time and achievable accuracy when using the BoM NWM constrained ZTD by including them

as pseudo-observations with a known precision to the case of estimating the troposphere as an unknown parameter. The analysis was done at four test sites with 5 days of data with hourly PPP solutions. The performance of PPP convergence time and achievable accuracy with the BoM NWM constrained troposphere was compared to the traditional case of estimating the troposphere as an unknown parameter. Improvements in vertical positioning accuracy was found at all the four sites during the first few minutes of initialisation. The BoM constrained troposphere model PPP had better vertical accuracy by 0.036-0.058m after 2 minutes, 0.023-0.038m after 3 minutes and 0.013-0.020m after 5 minutes of PPP initialisation. This result suggests that constraining the troposphere with the BoM NWM data may improve the PPP vertical convergence during the first few minutes of initialisation. This could be beneficial for applications where fast vertical convergence is required. Although the benefit may not be substantial, it may be more cost-effective to use the widely available NWM data rather than the more complicated approach of using precise troposphere corrections from an external provider that uses a local GNSS network.

Chapter 7: Maintaining Real-Time Precise Point Positioning during outages of Orbit and Clock Corrections

This chapter is covered by the following publication:

- El-Mowafy A, **Deo MN**, Kubo N (2016) Maintaining real-time precise point positioning during outages of orbit and clock corrections. GPS Solutions, 21(3), 937-947. DOI:10.1007/s10291-016-0583-4.

The paper presents a method for dealing with communication outages in real-time PPP applications, where the GPS satellite orbit and clock corrections are unavailable to the user. During such times, which may last from a few minutes to several hours, the PPP solution is lost and once the corrections are restored, the user has to wait for 30 minutes or more for the solution to re-converge within decimetre accuracy. The method presented in the paper maintains real-time PPP with better than decimetre 3D accuracy during communication outage. The real-time service (RTS) products sourced from open-access IGS are used to predict the precise orbit and clock corrections as time series during the outage. During short correction outages of a few minutes, the IGS-RTS orbits are predicted using a high-order polynomial, and for longer outages up to 3 h, the most recent IGS ultra-rapid orbits are used. The IGS-RTS clock corrections are predicted using a second-order

polynomial and sinusoidal terms. The predicted model parameters are estimated sequentially using a sliding time window with short intervals to reduce the computational load, such that they are available when needed.

The prediction model of the clock correction is built based on the analysis of their properties, including their temporal behaviour and stability. The proposed method can give prediction accuracy typically within 0.5 ns during the first hour and 1.0 ns for the second hour with std between 0.12 and 0.40 ns. In general, prediction of clock corrections for GPS block IIF satellites was better than that of block IIR-M and IIR, respectively, which show the improved stability of satellite clocks of the newer generation of satellites.

Validation of the proposed approach in the static and kinematic modes showed that when a break in communications is experienced, the use of the IGS Ultra-Rapid orbits (predicted half) with IGS-RTS predicted clock corrections can achieve better than 1 decimetre positioning precision after the solution converged. This accuracy was maintained for up to 2 h after the break. The number of data points needed to reliably estimate the prediction parameters was chosen within a time length corresponding to a significant autocorrelation, where 1–1.5 h of data was determined as sufficient for building the prediction model. When the PPP solution was initialized using the predicted corrections, the convergence time increased; however, positioning precision remained better than a decimetre after solution convergence.

Chapter 8: Improved Algorithms for Precise Point Positioning with Integer Ambiguity Resolution Using Triple-Frequency GNSS Data

This chapter is covered by the following publication:

- **Deo MN**, El-Mowafy A (2019) A method for Precise Point Positioning with Integer Ambiguity Resolution with Triple-frequency GNSS Data, Measurement Science and Technology, 30(6): 065009, https://doi.org/10.1088/1361-6501/ab0945.

This paper proposes a novel method for PPP ambiguity resolution (PPP-AR) with triple frequency GNSS data. Firstly, an enhanced linear combination is developed for rapid fixing of the extra wide-lane (EWL) and wide lane (WL) ambiguities, which has improved performance compared to the Melbourne-Wübbena (MW) linear combination. Compared to the MW linear combination for the GPS case, the measurement noise in the proposed combination was 6.7% lower for L1/L2,

12.7% lower for L1/L5 and a modest 0.7% lower for the L2/L5. Data analysis at four sites showed that the N_{21} WL ambiguities were fixed correctly with a single epoch for 88.9% of cases, an improvement over the MW method by 5.4%. The N_{51} WL ambiguities were fixed correctly with one epoch for 86.0% of cases, an improvement over the MW method by 5.9%; whereas all EWL ambiguities were fixed with one epoch for both methods. When using the proposed linear combination, all the EWL and WL ambiguities were fixed in less than two minutes. The performance of the proposed linear combination for GPS N_{21} WL ambiguity resolution was compared to Li's method (Li et al., 2014). Results showed that the proposed method gave slightly improved performance with $\sigma_{\Phi} = 0.002m$, and considerably improved performance as the carrier phase std increased. To fix the N_{21} WL ambiguity with a single epoch with probability of success rate (Ps) = 99.9% requires that $\sigma_{\mathrm{P}} \leq 0.18m$, which is possible with the modernised signals of the GNSS systems

After correctly fixing the EWL/ WL ambiguities, a full rank triple frequency carrier phase only PPP-AR model is proposed where the carrier phase equations are formulated in terms of an individual carrier phase ambiguity, e.g. the GPS N_2. The LAMBDA method is used to analyse the probability of AR success rate (Ps) of the N_2 ambiguity. Here, the PPP-AR performance is greatly improved when used with precise models for the ionosphere and troposphere. The results of the proposed model were compared to Li's method. It was shown that use of a precise troposphere model and a Regional Ionospheric Model (RIM) significantly improved the time to fix ambiguities. The model was validated with a range of values for carrier phase and RIM precisions, denoted by the respective standard deviations (std). When using a RIM with std=0.1TECU and carrier phase std = 0.002m, a Ps rate better than 99% was achieved with less than four epochs of data for fixing the N_2 ambiguity. Decreasing the RIM precision to 0.5TECU, while retaining the carrier phase std = 0.002m required up to six epochs of data to achieve $Ps \geq 99\%$. When using $\sigma_{RIM} = 0.5TECU$ and increasing carrier phase std=0.02m, the proposed method required up to 14 minutes to give $Ps \geq 99\%$. A Ps rate of 99.9% was achieved within one-hour for all the test cases when using the proposed method. In comparison, the Li's method with carrier phase std = 0.002m gave $Ps \geq 99\%$ with up to 13 epochs of data. When the carrier phase std was increased to 0.02m, the performance of this method deteriorated considerably. These results demonstrate

improved performance of the proposed PPP-AR method when used with precise atmospheric models.

The direct estimation of the NL integer ambiguity is attempted by multi-epoch averaging of a newly proposed triple frequency linear combination. This is done after fixing the EWL and WL ambiguities using the enhanced linear combination. The test results showed that 34.4% of the ambiguities were fixed in 5 minutes, 65.4% in 10 minutes, 90.2% in 20 minutes and 95.6% in 30 minutes. With this approach, AR with a probability success rate of 99.9% would require more than an hour of continuous carrier phase tracking. These results are comparable to the existing PPP-AR methods.

2 IMPROVED CYCLE SLIP DETECTION AND REPAIR WITH TRIPLE FREQUENCY DATA

Ensuring data quality assurance is a mandatary first step for any PPP software and if left unaccounted for, data quality issues such as cycle slips and clock jumps can adversely affect PPP convergence time, accuracy and precision. This chapter presents algorithms for detecting and repairing cycle slips and clock jumps using MFMC GNSS data and results of testing with real data.

This chapter is covered by the following publication:
Deo MN, El-Mowafy A (2015) Cycle Slip and Clock Jump Repair with Multi-Frequency Multi-Constellation GNSS data for Precise Point Positioning, IGNSS Conference, Surfers Paradise, Qld, Australia, 14-16 July 2015.

International Global Navigation Satellite Systems Society
IGNSS Symposium 2015

Outrigger Gold Coast, Qld Australia
14-16 July, 2015

Cycle Slip and Clock Jump Repair with Multi-Frequency Multi-Constellation GNSS data for Precise Point Positioning

Manoj Deo
PhD Candidate, Department of Spatial Sciences, Curtin University,
GPO Box U 1987, Perth WA 6845, Australia
Phone: +61 432163000
Email: manoj.deo01@gmail.com

Ahmed El-Mowafy
Assoc. Professor, Department of Spatial Sciences, Curtin University,
GPO Box U 1987, Perth WA 6845, Australia
Phone: +61 8 9266 3403
Fax: +61 8 9266 2703
Email: a.el-mowafy@curtin.edu.au

ABSTRACT

Detecting and repairing cycle slips and clock jumps are crucial data pre-processing steps when performing Precise Point Positioning (PPP). If left unrepaired, cycle slips and clock jumps can adversely affect PPP convergence time, accuracy and precision. This paper proposes algorithms for detecting and repairing cycle slips and clock jumps using multi-frequency and multi- constellation (MFMC) GNSS data. It is shown that availability of a third frequency enables reliable validation of detected cycle slips. This is because triple frequency analysis can identify the frequency on which the cycle slip occurred as part of the detection process. A clock jump detection and repair procedure is also proposed for a receiver with both carrier phase and code measurements showing jumps. The proposed method uses the average code and phase linear combination and applies to static data. A spline function is used to approximate the data for a pre-defined time window prior to each measuring epoch and a test is performed for detecting presence of a clock jump by comparing the interpolated value to measured value. The algorithm can effectively determine clock jumps for single frequency data from a single constellation as well as MFMC GNSS data. However, MFMC GNSS data adds redundancy, hence improves the reliability of the clock jump detection algorithm. It is recommended to detect and repair clock jumps when using PPP to allow improved modelling of the receiver clock offset in the dynamic model.

KEYWORDS: Precise Point Positioning, clock jumps, cycle slips, GNSS.

1. INTRODUCTION

A cycle slip is a sudden jump in the carrier phase measurement from a GNSS receiver by an integer number of cycles (Leick, 2004), caused by receiver failure, signal tracking interruption, low signal strength, or high receiver dynamics (Dai, 2012). A cycle slip normally occurs on measurements to one satellite at a particular frequency at a point in time, though simultaneous slips on multiple frequencies at an epoch is possible in challenging environments. Processing of cycle slips includes detecting the presence of each cycle slip, estimating the size of the cycle slip, validating its estimate, and correcting the effect of the cycle slip by adjusting phase measurements for the respective frequency and satellite. Correctly repairing a cycle slip, which is more difficult than its detection, will avoid re-initialisation of ambiguities in PPP and ensure faster convergence to the correct solution. If left unrepaired, cycle slips can deteriorate the accuracy, precision and convergence period in PPP.

El-Mowafy (2014a) compared several methods for detection of cycle slips with measurements from a single receiver. Methods that use dual-frequency carrier phase only measurements were based on the geometry-free (GF) linear combination and the time-rate change of the ionosphere (IOD) linear combination; whereas methods using dual-frequency carrier phase and code measurements included the Melbourne-Wübbena combination and the time change of multipath (dMP) combination. De Lacy et al. (2012) proposed a methodology for cycle slip detection with triple frequency GPS data. The method used a triple frequency code-phase linear combination for detecting 'big' jumps and a phase only combination for detecting 'small' jumps. Dai et al. (2009) used two GF linear combinations with triple frequency data to detect cycle slips and the LAMBDA method to search for cycle slip candidates in determining cycle slips. Each method has its pros and cons. For example, the GF combination contains the ionosphere term which may change rapidly during increased ionospheric activity, rising and setting of satellite or if the observation recording interval is set too long. The combinations that use code measurement have high noise, which make it difficult for detection of slips of a few cycles. All cycle slip detection algorithms involve dual-frequency linear combination, and although a cycle slip can be easy to detect, extra effort is required to identify the frequency on which the slip occurred; a problem that can be potentially overcome with triple frequency data.

This paper presents a method for detection of slips with triple frequency data, using two geometry free linear combinations. This is followed by determination of the size of the cycle slips and repairing the cycle slips prior to performing PPP. A cycle slip is flagged if the GF value at an epoch differs from a previous GF value by more than a prescribed threshold. Least squares method is used to calculate the size of the cycle slip. Availability of triple frequency carrier phase data simplifies the identification of the frequency on which the cycle slip occurred. This is because the time series of the GF observable formed between the non-affected frequencies will be smooth, whereas tests that include the erroneous frequency will show a jump (El-Mowafy, 2014a). The cycle slip detection and repair procedure is implemented and tested with triple frequency data from a continuous operating reference station. Although the tests include GPS data, the method can be applied to multi-frequency and multi- constellation (MFMC) GNSS data.

Clock jumps are caused by periodic resets of the GNSS receiver clock as geodetic receivers attempt to keep the time system of the receiver synchronised with the GPS time, but due to the use of low-cost internal frequency oscillators, the receiver clock drifts with time. To better

align with GPS time, the receiver introduces clock offsets of 1 ms when the difference between receiver and GPS time exceeds this tolerance. Although some researchers suggest treating clock jumps as cycle slips (Guo & Zhang, 2014), clock jumps cannot be picked up by commonly used linear combinations, such as GF, that are used in cycle slip detection. This is because phase measurements on all frequencies are affected by identical jumps and its effect is nullified when forming the linear combination. Depending on the receiver type, clock jump effects show a 'saw tooth' like signature when plotting the time series of the carrier phase or code measurements. Guo & Zhang (2014) argued that measurements should be compensated for clock jumps when the observation time tag and code measurements show jumps whereas phase data has a smooth trend, or when the observation time tag and carrier phase measurements have smooth trend whereas the code measurements show jumps. The authors reported that unrepaired clock jumps have significant effects on kinematic PPP. Therefore, clock jumps must be detected and measurements should be corrected for such effects in order to avoid problems with solution convergence.

This contribution proposes a method for clock jump detection and repair when it is experienced on both carrier phase and code measurements. The algorithm applies to static data and uses the average code and phase linear combination (C/P). This combination preserves the geometry, is free from ionosphere effects, and the code noise is reduced by a factor of two. In detecting clock jumps, a spline function is used to approximate the C/P data for a selected time window prior to each measuring epoch. The C/P value at each epoch is extrapolated and a clock jump is flagged if the difference between the extrapolated value and the actual C/P measurement is greater than a threshold value that is set based on a chosen statistical significance and standard deviation of the C/P residuals. Once detected, the clock jump magnitude is determined as an average of the values from all frequencies and all satellites in view. This is followed by repairing clock jump effects in the data. Since the C/P combination uses single frequency data, this method can be applied with single-constellation single-frequency as well as MFMC GNSS data.

2. CYCLE SLIP DETECTION AND REPAIR ALGORITHM

This section describes the cycle slip detection and repair algorithm and the results of testing the algorithm.

2.1 Methodology

The GF linear combination for frequencies *j* and *l* for the GNSS constellation, *G* (which may be GPS, for example) is presented as

$$[\boldsymbol{\phi}_r^{k_G}]_{GF} = \boldsymbol{\phi}(j)_r^{k_G} - \boldsymbol{\phi}(l)_r^{k_G} \quad (1)$$

where $\boldsymbol{\phi}(j)_r^{k_G}$ and $\boldsymbol{\phi}(l)_r^{k_G}$ are the carrier phase measurements in distance units. Ignoring multipath and hardware biases, the GF combination contains ionospheric errors and phase ambiguities that are constant in the absence of cycle slips. If the observation time interval is long (e.g. > 30 s) accompanied with large ionospheric activity, the GF observable shows significant variations. Also, the GF measurements change rapidly when the satellite is at low elevation, i.e. when it is rising or setting at the horizon. El-Mowafy (2014a) suggested increasing the threshold value used for cycle slip detection during such cases to avoid false cycle-slip detections.

The proposed cycle slip detection and repair method is demonstrated with GPS as an example, although it can be applied to any GNSS constellation. For a given satellite and the time series of carrier phase measurements, the procedure for detecting a cycle slip at an epoch, *t*, is summarised in the following steps:

1. Consider the geometry free measurements at an epoch, *t*, and the preceding epoch *t-1*. Form the GF combinations simultaneously between L1-L2, L1-L5 and L2-L5 for GPS measurements, if triple frequency data is observed.
2. Compare the difference between the GF value given in Eq. 1 at *t* to the GF value at *t-1*. A cycle slip is flagged if:

$$abs\left(\left[\boldsymbol{\phi}_r^{k_G}(\boldsymbol{t})\right]_{\boldsymbol{GF}} - \left[\boldsymbol{\phi}_r^{k_G}(\boldsymbol{t-1})\right]_{\boldsymbol{GF}}\right) > k\sigma + \Delta I_{max} \quad (2)$$

   the first part on the right hand side (kσ) is used to bound the stochastic changes and (ΔI_{max}) is an empirical value used to bound possible ionosphere changes between *t*-1 and *t*. For most stable ionosphere conditions,0.4m/hr can be used for ΔI_{max}. k is a scale factor based on chosen statistical significance and σ is the standard deviation of the observable on the left-hand side (LHS) of the equation, considering measurement noise, and satellite elevation. Users select the value of *k* depending on the confidence level required for the detection. For example *k=3* means a cycle slip is flagged if the LHS value at *t* is greater than 3 standard deviations of the observable with a significance of less than 0.03%.
3. In case of using triple frequency, the third frequency can help in detecting the frequency on which the cycle slip occurred. For example, if a slip is detected for L1-L2 and L2-L5, a cycle slip is declared for L2, which is the common frequency. In line with this, if a slip occurs in L1-L5 and L2-L5, a cycle slip is declared for L5; and if a slip occurs in L1-L2 and L1-L5, the cycle slip is declared for L1.

Once a cycle slip is detected, its size is determined using the GF observables as follows:

1. Select a sample of GF observables before and after *t* of suitable size (e.g. *m=20*) that can be accurately approximated by a second order polynomial. The sample size can be determined from examining the auto-correlation function (El-Mowafy and Lo, 2014). The start time for the sample is *t-Δt*, where *Δt=m × epoch interval*. If the start time occurs before the first epoch of the dataset, it is set as the first epoch. If there are any missing epochs between the start time and *t*, the start time is set to the epoch immediately after the missing epoch.
2. The GF observables are monitored between the start time and *t*, to scan if a cycle slip occurred in between, in which case the start time is reset to the epoch after the cycle slip occurrence.
3. The end time for the sample is determined in a similar manner, accounting for missing epochs, intermediate cycle slips and in case the end time occurs after *t+Δt*.
4. A second order polynomial is fit to the GF observables between start time and end time. This is assumed to approximate the data at few cm precision over short durations, i.e. 20 minutes for *m=20* and 30s epoch interval. For epochs after time *t* inclusive, where a cycle slip is suspected, a cycle slip parameter is introduced as an unknown variable.
5. Least squares is used to calculate the cycle slip size, as well as the polynomial coefficients which best fits the data.
6. For a slip flagged in L2, the size of the cycle slip determined from the L1-L2 GF

combination is compared to the size determined from L2-L5, if L5 is available. If the slip sizes are the same, cycle slip repair is carried out for L2. If the cycle slip sizes do not match and the slip size is 1-2 cycles, it is ignored since this could be a false detection. If only dual-frequency data is available, such comparison of cycle slip sizes cannot be made and another procedure is used, as described below.

7. The raw carrier phase measurements for the frequency detected are repaired by the determined cycle slip size for all consecutive epochs after *t* for as long as a missing epoch occurs. In case of a missing epoch, the cycle slip repair stops at that point, since the PPP software reinitialises the ambiguity after a missing epoch.

In case only dual-frequency data is available (e.g. L1 & L2) and a slip is flagged at *t* with the L1-L2 GF observable, the cycle slip could potentially occur in L1 or L2. The confirmation of the frequency and size of the slip is made as follows:

1. Assuming that the slip occurred on L1, determine the cycle slip size from step 5 above.
2. Assuming that the slip occurred on L2, determine the cycle slip size similar to previous step.
3. If the cycle slip size for L1 is greater than the cycle slip size from L2, and is more than a threshold number of cycles, (e.g. *n=2*), proceed with repairing cycle slip for L1. This allows for ignoring false detections that are likely to be due to increased noise or ionospheric change. For example, a slip size of +1 in L1 and -1 in L2 potentially signifies noisy data rather than an actual slip whereas a L1 slip of 50 cycles and L1 slip of -1 signifies an actual cycle slip on L1.
   Else if the L2 slip is greater than L1 and is greater than *n* slips, repair cycle slip for L2. Since the frequency on which the cycle slip occurred cannot be verified, as in the case of triple frequency data, this approach for cycle slip detection with dual-frequency data may not be effective in case of small slips. Thus, cycle slips less than 2 slips are not repaired. Alternatively, the single-satellite single-receiver validation method presented in El-Mowafy (2014b) may be used.

Since the GF observable changes rapidly during high ionospheric activity, with long epoch intervals, and at low satellite elevation angles, El-Mowafy (2014a) suggested increasing the value of σ, based on the satellite elevation angle in order to avoid false detections. However, setting a large value for σ may result in missed detection of small cycle slips particularly at low satellite elevation angles. In this research, the value for σ is determined as

$$\sigma = \sqrt{2\left(\sigma_{\phi j}^2 + \sigma_{\phi l}^2\right)} \cdot M(E) \qquad (3)$$

where $\sigma_{\phi j}$, $\sigma_{\phi l}$ are the standard deviations of carrier phase measurements for frequencies *j* and *l*. The assumed standard deviations are 0.0027m, 0.0017m and 0.0035m for GPS L1, L2 and L5 carrier phases. These are based on preliminary assessment of a sample dataset, but more realistic values may be determined from the methods discussed in El-Mowafy (2015). The standard deviation for L5 carrier phase is higher mainly due to an abnormal performance related to thermal effects in the satellite, as reported in Montenbruck et al (2011) and Tegedor & Øvstedal (2014). In assigning the standard deviations, the time correlations between epochs are ignored. *M(E)* is the satellite elevation dependent scaling factor calculated using Euler and Goad (1991) as

$$M(E) = 1.0 + 10e^{\frac{-E}{10}} \quad (4)$$

where E is the satellite elevation in degrees and e is the base of the natural logarithm.

Once the date has been repaired for cycle slips, the procedure can be repeated on the repaired dataset to account for cases where simultaneous slips occurred on two frequencies.

2.2 Testing the Cycle Slip Algorithm

Triple frequency RINEX data from the continuously operating reference station (CORS) CUT0, located at Curtin University was used to validate the cycle slip detection and repair procedure described in the previous section. The data used was selected for 17 March 2015 when severe geomagnetic storm was observed from Universal Time Coordinated (UTC) 13:58 and persisted for several hours, quietening towards the end of the UTC day (NOAA, 2015). It was found that the RINEX data set had missing measurements from GPS time 06:45:00 to 06:47:00. The following tests compare the performance of the cycle clip detection algorithm when scaling measurements according to satellite elevation angle. A navigation file is required for this approach for calculating the satellite elevation angle.

Figure 1 (a-c) shows the GF linear combinations formed between L1-L2, L1-L5 and L2-L5 observations for PRN9, with the detected cycle slips shown as red vertical lines, accompanied by jumps in the GF observable. Cycle slips are detected at epochs 241380 and 241920, which are attributed to L1 (351 slips), and L2 (395 slips), respectively.

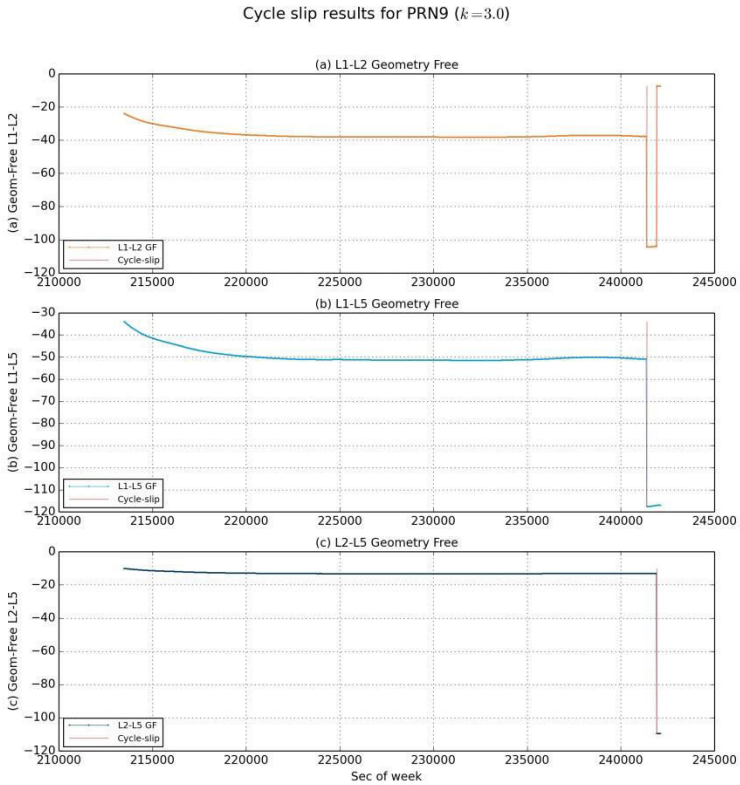

Figure 1. (a) L1-L2, (b) L1-L5 and (c) L2-L5 geometry-free linear combinations with vertical lines showing detected cycle slips for PRN9.

Figure 2 illustrates the same results for PRN1. As the figure depicts, the GF observable shows

considerable variation between second of week 207000-209000, particularly for the L1-L5 combinations. This has resulted in some falsely detected cycle slips. The ionospheric contribution factor, ΔI_{max} had to be experimentally increased to 6.0m/hr to account for the high rate of ionospheric change in storm activity, which resulted in elimination of false detections, as shown in Figure 3. Figure 4 shows the GF test values for L1-L2 and L1-L5 from Eq. 2 and the threshold values for testing cycle slips using $\Delta I_{max}=0.4m/hr$ which resulted in several false detections. Figure 5 shows the results when ΔI_{max} was increased to $6.0m/hr$. This shows that the cycle slip detection is sensitive to the ΔI_{max} value, which must be adjusted to a high value during geomagnetic storms in order to avoid false detections.

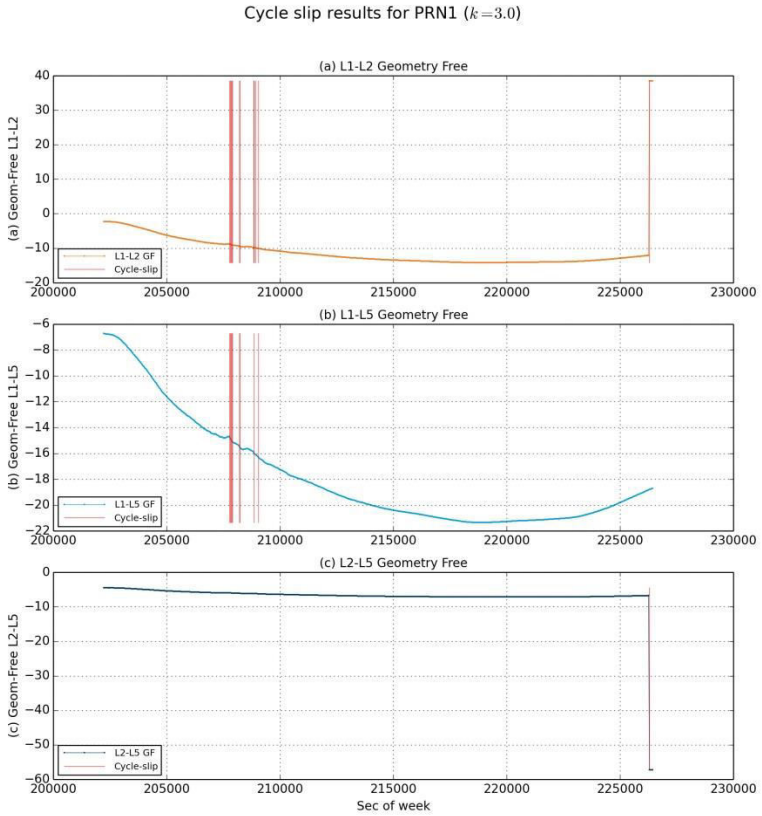

Figure 2: (a) L1-L2, (b) L1-L5 and (c) L2-L5 geometry-free linear combinations for PRN1with vertical lines showing detected cycle slips using a default ΔI_{max} value of 0.4m/hr.

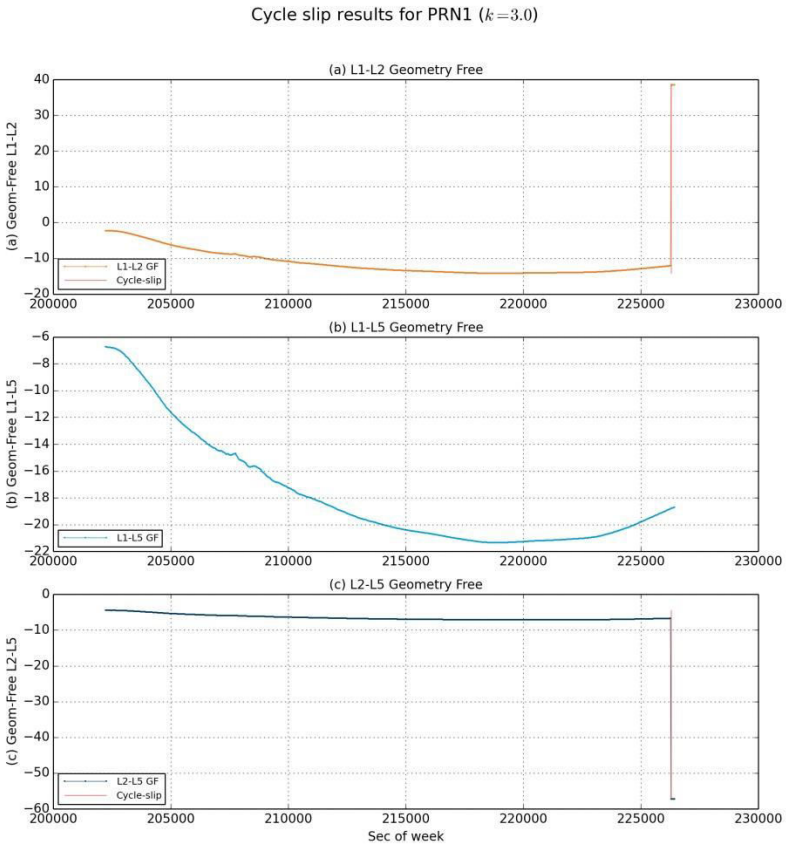

Figure 3: (a) L1-L2, (b) L1-L5 and (c) L2-L5 geometry-free linear combinations for PRN1with vertical lines showing detected cycle slips using adjusted ΔI_{max} value of 6.0m/hr.

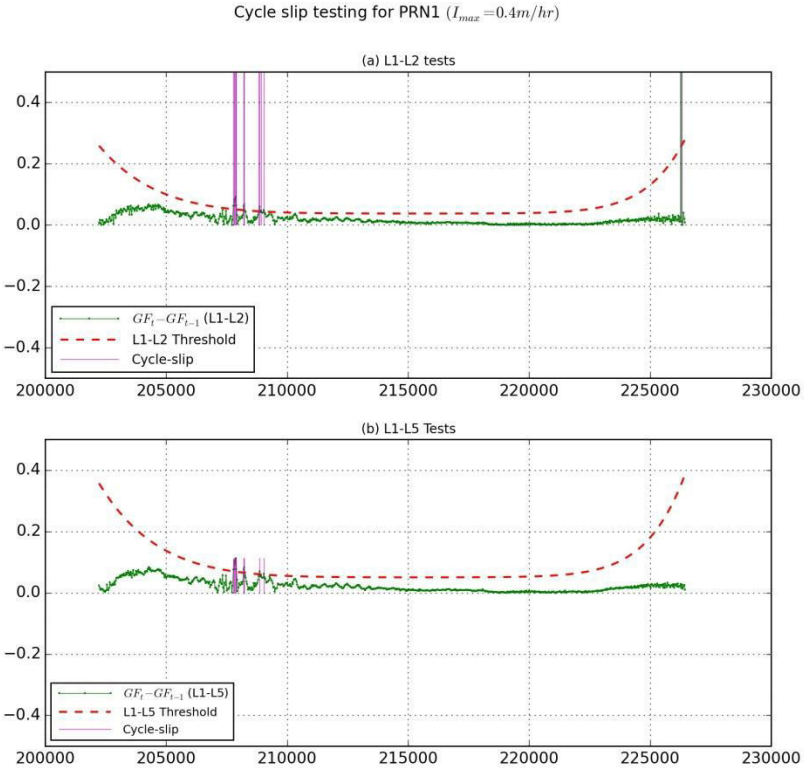

Figure 4: The L1-L2 and L1-L5 geometry-free test values and threshold value for testing cycle slips for PRN1 using a default ΔI_{max} value of 0.4m/hrs.

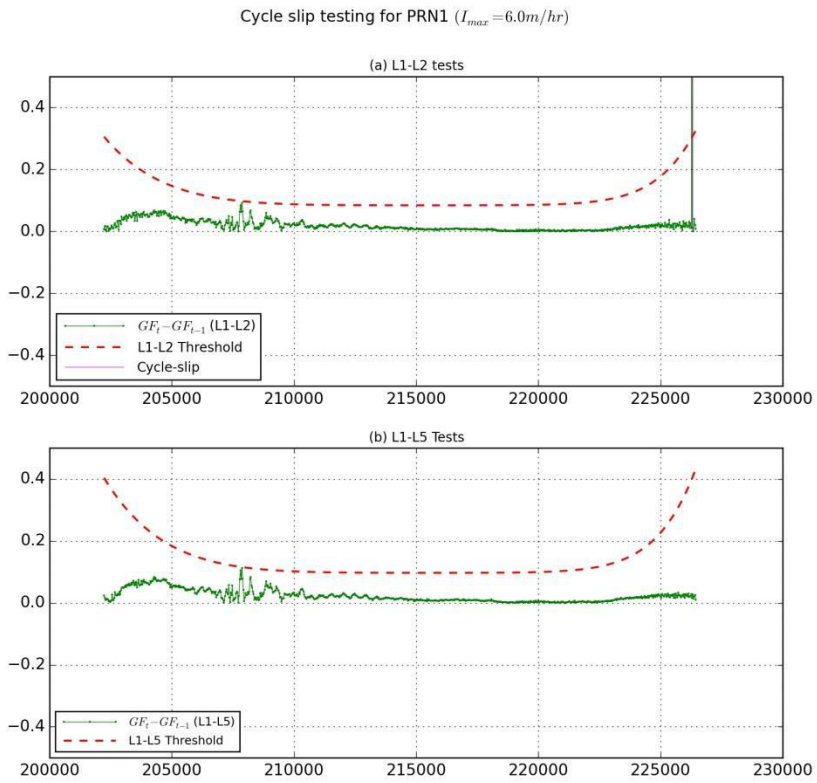

Figure 5: The L1-L2 and L1-L5 geometry-free test values and threshold value for testing cycle slips for PRN1 with ΔI_{max}= 6.0m/hr

3. CLOCK JUMP DETECTION AND REPAIR ALGORITHM

This section describes the proposed algorithm for detection of clock jumps in the static mode, such as the use of PPP in monitoring land deformation, and presents results of testing the algorithm with real data.

3.1 Methodology

Treatment of clock jumps is dependent on how the receiver introduces these jumps. Guo and Zhang (2014) describe four types of clock jumps. Type 1 is accompanied by jumps in time tags with smooth phase and code measurements. Type 2 is accompanied by jumps in time tags and code measurements, but smooth phase. Authors noted that Type 2 jumps are always accompanied by Type 1 jumps and Trimble 4000SSSI is an example of a receiver which has this type of jump. Type 3 is accompanied by jumps in code measurements, but smooth time tags and phase measurements. This type of jump occurs in SEPT POLARX2 receiver, for example. Type 4 manifest itself as jumps in code and phase measurements, but smooth time tags, which occurs in JPS Legacy receivers as an example. Type 1 and 4 receivers have the pseudorange and phase measurements consistent, thus the effects are absorbed in the receiver clock offset parameter when performing point positioning. However, Type 2 and 3 clock jumps have inconsistencies between the code and phase measurements where code measurements are readjusted leaving uncorrected phase data. Thus, clock jumps must be compensated when they are present in one type of raw measurement, i.e. code or phase measurement. When clock jumps are present in both code and phase measurements, they can be either estimated and treated separately or lumped with the estimated receiver clock error. One of the advantages of detecting and repairing clock jumps in such case is that the receiver

clock parameter becomes predictable, hence can be modelled more precisely when using a Kalman Filter in PPP.

Methods that utilise between-time GF or Melbourne-Wübbena linear combinations for clock jump detection, e.g. presented in Guo and Zhang (2014) are not suitable for data from receivers such as Trimble NetR9, which has clock jump effects in both code and phase measurements. This is because the clock jumps effects cancels out in the tested statistic used in this method. In this contribution, the linear combination used for clock jump detection is the average code and phase (scaled to distance) on the same frequency, denoted here as C/P, where:

$$[C/P(j)]_r^{k_G} = \left[\boldsymbol{\phi}(\boldsymbol{j})_r^{k_G} + \boldsymbol{P}(\boldsymbol{j})_r^{k_G}\right]/\mathbf{2} \quad (5)$$

where $\boldsymbol{\phi}(\boldsymbol{j})_r^{k_G}$ and $\boldsymbol{P}(\boldsymbol{j})_r^{k_G}$ are the carrier phase (in distance units) and code measurements for frequency *j*. This combination preserves the geometry, requires only single-frequency data, is free from ionosphere effects, and the code noise is reduced by a factor of two (Gao and Shen, 2002). Since this combination preserves geometry, it changes smoothly with respect to the satellite motion relative to a static receiver. A clock jump of 1ms has the size of 300km, which can be detected by approximating the C/P observable with a spline function and testing for large jumps. The proposed clock jump detection and repair procedure is performed only after the detection and repair of cycle slips to exclude their effects.

In the proposed clock jump detection and repair algorithm, at each measurement epoch, *t*, and for each observed satellite and measurement frequency, a test is carried out to check and flag the presence of a clock jump using the following procedure:

1. Collect all raw measurements for a prescribed number of points (e.g. 7 epochs), prior to *t*, that can be accurately modelled by a spline function. The number of sample points can be determined from examining auto-correlation of the data (El-Mowafy and Lo, 2014c). The residuals after fitting the spline function of a few meters will allow detection of 1ms clock jumps that are 300km.
2. Form the C/P linear combination
3. Fit a spline function to the collected sample of data prior to *t*, using least squares
4. Extrapolate the C/P value at *t*
5. Flag a clock jump if the difference between the extrapolated value, $\widehat{C/P}_r^{k_G}(\boldsymbol{j})_t$, and the actual C/P measurement, $\boldsymbol{C/P}_r^{k_G}(\boldsymbol{j})_t$, at *t* is greater than a threshold, *T*, which is a pre-set value, e.g. 15-20 m.

   $$abs\left(\boldsymbol{C/P}_r^{k_G}(\boldsymbol{j})_t - \widehat{C/P}_r^{k_G}(\boldsymbol{j})_t\right) > T \quad (6)$$

   The test examines that the temporal changes of C/P measurement in the static mode and in the absence of clock jumps are only due to satellite motion. *T* is set to bound possible changes in the ionosphere, troposphere, satellites orbit and code noise, where all are well below a range error that is equivalent to 1 ms (minimum value of a clock jump).
6. If a clock jump is flagged, its magnitude is taken as the difference between the extrapolated C/P value and the measured value.
7. Once a potential clock jump is flagged on one frequency, it is tested if the jump is also flagged on other frequencies, e.g. L1, L2 and L5. If the jumps exist of multiple frequencies, the jump values are averaged to determine the clock jump magnitude.

If a clock jump is flagged for a satellite on multiple frequencies, the above procedure is repeated for all satellites tracked at epoch *t* and a clock jump is suspected if detected in majority of the observed satellites, e.g. 70% of the satellites. The magnitude of the clock jump is determined as an average of the clock jump sizes for all satellites. After detecting a clock jump, a validation step is carried out to verify the jump magnitude to be an integral of 1ms.

After detection of a clock jump, the code and phase measurements are repaired by adding the clock jump value to the raw measurements on all frequencies for all tracked satellites for subsequent epochs after the jump epoch *t*, inclusive. This approach can effectively repair multiple clock jumps occurring at several epochs at varying intervals, since the jump effects tend to be cumulative and can be corrected as they are detected at different times.

3.2 Testing Clock Jump Detection

The presented clock jump algorithm was tested for one full day of GPS data collected on 17 March 2015 at CUT0. A Trimble NetR9 receiver was used, which exhibits jumps for both phase and code measurements. Figure 6(a) shows the C/P linear combination for PRN9 before clock jump detection and repair; whereas Figure 6(b) shows the combination after the clock jumps have been repaired. Figure 7(a) and 7(b) show the same for PRN6. A total of 13 clock jumps were detected for the day's data, at epochs 172800, 175500, 182370, 190170, 198900, 207360, 215760, 223620, 230940, 237750, 244230, 250500, and 256530. Figure 8 shows the difference between predicted and observed C/P values for L1, L2 and L5 and the threshold value used for detecting a clock jump. A sample size of 7 points was used to fit a spline function to the data, which was shown to show close approximation of the C/P observable at the 5-10m level.

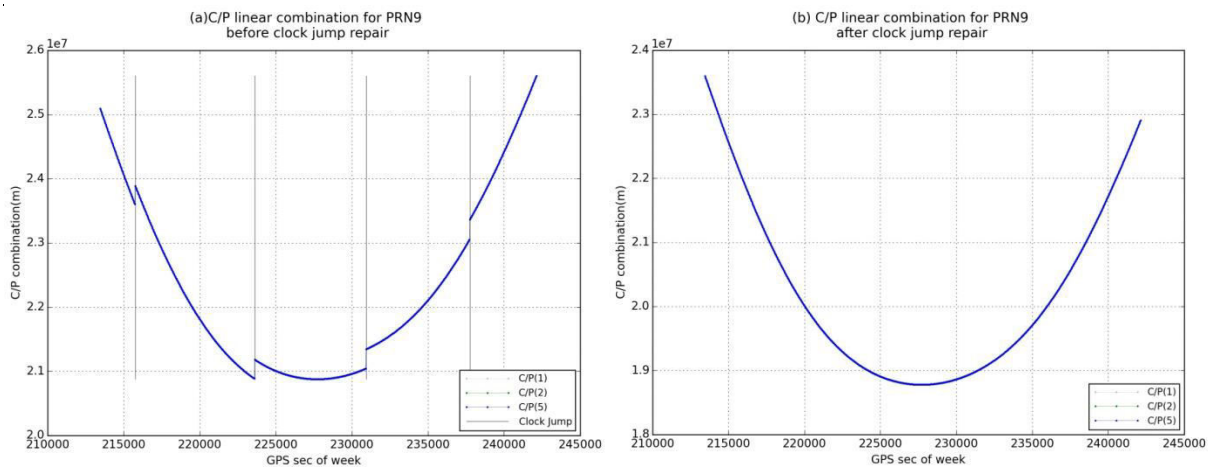

Figure 6: (a) C/P linear combination for PRN9 before clock jump detection and repair; (b) C/P linear combination after clock jump detection and repair.

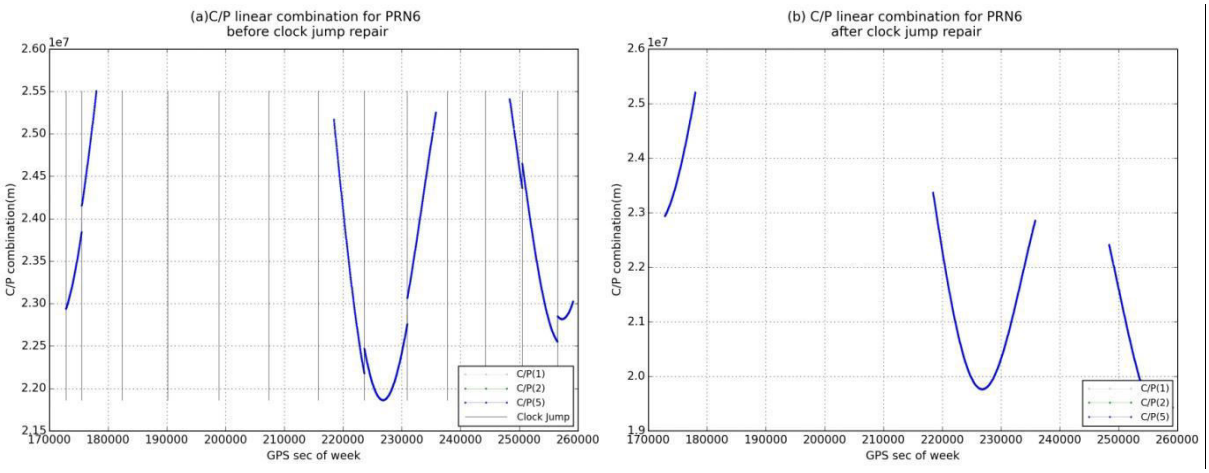

Figure 7: (a) C/P linear combination for PRN6 before clock jump detection and repair; (b) C/P linear combination after clock jump detection and repair.

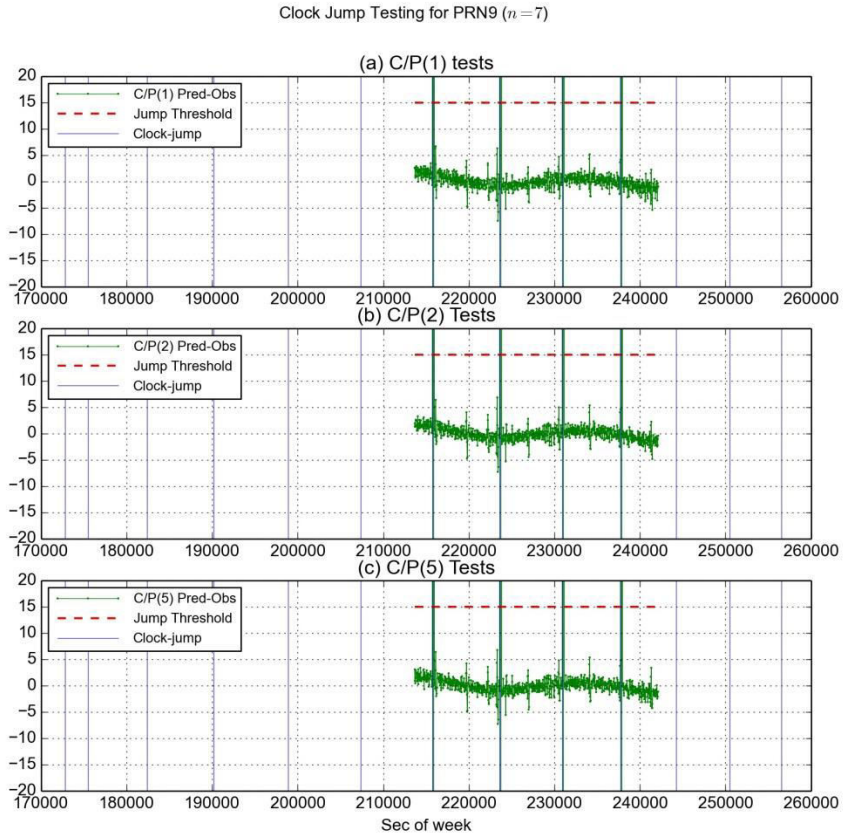

Figure 8: The C/P test values and threshold value used for testing clock jumps for PRN9.

3.3 Clock Jump Effects on PPP Convergence

To study the effects of clock jumps on PPP, one full day of GPS data (1st December 2013) at CUT0 was analysed firstly without repairing clock jumps, and then after detecting and repairing clock jump effects. The PPP software was developed in-house, based on the traditional PPP model (Hėroux and Kouba, 2001). A Kalman Filter is used, which represents a set of equations recursively applied to obtain the state of a system using measurements at discrete time intervals (Deakin, 2006). A full explanation of Kalman Filter equations for PPP is given in Abdel-Salam (2005). The state parameters include receiver position, tropospheric

Zenith Wet Delay (ZWD) and ionosphere-free float ambiguities. The measurements used are the L1-L2 dual-frequency ionosphere-free pseudorange and carrier phase measurements. One of the complexities in implementing the Kalman Filter is the proper modelling of state parameters in the dynamic system, represented by a process noise covariance matrix. The process noise of the parameters may not be purely random and may exhibit time correlation. In the PPP software used, ZWD and receiver clock parameters follow Random Walk (RW) model, which considers time based correlation of parameters. The process noise covariance matrix for the RW model is evaluated as $q\Delta t$, where q is the parameter spectral density and Δt is the epoch interval. If using static data, the position parameters apart from the float ambiguities are constants, thus their process noise is assumed zero. The spectral density for the ZWD was 2cm/√hr. When clock jumps are not treated, the spectral density for receiver clock parameter was set to a large value of 10^5 m^2/s or higher, (practically unconstrained). If clock jumps are detected and repaired, this value is reduced to 1.2×10^3 m^2/s, since the clock behaviour becomes more predictable.

Figure 9 shows the results of the PPP using a Kalman filter solution derived without correcting for clock jumps. The receiver clock errors have been rescaled (multiplying by 10^{-5}) to fit in the plot. As the figure shows, the clock jump effects are absorbed by the clock offset parameter, but position parameters show smooth convergence of the position parameters. Figure 10 shows the PPP solution after clock jumps have been detected and repaired. Note that the receiver clock error is rescaled by a different factor (10^{-6}). As shown, the receiver clock offset does not exhibit the jumps shown in Figure 9, since clock jumps have now been repaired. The convergence of position parameters shows no noticeable change.

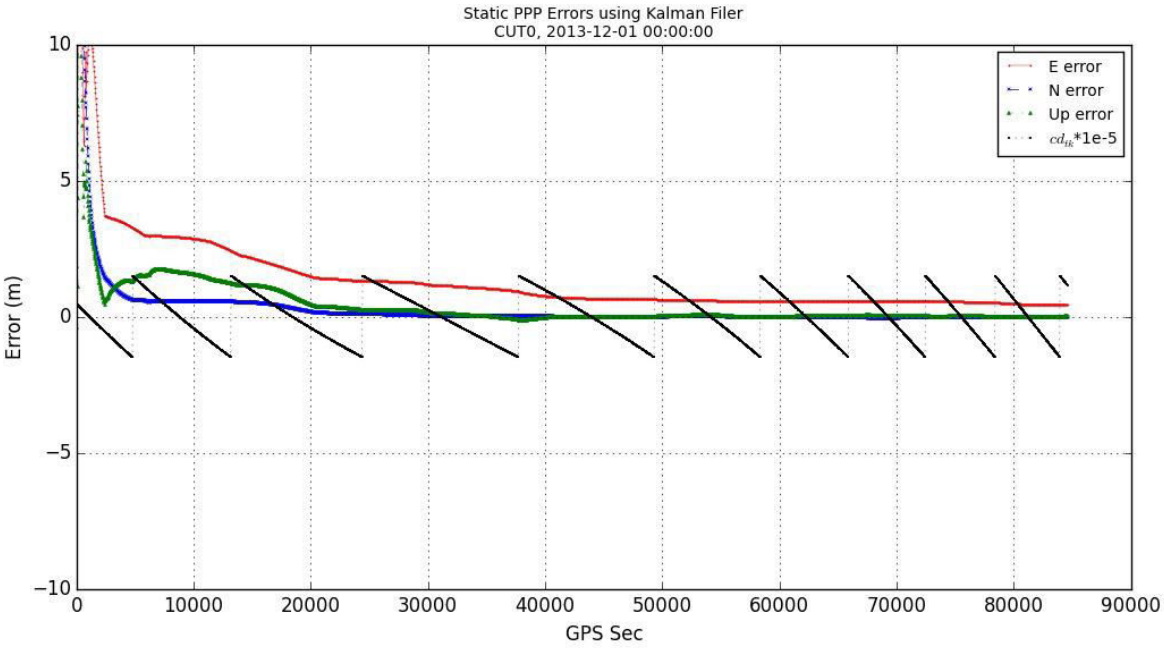

Figure 9: PPP solution without detecting and repairing clock jumps.

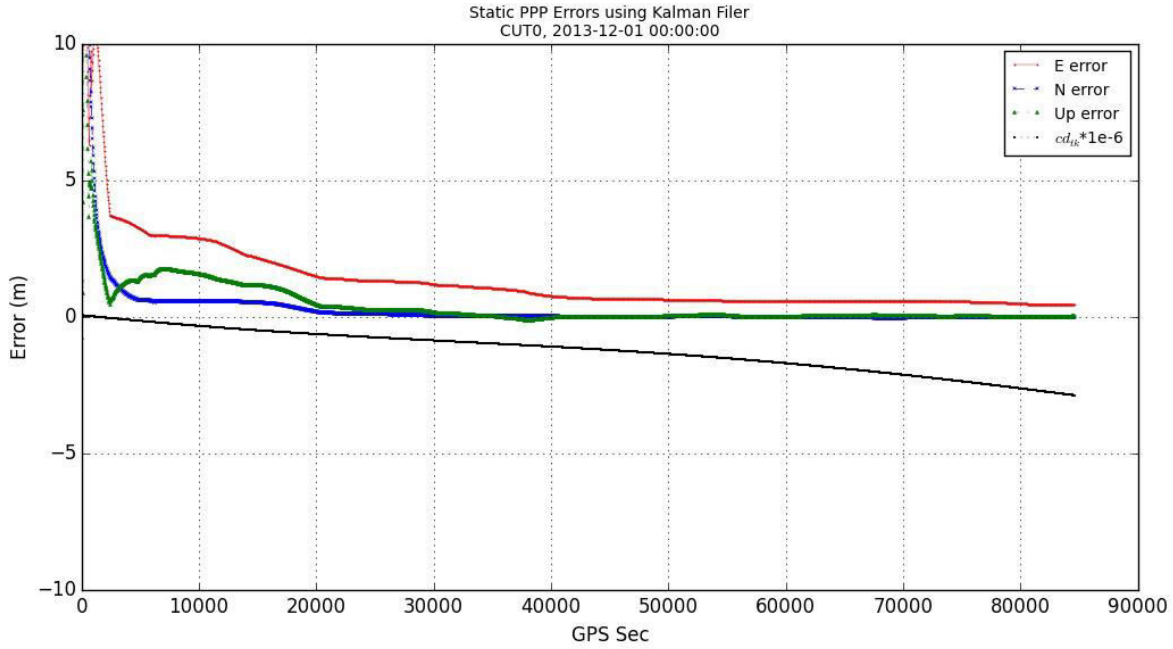

Figure 10: PPP solution after detection and repair of clock jumps.

4. CONCLUSIONS

A cycle slip detection and repair method was presented for triple frequency GNSS data. The performance of the algorithm was tested during a geomagnetic storm. Results show that it is necessary to adjust the ionosphere contribution in the threshold value during such a period to avoid false detection of cycle slips.

A proposed algorithm was presented for the detection and repair of clock jumps in the static mode for receivers having clock jumps in both phase and code measurements, if it is desirable to separate clock jumps from clock offsets. The algorithm uses the average code and phase linear combination. Tests with real measurements from station CUT0 gave reliable results. Since a single frequency linear combination is used in the fundamental model for detecting clock jumps, the proposed algorithm can be applied in single constellation, single frequency GNSS data as well as MFMC data. Clock jumps affect data from all satellites on all frequencies transmitted by all satellites at the jump time. This builds redundancy into the detection model by introducing a verification step to validate the clock jump in other frequencies and satellites observed at the suspected jump time. Detecting and repairing clock jumps improved modelling of the clock offset parameter in the dynamic model used.

ACKNOWLEDGEMENTS

The authors wish to acknowledge the valuable comments and suggestions provided by Prof Chris Rizos, School of Civil and Environmental Engineering, University of New South Wales.

REFERENCES

Abdel-salam MA (2005) Precise Point Positioning Using Un-differenced Code and Carrier Phase Observations, PhD Dissertation, University of Calgary, Alberta,Canada.

Dai Z (2012) MATLAB software for GPS cycle-slip processing. GPS Solutions 16: 267-272.

Dai Z, Knedlik S, Loffeld O (2009) Instantaneous Triple-Frequency GPS Cycle-Slip Detection and Repair, International Journal of Navigation and Observation,

de Lacy MC, Reguzzoni M, Sanso, F (2012) Real-time cycle slip detection in triple-frequency GNSS, GPS Solutions 16: 353-362. Article ID 407231, DOI:10.1155/2009/407231.

Deakin RE (2006) The Kalman Filter: A Look Behind the Scene, Presented at theVictorian Regional Survey Conference, Mildura, 23-25 June, 2006, The Institution of Surveyors, Victoria.

El-Mowafy A (2014a) Quality Monitoring of BeiDou GEO/IGSO/MEO Satellite Observations. IEEE Workshop on Asia-Pacific Satellite Navigation and Positioning, 27 February–1 March, 2014.

El-Mowafy A (2014b) GNSS Multi-frequency Receiver Single-Satellite Measurement Validation Method, GPS Solutions, 18(4): 553-561, DOI:10.1007/s10291-013-0352-6.

El-Mowafy A, Lo J (2014) Dynamic modeling of GNSS troposphere wet delay for estimation of PrecipitableWater Vapour, J. App. Geodesy 8(1):31-42.

El-Mowafy A (2015) Estimation of multi-constellation GNSS observation stochastic properties using single receiver single satellite data validation method, Survey Review 47(341):99-108, DOI 10.1179/1752270614Y.0000000100.

Euler H-J and Goad C (1991) On optimal filtering of GPS dual frequency observations without using orbit information, Bulletin Geodesique, 65, 130-143.

Gao Y and Shen X (2002) A New Method for Carrier-Phase Based Precise Point Positioning, Navigation, 40(2): 109-116, Summer 2002.

Guo F and Zhang X (2014) Real-time clock jump compensation for precise point positioning. GPS Solutions 18(1): 41-50. doi: 10.1007/s10291-012-0307-3.

Heroux P and Kouba J (2001) GPS precise point positioning using IGS orbit products, Physics and Chemistry of the Earth, Part A: Solid Earth and Geodesy, 26(6-8):573-578.

Leick A (2004) GPS Satellite Surveying (third edition), Wiley, New York, 435pp.

NOAA (2015) G4 (Severe) Geomagnetic Storm Observed, published: Tuesday, March 17, 2015 20:17 UTC, <http://www.swpc.noaa.gov/sites/default/files/images/u39/Space%20Weather%20Press%20Briefing.mp3>, Accessed 31 March 2015.

Montenbruck O, Hugentobler U, Dach R, Steigenberger P and Hauschild A (2011) Apparent clock variations of the Block IIF-1 (SVN62) GPS satellite, GPS Solutions, 16(3): 303-313. https://doi.org/10.1007/s10291-011-0232-x.

Tegedor and Øvstedal (2014) Triple carrier precise point positioning (PPP) using GPS L5, Survey Review, 46(337): 288-297, https://doi.org/10.1179/1752270613Y.0000000076

3 DEALING WITH BIASES IN PPP WITH MULTI-FREQUENCY AND MULTI-CONSTELLATION DATA

Integration of MFMC data results in various inter-system and inter-frequency biases (if using GLONASS) that must be dealt with in order to get the highest precision. This chapter presents a detailed study on these biases and proposes models to account for them in the PPP model.

This chapter is covered by the following publication:

- El-Mowafy A, Deo MN, Rizos C (2015) On biases in precise point positioning with multi-constellation and multi-frequency GNSS data, Measurement Science Technology 27 (2016), 10pp, doi:10.1088/0957-0233/27/3/035102.

On biases in precise point positioning with multi-constellation and multi-frequency GNSS data

IOP Publishing Measurement Science and Technology
Meas. Sci. Technol. **27** (2016) 035102 (10pp) doi:10.1088/0957-0233/27/3/035102

On biases in precise point positioning with multi-constellation and multi-frequency GNSS data

A El-Mowafy[1], M Deo[2] and C Rizos[3]

[1] Department of Spatial Sciences, Curtin University, GPO Box U 1987, Perth WA 6845, Australia
[2] Air Services Australia, Canberra, Australia
[3] School of Civil and Environmental Engineering, University of New South Wales, Kensington, NSW 2052, Australia

E-mail: a.El-Mowafy@curtin.edu.au

Received 12 November 2015, revised 16 December 2015
Accepted for publication 29 December 2015
Published 19 January 2016

Abstract

Various types of biases in Global Navigation Satellite System (GNSS) data preclude integer ambiguity fixing and degrade solution accuracy when not being corrected during precise point positioning (PPP). In this contribution, these biases are first reviewed, including satellite and receiver hardware biases, differential code biases, differential phase biases, initial fractional phase biases, inter-system receiver time biases, and system time scale offset. PPP models that take account of these biases are presented for two cases using ionosphere-free observations. The first case is when using primary signals that are used to generate precise orbits and clock corrections. The second case applies when using additional signals to the primary ones. In both cases, measurements from single and multiple constellations are addressed. It is suggested that the satellite-related code biases be handled as calibrated quantities that are obtained from multi-GNSS experiment products and the fractional phase cycle biases obtained from a network to allow for integer ambiguity fixing. Some receiver-related biases are removed using between-satellite single differencing, whereas other receiver biases such as inter-system biases are lumped with differential code and phase biases and need to be estimated. The testing results show that the treatment of biases significantly improves solution convergence in the float ambiguity PPP mode, and leads to ambiguity-fixed PPP within a few minutes with a small improvement in solution precision.

Keywords: GNSS, precise point positioning, biases, GPS

(Some figures may appear in colour only in the online journal)

1. Introduction

In precise point positioning (PPP), it is crucial to account for all biases during measurement processing to achieve high accuracy. For instance, the use of the International Global Navigation Satellite System (GNSS) Service (IGS) clock corrections computed from ionosphere-free observations that have embedded differential code biases (DCBs) introduces these biases into phase observations. These biases, in addition to the biases of the phase observations, propagate with phase ambiguities. Hence, proper treatment of these biases will allow integer ambiguity resolution in PPP, leading to an overall improvement in positioning performance. This treatment has to consider that not all biases can be estimated, such as additional unknowns in the PPP model along with the position, phase ambiguities, and atmospheric parameters. This is mainly due to the fact that different biases, if considered individually, are identically modeled, resulting in a rank deficiency. Thus, one strategy to handle biases is to take advantage of the relatively stable nature of satellite-related biases, to estimate these biases externally using reference stations, and to provide them to users to calibrate them out. At the receiver end, the use of between-satellites single-differences (BSSDs) is an effective approach for canceling receiver-related biases from the same frequency band from satellites that belong to the same constellation.

Ge *et al* (2008) discussed the estimation of satellite single-differenced phase biases using a ground-tracking network. The estimation of phase biases was affected by code biases. An alternate wide-lane phase bias calibration method was proposed by Banville *et al* (2008). Collins *et al* (2010) merged code and phase biases separately with clock offsets in a decoupled clock model. A similar model was presented in Laurichesse *et al* (2008, 2009) and Laurichesse (2015) using 'phase clocks', assuming that the code biases are known. Wen *et al* (2011) proposed the estimation of geometry-free receiver and satellite phase biases as additional parameters in Kalman filtering and sequentially fixing undifferenced ambiguities. Khodabandeh and Teunissen (2014) discussed computing differential phase biases (DPBs) combined with other biases using an array of antennas separated by very short distances to reduce the code-dominant noise and multipath errors. Wübbena *et al* (2014) discussed the exchange of satellite phase bias data using the Radio Technical Commission for Maritime Services (RTCM) State Space Representation (SSR) format, message types (1265–1270) for different constellations in uncombined form to allow for implementation within different methods of ambiguity resolution. Laurichesse (2015) showed the successful implementation of the individual satellite phase biases using multi-frequency scenarios.

Compared with the traditional use of dual-frequency single constellation data in PPP, the use of multi-frequency and multi-constellation data offers several advantages. These advantages include improved accuracy and precision, and a reduction of convergence time. For instance, Cai (2009) integrated Global Positioning System (GPS) and Global Navigation Satellite System (GLONASS) measurements into a PPP algorithm and reported an improvement of about 24% in positional accuracy. Similar improvements were achieved by Li *et al* (2013) when combining GPS and BeiDou in PPP. However, when integrating measurements from multiple constellations, additional biases such as inter-system receiver time biases (ISBs) and time scale offsets (ISTBs) are encountered.

In this contribution we revisit the topic of dealing with biases in PPP using multi-constellation GNSS data motivated by the following. First, most of the literature introduces biases in a combined form with little detail and focuses only on the use of dual-frequency observations. In this manuscript, we provide more insight into the source and presentation of biases that would be useful for further investigations. Second, when users implement biases that are externally provided from a service network, we highlight the interoperability issue where a user should utilize measurements that are compatible with the ones used in the service network to generate these biases. Therefore, this paper aims to clarify different types of biases that are involved when using different possible measurement combinations, particularly when integrating data from multiple constellations and frequencies. In addition, this paper discusses the sources freely available to compensate for some of these biases.

The characteristics of our strategy in this study that deals with biases in PPP, targeting integer-ambiguity fixing, include the following: (i) The use of the precise orbits, clock corrections, and DCBs that are generated by the IGS multi-GNSS experiment (MGEX); (ii) the bias terms are reparametrized; (iii) fractional phase cycle biases are assumed to be computed from a reference network; (iv) BSSD observations are used; and finally (v) ionosphere-free observations from single or multiple GNSS constellations are considered.

The remainder of this paper is organized as follows. The next section reviews the different types of measurement biases that affect single and multi-constellation PPP. Several PPP models are discussed in the following section, which provides a rigorous treatment of biases. The modelling options for these biases in the more challenging case of multi-frequency, multi-constellation GNSS data is presented. The results and conclusions are presented thereafter.

2. Biases in single GNSS constellation observation equations

For the PPP model, where precise orbits and clock corrections are used, the observation equations for pseudorange code and phase measurements for satellite k from a GNSS constellation, such as GPS (denoted here as G), to receiver r for signal c_i on frequency i in length units can be formulated as:

$$P(c_i)_r^{k_G} = \rho_r^{k_G} + c(\mathrm{d}t_{r_G} - \mathrm{d}t^{k_G} + d_{r_G}(c_i) - d^{k_G}(c_i)) + T^{k_G} + \mu_i I^{k_G} + \varepsilon_{P(c_i)_r^{k_G}} \quad (1)$$

$$\phi(c_i)_r^{k_G} = \rho_r^{k_G} + c(\mathrm{d}t_{r_G} - \mathrm{d}t^{k_G}) + \delta_{r_G}(c_i) - \delta^{k_G}(c_i) + T^{k_G} + \lambda_i(N_r^{k_G}(c_i) + \mathrm{IFPB}(c_i) - \mu_i I^{k_G} + \varepsilon_{\phi(c_i)_r^{k_G}} \quad (2)$$

where $P(c_i)_r^{k_G}$ and $\phi(c_i)_r^{k_G}$ denote the code and phase measurements, respectively; $\rho_r^{k_G}$ is the satellite-to-receiver geometric range; c is the speed of light in a vacuum; $\mathrm{d}t_{r_G}$ and $\mathrm{d}t^{k_G}$ are the receiver and satellite clock offsets, where the latter is eliminated in PPP by the use of clock corrections. T^{k_G} is the troposphere delay modeled as one vertical component for all the satellites projected along the receiver-to-satellite direction using a mapping function (Tuka and El-Mowafy 2013); λ_i denotes the wavelength for frequency i; $\mu_i = \frac{f_1^2}{f_i^2}$ is the dispersive coefficient of the ionosphere; I is the ionosphere error for a reference frequency, e.g. L1 for GPS, and $N_r^{k_G}(c_i)$ is the integer ambiguity. $\varepsilon_{\phi(c_i)_r^{k_G}}$ and $\varepsilon_{P(c_i)_r^{k_G}}$ include the measurement noise and multipath of the phase and code measurements. $d_{r_G}(c_i)$ and $d^{k_G}(c_i)$ are the receiver and satellite hardware biases in time units for code measurement, respectively. $\delta_{r_G}(c_i)$ and $\delta^{k_G}(c_i)$ are the receiver and satellite hardware biases for phase observation in length units. It is assumed that the receiver hardware biases $\delta_{r_G}(c_i)$ and $d_{r_G}(c_i)$ are the same for measurements of the same frequency for all the satellites from the same constellation.

IFPB denotes the geometric initial fractional phase cycle bias. It may exist due to the receiver tracking method, and represents the geometric difference between the measured phase (after compensation for ambiguities and excluding other biases) and the actual receiver-to-satellite range at the receiver initialization (switch-on). In equation (2), IFPB is not

merged with the hardware delay as they differ in the sense that IFPB is constant for each session as long as the receiver keeps tracking the satellite, and it may change with a switch-on and off of the receiver, whereas the phase hardware delay is stable and changes very slowly with time. However, in practice, IFPB is inseparable from the hardware delay, and we do not attempt to do that here, as will be clarified later. For a single receiver, IFPB is frequency dependent, and it is assumed the same for measurements on the same frequency for all the satellites from the same constellation.

In PPP, users mostly employ IGS corrections to clock offsets that are computed from an ionosphere-free combination of primary signals. They may additionally employ measurement combinations of other signals as well as measurements from multiple constellations. The next section discusses different types of biases that are present in these cases and the following section will discuss the parametrization of these biases.

3. Types of biases

This section introduces different types of biases that affect multi-frequency single and multi-constellation GNSS measurements. The inter-frequency channel biases of GLONASS measurements and the quarter-cycle phase shifts between the in-phase and quadrature signals will not be covered here as the former were discussed in Reussner and Wanninger (2011) and Aggrey and Bisnath (2014), and the latter were discussed in Wübbena *et al* (2009).

3.1. Inter-system time biases (ISTBs)

Measurements from each GNSS constellation have satellite clock offsets that are referenced to its time scale. To account for these inter-system time offsets, two methods can be used. The first is to estimate it as an independent parameter for each system, while the second is to estimate the clock offset for one system and then estimate the time differences for the other systems relative to the reference one. These are defined as inter-system time offset (biases) (ISTBs), which need to be modeled as extra parameters in PPP. This parameter can be combined into one parameter with the receiver time offset (ISB), as will be discussed in section 3.5. In the future, precise clock corrections for the new constellations generated by MGEX will be referenced to the GPS time scale (Steigenberger *et al* 2014). Hence, there will be no need to consider ISTBs when using MGEX products.

3.2. Hardware biases

The receiver and satellite hardware biases (d_{r_G}, δ_{r_G}) and (d^{k_G}, δ^{k_G}) are caused by several sources including digital delays in the signal generator, signal distortion, the processing filters, correlator differences handling signal modulation, firmware biases, bandwidth dissimilarities, in addition to the signal path through the antenna, splitter, cabling, and amplifier (Phelts 2007). Moreover, hardware biases may exist due to incoherence (misalignment) between the signal code and phase signals. This effect has been observed on the L5 signals of the GPS Block IIF satellites, but it has not been observed on the GPS L1 signals (EU-US 2015). Furthermore, a combination of signals on different frequencies assumes that the signals are synchronized at the time of their broadcast. However, electronic components introduce different amounts of signal delay at different frequencies producing an inter-frequency bias that is nominally constant. This offset is estimated and broadcast to the user as part of the navigation data.

3.3. Differential code biases (DCBs)

In PPP, dual-frequency observations are typically used to eliminate the first-order effects of the ionosphere. Hence, differences between the hardware dependent biases will appear in the observation equations, defined as DCBs. For example, when differencing the signals c_i and c_j on frequencies i and j:

$$\begin{aligned}\mathrm{DCB}_{r_G}(c_i, c_j) &= d_{r_G}(c_i) - d_{r_G}(c_j);\ \text{and}\ \mathrm{DCB}^{k_G}(c_i, c_j)\\ &= d^{k_G}(c_i) - d^{k_G}(c_j)\end{aligned} \tag{3}$$

where $\mathrm{DCB}_{r_G}(c_i, c_j)$ and $\mathrm{DCB}^{k_G}(c_i, c_j)$ denote the receiver and satellite DCBs, respectively. When ionosphere-free combinations are applied, the DCBs for the frequencies i and j are scaled by the factors:

$$\alpha_{i,j} = \frac{f_i^2}{f_i^2 - f_j^2},\ \beta_{i,j} = \frac{f_j^2}{f_i^2 - f_j^2} \tag{4}$$

such that:

$$\begin{aligned}\mathrm{DCB}_{r_G}(\mathrm{IF}_{c_i,c_j}) &= \alpha_{i,j}\, d_{r_G}(c_i) - \beta_{i,j}\, d_{r_G}(c_j);\ \text{and}\ \mathrm{DCB}^{k_G}(\mathrm{IF}_{c_i,c_j})\\ &= \alpha_{i,j}\, d^{k_G}(c_i) - \beta_{i,j}\, d^{k_G}(c_j)\end{aligned} \tag{5}$$

where IF denotes the ionosphere-free operator. For example, the precise orbits and clock corrections provided by the IGS are based on an ionosphere-free combination of code and phase measurements. To minimize the bias problem, the IGS-MGEX lumps the associated DCBs into the receiver clock offsets. These 'conventional' IGS clock corrections are based on $P(Y)$ code measurements on the L1/L2 frequencies for GPS, and E_1/E_{5a} for Galileo. Thus, assuming the primary signals are defined as c_1 and c_2, the satellite clock offset is (Montenbruck and Hauschild 2013):

$$\begin{aligned}\mathrm{d}t(\mathrm{IF}_{c_1,c_2})^{k_G} &= \mathrm{d}t^{k_G} - \mathrm{DCB}^{k_G}(\mathrm{IF}_{c_1,c_2})\ \text{or}\ \mathrm{d}t^{k_G}\\ &= \mathrm{d}t(\mathrm{IF}_{c_1,c_2})^{k_G} + \mathrm{DCB}^{k_G}(\mathrm{IF}_{c_1,c_2})\end{aligned} \tag{6}$$

Hence, the ionosphere-free code observations modelled from these 'primary' frequencies will not include DCBs. However, for raw (undifferenced) observations and for an ionosphere-free combination of other signals, DCBs should be included.

The ionosphere-free DCB ($\mathrm{DCB}^{k_G}(\mathrm{IF}_{c_1,c_2})$) is not computed by the IGS, and it can be formulated by pre-multiplying the DCB^{k_G} in equation (3) by $\beta_{i,j}$ in one case and by $\alpha_{i,j}$ in another case, such that:

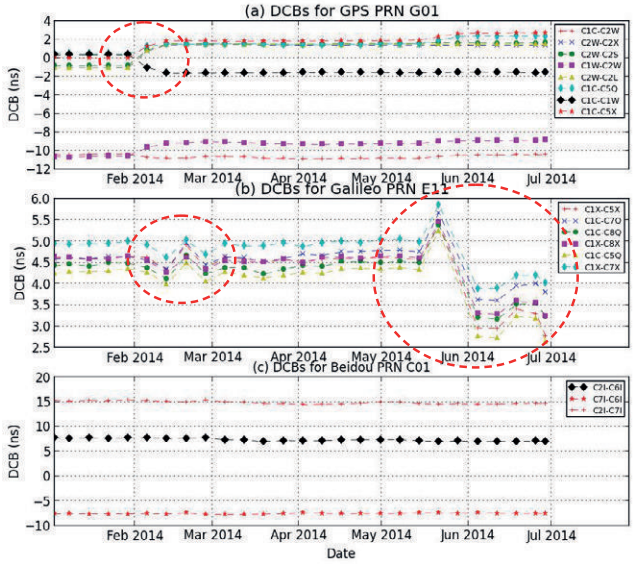

Figure 1. DCBs for (a) GPS PRN 01; (b) Galileo PRN E11; and (c) BeiDou PRN C01 from January to July 2014, obtained from IGS MGEX.

$$\begin{aligned}\mathrm{DCB}^{k_G}(\mathrm{IF}_{c_1,c_2}) &= \alpha_{i,j}\, d^{k_G}(c_1) - \beta_{i,j} d^{k_G}(c_2)\\ &= \beta_{1,2}\mathrm{DCB}^{k_G}(c_1,c_2) + d^{k_G}(c_1)\\ &= \alpha_{1,2}\mathrm{DCB}^{k_G}(c_1,c_2) + d^{k_G}(c_2)\end{aligned} \tag{7}$$

Thus, for the signal c_i, we have:

$$\begin{aligned}\mathrm{d}t^{k_G} + d^{k_G}(c_i) &= \mathrm{d}t(\mathrm{IF}_{c_1,c_2})^{k_G} + \beta_{1,2}\mathrm{DCB}^{k_G}(c_1,c_2)\\ &\quad - \mathrm{DCB}^{k_G}(c_i,c_1)\end{aligned} \tag{8}$$

Similarly in the case for the receiver biases.

For the satellite DCBs (i.e. DCB^{k_G}), when processing the legacy L1 or L2 $P(Y)$ signals, a time group delay (TGD) parameter is provided in the GPS navigation message, which represents a scaled version of the satellite-differential L1/L2 $P(Y)$ code. In addition, inter-signal corrections (ISCs) will be provided in the new civil navigation (CNAV) data of the L2C and L5 signals as well as the CNAV-2 message data for the future L1C signal. The TGDs and ISCs are fully equivalent to the satellite DCB (Montenbruck *et al* 2014). For legacy signals, the DCBs for the GPS and GLONASS satellites available from the Centre for Orbit Determination in Europe (CODE) (Schaer and Dach 2010) are applicable for the dual-frequency code measurements with the naming convention consistent with receiver independent exchange format (RINEX) version 2 (e.g. C1, C2, P1, and P2). With the modernization of GPS and the advent of multi-constellation GNSS, DCBs that are consistent with RINEX version 3 tracking modes should be used. These DCBs for various code measurements and tracking modes of GPS, Galileo, and BeiDou observations, with a daily repeatability of 0.05–0.3 ns, are provided by MGEX (see ftp://cddis.gsfc.nasa.gov/pub/gps/products/mgex/dcb). DCBs for the Quasi-Zenith Satellite System (QZSS) are not provided at present since more than one operational satellite is needed to establish a constellation mean. Figure 1 shows as an example the DCBs obtained from MGEX for GPS PRN 1, Galileo PRN E11, and BeiDou PRN C01 from January to July 2014. In general, the DCBs of the various signals were between −10.89 ns and 15.38 ns (−3.267 m and 4.614 m), with an overall standard deviation of 0.52 ns. During a certain period, the computed DCBs vary from their expected long-term stable values, as shown in figure 1. This variation can be attributed to a variation in the constellation mean. A possible method for the validation of the DCBs is to treat them as quasi-observations, and apply the single-receiver single-channel validation method described in El-Mowafy (2014, 2015a, 2015b).

In PPP, users need to use appropriate DCBs to make code measurements consistent with the precise orbits and satellite clock corrections used. For example, since the IGS products are produced using the ionosphere-free combination of the $P(Y)$ code measurements of GPS L1 and L2, dual-frequency PPP users measuring the C1 (C/A) code need to apply the P1–C1 DCB corrections to convert it to P1.

3.4. Differential phase biases (DPBs)

Similar to DCBs, the use of dual-frequency observations in PPP will result in DPBs, which are the difference between hardware-dependent phase biases in the satellite and receiver. With reference to equation (2), and for signals (c_i, c_j), the DPB in length units are:

$$\mathrm{DPB}_{r_G}(c_i,c_j) = c\{\delta_{r_G}(c_i) - \delta_{r_G}(c_j)\} \tag{9}$$

$$\mathrm{DPB}^{k_G}(c_i,c_j) = c\{\delta^{k_G}(c_i) - \delta^{k_G}(c_j)\} \tag{10}$$

and for the ionosphere-free case we have:

$$\mathrm{DPB}_{r_G}(\mathrm{IF}_{c_i,c_j}) = \alpha_{i,j}\delta_{r_G}(c_i) - \beta_{i,j}\delta_{r_G}(c_j) \tag{11}$$

$$\mathrm{DPB}^{k_G}(\mathrm{IF}_{c_i,c_j}) = \alpha_{i,j}\delta^{k_G}(c_i) - \beta_{i,j}\delta^{k_G}(c_j) \tag{12}$$

The satellite and receiver DPBs and IFPBs are difficult to be estimated independently since they are almost constant and as they have the same characteristics of phase ambiguities, they are practically inseparable. Hence, prior accounting for the satellite DPBs and IFPBs is crucial for multi-frequency PPP with an integer-ambiguity solution.

3.5. Inter-system biases (ISBs)

Assuming that the signal characteristics of the satellites from the same GNSS constellation on the same spectral occupation are identical, it is generally assumed that the receiver-dependent biases are the same for each satellite. However, for multi-constellation data, it cannot be assumed that receiver hardware biases are the same for signals from different GNSS constellations, even if they are transmitted on the same frequency (Hegarty *et al* 2004). Hence, multi-constellation PPP models must deal with inter-system biases (ISBs).

To enable the joint processing of measurements from different systems, all observations should refer to a reference system time scale, and when using observations from other

systems add the difference between their system clock offset and the reference system clock offset. At the satellite end this is dealt with as the ISTB. However, at the receiver end, the inter-system clock offset (denoted as ISB) is receiver-specific, and has to be estimated as an additional parameter for each system used in conjunction with a GPS. For example, for Galileo, assuming that the primary frequencies for Galileo are denoted as (E_1, E_{5a}), the ISB for ionosphere-free combinations is (Montenbruck and Hauschild 2013):

$$\mathrm{ISB}_{E-G} = \mathrm{d}t(\mathrm{IF}_{E_1,E_{5a}})_{r_\mathrm{E}} - \mathrm{d}t(\mathrm{IF}_{c_1,c_2})_{r_\mathrm{G}} \tag{13}$$

and for the individual uncombined observations it is:

$$\mathrm{ISB}_{E-G} = \mathrm{d}t_{r_\mathrm{E}} - \mathrm{d}t_{r_\mathrm{G}} \tag{14}$$

Both the ISTB and ISB can be combined as one parameter per constellation that is additional to GPS. Odijk and Teunissen (2013) showed that ISBs differ for receivers from different manufacturers and that they are stable over several hours. The magnitude of these ISBs reached up to 0.13 ns and 5.5 ns for phase and code observations, respectively. ISBs can also be absorbed into the estimated receiver clock offset such that a different receiver clock offset is associated with each system.

4. Biases in the PPP models

This section describes the parametrization of biases in single and multi-constellation PPP. Two cases will be discussed; the ionosphere-free dual-frequency combination of primary signals; and the ionosphere-free combination involving measurements other than the primary ones. The between-satellite single difference (BSSD) observation model and MGEX or similar products are utilized to account for some biases.

4.1. Ionosphere-free dual-frequency combination of primary signals

As discussed earlier, using IGS products, the ionosphere-free code observations modeled from the 'primary' frequencies (defined as c_1 and c_2) will not include satellite DCBs, i.e. $\mathrm{DCB}^{k_\mathrm{G}}(\mathrm{IF}_{c_1,c_2})$, such that the code observation equation after applying corrections for the satellite clock offset ($\mathrm{d}t(\mathrm{IF}_{c_1,c_2})^{k_\mathrm{G}}$) is:

$$P(\mathrm{IF}_{c_1,c_2})_r^{k_\mathrm{G}} = \rho_r^{k_\mathrm{G}} + c\mathrm{d}t(\mathrm{IF}_{c_1,c_2})_{r_\mathrm{G}} + \mathrm{DCB}_{r_\mathrm{G}}(\mathrm{IF}_{c_1,c_2}) + T^{k_\mathrm{G}} + \varepsilon_{P(\mathrm{IF}_{c_1,c_2})_r^{k_\mathrm{G}}} \tag{15}$$

Given that the ionosphere-free satellite clock corrections comprise clock offsets and DCBs, using the same clock corrections in ionosphere-free phase observation equations will bring in satellite DCBs, where:

$$\phi(\mathrm{IF}_{c_1,c_2})_r^{k_\mathrm{G}} = \rho_r^{k_\mathrm{G}} + c\mathrm{d}t(\mathrm{IF}_{c_1,c_2})_{r_\mathrm{G}} + c\mathrm{DCB}^{k_\mathrm{G}}(\mathrm{IF}_{c_1,c_2}) + \mathrm{DPB}_{r_\mathrm{G}}(\mathrm{IF}_{c_1,c_2}) - \mathrm{DPB}^{k_\mathrm{G}}(\mathrm{IF}_{c_1,c_2}) + \mathrm{IFPB}(\mathrm{IF}_{c_1,c_2}) + T^{k_\mathrm{G}} + \lambda_{\mathrm{IF}_{c_1,c_2}} N_r^{k_\mathrm{G}}(IF_{c_1,c_2}) + \varepsilon_{\phi(\mathrm{IF}_{c_1,c_2})_r^{k_\mathrm{G}}} \tag{16}$$

which can be re-written as:

$$\phi(\mathrm{IF}_{c_1,c_2})_r^{k_\mathrm{G}} = \rho_r^{k_\mathrm{G}} + c\mathrm{d}t(\mathrm{IF}_{c_1,c_2})_{r_\mathrm{G}} + \nu(\mathrm{IF}_{c_1,c_2})_{r_\mathrm{G}} - \nu(\mathrm{IF}_{c_1,c_2})^{k_\mathrm{G}} + T^{k_\mathrm{G}} + \lambda_{\mathrm{IF}_{c_1,c_2}} N_r^{k_\mathrm{G}}(\mathrm{IF}_{c_1,c_2}) + \varepsilon_{\phi(\mathrm{IF}_{c_1,c_2})_r^{k_\mathrm{G}}} \tag{17}$$

where $\nu(\mathrm{IF}_{c_1,c_2})_{r_\mathrm{G}}$ and $\nu(\mathrm{IF}_{c_1,c_2})^{k_\mathrm{G}}$ are the lumped receiver and satellite nuisance bias terms, such that:

$$\nu(\mathrm{IF}_{c_1,c_2})^{k_\mathrm{G}} = c\mathrm{DCB}^{k_\mathrm{G}}(\mathrm{IF}_{c_1,c_2}) + \mathrm{DPB}^{k_\mathrm{G}}(\mathrm{IF}_{c_1,c_2}) \tag{18}$$

$$\nu(\mathrm{IF}_{c_1,c_2})_{r_\mathrm{G}} = \mathrm{DPB}_{r_\mathrm{G}}(\mathrm{IF}_{c_1,c_2}) + \mathrm{IFPB}(\mathrm{IF}_{c_1,c_2}) \tag{19}$$

where $\mathrm{IFPB}(\mathrm{IF}_{c_1,c_2}) = \alpha_{1,2}\mathrm{IFPB}(c_1) - \beta_{1,2}\mathrm{IFPB}(c_2)$. Note that $\mathrm{DCB}^{k_\mathrm{G}}(\mathrm{IF}_{c_1,c_2})$ is not estimated by the MGEX. Although the *DPB* and IFPB are not estimated separately, and hence are considered in most of the literature as one term, we leave them separate without being estimated independently in the formulation since in principle they have assumed different characteristics, as explained in section 2.

For parameterization in a solution model, receiver biases are hardware dependent, and thus are required either to be individually calibrated or to be estimated as additional unknowns. Instead, under the assumption that the receiver code hardware biases from the same spectral occupation of a GNSS constellation are the same for all satellites from the same constellation, using the BSSD model will cancel $\mathrm{d}t(\mathrm{IF}_{c_1,c_2})_{r_\mathrm{G}}$, $\mathrm{DCB}_{r_\mathrm{G}}(\mathrm{IF}_{c_1,c_2})$ and $\nu(\mathrm{IF}_{c_1,c_2})_{r_\mathrm{G}}$. The main challenge left is to separate $\nu(\mathrm{IF}_{c_1,c_2})^{k_\mathrm{G}}$ from the phase ambiguities per satellite since they have the same modeling and characteristics, and solving for the two would introduce rank deficiency. Since $\nu(\mathrm{IF}_{c_1,c_2})^{k_\mathrm{G}}$ is satellite dependent, and due to the fact that these biases are usually stable during a typical observation session of a few hours, they can be estimated using a network of known stations and be applied by the user. This can either be for the whole quantity or only for the fractional part (also known as fractional cycle bias, FCB), where for the latter case the integer part can be added to the individual integer ambiguities that can be solved using known methods, such as the least-squares ambiguity decorrelation adjustment method (LAMBDA). One problem here is the short wavelength of the ionosphere-free combination for some combinations. For example, for the L1/L2 ionosphere combination the wavelength is 6.3 mm, computed as $\frac{2\times c\times f_0}{f_1^2 - f_2^2}$, for the integer ambiguity combination $(77N_1 - 60N_2)$, where f_o is 10.23 MHz. Hence, the ambiguities cannot be solved directly.

Several methods have been presented to solve the ionosphere-free PPP ambiguities. For example, under the assumption that a service provider supplies the wide-lane and narrow-lane phase biases, denoted as $\nu(wl_{c_1,c_2})^{k_\mathrm{G}}$ and $\nu(nl_{c_1,c_2})^{k_\mathrm{G}}$ respectively, which are estimated from an ambiguity-fixed network solution (Ge *et al* 2008). The wide-lane biases are stable over several hours to a few days, whereas the narrow-lane biases are only stable for a shorter period (fifteen minutes to two hours); therefore, they can be updated with different rates. At the user end, we solve first for the wide-lane ambiguities using code and the carrier Melbourne–Wübbena linear combination with the received values for $\nu(wl_{c_1,c_2})^{k_\mathrm{G}}$. Next,

narrow-lane ambiguities are formed using the ionosphere-free observations and their resolution is attempted (for more detail see Ge *et al* (2008) and Geng *et al* (2012)). Once the wide-lane and narrow-lane integer ambiguities are fixed, the ionosphere-free ambiguities are computed as (Geng *et al* 2012):

$$\lambda_{\mathrm{IF}_{c_1,c_2}}\widetilde{N}_r^{k_\mathrm{G}}(\mathrm{IF}_{c_1,c_2}) = \frac{f_1}{f_1+f_2}\,\lambda_{nl_{c_1,c_2}}\{N_r^{k_\mathrm{G}}(nl)+\nu(nl_{c_1,c_2})^{k_\mathrm{G}}\} + \frac{f_1 f_2}{f_1^2-f_2^2}\,\lambda_{wl_{c_1,c_2}}N_r^{k_\mathrm{G}}(wl) \tag{20}$$

where $\lambda_{\mathrm{IF}_{c_1,c_2}}\widetilde{N}_r^{k_\mathrm{G}}(\mathrm{IF}_{c_1,c_2})$ replaces $(\lambda_{\mathrm{IF}_{c_1,c_2}}N_r^{k_\mathrm{G}}(\mathrm{IF}_{c_1,c_2})+\nu(\mathrm{IF}_{c_1,c_2})^{k_\mathrm{G}})$ in equation (17), $N_r^{k_\mathrm{G}}(nl)$ and $N_r^{k_\mathrm{G}}(wl)$ are the narrow-lane and wide-lane integer ambiguities, respectively, $\lambda_{nl_{c_1,c_2}}$ and $\lambda_{wl_{c_1,c_2}}$ are their corresponding wavelengths.

Similarly for other constellations, for example Galileo, using the primary frequencies (assumed as E_1, E_{5a}) for satellite l we have:

$$P(\mathrm{IF}_{E_1,E_{5a}})_r^{l_\mathrm{E}} = \rho_r^{l_\mathrm{E}} + c\{\mathrm{d}t(\mathrm{IF}_{c_1,c_2})_{r_\mathrm{G}} + \mathrm{ISB}_{\mathrm{E-G}} + \mathrm{DCB}_{r_\mathrm{E}}(\mathrm{IF}_{E_1,E_{5a}}) - \mathrm{ISTB}_{E-G}\} + T^{l_\mathrm{E}} + \varepsilon_{P(\mathrm{IF}_{E_1,E_{5a}})_r^{l_\mathrm{E}}} \tag{21}$$

where the satellite clock offset $\mathrm{d}t(\mathrm{IF}_{E_1,E_{5a}})^{l_\mathrm{E}}$ is eliminated by the use of clock corrections. It is assumed that these clock corrections include the DCB component $\mathrm{DCB}^{l_\mathrm{E}}(\mathrm{IF}_{E_1,E_{5a}})$ similar to the case of the GPS. The $\mathrm{ISTB}_{\mathrm{E-G}}$ can be eliminated in the future when using MGEX clock corrections, as mentioned earlier. Similarly, the phase observation equation reads:

$$\phi(\mathrm{IF}_{E_1,E_{5a}})_r^{l_\mathrm{E}} = \rho_r^{l_\mathrm{E}} + c\{\mathrm{d}t(\mathrm{IF}_{c_1,c_2})_{r_\mathrm{G}} + \mathrm{ISB}_{\mathrm{E-G}} - \mathrm{ISTB}_{\mathrm{E-G}}\} + T^{l_\mathrm{E}} + \nu(\mathrm{IF}_{E_1,E_{5a}})_{r_\mathrm{E}} - \nu(\mathrm{IF}_{E_1,E_{5a}})^{l_\mathrm{E}} + \lambda_{\mathrm{IF}_{E_1,E_2}}N_r^{l_\mathrm{E}}(\mathrm{IF}_{E_1,E_{5a}}) + \varepsilon_{\phi(\mathrm{IF}_{E_1,E_{5a}})_r^{l_\mathrm{E}}} \tag{22}$$

with

$$\nu(\mathrm{IF}_{E_1,E_{5a}})^{l_\mathrm{E}} = c\mathrm{DCB}^{l_\mathrm{E}}(\mathrm{IF}_{E_1,E_{5a}}) + \mathrm{DPB}^{l_\mathrm{E}}(\mathrm{IF}_{E_1,E_{5a}}) \tag{23}$$

$$\nu(\mathrm{IF}_{E_1,E_{5a}})_{r_\mathrm{E}} = \mathrm{DPB}_{r_\mathrm{E}}(\mathrm{IF}_{E_1,E_{5a}}) + \mathrm{IFPB}(\mathrm{IF}_{E_1,E_{5a}}) \tag{24}$$

When referencing to a pivot GPS satellite, for example, the use of the BSSD model will eliminate $\mathrm{d}t(\mathrm{IF}_{c_1,c_2})_{r_\mathrm{G}}$; however, it cannot remove $\mathrm{ISB}_{\mathrm{E-G}}$, which is a receiver time offset between the GPS and Galileo.

In summary, the terms $\mathrm{ISB}_{\mathrm{E-G}}$, $\mathrm{ISTB}_{\mathrm{E-G}}$, $\mathrm{DCB}_{r_\mathrm{E}}(\mathrm{IF}_{E_1,E_{5a}})$ and $\nu(\mathrm{IF}_{E_1,E_{5a}})_r$ are assumed to be common for all Galileo satellites and need to be estimated. To reduce the number of unknowns, $\mathrm{ISB}_{\mathrm{E-G}}$, $\mathrm{ISTB}_{\mathrm{E-G}}$ and $\mathrm{DCB}_{r_\mathrm{E}}(\mathrm{IF}_{E_1,E_{5a}})$ are lumped into one term for the code observations (they are inseparable anyway as they share the same parameterization in the model). Similarly, $\mathrm{ISB}_{\mathrm{E-G}}$, $\mathrm{ISTB}_{\mathrm{E-G}}$ and $\nu(\mathrm{IF}_{E_1,E_{5a}})_{r_\mathrm{E}}$ are lumped into one term for phase observations. In the same way, two terms are introduced when integrating additional constellations with the GPS.

4.2. Ionosphere-free dual-frequency combination of signals that involve measurements other than the primary ones

The models presented so far can be extended to include ionosphere-free combinations using observations of a third or fourth frequency (e.g. L5 for GPS, E5b, or E6 for Galileo) or when using signals from different tracking modes (i.e. different signals modulated on the same frequency). Let us consider the general case using signals c_i and c_j that are different from the primary signals c_1 and c_2 from constellation G, the ionosphere-free code observation equation is:

$$P(\mathrm{IF}_{c_i,c_j})_r^{k_\mathrm{G}} = \rho_r^{k_\mathrm{G}} + c\{\mathrm{d}t(\mathrm{IF}_{c_1,c_2})_{r_\mathrm{G}} + \mathrm{DCB}_{r_\mathrm{G}}(\mathrm{IF}_{c_i,c_j}) - (\mathrm{DCB}^{k_\mathrm{G}}(\mathrm{IF}_{c_i,c_j}) - \mathrm{DCB}^{k_\mathrm{G}}(\mathrm{IF}_{c_1,c_2}))\} + T^{k_\mathrm{G}} + \varepsilon_{P(\mathrm{IF}_{c_i,c_j})_r^{k_\mathrm{G}}} \tag{25}$$

where the satellite clock offset $\mathrm{d}t(\mathrm{IF}_{c1,c2})^{k_\mathrm{G}}$ is eliminated by the use of its correction, and $\mathrm{DCB}^{k_\mathrm{G}}(\mathrm{IF}_{c_1,c_2})$ re-appears due to the use of clock corrections that include the bias of the primary frequencies. The bias term $\mathrm{DCB}^{k_\mathrm{G}}(\mathrm{IF}_{c_i,c_j})$ reads (Montenbruck and Hauschild 2013):

$$\mathrm{DCB}^{k_\mathrm{G}}(\mathrm{IF}_{c_i,c_j}) = \alpha_{i,j}\mathrm{DCB}^{k_\mathrm{G}}(c_i,\mathrm{IF}_{c_1,c_2}) - \beta_{i,j}\mathrm{DCB}^{k_\mathrm{G}}(c_j,\mathrm{IF}_{c_1,c_2}) \tag{26}$$

where:

$$\mathrm{DCB}^{k_\mathrm{G}}(c_i,\mathrm{IF}_{c_1,c_2}) = \{-\beta_{1,2}\mathrm{DCB}^{k_\mathrm{G}}(c_1,c_2) + \mathrm{DCB}^{k_\mathrm{G}}(c_i,c_1)\} \tag{27}$$

and similarly, $\mathrm{DCB}^{k_\mathrm{G}}(c_j,\mathrm{IF}_{c_1,c_2})$. An expression for $\mathrm{DCB}_{r_\mathrm{G}}(\mathrm{IF}_{c_i,c_j})$ can be obtained in the same way as $\mathrm{DCB}^{k_\mathrm{G}}(\mathrm{IF}_{c_i,c_j})$.

In principle, without biases, $\mathrm{d}t(\mathrm{IF}_{c_1,c_2})_{r_\mathrm{G}}$ should be equivalent to $\mathrm{d}t(\mathrm{IF}_{c_i,c_j})_{r_\mathrm{G}}$ and $\mathrm{d}t(\mathrm{IF}_{c_1,c_2})^{k_\mathrm{G}}$ should be equal to $\mathrm{d}t(\mathrm{IF}_{c_i,c_j})^{k_\mathrm{G}}$. Thus, using the former, which is available from the IGS, in place of the latter introduces $\mathrm{DCB}^{k_\mathrm{G}}(\mathrm{IF}_{c_1,c_2})$ into the phase equation, such that:

$$\phi(\mathrm{IF}_{c_i,c_j})_r^{k_\mathrm{G}} = \rho_r^{k_\mathrm{G}} + c\mathrm{d}t(\mathrm{IF}_{c_1,c_2})_{r_\mathrm{G}} + \nu(\mathrm{IF}_{c_i,c_j})_r - \nu(\mathrm{IF}_{c_i,c_j})^{k_\mathrm{G}} + T^{k_\mathrm{G}} + \lambda_{\mathrm{IF}_{c_i,c_j}}N_r^{k_\mathrm{G}}(\mathrm{IF}_{c_i,c_j}) + \varepsilon_{\phi(\mathrm{IF}_{c_i,c_j})_r^{k_\mathrm{G}}} \tag{28}$$

where

$$\nu(\mathrm{IF}_{c_i,c_j})^{k_\mathrm{G}} = c\mathrm{DCB}^{k_\mathrm{G}}(\mathrm{IF}_{c_1,c_2}) + \mathrm{DPB}^{k_\mathrm{G}}(\mathrm{IF}_{c_i,c_j}) \tag{29}$$

$$\nu(\mathrm{IF}_{c_i,c_j})_{r_\mathrm{G}} = \mathrm{DPB}_{r_\mathrm{G}}(\mathrm{IF}_{c_i,c_j}) + \mathrm{IFPB}(\mathrm{IF}_{c_i,c_j}) \tag{30}$$

Again, the receiver offsets $\mathrm{DCB}_{r_\mathrm{G}}(\mathrm{IF}_{c_i,c_j})$ and $\mathrm{d}t(\mathrm{IF}_{c_1,c_2})_{r_\mathrm{G}}$ are assumed to be the same for all the satellites from the same spectral occupation of a GNSS constellation. Therefore, they will cancel when applying the BSSD model. For constellations other than the GPS, for example Galileo, and using signals E_i and E_j that are different from the primary signals (E_1, E_{5a}) used in the generation of the clock corrections, the equation of the ionosphere-free combination for the code observations is:

Table 1. Summary of the possible treatment of biases in multi-constellation multi-frequency PPP.

Bias type	Method of treatment	Remarks
Satellite hardware bias (if undifferenced frequencies are considered; i.e. no DCB or DPB)	Code biases are removed using the BSSD model; phase biases are absorbed in phase ambiguities if untreated (resulting in float ambiguities). For PPP with ambiguity fixing, they are combined with IFPB and externally obtained	Satellite phase hardware biases are relatively stable during operation of a few hours
Satellite DCBs	Use IGS MGEX DCB products when needed	Not present for the primary code observations GPS L1/L2 P(Y), and Galileo E_1/E_{5a} but affects phase observations and are present in other types of observations
Satellite DPBs	Calibrated by external information (within the term ν); or considered to be absorbed in the phase ambiguities (i.e. float ambiguities)	Satellite DPBs result in non-integer ambiguity terms
Receiver hardware biases (if undifferenced frequencies are considered; i.e. no DCB or DPB)	Assumed canceled for the same frequency when using the BSSD model	
Receiver DCBs	Assumed canceled when using the BSSD model for the same frequencies for a single constellation, but needs to be estimated in the case of multiple GNSS with a pivot GPS satellite	
Receiver DPBs	Assumed canceled when using the BSSD for the same frequencies for a single constellation; can be absorbed with ambiguities in the case of multiple GNSS	
ISTB among satellite clock corrections of multi-constellations	Needs to be estimated, combined with the receiver ISB	Future MGEX clock corrections for all constellations will be referenced to the GPS
ISBs	The ISB at the receiver should be estimated as a parameter, can be combined with the ISTB and receiver DCB	The ISB is an individual receiver-dependent parameter for each additional constellation to GPS

$$P(\mathrm{IF}_{E_i,E_j})_r^{l_\mathrm{E}} = \rho_r^{l_\mathrm{E}} + c\{\mathrm{d}t(\mathrm{IF}_{c_1,c_2})_{r_\mathrm{G}} + \mathrm{ISB}_{\mathrm{E-G}} - \mathrm{ISTB}_{\mathrm{E-G}} + \mathrm{DCB}_{r_\mathrm{E}}(\mathrm{IF}_{E_i,E_j}) - (\mathrm{DCB}^{l_\mathrm{E}}(\mathrm{IF}_{E_i,E_j}) - \mathrm{DCB}^{l_\mathrm{E}}(\mathrm{IF}_{E_1,E_{5a}}))\} + T^{l_\mathrm{E}} + \varepsilon_{P(\mathrm{IF}_{E_i,E_j})_r^{l_\mathrm{E}}} \quad (31)$$

where $\mathrm{DCB}_{r_\mathrm{E}}(\mathrm{IF}_{E_i,E_j})$, $\mathrm{DCB}^{l_\mathrm{E}}(\mathrm{IF}_{E_i,E_j})$, $\alpha_{i,j}$ and $\beta_{i,j}$ are formulated using equations (4), (5) and (7) employing the Galileo frequencies, and $\mathrm{DCB}^{l_\mathrm{E}}(\mathrm{IF}_{E_1,E_{5a}})$ re-appears due to the use of clock corrections that include this bias. However, as mentioned earlier, the use of a pivot GPS satellite will not eliminate the $\mathrm{ISB}_{\mathrm{E-G}}$, $\mathrm{ISTB}_{\mathrm{E-G}}$ or these DCBs; therefore, they need to be estimated. In analogy with equation (22), the phase observation equation in this case will be:

$$\phi(\mathrm{IF}_{E_i,E_j})_r^{l_\mathrm{E}} = \rho_r^{l_\mathrm{E}} + c\{\mathrm{d}t(\mathrm{IF}_{c_1,c_2})_{r_\mathrm{G}} + \mathrm{ISB}_{\mathrm{E-G}} - \mathrm{ISTB}_{\mathrm{E-G}}\} + T^{k_\mathrm{G}} + \nu(\mathrm{IF}_{E_i,E_j})_{r_\mathrm{E}} - \nu(\mathrm{IF}_{E_i,E_j})^{l_\mathrm{E}} + \lambda_{\mathrm{IF}_{E_i,E_j}} N_r^{l_\mathrm{E}}(\mathrm{IF}_{E_i,E_j}) + \varepsilon_{\phi(\mathrm{IF}_{E_i,E_j})_r^{l_\mathrm{E}}} \quad (32)$$

where

$$\nu(\mathrm{IF}_{E_i,E_j})^{l_\mathrm{E}} = c\mathrm{DCB}^{l_\mathrm{E}}(\mathrm{IF}_{c_1,c_2}) + \mathrm{DPB}^{l_\mathrm{E}}(\mathrm{IF}_{E_i,E_j}) \quad (33)$$

$$\nu(\mathrm{IF}_{E_i,E_j})_{r_\mathrm{E}} = \mathrm{DPB}_{r_\mathrm{E}}(\mathrm{IF}_{E_i,E_j}) + \mathrm{IFPB}(\mathrm{IF}_{E_i,E_j}) \quad (34)$$

The case where either one of the signals i or j is one of the primary signals (i.e. $i = 1$ or 2, or $j = 1$ or 2) can easily be derived by replacing i or j by 1 or 2 in equations (25)–(33). As discussed earlier, $\mathrm{ISB}_{\mathrm{E-G}}$, $\mathrm{ISTB}_{\mathrm{E-G}}$ and $\mathrm{DCB}_{r_\mathrm{E}}(\mathrm{IF}_{E_i,E_j})$ are lumped into one term in the code observations, and likewise $\mathrm{ISB}_{\mathrm{E-G}}$, $\mathrm{ISTB}_{\mathrm{E-G}}$ and $\nu(\mathrm{IF}_{E_i,E_j})_r$ are joined in a second term for the phase observations. Both terms are common for all the Galileo satellite observations on frequencies i and j.

Table 1 gives some options discussed so far for the treatment of a number of biases in single-constellation and multi-constellation PPP processing. In summary, products from major service providers such as IGS, MGEX, and CODE are designed to minimize the impact of DCBs when ionosphere-free primary signals are used. However, the use of other types of observations will include DCBs that need to be accounted for during processing. In addition, when integrating observations from multiple constellations, several biases remain and thus need to be estimated such as ISBs, which are receiver dependent. A user should carefully consider the interoperability of the externally provided biases by utilizing consistent modeling of these biases within the observation equations that are compatible with the ones used at the service network to generate these biases. This will need also some details that have not been addressed in this manuscript, such as the use of the same satellite attitude convention in order to guarantee a consistent computation of the phase wind-up.

5. Testing

First, the impact of taking biases such as DCBs into account is demonstrated using simulated data with an epoch interval of 30 s at the IGS station CEDU in Australia. L1, L2, and L5 GPS signals were simulated for all the satellites. The PPP algorithm was implemented, as discussed above for three cases. The first is when using only the L1–L2 ionosphere-free combination. The second case is when using the L1–L5 ionosphere-free combination, and finally when combining the two combinations, defined here as L1–L2–L5. The analysis was carried out first by applying the satellite DCBs obtained from the MGEX in a float PPP solution, and second without applying them. The BSSD model was used in all cases. Analysis of the PPP results for the first 1000 epochs of data (8h:20m) are presented in table 2. The results are compared in terms of positioning convergence time, accuracy, and precision. The convergence time is defined as the time when a 3D positional precision of 0.05 m is reached and maintained. Accuracy is described by the mean of the errors (defined as the difference between the computed and known station coordinates) after convergence is achieved, and the precision is presented by the solution standard deviations (Stdev).

The L1–L2 IF are the primary signals used to generate the precise orbits and clock products, and thus the DCBs were removed in code observations and absorbed with the float ambiguities in the phase observations. For the L1–L5 IF case, the solution when the DCBs were applied converged earlier by 8.5 min from the solution without using the DCBs, and the Stdev were significantly better. The L1–L5 IF results with DCB corrections were slightly better than the L1–L2 IF results. This is because the noise frequency-dependent propagation factor for the L1–L5 IF combination (2.588), propagated from the noise of the unreferenced signals, is less than the L1–L2 IF factor (2.978). It is clear that any combination that involves L5 (i.e. L1–L5 and L1–L2–L5) gave poorer results when the DCBs were not included.

Next, testing was performed on 14 January 2015 in the static mode using real data with 30 s observation intervals of the IGS station DLF1 and using IGS rapid precise orbits and clock corrections. The phase biases were computed from 12 IGS stations, located in the Netherlands, Belgium, Germany, and France. The BSSD model was used. The data spanned approximately 75 min where only GPS observations were used at this stage. We plan to include other constellations in our future work. During the test period, ten GPS satellites were observed, only four of which were from Block IIF with L5 frequency; hence, positioning was performed with a mix of dual and triple-frequency observations. The data were processed twice. The first time, integer-ambiguity fixing was performed; and the second processing time only the float ambiguities were determined. The results of the two approaches were compared. The DCBs were used in both cases. The phase biases were estimated for all the satellite pairs by averaging the fractional parts of all the involved ambiguity estimates derived from the network solution. At the user end, the float *wl* ambiguities were estimated using the Melbourne–Wübbena observation combination and the *wl* phase biases were employed to fix

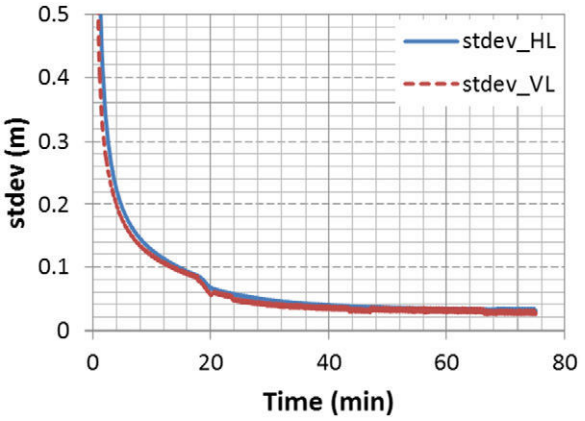

Figure 2. Positioning precision with float ambiguities. stdev_HL: Horizontal stdev; stdev_VL: Vertical stdev.

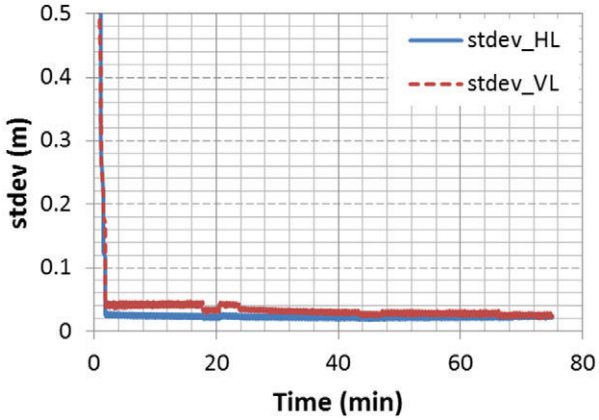

Figure 3. Positioning precision with fixed ambiguities. stdev_HL: Horizontal stdev; stdev_VL: Vertical stdev.

them to integers. This process was performed within a few seconds. The integer *wl* ambiguities were next used as fixed parameters to estimate the *nl* phase ambiguities. Once these *nl* float ambiguities were corrected with the *nl* phase biases, their integer values were resolved by applying the LAMBDA method. The obtained ambiguity fixing rate was 97%. The ionosphere-free combinations with integer ambiguities were next formed to determine the position coordinates (as shown in Geng *et al* 2012), the receiver clock offset, and the troposphere zenith wet delay (ZTD), where the dry troposphere was modeled out using the Saastamoinen model.

Figure 2 shows the horizontal and vertical solution Stdev of the float-ambiguity solution, and figure 3 depicts the results of processing the same data set but with integer ambiguity fixing. The horizontal stdev is the square root of the sum of the stdevs in Easting and Northing. As figure 3 shows, PPP with integer ambiguity resolution was able to significantly shorten the solution convergence time using a mix of dual and triple-frequency data. In the float ambiguity mode, 42 min and 20 min convergence time were needed to reach a precision below 5 cm and 10 cm, respectively. On the other hand, this level of precision was achieved after about 3 min by fixing the ambiguities. Table 3 shows the solution conversion time in both the float and integer ambiguity solution modes in addition to the average precision after converging to <5 cm in the

Table 2. Results for GPS L1–L2, L1–L5, and triple-frequency PPP with/without DCBs.

Algorithm	DCB applied Yes/No	Conver-gence time (min)	Easting mean Err (mm)	Northing mean Err (mm)	Up mean Err (mm)	Easting Stdev (mm)	Northing Stdev (mm)	Up Stdev (mm)
L1–L2 IF	Not needed	19	2	1	1	3	2	6
L1–L5 IF	Y	19	1	0	−2	1	1	4
	N	27.5	6	−1	−1	6	6	6
L1–L2–L5	Y	19	−1	0	−1	3	1	5
	N	27.5	3	−1	−4	5	2	5

Table 3. Float and ambiguity-fixed PPP results.

Ambiguity solution	Convergence to <5 cm (min)	Convergence to <10 cm (min)	Average Easting stdev converging to <5 cm (cm)	Average Northing stdev converging to <5 cm (cm)	Average Up stdev converging to <5 cm (cm)
Float	42	20	3.30	3.51	3.12
Integer	3	3	2.29	3.02	3.04

Easting, Northing, and Up position components. There was also an improvement in precision by a few mm in the case of the ambiguity-fixed solution compared with the float solution, in particular for the Easting component.

6. Conclusion

Accounting for biases is necessary in order to reduce the PPP convergence time, to improve accuracy, and to allow for integer ambiguity resolution. Single-constellation and multi-constellation PPP models were presented using an ionosphere-free combination of measurements. The options for the treatment of different biases are summarized in table 1. It is shown that the biases that need to be considered in the observation equations vary according to the type and combination of signals used. We have two cases that have been presented in detail that allow for the use of all signals from multi-frequency GNSS. The first case is when using the ionosphere-free dual-frequency primary signals that are used for the generation of clock corrections and precise orbits (such as L1 and L2 $P(Y)$ for GPS, and E_1 and E_{5a} for Galileo). The second case is when using dual-frequency signals other than the primary ones.

The use of BSSD measurements from the same constellation is recommended as it cancels receiver-related biases including DCBs, receiver IFPB, receiver clock offset, and common-mode satellite errors. However, these biases do not cancel when using differenced measurements between a pivot GPS satellite with satellites from other constellations. Additionally, ISBs and ISTB are introduced in this case. Currently, the use of MGEX products can compensate for satellite DCBs. IGS can play a major role in supporting multi-frequency and multi-constellation PPP users by producing precise orbits and clock corrections for each GNSS satellite and each individual frequency. This will enable PPP users to apply these corrections to raw measurements prior to forming any linear combination, thus avoiding further complications. Furthermore, the calibration of satellites (DPBs + IFPB) by an external organization would enable PPP users to perform integer ambiguity resolution resulting in a significantly reduced solution convergence time. The results from the analysis of the simulated data show that it is necessary to apply corrections to the DCB when using signals other than the primary ones. The results from the tested GPS data set in a static mode showed that correcting for the biases allowed ambiguity-fixed PPP, which significantly shortened the solution convergence to 3 min at <5 cm, and 10 cm precision levels from almost 42 min and 20 min in the float ambiguity mode. An improvement in precision of a few mm was also achieved, particularly in the Easting positioning component. Our future work will include the application of the proposed models for the multi-constellation case.

References

Aggrey J and Bisnath S 2014 Analysis and modelling of pseudorange and carrier-phase biases in GNSS Precise Point Positioning *Proc. of the 27th Int. Technical Meeting of ION GNSS-2014 (Tampa, FL, 8–12 September 2014)* pp 2512–22

Banville S, Santerre R, Cocard M and Langley R 2008 Satellite and receiver phase bias calibration for undifferenced ambiguity resolution *Proc. of the 2008 National Technical Meeting of the Institute of Navigation (San Diego, January 2008)* pp 711–9

Cai C 2009 Precise point positioning using dual-frequency GPS and GLONASS measurements *Masters Thesis* Department of Geomatics Engineering, University of Calgary, AB, Canada

Collins P, Bisnath S, Lahaye F and Héroux P 2010 Undifferenced GPS ambiguity resolution using the decoupled clock model and ambiguity datum fixing *Navig. J. Inst. Navig.* **57** 123–35

El-Mowafy A 2014 GNSS Multi-frequency receiver single-satellite measurement validation method *GPS Solut.* **18** 553–61

El-Mowafy A 2015a Estimation of multi-constellation GNSS observation stochastic properties using a single-receiver single-satellite data validation method *Surv. Rev.* **47–341** 99–108

El-Mowafy A 2015b Diagnostic tools using a multi-constellation single-receiver single-satellite data validation method *J. Navig.* **68** 196–214

EU-U.S. Cooperation on Satellite Navigation Working Group 2015 C-ARAIM Technical Subgroup Milestone 2 Report http://gps.gov/policy/cooperation/europe/2015/working-group-c/ARAIM-milestone-2-report.pdf (Accessed 10 November 2015)

Ge M, Gendt G, Rothacher M, Shi C and Liu J 2008 Resolution of GPS carrier phase ambiguities in precise point positioning (PPP) with daily observations *J. Geod.* **82** 389–99

Geng J, Shi C, Ge M, Dodson A, Lou Y, Zhao Q and Liu J 2012 Improving the estimation of fractional-cycle biases for ambiguity resolution in precise point positioning *J. Geod.* **86** 579–89

Hegarty C, Powers E and Fonville B 2004 Accounting for timing biases between GPS, modernized GPS, and Galileo signals *36th Annual Precise Time & Time Interval (PTTI) Meeting (Washington DC, 7–9 December 2004)* pp 307–17

Khodabandeh A, Teunissen P J G 2014 Array-based satellite phase bias sensing: theory and GPS/BeiDou/QZSS results *Meas. Sci. Technol.* **25** 095801

Laurichesse D 2015 Handling the biases for improved triple-frequency PPP convergence *GPS World* **26** 42–9

Laurichesse D, Mercier F, Berthias J P and Bijac J 2008 Real-time zero-difference ambiguities fixing and absolute RTK *Proc. ION NTM 2008 (San Diego, 28–30 January 2008)* pp 747–55

Laurichesse D, Mercier F, Berthias J P, Brocca P and Cerri L 2009 Integer ambiguity resolution on undifferenced GPS phase measurements and its application to PPP and satellite precise orbit determination *Navigation* **56** 135–49

Li W, Teunissen P J G, Zhang B and Verhagen J S 2013 Precise point positioning using GPS and compass observations *China Satellite Navigation Conf. (CSNC) 2013 Proc.* ed J Sun *et al* (Berlin: Springer) pp 367–78

Montenbruck O and Hauschild A 2013 Code biases in multi-GNSS point positioning *Proc. ION-ITM-2013 (San Diego, 28–30 January 2013)* pp 616–28

Montenbruck O, Hauschild A and Steigenberger P 2014 Differential code bias estimation using multi-GNSS observations and global ionosphere maps *Navigation* **61** 191–201

Odijk D and Teunissen P J G 2013 Characterization of between-receiver GPS-Galileo inter-system biases and their effect on mixed ambiguity resolution *GPS Solut.* **17** 521–33

Phelts R E 2007 Range biases on modernized GNSS codes *European Navigation Conference GNSS/TimeNav (Geneva, Switzerland, 29 May–1 June 2007)*

Reussner N and Wanninger L 2011 GLONASS inter-frequency biases and their effects on RTK and PPP carrier-phase ambiguity resolution *Proc. of ION GNSS 2011 (Portland, OR)* pp 712–6

Schaer S and Dach R 2010 Biases in GNSS analysis *IGS Workshop (Newcastle, England, 28 June–2 July 2010)*

Steigenberger P, Hugentobler U, Loyer S, Perosanz F, Prang L, Dach R, Uhlemann M, Gendt G and Montenbruck O 2014 Galileo orbit and clock quality of the IGS multi-GNSS experiment *Adv. Space Res.* **55** 269–81

Tuka A and El-Mowafy A 2013 Performance evaluation of different troposphere delay models and mapping functions *Measurement* **46** 928–37

Wen Z, Henkel P and Günter C 2011 Reliable estimation of phase biases of GPS satellites with a local reference network *Proc. ELMAR (Zadar, 14–16 Sept. 2011)* pp 321–4

Wübbena G, Schmitz M and Bagge A 2009 Some thoughts on satellite induced phase shifts aka 'the L2C Quarter Cycle Problem' and the impact on RINEX and RTCM *Geo + + White Paper* http:// geopp.de /media/docs/pdf/geopp_phase_shift_l2c.pdf (Accessed online on 4 December 2014)

Wübbena G, Schmitz M and Bagge A 2014 PPP with ambiguity resolution (AR) using RTCM-SSR *IGS Workshop (Pasadena, CA, 23–27 June 2014)*

4 TRIPLE FREQUENCY GNSS MODELS FOR PPP WITH FLOAT AMBIGUITY ESTIMATION

The availability of triple frequency measurements provides an opportunity to enhance the conventional dual-frequency PPP models with float ambiguity estimation. The first publication of this chapter presents three float-ambiguity PPP models that use triple frequency data. The first model is based on the conventional dual-frequency PPP model (Zumberge et al., 1997) where a triple-frequency ionosphere-free linear combination is used, the second model is based on the mixed code-carrier model (Gao and Shen, 2002) and the third model estimates the slant ionospheric error using additional frequency measurements, rather than forming linear combinations to eliminate it. The three models were validated using triple-frequency GPS data and their performance was compared to the traditional dual-frequency traditional model.

The second publication of this chapter extends first model to the multi-constellation scenario, where additional biases must be considered to get the best accuracy. The triple frequency ionosphere-free PPP model was tested with multi-constellation data from the GPS, Beidou and Galileo constellations at four Australian sites.

This chapter is covered by the following two publications:

- **Deo MN**, El-Mowafy A (2018) Triple Frequency GNSS Models for PPP with Float Ambiguity Estimation – Performance Comparison using GPS, Survey Review, 50(360): 249-261, doi: 10.1080/00396265.2016.1263179.
- **Deo MN**, El-Mowafy A (2016) Triple Frequency precise point positioning with multi-constellation GNSS, IGNSS Conference, UNSW Australia, 6–8 December 2016.

Survey Review

ISSN: 0039-6265 (Print) 1752-2706 (Online) Journal homepage: http://www.tandfonline.com/loi/ysre20

Triple-frequency GNSS models for PPP with float ambiguity estimation: performance comparison using GPS

M. Deo & A. El-Mowafy

To cite this article: M. Deo & A. El-Mowafy (2016): Triple-frequency GNSS models for PPP with float ambiguity estimation: performance comparison using GPS, Survey Review, DOI: 10.1080/00396265.2016.1263179

To link to this article: http://dx.doi.org/10.1080/00396265.2016.1263179

Published online: 02 Dec 2016.

Triple-frequency GNSS models for PPP with float ambiguity estimation: performance comparison using GPS

M. Deo* **and A. El-Mowafy**

This contribution proposes two new precise point positioning (PPP) models that use triple-frequency data, designed to accelerate convergence of carrier-phase float ambiguities. The first model uses a triple-frequency ionosphere-free linear combination that has minimum noise propagation and geometry-preserving properties. The second model uses a mixed code and carrier-phase linear combination with the same properties. A third model was also implemented, which uses individual uncombined triple-frequency measurements. The three models were validated using triple-frequency GPS data and their performance was compared to the traditional dual-frequency model in terms of the convergence time taken to achieve and maintain a uniform three-dimensional accuracy of 5 cm. Testing includes PPP processing of 1-h measurement blocks using 1–8 days of data from three locations in Australia. It was shown that all the three triple-frequency models had improved solution convergence time compared to the traditional PPP dual-frequency model although they gave almost similar accuracy and precision. The convergence time, when using the triple-frequency ionosphere-free model improved, by 10%, the improvement was 9% when using the mixed code-phase model, whereas the individual uncombined model resulted in 8% improvement.

Keywords: Precise point positioning, Convergence, Linear combinations, Multi-frequency, GNSS

Introduction

Precise point positioning (PPP) (Zumberge *et al.* 1997) is a well-established technique for achieving cm to sub-decimetre level positioning accuracy using a standalone GNSS receiver. It is used in various applications, such as deformation monitoring, volcanic monitoring and crustal motion studies. However, one concern in PPP is its need for a lengthy period, typically 30 min under normal conditions, to reduce the impact of the code noise such that the float ambiguities converge and give a solution better than a decimetre level of accuracy. This presents a major problem for many real-time applications that require the convergence to occur quickly prior to commencing the actual positioning. The solution convergence depends on several factors, such as number of satellites observed (redundancy), satellite geometry, multipath, atmospheric effects (troposphere and ionosphere) and the level of pseudorange noise, which is magnified when using the ionosphere-free combination. In addition, PPP errors may vary from day to day at the same site, despite the GPS constellation repeating itself almost every 12 h (Bisnath and Gao 2009). A number of research efforts have been made to reduce PPP convergence time to make it more practical. Gao and Shen (2002) introduced a mixed code-phase ionosphere-free linear combination that showed marginal improvements in convergence time. Ge *et al.* (2008) presented a PPP method with integer ambiguity resolution (PPP-AR), which was further refined in Geng *et al.* (2010). PPP-AR typically involves three steps: (1) estimating reliable float ambiguities, (2) solving integer ambiguities and (3) validating the integer solution. The receiver fractional phase biases are removed by performing between-satellite-single differencing (BSSD). Some PPP-AR methods estimate or use calibrated values of the satellite non-integer fractional phase biases, also known as fractional cycle biases. Other PPP-AR methods have been proposed, such as the integer-recovery clock method (Laurichesse *et al.* 2009) and the decoupled clock model (Collins *et al.* 2010). However, the convergence time in these ambiguity fixing PPP algorithms using dual-frequency measurements still remains to be around 30 min. The stabilisation and quick convergence of float ambiguities is a crucial first step for PPP-AR as well as conventional PPP.

The availability of triple-frequency measurements from modernised GPS Block IIF satellites, BeiDou and Galileo as well as other regional systems, such as QZSS, provides an opportunity to improve the performance of PPP.

Department of Spatial Sciences, Curtin University, Perth, Western Australia

*Corresponding author, email manoj.deo01@gmail.com

Received 30 May 2016; accepted 16 November 2016
DOI 10.1080/00396265.2016.1263179

For example, Geng and Bock (2013) presented a PPP-AR method designed for rapid ambiguity resolution using triple-frequency data. The method was based on the strategy used in Ge *et al.* (2008) and Geng *et al.* (2010), and commences with solving the L2/L5 extra wide-lane ambiguity using Melbourne–Wübbena linear combination, instead of the L1/L2 wide-lane ambiguity used in former studies. This is followed by solving an ionosphere-free wide-lane ambiguity, and subsequently the narrow-lane ambiguities. Continuously operating reference station (CORS) network data are required to solve for the fractional phase biases, and the authors claimed wide-lane and narrow-lane ambiguity correctness rate of 99% in 20 and 65 s, respectively. The study was based on simulated triple-frequency GPS data and the model did not consider treatment of initial fractional phase biases, which must be corrected prior to ambiguity fixing. As a refinement to conventional PPP, Banville *et al.* (2014) used global and regional ionospheric corrections, together with satellite phase biases for reducing the convergence time. However, users of this method must use specific ionospheric corrections that are compatible with this methodology. Seepersad and Bisnath (2014) focused on code noise and multipath reduction to improve convergence, reporting a 34% improvement. Shi *et al.* (2014) proposed local troposphere model to augment real-time PPP where data from a CORS network were used to estimate the Zenith Wet Delay (ZWD) at each station. This was modelled with optimal fitting coefficients and broadcast to users where decimetre accuracy was achieved within an improved 20 min, which shows that the PPP model is strengthened if external information is provided on the troposphere.

Recent research interest is also being focussed on the development of suitable linear combinations for PPP. Henkel and Günther (2008) discussed triple-frequency low-noise code-phase linear combinations that are suitable for estimating integer ambiguities in PPP. Elsobeiey (2015) compared nine triple-frequency linear combinations to study improvements in PPP convergence time and precision using GPS. However, no mathematical background was provided in the derivation of these linear combinations and the linear combination that was found to give best performance for GPS L1, L2 and L5 had the coefficients 2.7018, −2.1053, 0.4035, which give a significant noise propagation of 3.85 and is not completely ionosphere-free (ionospheric content was −0.0419 of the delay in L1). Also, the analysis did not consider anomalies in the L5 carrier-phase measurements owing to the thermal variations at the satellite (Montenbruck *et al.* 2012; Tegedor and Øvstedal 2014), and there were only two Block IIF satellites that were simultaneously tracked in the dataset for that study.

This contribution proposes two new linear combinations to improve convergence time of the dual-frequency ionosphere-free combinations used in conventional PPP utilising triple-frequency data. These combinations are as follows:

(i) Ionosphere-free, geometry-preserving triple-frequency linear combination of phase-only or code-only measurements that has lowest noise propagation.

(ii) A mixed code and phase linear combination that also has the above properties, which is an extension of the approach taken in Gao and Shen (2002) by considering a third frequency to further reduce the code noise.

It is hypothesised that minimising the pseudorange noise while keeping the measurements ionosphere-free would give optimum results. The first part of this paper presents triple-frequency observation equations, followed by derivation of the two new linear combinations. Another PPP model is also tested, which uses individual uncombined signals. Simulated GPS data are used to evaluate the performance of these models in terms of convergence time and accuracy compared with the standard L1/L2 dual-frequency traditional PPP solutions. Finally, the results are discussed and conclusions are presented.

Observation equations

The observation equations for the triple-frequency pseudorange and carrier-phase measurements (scaled to distance units), for satellite k from a GNSS constellation, such as GPS (denoted here as G), to receiver r are as follows:

$$P(i)_r^{k_G} = \rho_r^{k_G} + c(dt_{r_G} - dt^{k_G} + d(i)_{r_G} + d(i)^{k_G}) + T^{k_G} + \mu_i I^{k_G} + \varepsilon^{k_G}_{P(i)_r} \quad (1)$$

$$\phi(i)_r^{k_G} = \rho_r^{k_G} + c(dt_{r_G} - dt^{k_G}) + T^{k_G} - \mu_i I^{k_G} + \lambda_1(N(i)_r^{k_G} + \delta(i)_{r_G} + \delta(i)^{k_G}) + \varepsilon^{k_G}_{\phi(i)_r} \quad (2)$$

where i is the frequency identifier, such that $i = 1, 2, 5$ for GPS L1, L2 and L5, respectively as an example; $P(i)$ and $\phi(i)$ are the pseudorange and carrier-phase measurements, whereas frequency is denoted as f_i. ρ is the satellite-to-receiver geometric range; c is the speed of light in vacuum; dt_{r_G} and dt^{k_G} are the receiver and satellite clock offsets for GPS, where the latter is eliminated in PPP by the use of precise clock corrections. It is noted here that the International GNSS Service (IGS) precise clock corrections are modelled for L1/L2 ionosphere-free combinations and biases must be considered when using individual signals or other linear combinations as shown in El-Mowafy *et al.* (2016). T^{k_G} is the tropospheric delay; λ_i denotes the wavelength for frequency i. $\mu_i = (f_1^2/f_i^2)$ is the dispersive coefficient and I^{k_G} is the ionosphere error for a reference frequency, e.g. L1 for GPS. $\varepsilon^{k_G}_{\phi(i)_r}$ includes measurement noise and multipath of the carrier-phase measurement, whereas $\varepsilon^{k_G}_{P(i)_r}$ denotes code measurement noise and multipath. $d(i)_{r_G}$ is the receiver hardware bias for code measurement for frequency i; $d(i)^{k_G}$ is the satellite hardware bias. The IGS satellite clock offsets are determined from ionosphere-free measurements with embedded P1 and P2 Differential Code Biases (DCBs). $d(i)^{k_G}$ includes the additional satellite DCBs if using signals other than the reference signals P1 and P2, triple-frequency combinations or individual uncombined in the PPP model. These DCBs are available as an IGS Multi-GNSS Experiment product (Montenbruck *et al.* 2014). The receiver-dependent code hardware delays remain in the equations. $N(i)_r^{k_G}$ is the integer ambiguity term, whereas $\delta(i)_{r_G}$ and $\delta(i)^{k_G}$ are the receiver and satellite hardware biases for the carrier-phase measurements, respectively, which make the ambiguity a non-integer term (Shi and Gao 2014). One strategy to deal with the receiver clock and hardware biases is to apply the

BSSD model, which removes common receiver-related biases for both pseudorange and phase signals from the same frequencies of the same constellation (El-Mowafy *et al.* 2016). Another approach is to lump the receiver biases with other unknowns, such as clock offsets, for individual constellations and estimate it as part of the inter-system biases (El-Mowafy *et al.* 2016).

Modelling different types of biases in the uncombined form presents additional complexities because they have the same coefficients in the solution design matrix, resulting in rank deficiency and inability to separate them. The preferred approach for satellite biases is to estimate them externally and provide them to users as 'calibration' quantities. Alternatively, when solving float ambiguities, the biases may be lumped with the phase ambiguity terms and considered to be constant during the observation period since the biases are usually stable over several hours. Assuming that all biases except for the initial fraction phase biases have been accounted for by any of these approaches, BSSD measurements are used and the IGS precise clock corrections are applied, the observations, equations (1) and (2), are simplified to

$$P(i) = \rho + \mu_i I + T + \varepsilon_{P(i)} \tag{3}$$

$$\phi(i) = \rho - \mu_i I + \lambda_1 N(i)^* + T + \varepsilon_{\phi(i)} \tag{4}$$

where $N(i)^*$ is real numbers that includes the integer ambiguities and observation biases. The system and receiver identifiers have been removed when we are dealing with measurements from one constellation and since only a single receiver is considered in PPP. However, one should note that integration of multi-constellation data introduces additional biases, such as inter-system bias, constellation and receiver time offsets and DCBs. Dealing with these biases is beyond the scope of this paper and a comprehensive discussion on their source, modelling and treatment is given in our earlier work in El-Mowafy *et al.* (2016).

PPP using triple-frequency observations

In this section, we introduce the proposed models using the triple-frequency data.

The use of individual uncombined signals

The individual uncombined multi-frequency GNSS measurements can form the PPP model. Such a model avoids noise propagation by not creating linear combinations of observations. Thus, equations (3) and (4) are used for the code and phase measurements for each frequency (e.g. L1, L2 and L5 for GPS). The ionospheric bias is estimated using the third frequency measurement rather than forming ionosphere-free combinations. The unknown parameters include three position parameters and a troposphere ZWD parameter, which is assumed common to all satellite measurements and is modelled by applying a wet troposphere mapping function to map the ZWD to the slant receiver-satellite line of sight. The hydrostatic troposphere delay is modelled using an empirical model (Tuka and El-Mowafy 2013). Each satellite introduces a slant ionosphere delay and three ambiguity parameters. If BSSD is not used, there is also an additional receiver clock offset parameter.

Low-noise, ionosphere-free, geometry preserving triple-frequency phase-only and code-only linear combination

This section proposes a PPP model which uses a triple-frequency linear combination that is ionosphere-free, geometry-preserving and has lowest noise propagation, designed for faster ambiguity convergence compared to the traditional dual-frequency model. Concurrently with our study, Guo *et al.* (2016) presented a similar approach for BeiDou-only observations where only approximate values of the model coefficients were given. In our study, the derivation of the combination coefficients for all constellations, including GPS, QZSS, Galileo, BeiDou and the proposed GLONASS K2 Code Division Multiple Access (CDMA) signals, is given (Urlichich *et al.* 2011). This triple-frequency linear combination is applied to both carrier-phase and code measurements. A linear combination of triple-frequency phase measurements, where the frequencies are denoted in general as f_1, f_2 and f_3, is given as (Cocard *et al.* 2008) follows:

$$P = \alpha_1 P1 + \alpha_2 P2 + \alpha_3 P3 \tag{5}$$

$$\phi = \alpha_1 \phi 1 + \alpha_2 \phi 2 + \alpha_3 \phi 3 \tag{6}$$

where α_1, α_2 and α_3 are the linear combination coefficients for the three-frequency measurements. The geometry preservation condition is achieved by

$$\alpha_1 + \alpha_2 + \alpha_3 = 1 \tag{7}$$

The first-order ionosphere-free condition, which contains the majority of the ionospheric effects, is removed when

$$\frac{\alpha_1 \cdot 40.3\text{TEC}}{f_1^2} + \frac{\alpha_2 \cdot 40.3\text{TEC}}{f_2^2} + \frac{\alpha_3 \cdot 40.3\text{TEC}}{f_3^2} = 0 \tag{8}$$

The carrier frequencies are expressed in terms of a base GNSS frequency f_0, such that $f_j = \sqrt{k_j} f_0$, where f_0 is 10.23 MHz, and $\sqrt{k_j}$ is the frequency multiplier. The frequency multipliers for GPS, QZSS, Galileo, BeiDou and the proposed GLONASS K2 CDMA are given in Table 1. Accordingly, equation (8) can be simplified to

$$\frac{\alpha_1}{k_1} + \frac{\alpha_2}{k_2} + \frac{\alpha_3}{k_3} = 0 \tag{9}$$

Richert and El-Sheimy (2007) suggested that many coefficients can satisfy the above two criteria given in (equations (7) and (9)). However, the dual-frequency ionosphere-free observation combination used in the traditional PPP model has a high-noise amplification factor $\epsilon = \sqrt{\alpha_1^2 + \alpha_2^2} = 2.978$ for L1–L2 measurements for example. In this study, we use the measurement from a third frequency to form a separate condition that results in a minimum noise propagation. In a simplified form, assuming that the noise is the same for phase measurements on all frequencies, the noise propagation is directly proportional to $\sigma_\phi^2 = \sigma_{\phi j}^2(\alpha_1^2 + \alpha_2^2 + \alpha_3^2) = \sigma_{\phi j}^2 \epsilon^2$. Hence, the noise amplification factor is minimised by the

Table 1 Multi-constellation GNSS frequencies and frequency multipliers of a base frequency 10.23 MHz

GNSS constellation	Signal	Frequency multiplier ($\sqrt{k}$)
GPS/QZSS	L1	154
	L2	120
	L5	115
	LEX (QZSS only)	125
Galileo	E1	154
	E5a	115
	E5b	118
	E5 (a + b)	116.5
	E6	125
BeiDou	B1	152.6
	B2	118
	B3	124
GLONASS K2 (CDMA)	L1	156.5
	L2	122
	L3	117.5

following condition:

$$(\alpha_1^2 + \alpha_2^2 + \alpha_3^2) = \epsilon^2 = \text{MIN} \tag{10}$$

Satisfying the above three conditions (equations (7), (9) and (10)) would result in a linear combination with the potential to reduce PPP solution convergence time and improve positional accuracy. A solution for α_1, α_2 and α_3, from equations (7), (9) and (10), is now derived algebraically. Rearranging equation (7) as $\alpha_1 = 1 - \alpha_2 - \alpha_3$, substituting into equation (9) and rearranging in terms of α_2 results in

$$\alpha_2 = \frac{\alpha_3(k_2k_3 - k_1k_2) - k_2k_3}{k_1k_3 - k_2k_3} \tag{11}$$

and

$$\alpha_2^2 = \frac{\alpha_3^2(k_2k_3 - k_1k_2)^2 - 2\alpha_3k_2k_3(k_2k_3 - k_1k_2) + (k_2k_3)^2}{k_3^2(k_1 - k_2)^2} \tag{12}$$

Substituting equation (11) into (7) and rearranging in terms of α_1 gives

$$\alpha_1 = \frac{\alpha_3(k_1k_2 - k_1k_3) - k_1k_3}{k_1k_3 - k_2k_3} \tag{13}$$

and

$$\alpha_1^2 = \frac{\alpha_3^2(k_1k_2 - k_1k_3)^2 - 2\alpha_3k_1k_3(k_1k_2 - k_1k_3) + (k_1k_3)^2}{k_3^2(k_1 - k_2)^2} \tag{14}$$

Substituting equations (12) and (14) into (10) results in a quadratic equation of the form

$$A\alpha_3^2 + B\alpha_3 + C = 0 \tag{15}$$

where the constants A, B and C are

$$A = (k_1k_2 - k_1k_3)^2 + (k_2k_3 - k_1k_2)^2 + (k_1k_3 - k_2k_3)^2 \tag{16}$$

$$B = 2k_1k_3(k_1k_2 - k_1k_3) - 2k_2k_3(k_2k_3 - k_1k_2) \tag{17}$$

$$C = (k_1k_3)^2 + (k_2k_3)^2 - \epsilon^2(k_1k_3 - k_2k_3)^2 \tag{18}$$

The quantities A and B are constants, whereas C contains an unknown value for the noise amplification factor ϵ. There are two unknown variables α_3 and ϵ, in these equations, and the discriminant $B^2 - 4AC$ should be greater than zero for a real-value solution for α_3. Furthermore, the noise amplification factor is minimised when the discriminant is exactly zero, resulting in only one real root. C is obtained by

$$C = \frac{B^2}{4A} \tag{19}$$

From equation (15), a solution for α_3 is obtained as follows:

$$\alpha_3 = \frac{-B}{2A} = \frac{-q}{A} = \frac{C}{q} \tag{20}$$

where $q = -0.5B$. The value of α_3 is substituted into equation (11) and (7) to solve for α_2 and α_1, respectively. These coefficients for the triple-frequency linear combination α_1, α_2 and α_3, are given in Table 2 for GPS, QZSS, Galileo, BeiDou and GLONASS K2 CDMA signals, based on the frequency multiplier values given in Table 1. Also given in Table 2 are the values for the noise amplification factor, ϵ, calculated as

$$\epsilon = \sqrt{\frac{(k_1k_3)^4 + (k_2k_3)^4 - C}{(k_1^2k_3^2 - k_2^2k_3^2)^2}} \tag{21}$$

Table 2 additionally shows the percentage change in noise when using the given triple-frequency combinations with values of α_1, α_2 and α_3 from the proposed ionosphere-free combination, compared to the ionosphere-free dual-frequency combinations that are used for generating precise clock corrections by the IGS. These reference signals are L1/L2 for GPS, B1/B2 for BeiDou (Zhao *et al.* 2013) and E1/E5a for Galileo (Prange *et al.* 2012; Uhlemann *et al.* 2012). For GLONASS K2, the L1/L2 CDMA signals are assumed as the reference signals. A significant noise reduction is obtained using the proposed method at 14% for GPS, 3.1% for Galileo, 1.1% for BeiDou and 13.6% for GLONASS K2.

A refined dual-frequency mixed code-carrier PPP model

The previous section presented a triple-frequency combination for carrier phase and code observations separately. In this section, a mixed code-carrier phase linear combination is formed that is ionosphere-free, geometry-preserving and has minimum noise propagation. This PPP model is built from linear combinations of two dual-frequencies, such as L1/L2 and L1/L5 for GPS, as well as the carrier-phase only dual-frequency ionosphere-free combinations for the same frequencies to complete the model. This model solves for the individual non-integer carrier-phase ambiguities for each frequency (i.e. $N1^*$, $N2^*$ and $N5^*$ for GPS) as well as the receiver position and troposphere error. Using a pair of code and carrier-phase measurements of frequencies from the same GNSS constellation, e.g. L1 and L2 GPS, the

Table 2 Coefficients for triple-frequency linear combinations for different GNSS constellations and signals, with percentage change in noise compared to dual-frequency reference signals

GNSS constellation	Signal combination	α_1	α_2	α_3	Noise amp. factor (ϵ)	Percentage change
GPS	L1-L2-L5	2.326944	−0.359 646	−0.967299	2.546	−14.5%
QZSS	L1-LEX-L5	2.269122	−0.024 529	−1.244592	2.588	−13.1%
Galileo	E1-E5a-E5b	2.314925	−0.836 269	−0.478656	2.507	−3.1%
BeiDou	B1-B3-B2	2.566439	−0.337 510	−1.228930	2.865	−1.1%
GLONASS K2 (CDMA)	L1-L2-L3	2.359142	−0.404 596	−0.954546	2.577	−13.6%

For GLONASS K2, the L1/L2 CDMA signals are assumed as the reference signals.

Table 3 Coefficients for mixed code-carrier phase linear combinations with measurement noise (m), using $\sigma_P = 0.2m$ and $\sigma_\phi = 0.002m$

GNSS constellation	Signal combination	α_1	α_2	β_1	β_2	ϵ	Noise (m)
GPS	L1-L2	2.529802	−1.533226	0.001509	0.001915	2.968	0.006
GPS	L1-L5	2.250109	−1.252675	0.001108	0.001458	2.582	0.005
GPS	L2-L5	10.078988	−9.169588	0.044338	0.046263	15.057	0.030
QZSS	L1-LEX	2.905273	−1.910056	0.002150	0.002632	3.493	0.007
QZSS	LEX-L2	10.329707	−9.426643	0.047481	0.049456	15.575	0.031
QZSS	LEX-L5	6.166649	−5.194059	0.013137	0.014273	8.293	0.017
BeiDou	B1-B2	2.472483	−1.475721	0.001422	0.001816	2.889	0.006
BeiDou	B1-B3	2.917418	−1.922248	0.002173	0.002657	3.511	0.007
BeiDou	B2-B3	−8.209041	9.138934	0.035920	0.034186	13.248	0.026
Galileo	E1-E5a	2.250109	−1.252675	0.001108	0.001458	2.582	0.005
Galileo	E1-E5b	2.408595	−1.411632	0.001327	0.001709	2.800	0.006
Galileo	E5a-E5b	−11.70299	12.514784	0.095313	0.092891	21.696	0.043
GLONASS K2	L1-L2	2.533086	−1.536521	0.001514	0.001921	2.973	0.006
GLONASS K2	L1-L3	2.280974	−1.283628	0.001149	0.001506	2.624	0.005
GLONASS K2	L2-L3	10.812700	−9.923189	0.054208	0.056281	16.627	0.033

Table 4 Summary of PPP models being compared, the first three rows include three-code and three-phase observations

PPP model	Primary model equations	Number of obs. for n satellites	Number of unknowns	Parameter description
Individual uncombined signals	$\phi 1$, $\phi 2$, $\phi 5$ $P1$, $P2$, $P5$ (equations (3) and (4))	$6(n-1) = 6n-6$	$4+4(n-1) = 4n$	X, Y, Z, ZWD, $(n-1)\{I, N1^*, N2^*, N5^*\}$
Triple-frequency ionosphere-free	ϕ, P (equations (5) and (6))	$2(n-1) = 2n-2$	$4+(n-1) = 3+n$	X, Y, Z, ZWD, $(n-1)(N^*)$
Mixed code-phase	$\phi 12$, $\phi 15$ $\Theta 12$, $\Theta 15$, (equation (22))	$4(n-1) = 4n-4$	$4+3(n-1) = 1+3n$	X, Y, Z, ZWD, $(n-1)(N1^*, N2^*, N5^*)$
Traditional dual-frequency ionosphere-free	$\phi 12$, $P12$	$2(n-1) = 2n-2$	$4+(n-1) = 3+n$	X, Y, Z, ZWD, $(n-1)\{N^*\}$

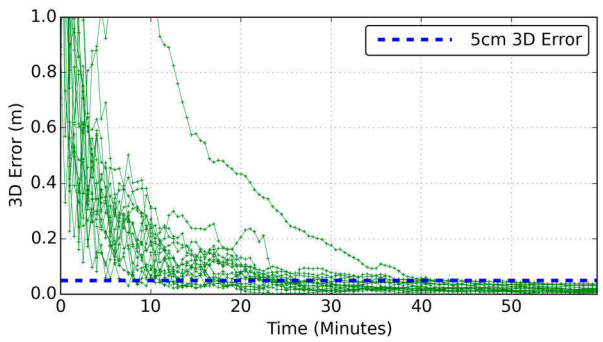

1 Dual-frequency (L1/L2) ionosphere-free PPP 3D positioning errors for the 24-hourly solutions at HOB2

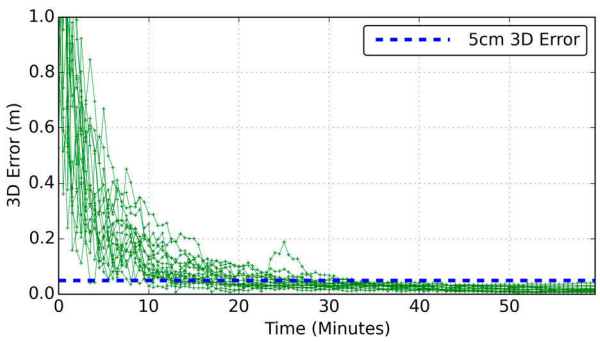

2 Triple-frequency ionosphere-free PPP 3D positioning errors for the 24-hourly solutions at HOB2

Table 5 Mean RMSE (East, North and Up) and convergence time for the GPS PPP algorithms tested with hourly data sessions

PPP model	Mean convergence time (min)	Mean RMSE – East converged (m)	Mean RMSE – North converged (m)	Mean RMSE – Up Converged (m)
Dual-frequency ionosphere-free (L1–L2)	29.451	0.014	0.005	0.020
Triple-frequency ionosphere-free	26.318	0.014	0.005	0.019
Mixed code-phase	26.831	0.013	0.005	0.019
Individual uncombined signals	27.036	0.014	0.005	0.019

Columns 3–5 present statistics for solutions that converged within 3D accuracy of 5 cm in less than 1 h.

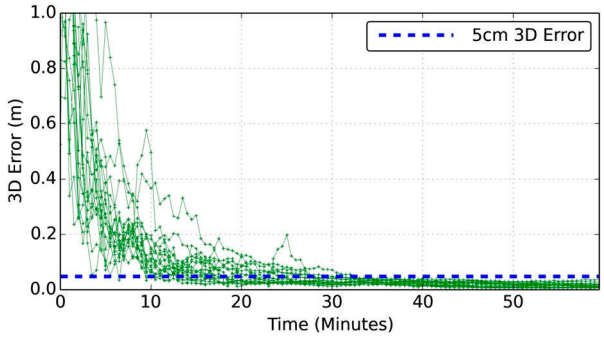

3 Mixed code-phase PPP 3D positioning errors for the 24-hourly solutions at HOB2

mixed code-carrier phase combination is expressed as

$$\Theta 12 = \alpha_1 \phi 1 + \alpha_2 \phi 2 + \beta_1 P1 + \beta_2 P2 \qquad (22)$$

where α_1 and α_2 are the coefficients for the carrier-phase measurements and β_1 and β_2 are the coefficients for the code measurements. The ionosphere-free condition is formed by

$$40.3TEC\left[\frac{-\alpha_1}{f_1^2} + \frac{-\alpha_2}{f_2^2} + \frac{\beta_1}{f_1^2} + \frac{\beta_2}{f_2^2}\right] = 0 \qquad (23)$$

and the geometry-preserving condition is

$$\alpha_1 + \alpha_2 + \beta_1 + \beta_2 = 1 \qquad (24)$$

Let us assume that the code noise is higher than the phase noise by a factor, a, e.g. $a = 100$ for GPS, and the noise for carrier-phase measurements on all its frequencies is the same, i.e. $\sigma_\phi = \sigma_{\phi 1} = \sigma_{\phi 2}$. The noise in the combination is minimised by minimising the amplification factors using the following condition:

$$\alpha_1^2 + \alpha_2^2 + a^2\beta_1^2 + a^2\beta_2^2 = \epsilon^2 = MIN \qquad (25)$$

The code and carrier-phase measurements are now weighted according to their measurement noise. A solution that satisfies the above three conditions will give the required coefficients α_1, α_2, β_1 and β_2 for the mixed code-carrier linear combination. The derivation of these coefficients is given in the Appendix for the interested reader.

Table 3 shows the derived coefficients α_1, α_2, β_1 and β_2, as well as the noise amplification factor ϵ for GPS, QZSS, Galileo, GLONASS K2 and BeiDou. The actual noise in the combination, in distance units, is evaluated by $\epsilon\sigma_\phi$, where σ_ϕ is the carrier-phase noise, typically a few millimetres for GPS. As shown in the table, the contribution of code measurement noise is supressed in the mixed code-phase combinations, since the absolute values of their coefficients are much smaller than those of the carrier-phase coefficients. Note here that since the code coefficients are multiplied by pseudoranges, which are large values in thousands of kilometres; thus, the linear combination value is significant and is numerically stable. As an example, if we assume the phase noise is $\sigma_\phi = 0.002m$ and the corresponding code noise is $\sigma_P = 0.2m$ for GPS L1 and L2, the total noise in the proposed mixed code-phase combination is just $0.006m$.

For the triple-frequency code and phase measurements, there would be only two independent mixed code-phase combinations. Considering GPS as an example, the mixed code-phase combinations L1/L2 and L1/L5 may be used in the same model. These two mixed code-phase combinations are used with the corresponding carrier-phase only dual-frequency ionosphere-free combinations L1/L2 and L1/L5 to complete the mixed code-phase PPP model. This model will have correlations between

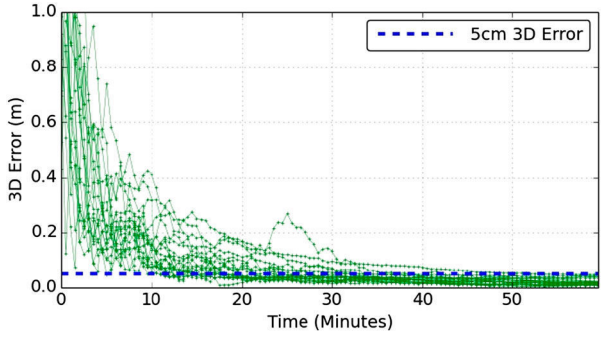

4 Individual uncombined signals PPP 3D positioning errors for the 24-hourly solutions at HOB2

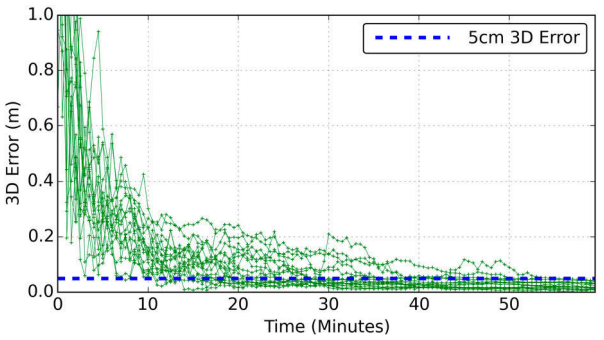

5 Dual-frequency (L1/L2) ionosphere-free PPP 3D positioning errors for the 24-hourly solutions at CEDU

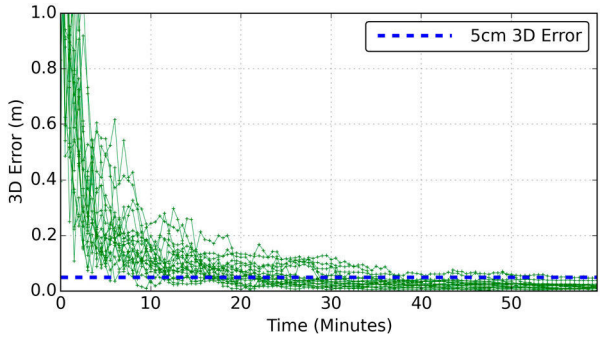

6 Triple-frequency ionosphere-free PPP 3D positioning errors for the 24-hourly solutions at CEDU

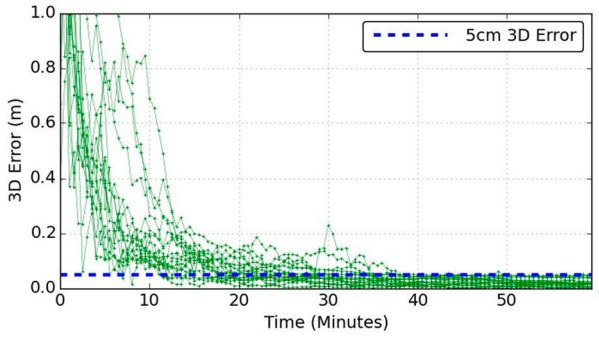

7 Mixed code-phase PPP 3D positioning errors for the 24-hourly solutions at CEDU

the linear combinations used, which will be discussed in a later section.

Summary of PPP models

Table 4 summarises the presented PPP models compared to the traditional dual-frequency PPP model in terms of the observation equations, number of observations, unknown parameters and their descriptions. The BSSD approach is used where one satellite is taken as a pivot and measurements from the remaining satellites are differenced with its measurements. All the presented triple-frequency models require a minimum of five satellites. The troposphere term is separated into a zenith hydrostatic component and a wet component, with the use of a mapping function, such as the Vienna Mapping Function (Bohem *et al.* 2006), to map the slant delays to the zenith direction. The zenith hydrostatic delay is modelled using an empirical model, such as Saastamoinen (Davis *et al.* 1985). The unknown parameters include three position parameters and ZWD, which are common in all model equations. There are $n-1$ ambiguities to resolve for each carrier-phase combination in the triple-frequency ionosphere-free model. For the mixed code-phase and individual uncombined models, the ambiguities are resolved for each frequency; thus there are $3(n-1)$ ambiguities to resolve. Although it may appear that a solution is possible with four satellites for the individual uncombined model, the two extra measurements of the third frequency do not add to the required geometry of the observed satellites, thus five satellites are still needed to form four single differences for eliminating

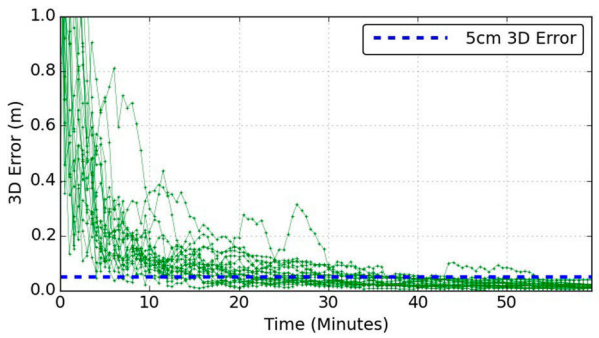

8 Individual uncombined signals PPP 3D positioning errors for the 24-hourly solutions at CEDU

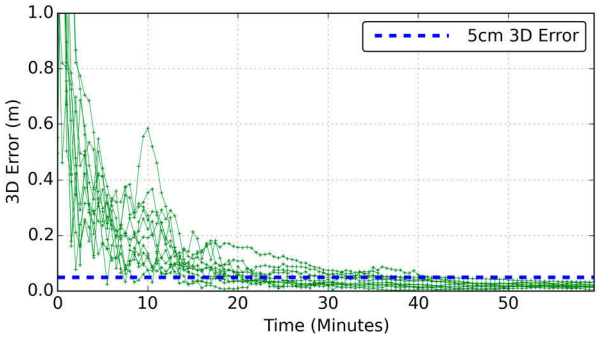

9 Dual-frequency (L1/L2) ionosphere-free PPP 3D positioning errors for the 24-hourly solutions at TIDB

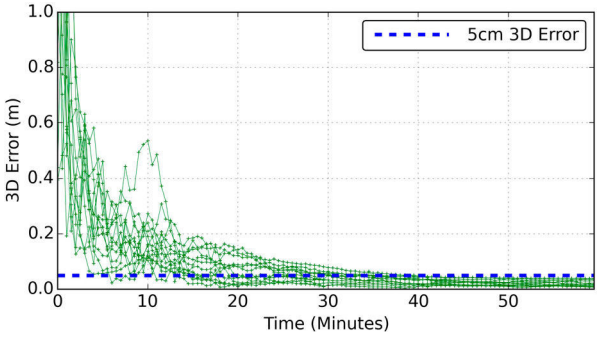

10 Triple-frequency ionosphere-free PPP 3D positioning errors for the 24-hourly solutions at TIDB

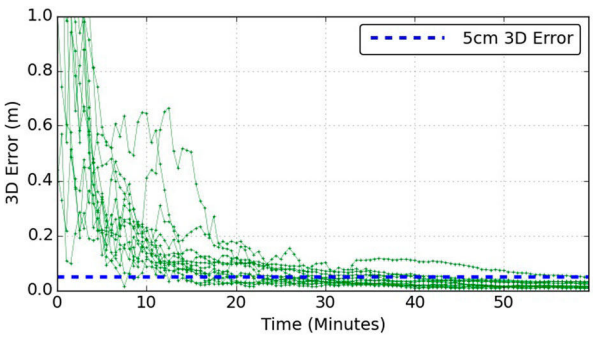

11 Mixed code-phase PPP 3D positioning errors for the 24-hourly solutions at TIDB

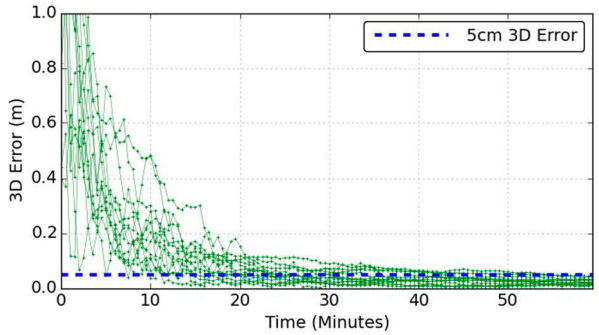

12 Individual uncombined signals' PPP 3D positioning errors for the 24-hourly solutions at TIDB

the receiver clock offset and estimating the three position components and ZWD. Although the three different models differ in their functional model, they are expected to give similar performance since they all provide the same observations.

Stochastic modelling of the observations

The satellite elevation-dependent weighting scheme is applied and the variance matrix of the individual measurements model for GPS as an example is

$$Q = diag[\,\sigma^2_{\phi_1} \quad \sigma^2_{\phi_2} \quad \sigma^2_{\phi_5} \quad \sigma^2_{P_1} \quad \sigma^2_{P_2} \quad \sigma^2_{P_5}\,] \qquad (26)$$

with off-diagonal terms zero where no-correlation is assumed among the individual observations at each epoch. The values for standard deviations can be estimated and validated as shown in El-Mowafy (2014, 2015). For the low-noise triple-frequency ionosphere-free model, the covariance matrix is evaluated with the error propagation law as

$$Q_l = DQD^T \qquad (27)$$

where

$$D = \begin{bmatrix} \frac{\partial\phi}{\partial\phi_1} & \frac{\partial\phi}{\partial\phi_2} & \frac{\partial\phi}{\partial\phi_5} & \frac{\partial\phi}{\partial P_1} & \frac{\partial\phi}{\partial P_2} & \frac{\partial\phi}{\partial P_5} \\ \frac{\partial P}{\partial\phi_1} & \frac{\partial P}{\partial\phi_2} & \frac{\partial P}{\partial\phi_5} & \frac{\partial P}{\partial P_1} & \frac{\partial P}{\partial P_2} & \frac{\partial P}{\partial P_5} \end{bmatrix} = \begin{bmatrix} \alpha_1 & \alpha_2 & \alpha_3 & 0 & 0 & 0 \\ 0 & 0 & 0 & \alpha_1 & \alpha_2 & \alpha_3 \end{bmatrix} \qquad (28)$$

where ϕ and P are defined in equations (5) and (6). The matrix Q_l results in a diagonal matrix with off-diagonal terms as zero, indicating the linear combinations used in the model are uncorrelated. For the mixed code-phase

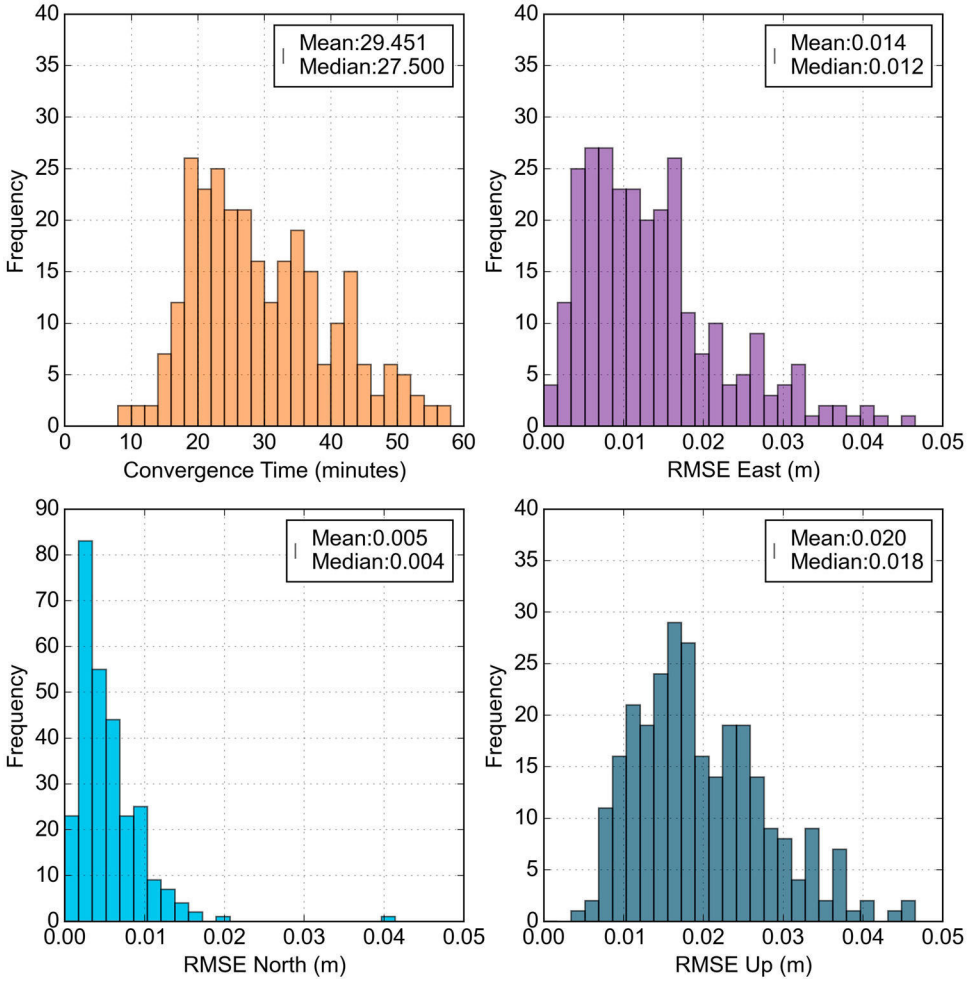

13 Histograms for the convergence time and the RMSE (in m) for East, North and Up obtained solutions using the L1/L2 dual-frequency traditional PPP model for all converged solutions. The mean and median of the histogram are given

model, the D matrix reads

$$D = \begin{bmatrix} \frac{\partial\phi_{12}}{\partial\phi_1} & \frac{\partial\phi_{12}}{\partial\phi_2} & \frac{\partial\phi_{12}}{\partial\phi_5} & \frac{\partial\phi_{12}}{\partial P_1} & \frac{\partial\phi_{12}}{\partial P_2} & \frac{\partial\phi_{12}}{\partial P_5} \\ \frac{\partial\phi_{15}}{\partial\phi_1} & \frac{\partial\phi_{15}}{\partial\phi_2} & \frac{\partial\phi_{15}}{\partial\phi_5} & \frac{\partial\phi_{15}}{\partial P_1} & \frac{\partial\phi_{15}}{\partial P_2} & \frac{\partial\phi_{15}}{\partial P_5} \\ \frac{\partial\Theta_{12}}{\partial\phi_1} & \frac{\partial\Theta_{12}}{\partial\phi_2} & \frac{\partial\Theta_{12}}{\partial\phi_5} & \frac{\partial\Theta_{12}}{\partial P_1} & \frac{\partial\Theta_{12}}{\partial P_2} & \frac{\partial\Theta_{12}}{\partial P_5} \\ \frac{\partial\Theta_{15}}{\partial\phi_1} & \frac{\partial\Theta_{15}}{\partial\phi_2} & \frac{\partial\Theta_{15}}{\partial\phi_5} & \frac{\partial\Theta_{15}}{\partial P_1} & \frac{\partial\Theta_{15}}{\partial P_2} & \frac{\partial\Theta_{15}}{\partial P_5} \end{bmatrix}$$

$$= \begin{bmatrix} \frac{f_1^2}{f_1^2-f_2^2} & \frac{-f_2^2}{f_1^2-f_2^2} & 0 & 0 & 0 & 0 \\ \frac{f_1^2}{f_1^2-f_5^2} & 0 & \frac{-f_5^2}{f_1^2-f_5^2} & 0 & 0 & 0 \\ \alpha_{1(1,2)} & \alpha_{2(1,2)} & 0 & \beta_{1(1,2)} & \beta_{2(1,2)} & 0 \\ \alpha_{1(1,5)} & 0 & \alpha_{2(1,5)} & \beta_{1(1,5)} & 0 & \beta_{2(1,5)} \end{bmatrix} \quad (29)$$

and the measurement covariance matrix is computed using equation (27), resulting in a fully populated matrix.

As an example, assuming uncorrelated raw phase and code measurements with $\sigma_{\phi_1} = \sigma_{\phi_2} = \sigma_{\phi_5} = 0.002m$ and $\sigma_{P_1} = \sigma_{P_2} = \sigma_{P_5} = 0.2m$; the measurement covariance matrix computed at the zenith is

$$Q_y = \begin{bmatrix} 3.55 & 2.30 & 3.52 & 2.29 \\ 2.30 & 2.68 & 2.29 & 2.67 \\ 3.52 & 2.29 & 3.52 & 2.28 \\ 2.29 & 2.67 & 2.28 & 2.67 \end{bmatrix}^{\times 10^{-5}} \quad (30)$$

which gives correlation between observations reaching above 0.7. This indicates that the correlations between the linear combinations used in this model must be considered in the stochastic modelling of the observations.

Validation of the presented PPP models

This section compares the performance of the presented PPP models, commencing with a description of the data used and followed by validation of the models. The validation process uses GPS as an example, where it equally applies to any single GNSS constellation.

Test description

Triple-frequency GPS static data from three Australian continuously operating GNSS stations, HOB2, TIDB and CEDU were used to test the proposed PPP models.

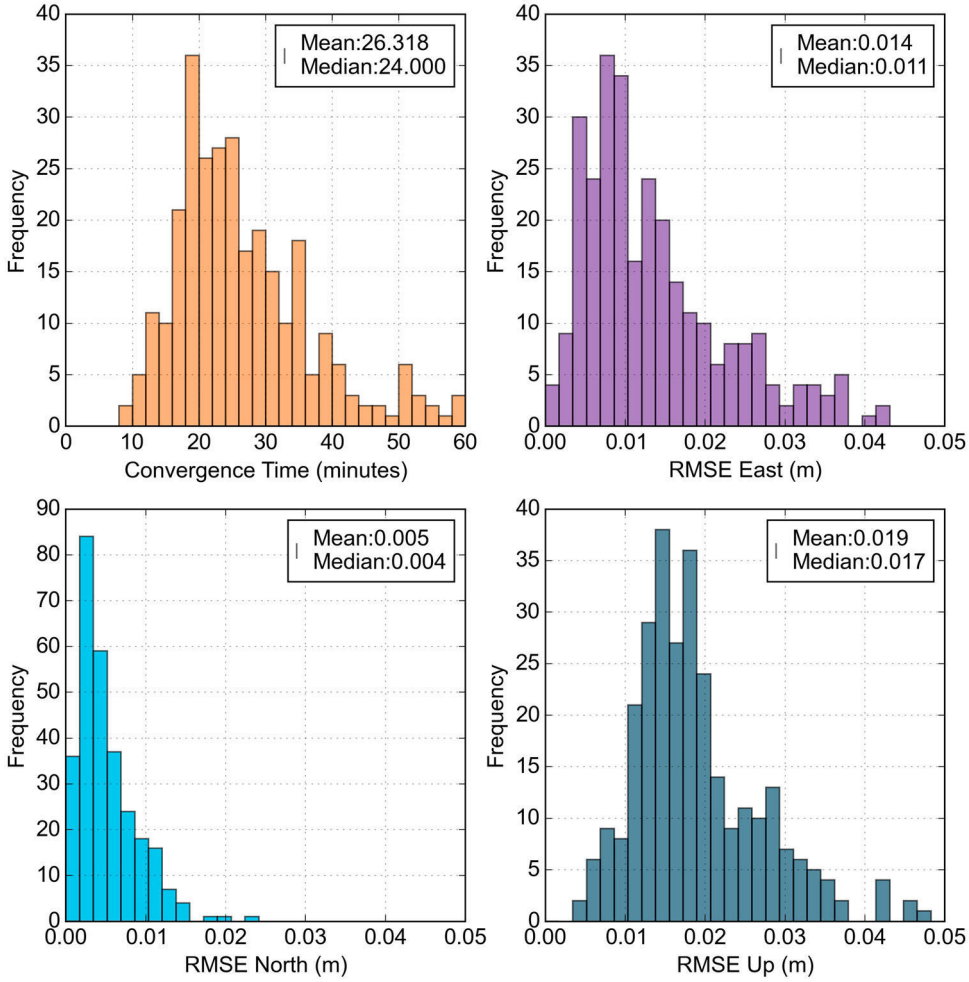

14 Histograms for the convergence time and the RMSE (in m) for East, North and Up obtained solutions using the low noise, ionosphere-free triple-frequency PPP model for all converged solutions. The mean and median are given

The measurement modelling and simulation were carried out with the following approach:

(i) The following IGS products were used: final precise ephemeris; IGS satellite clock product for satellite clock error, dt^{kG}; IGS ZTD product for the troposphere; and the broadcast Klobuchar model for the ionospheric delay. IGS produces ZTD and station receiver clock products for selected IGS stations using standard PPP, which were used to estimate realistic errors in the simulated data.

(ii) The satellite and receiver DCBs were ignored. Inter-system biases are not applicable in this case because a single constellation is used where all satellites are transmitting measurements on the same frequencies.

(iii) Measurement noise was generated assuming it has a normal distribution with zero mean and standard deviation of 0.4 m for code and 0.01 cycles for carrier phase. A satellite elevation mask angle of 10 degrees was used.

The accuracy of PPP results was assessed by referencing them to the known stations precise coordinates that were obtained from the Asia Pacific Reference Frame project records. The period of data analysed per station was 8 days at HOB2, 6 days at TIDB and 1 day at CEDU, with a sampling interval of 15 s. The data were processed in hourly blocks, with the ambiguities re-initialised at the start of each hour.

Analysis and discussion of results

The three proposed PPP models were implemented using the Kalman filter processing. Results are compared in terms of solution convergence time, accuracy and precision where the convergence time is defined as the time when a 3-dimentional (3D) positional accuracy of 0.05 m is reached and maintained thereafter. This accuracy is targeted towards the surveying and high precision industry sector, which accounts for 23.3% of the GNSS market users where 47.8% of this sector requires accuracy within 1–5 cm (GPS World 2016). The accuracy is defined as the root mean squared errors (RMSE) after convergence is achieved with respect to the known station position.

The mean convergence times and RMSE (in East, North, Up) from PPP analysis for the four algorithms are given in Table 5. Compared to that of the dual-frequency traditional PPP model, the convergence time for the triple-frequency ionosphere-free model improved by 11% (3.1 min), the mixed code-phase model improved by 9% (2.6 min), whereas the individual signal model improved by 8% (2.4 min). The accuracy results given in columns 3–5 represent the solutions that converged within 5 cm 3D positioning accuracy in less than 1 h. The change in the RMSE in East, North and Up directions was insignificant (at or below 1 mm) for all the three PPP models, which indicate that they gave the same positioning

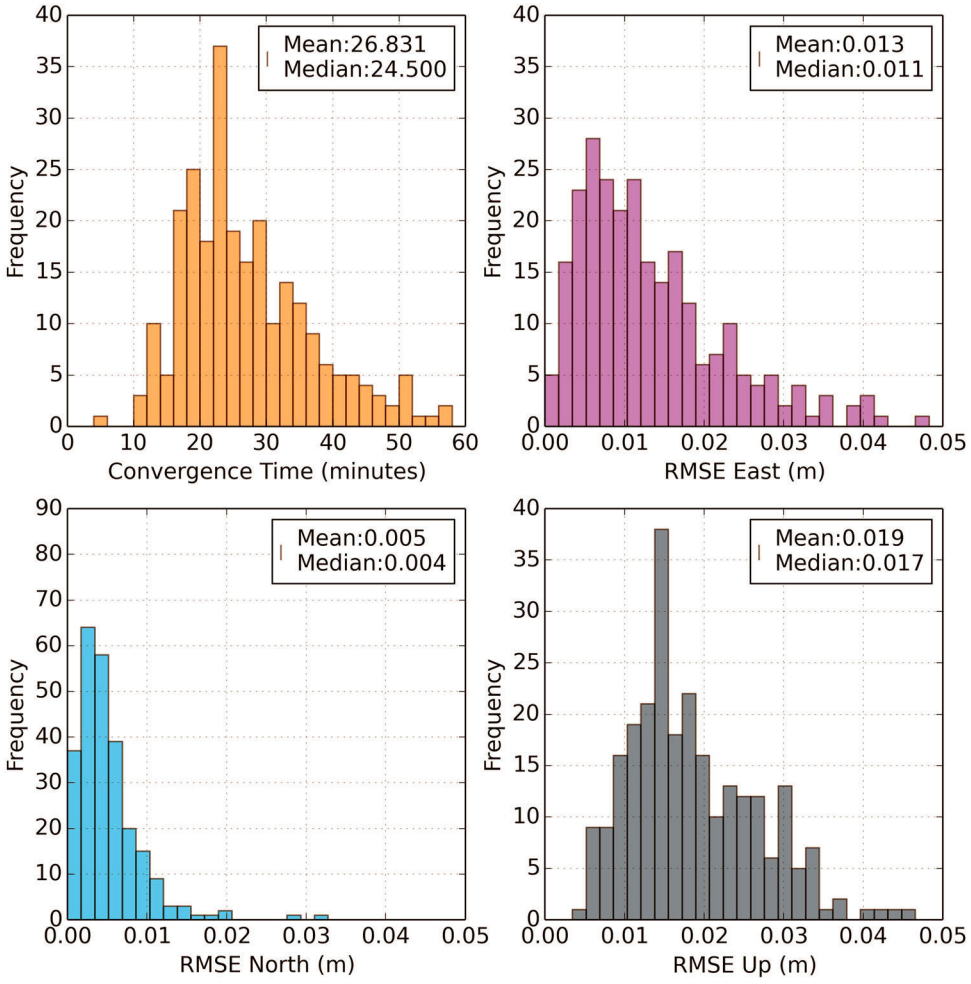

15 Histograms for the convergence time and the RMSE (in m) for East, North and Up obtained solutions using mixed code-phase PPP model for all converged solutions. The mean and median are given

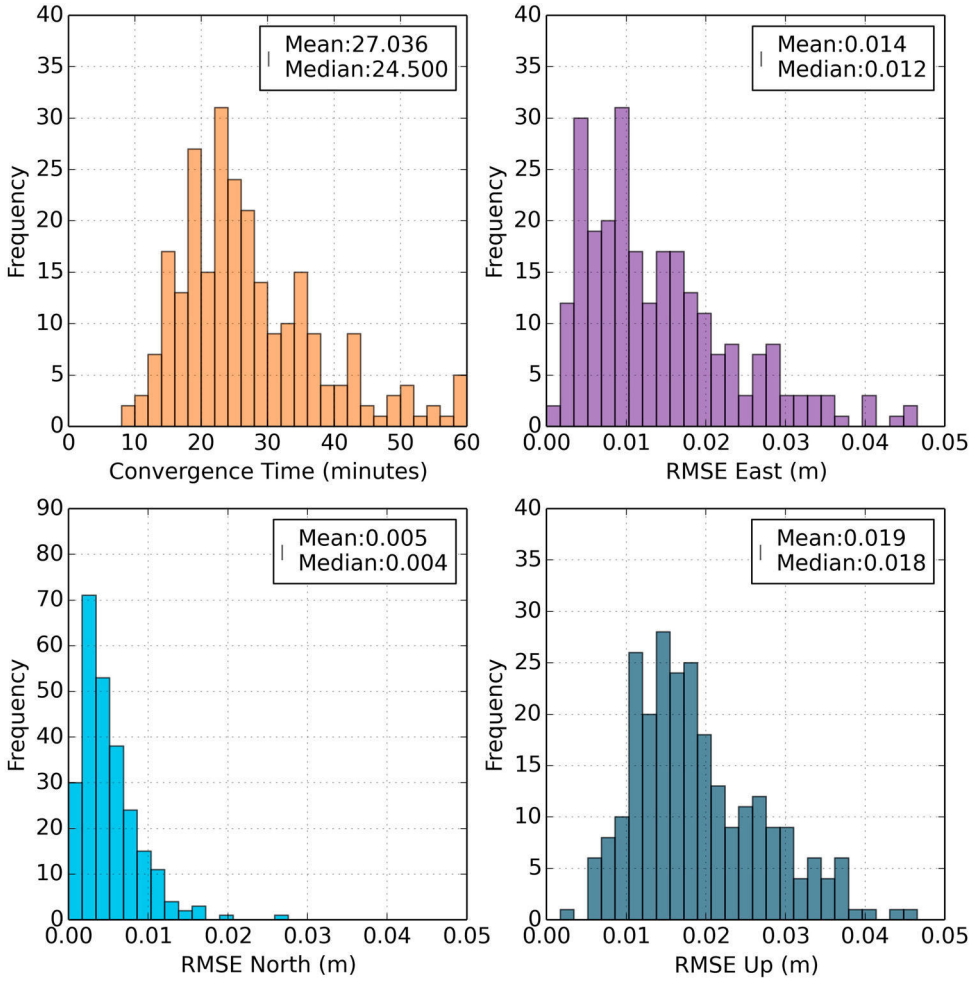

16 Histograms for the convergence time and the RMSE (in m) for East, North and Up obtained solutions using individual uncombined PPP model for all converged solutions. The mean and median are given

accuracy. This is expected since even though the three different triple-frequency models differ in their functional model and parameterisations, they have the same information content; i.e. use of triple-frequency phase and code data with the same precise orbit and clock correction products.

The individual uncombined model has no noise propagation, but this did not markedly improve its performance compared to the other triple-frequency models because of considering this amplification in the observation covariance and weights. Further testing was done to investigate whether estimation of the extra ionospheric parameter by processing a day's simulated GPS data by first estimating the ionosphere error as an unknown PPP parameter, and secondly removing it by applying an ionosphere model (the known Klobuchar's model). The mean convergence time for the 24-hourly solutions was 26.7 min when estimating the ionospheric error, whereas it was reduced to only 9.4 min when the ionosphere delay was eliminated assuming that is provided externally. This indicates that using the individual uncombined model with ionosphere augmentation will significantly improve convergence time.

Figure 1 shows, as an example, the PPP 3D positioning errors for the 24-hourly sessions at HOB2 using the traditional L1/L2 dual-frequency model. Figure 2 shows the positioning errors using the same data set but when using the triple-frequency low-noise ionosphere-free model, whereas Fig. 3 shows the result with the mixed code-phase model and Fig. 4 shows the result for the individual uncombined model. Moreover, Figs. 5–8 show the same plots for CEDU, whereas the plots for TIDB are given in Figs. 9–12. The histograms for the convergence time and the RMSE East, North and Up are depicted in the Figs. 13–16 for the solutions using the dual-frequency traditional PPP model, the triple-frequency low-noise ionosphere-free model, the mixed code-phase model and the individual uncombined model, respectively. Comparing the distribution of the convergence time in these figures shows that most of the solutions from the triple-frequency model converged faster than the dual-frequency case, with means between 26 and 27 min, compared to 29 min for the dual-frequency case. The RMSE values in East and Up are lower for most of the converged solutions that used the triple-frequency model.

Conclusion

In this contribution, three triple-frequency PPP models were presented for faster convergence of carrier-phase float ambiguities. In the first model, a new triple-frequency ionosphere-free linear combination was developed with minimum noise propagation and geometry-

preserving properties. The second proposed model used mixed code and carrier-phase linear combinations with two dual-frequency data, which also has the same properties. A third PPP model was also tested that uses individual uncombined triple-frequency measurements.

These models were validated with several days of triple-frequency data and the results were compared to the traditional dual-frequency model. It was shown that all three triple-frequency models had improved the solution convergence time required to achieve and maintain a 3D positional accuracy of 5 cm, compared to the dual-frequency traditional PPP model. The triple-frequency code-only and phase-only ionosphere-free model, the mixed code and phase model and the individual uncombined model resulted in the improvement of the convergence time by 11% (3.1 min), 9% (2.6 min) and 8% (2.4 min), respectively. The positioning accuracy after convergence for all triple-frequency algorithms was similar and showed marginal improvement at approximately 1 mm, compared to the present dual-frequency model. The individual uncombined model with externally provided ionosphere corrections can significantly improve convergence time to achieve 5 cm 3D accuracy.

References

Banville, S., *et al.*, 2014. Global and regional ionospheric corrections for faster PPP convergence. *Navigation*, 61 (2), 115–124.

Bisnath, S. and Gao, Y., 2009. Precise point positioning a powerful technique with a promising future, GPS World, April 2009.

Bohem, J., Werl, B., and Schuh, H., 2006. Troposphere mapping functions for GPS and VLBI from ECMWF operational analysis data. *Journal of geophysical research*, 111 (B02406), 82–90.

Cocard, M., *et al.*, 2008. A systematic investigation of optimal carrier-phase combinations for modernized triple-frequency GPS. *Journal of geodesy*, 82, 555–564.

Collins, P., *et al.*, 2010. Undifferenced GPS ambiguity resolution using the decoupled clock model and ambiguity datum fixing. *Journal of the institute of navigation*, 57 (2), 123–135.

Davis, J.L., *et al.*, 1985. Geodesy by radio interferometry: effects of atmospheric modelling errors on estimates of baseline length. *Radio science*, 20 (6), 1593–1607.

El-Mowafy, A., 2014. GNSS multi-frequency receiver single-satellite measurement validation method. *GPS solutions*, 18 (4), 553–561.

El-Mowafy, A., 2015. Estimation of multi-constellation GNSS observation stochastic properties using a single-receiver single-satellite data validation method. *Survey review*, 47 (341), 99–108.

El-Mowafy, A., Deo, M., and Rizos, C., 2016. On biases in precise point positioning with multi-constellation and multi-frequency GNSS data. *Measurement science and technology*, 27 (3), 035102.

Elsobeiey, M., 2015. Precise point positioning using triple-frequency GPS measurements. *The journal of navigation*, 68, 480–492.

Gao, Y. and Shen, X., 2002. A New method for carrier phase based precise point positioning. *Navigation*, 49 (2), 109–116.

Ge, M., *et al.*, 2008. Resolution of GPS carrier-phase ambiguities in precise point positioning (PPP) with daily observations. *Journal of geodesy*, 82 (7), 389–399.

Geng, J., *et al.*, 2010. Rapid re-convergences to ambiguity-fixed solutions in precise point positioning. *Journal of geodesy*, 84 (12), 705–714.

Geng, J. and Bock, Y., 2013. Triple-frequency GPS precise point positioning with rapid ambiguity resolution, *Journal of geodesy*, 87, 449–460.

GPS World, 2016. 2016 state of the GNSS industry. GPS World. September 2016, 41–46.

Guo, F., *et al.*, 2016. Modeling and assessment of triple-frequency BDS precise point positioning. *Journal of geodesy*, 90 (11), 1223–1235.

Henkel, P. and Günther, C., 2008. Precise point positioning with multiple Galileo frequencies. *In*: *Proceedings of the IEEE/ION symposium on position, location and navigation*, Monterey, CA, 592–599.

Laurichesse, D., *et al.*, 2009. Integer ambiguity resolution on undifferenced GPS phase measurements and its application to PPP and satellite precise orbit determination. *Navigation*, 56 (2), 135–149.

Montenbruck, O., *et al.*, 2012. Apparent clock variations of the block IIF-1 (SVN62) GPS satellite. *GPS solutions*, 16 (3), 303–313.

Montenbruck, O., Hauschild, A., and Steigenberger, P., 2014. Differential code bias estimation using Multi-GNSS observations and global ionosphere maps, ION-ITM-2014, 27–29 January, San Diego, USA.

Prange, L., *et al.*, 2012. MGEX data analysis at CODE – first experiences, IGS workshop, 23–27 July, Olsztyn, Poland.

Richert, T. and El-Sheimy, N., 2007. Optimal linear combinations of triple frequency carrier phase data from future global navigation satellite systems. *GPS solutions*, 11 (1), 11–19.

Seepersad, G. and Bisnath, S., 2014. Reduction of PPP convergence period through pseudorange multipath and noise mitigation. *GPS solution*, 19 (3), 369–379.

Shi, J., *et al.*, 2014. Local troposphere augmentation for real-time precise point positioning. *Earth, planets and space*, 66, 30.

Shi J. and Gao Y., 2014. A comparison of three PPP integer ambiguity resolution methods. *GPS solution*, 18 (4), 519–528.

Tegedor, J. and Øvstedal, O., 2014. Triple carrier precise point positioning (PPP) using GPS L5. *Survey review*, 46 (337), 288–297.

Tuka, A. and El-Mowafy, A., 2013. Performance evaluation of different troposphere delay models and mapping functions. *Measurement*, 46 (2), 928–937.

Uhlemann, M., Ramatschi, M. and Gendt, G., 2012. GFZ's global multi-GNSS network and first data processing results, IGS workshop, 23–27 July, Olsztyn, Poland.

Urlichich, Y., *et al.*, 2011. GLONASS modernisation. *GPS world*, 22 (11), 4 p.

Zhao, Q., *et al.*, 2013. Initial results of precise orbit and clock determination for COMPASS navigation satellite system. *Journal of geodesy*, 87, 475–486.

Zumberge, J.F., *et al.*, 1997. Precise point positioning for the efficient and robust analysis of GPS data from large networks. *Journal of geophysical research: solid earth*, 102 (B3), 5005–5017.

Appendix

In this section, we provide the full derivation of the coefficients for the mixed code-carrier linear combination. Rearranging Eq. 24 gives:

$$\alpha_2 = 1 - \alpha_1 - \beta_1 - \beta_2 \tag{A1}$$

and substituting Eq. A1 into 23 and presenting in terms of the frequency multipliers results in:

$$\beta_1 = \frac{k_2\alpha_1 + k_1 - k_1\alpha_1 - 2k_1\beta_2}{k_1 + k_2} \tag{A2}$$

Squaring Eq. A2 gives

$$\beta_1^2 = \frac{(k_2\alpha_1 + k_1 - k_1\alpha_1)^2 - 4k_1\beta_2(k_2\alpha_1 + k_1 - k_1\alpha_1) + 4k_1^2\beta_2^2}{(k_1 + k_2)^2} \tag{A3}$$

and substituting Eq. A2 into A1 we have:

$$\alpha_2 = \frac{k_2 - 2k_2\alpha_1 + \beta_2(k_1 - k_2)}{k_1 + k_2} \tag{A4}$$

and its squaring gives:

$$\alpha_2^2 = \frac{k_2^2(1 - 2\alpha_1)^2 + 2k_2\beta_2(1 - 2\alpha_1)(k_1 - k_2) + \beta_2^2(k_1 - k_2)^2}{(k_1 + k_2)^2} \tag{A5}$$

Substituting Eq. A3 and Eq. A5 into Eq. 25 results in a quadratic equation $A\beta_2^2 + B\beta_2 + C = 0$ where β_2 and ϵ are the unknown variables. The constants A, B, and C are:

$$A = a^2(k_1 + k_2)^2 + (k_1 - k_2)^2 + 4a^2k_1^2 \tag{A6}$$

$$B = 2k_2(1-2\alpha_1)(k_1-k_2) - 4a^2k_1(k_2\alpha_1 + k_1 - k_1\alpha_1) \quad \text{(A7)}$$

$$C = (k_1+k_2)^2\alpha_1^2 + k_2^2(1-2\alpha_1)^2 + a^2(k_2\alpha_1 + k_1 - k_1\alpha_1)^2 - (k_1+k_2)^2\epsilon^2 = C_0 - (k_1+k_2)^2\epsilon^2 \quad \text{(A8)}$$

where $C_0 = (k_1+k_2)^2\alpha_1^2 + k_2^2(1-2\alpha_1)^2 + a^2(k_2\alpha_1 + k_1 - k_1\alpha_1)^2$ is a constant and C is calculated directly in analogy with Eq. 19. The noise amplification factor in the combination $\Theta 12$ is evaluated by:

$$\epsilon = \sqrt{\frac{C_0 - C}{(k_1+k_2)^2}} = \frac{\sqrt{C_0 - C}}{k_1+k_2} \quad \text{(A9)}$$

Since α_1 is present as a variable in Eq. A7, its direct analytical solution at a minimum noise is obtained by assigning the first derivation of Eq. A9 with respect to α_1 to 0, such that:

$$\epsilon'(\alpha_1) = \frac{C'_0(\alpha_1) - C'(\alpha_1)}{2(k_1+k_2)\sqrt{C_0 - C}} \quad \text{(A10)}$$

The minimum value of α_1 occurs when the above Eq. A10 (its numerator) is equated to 0, which results in:

$$C'_0(\alpha_1) - C'(\alpha_1) = 0 \quad \text{(A11)}$$

where:

$$C'_0(\alpha_1) = X_1\alpha_1 + X_2 \quad \text{(A12)}$$

with

$$X_1 = \alpha_1(2(k_1+k_2)^2 + 8k_2^2 + 2a^2(k_2-k_1)^2) \quad \text{(A13)}$$

and

$$X_2 = -4k_2^2 + 2a^2(k_2-k_1)k_1 \quad \text{(A14)}$$

$C'_0(\alpha_1)$ is evaluated as:

$$C'_0(\alpha_1) = \frac{2X_3}{A}(\alpha_1 X_3 + X_5) \quad \text{(A15)}$$

with

$$X_3 = -2k_2(k_1-k_2) - 2a^2k_1k_2 - 2a^2k_1^2 \quad \text{(A16)}$$

and

$$X_5 = k_2(k_1-k_2) - 2a^2k_1^2 \quad \text{(A17)}$$

The variable A, which is evaluated using Eq. A6, is used to obtain a solution for α_1 as

$$\alpha_1 = \frac{2X_3X_5 - AX_2}{AX_1 - X_3^2} \quad \text{(A18)}$$

The corresponding value for β_2 is calculated as $\beta_2 = -B/2A$; whereas α_2 and β_1 are calculated using Eq. A4 and A2, respectively.

International Global Navigation Satellite Systems Association
IGNSS Conference 2016

Colombo Theatres, Kensington Campus, UNSW Australia
6 – 8 December 2016

Triple Frequency precise point positioning with multi-constellation GNSS

Manoj Deo
PhD Candidate, Department of Spatial Sciences, Curtin University,
GPO Box U 1987, Perth WA 6845, Australia
Phone: +61 432163000
Email: manoj.deo01@gmail.com

Ahmed El-Mowafy
Assoc. Professor, Department of Spatial Sciences, Curtin University,
GPO Box U 1987, Perth WA 6845, Australia
Phone: +61 8 9266 3403
Fax: +61 8 9266 2703
Email: a.el-mowafy@curtin.edu.au

ABSTRACT

The availability of signals on three or more frequencies from multiple GNSS constellations provides opportunities for improving precise point positioning (PPP) convergence time and accuracy, compared to when using dual-frequency observations from a single constellation. Although the multi-frequency and multi-constellation (MFMC) data may be used with present day precise orbit and clock products, there are several biases that must be considered to get the best results. When using IGS products, the precise orbit and clock corrections are generated using dual-frequency ionosphere-free combinations of a 'base' pair of signals, and usage of other signals in the PPP model results in differential code biases (DCB). Other biases to consider include differential phase biases (DPB) for the satellites and receiver and satellite antenna offsets for individual frequencies. Integrating multi-constellation data introduces additional biases, such as inter-system hardware and time biases and inter-frequency bias. Although the integration of MFMC data introduces such biases, it improves the measurement model strength and hence can potentially improve PPP performance through reducing solution convergence time and increasing precision and accuracy.
A brief overview of the MFMC biases and strategies that may be used to treat them is discussed. A proposed PPP model that uses triple frequency ionosphere-free low-noise linear combination for float ambiguity estimation is tested and analysed. MFMC data from four Australian sites is used to demonstrate the improvements in PPP solution convergence time, accuracy and precision, when comparing single- to multi-constellation GNSS data.

KEYWORDS: precise point positioning, multi-constellation, multi-frequency, biases, solution convergence.

1. INTRODUCTION

The PPP technique can determine the position of a GNSS receiver to cm-level accuracy for static surveying and sub-decimetre accuracy for kinematic applications, without relying on data from a single or network of reference stations. The first advent in PPP was made in Zumberge et al. (1997), where it was shown that cm-level repeatability can be achieved with dual-frequency undifferenced GPS measurements augmented with precise orbit and clock corrections. This is often known as the traditional PPP model, where the functional model consists of ionosphere-free linear combinations of dual-frequency pseudorange and carrier phase measurements. A major limitation of this technique is the time needed to achieve convergence of the solution to sub-decimetre accuracy, typically around 30 minutes, which restricts many real-time users from using this technique. At present, several commercial satellite subscription services provide real-time orbit and clock corrections for PPP such as StarFire (Deere), RTX (Trimble), Atlas (Hemisphere), Terrastar (Veripos) and MagicGNSS. However, convergence time remains to be a problem especially in areas obstructed by trees, buildings or canyons, where the PPP convergence is interrupted several times and for each time, the user needs to wait for the convergence to reoccur (Gaksatter, 2016).

The availability of data on three or more frequencies from multiple GNSS constellations provides an opportunity for improving the PPP performance in terms of reducing the solution convergence time and increasing the accuracy and precision. However, such integration of MFMC data results in several biases and handling of these biases is a complex problem that requires careful modelling. We restrict attention here to the use of IGS precise orbit and clock corrections which are generated from ionosphere-free combinations of a 'base' pair of signals, (e.g. GPS L1/L2, Galileo E1/E5a and Beidou B1/B2) and usage of other signals in the PPP model results in differential code biases (DCB) which must be treated. Integration of MFMC data also results in other biases such as differential phase biases (DPB) (including the initial fractional phase biases) in the satellites and receiver, and satellite antenna offsets for individual frequencies (rather than the ionosphere-free combination of the 'base signal pair'), inter-system hardware and time biases (ISB and ISTB) and inter-frequency bias. A detailed analysis of these biases and recommendations for their modelling is presented in El-Mowafy et al. (2016).

The availability of triple frequency data may potentially reduce PPP convergence time, compared to the dual-frequency case. This will make the PPP technique more practical for real-time applications. Deo and El-Mowafy (2016a) compared the performance of three PPP models that use triple frequency data. However, the testing was done for a GPS only case. PPP with multi-constellation GNSS has been widely studied for dual-frequency measurements. Multi-constellation provides improved satellite geometry for better PPP performance in challenging environments like open-pit mines, urban canyons and forests. An early GPS-GLONASS combined PPP model was presented in Cai and Gao (2007), which showed improvements in accuracy and solution convergence time. A GPS-Galileo combined PPP model was attempted in Cao et al. (2010). Li et al. (2013) presented PPP results using GPS and Beidou integration, which had 12 satellites from the latter system at the time of writing. The results showed a slight improvement in convergence time, but only marginal improvement was noted in positioning accuracy. The traditional dual-frequency PPP model

was adopted in all these studies, though results were not conclusive due to the partial completion of the GLONASS, Galileo and Beidou constellations at the time of study.

In this paper, the PPP model that uses a triple frequency ionosphere-free low-noise linear combination presented in Deo and El-Mowafy (2016a) is extended to a multi-constellation applications using GPS, Galileo and Beidou observations. This linear combination was developed for triple frequency data by applying three conditions of noise minimisation, ionosphere-free and geometry preservation. Firstly, the models for the MFMC observation equations are given, followed by a discussion of the biases and recommended practices for treating them. The next section presents the functional model for the triple frequency PPP model when using the three constellations, followed by a description of the stochastic modelling of observations. Next, the analysis and testing of data at four Australian GNSS continuous operating stations is presented. Following this, results comparing the convergence time, accuracy and precision for triple frequency PPP using GPS only, GPS+Galileo, GPS+Beidou and GPS+Galileo+Beidou are presented. Lastly, the conclusions are stated.

2. GNSS OBSERVATION MODEL

The observation equation of the carrier phase and pseudorange code measurements for satellite o from one GNSS constellation such as GPS (denoted as G) on frequency i in length units can be formulated as follows:

$$P_i^{o_G} = \rho^{o_G} + c\left(dt_{\mathrm{G}} - dt^{o_G} + d_{i_G} - d_i{}^{o_G}\right) + T^{o_G} + \mu_i I^{o_G} + \varepsilon_{\mathrm{P}_i}^{o_G} \quad (1)$$

$$\phi_i^{o_G} = \rho^{o_G} + c(dt_{\mathrm{G}} - dt^{o_G}) + T^{o_G} - \mu_i I^{o_G} + \lambda_i\left(N_i^G + \delta_{i_G} - \delta_i{}^{o_G}\right) + \varepsilon_{\phi_i}^{o_G} \quad (2)$$

where $P_i^{o_G}$ is the code and $\phi_i^{o_G}$ is the phase measurement, ρ^{o_G} is the satellite-to-receiver geometric range, c is the speed of light in vacuum; dt_{G} and dt^{o_G} are the receiver and satellite clock offsets; $d_{i_{\mathrm{G}}}$ and $d_i{}^{o_G}$ are the receiver and satellite code hardware biases in time units, respectively; δ_{i_G} and $\delta_i{}^{o_G}$ are the receiver and satellite phase biases in cycles, respectively; N_i^G is the integer carrier phase ambiguity; T^{o_G} is the tropospheric delay, $\mu_i = \frac{f_1^2}{f_i^2}$ is the dispersive coefficient of the ionosphere, I^{o_G} is the ionosphere error for the L1 reference frequency; $\varepsilon_{Pi}^{o_G}$ and $\varepsilon_{\phi_i}^{o_G}$ comprises code and phase measurement combined noise and multipath, respectively.

For the Beidou constellation (denoted as C) with frequency j from satellite p, the equations for carrier phase and pseudorange code measurement for frequency j are (El-Mowafy et al., 2016):

$$P_j^{p_C} = \rho^{p_C} + c\left(dt_G - dt^{p_C} + d_{j_C} - d_j{}^{p_C}\right) + T^{p_C} + \mu_j I^{p_C} + ISTB_{G-C} + \varepsilon_{P_j}^{p_C} \quad (3)$$

$$\phi_j^{p_C} = \rho^{p_C} + c(dt_G - dt^{p_C}) + T^{p_C} - \mu_j I^{p_C} + ISTB_{G-C} + \lambda_j\left(N_j^{p_C} + \delta_{j_G} - \delta_j{}^{p_C}\right) + \varepsilon_{\phi_j}^{p_C} \quad (4)$$

The terms are similar to the ones described for system G above. $ISTB_{G-C}$ is the inter-system time bias between systems G and C (i.e. GPS and Beidou), combined for the receiver and the satellite. Similar equations are derived for the Galileo constellation (denoted as E). When integrating data from multiple constellations, users have to consider the differences in

coordinate frames, particularly when using broadcast orbits. When using the precise orbits from International GNSS Service (IGS) or its subordinate Multi-GNSS Experiment (M-GEX), the orbits for all constellations are consistent with the International Terrestrial Reference Frame (ITRF).

3. MODELLING OF BIASES

This section describes the modelling of biases that occur in a single constellation as well as biases that occur when integrating multi-constellation GNSS data.

3.1 Single Constellation Biases

Satellite and receiver hardware biases

The satellite and receiver hardware biases exist for both code and phase measurements and are caused by several sources. These include digital delays in the signal generator, signal distortion, the processing filters, correlator differences handling signal modulation, firmware biases, bandwidth dissimilarities, in addition to the signal path through the antenna, splitter, cabling, and amplifier. This hardware bias tends to be stable and slowly changing with time. At the receiver end, it is the same for signals of the same frequency from the same constellation. Thus, the receiver hardware biases can be modelled out by the use of between satellite single differencing (BSSD) (El-Mowafy et al., 2016). At the satellite end, hardware biases are stable for hours and will be constant for a typical PPP session, however this may differ for each satellite.

Differential Code Bias (DCB)

The code hardware biases are different for each frequency. Hence when the ionosphere-free or other combination is formed between different frequencies, the impacts of these differences in hardware biases are transferred to the combination. For GPS, as an example, the precise orbit and clock products from IGS are formed from the dual-frequency ionosphere-free combination of L1/L2 and its DCB is included with transmitted clock corrections. Thus, DCBs won't affect PPP code observations when using this combination, but it will be present if using individual signals, or other linear combinations and in phase observations because the same satellite clock offset is used for both code and phase observations. The DCBs of the base frequency that appear in the phase observations is usually lumped with the float carrier-phase ambiguity term. A full mathematical treatment of DCBs for such cases is discussed in El-Mowafy et al. 2016. The satellite DCB products from the IGS multi-GNSS Experiment (M-GEX) are now available for multi-frequency combinations of several constellations (Montenbruck et al., 2014). Since hardware biases are the same for signals from the same frequency and constellation, receiver DCBs are eliminated by forming BSSD.

The mathematical models for the code measurements, considering DCBs produced from M-GEX when applying IGS clock corrections, are written below for GPS and Galileo using RINEX version 3 notations available at the website ftp://igs.org/pub/data/format/rinex303.pdf.

For GPS:

$$CIC^{oG} = \rho^{*oG} - c\left(DCB_{C1W-C1C} + \frac{f_2^2}{f_1^2-f_2^2} DCB_{C1W-C2W}\right) \quad (5)$$

$$CIW^{oG} = \rho^{*oG} - c\left(\frac{f_2^2}{f_1^2-f_2^2} DCB_{C1W-C2W}\right) \quad (6)$$

$$C2W^{o_G} = \rho^{*o_G} - c\left(\frac{f_1^2}{f_1^2 - f_2^2} DCB_{C1W-C2W}\right) \quad (7)$$

$$C5Q^{o_G} = \rho^{*o_G} - c\left(DCB_{C1W-C5Q} + \frac{f_2^2}{f_1^2 - f_2^2} DCB_{C1W-C2W}\right) \quad (8)$$

$$C5X^{o_G} = \rho^{*o_G} - c\left(DCB_{C1W-C5X} + \frac{f_2^2}{f_1^2 - f_2^2} DCB_{C1W-C2W}\right) \quad (9)$$

with $\rho^{*o_G} = \rho^{o_G} + c(dt_{\mathrm{G}} - dt^{o_G}{}_{IGS}) + T^{o_G} + \mu_i I^{o_G} + \varepsilon_{P_i}^{o_G}$. The primary code measurements used to generate the broadcast clock corrections are C1W (P1) and C2W (P2). Note that the C2X and C2S code measurements may be converted to C2W as $C2W_r^{o_G} = C2S_r^{o_G} + (DCB_{C2W-C2S})$, $C2W_r^{o_G} = C2X_r^{o_G} + (DCB_{C2W-C2x})$.

For Galileo, the primary code measurements used to generate the broadcast clock corrections are C1X (E1 B+C) and C5X (E5a I+Q) (Uhlemann et al., 2015, Prange et al., 2015). Note that since the Galileo $DCB_{C1X-C1X}$ is not currently available, C1C is assumed to be equivalent to C1X, thus $DCB_{C1X-C1X} = 0$. Similarly $DCB_{C5X-C5Q}$ and $DCB_{C1X-C7Q}$ are not available; thus it is assumed that C5X=C5Q and C7X=C7Q. The DCB corrections are applied as

$$CIC^{q_E} = \rho^{*q_E} - c\left(DCB_{C1X-C1C} + \frac{f_{E5a}^2}{f_{E1}^2 - f_{E5a}^2} DCB_{C1X-C5X}\right) \quad (10)$$

$$CIX^{q_E} = \rho^{*q_E} - c\left(\frac{f_{E5a}^2}{f_{E1}^2 - f_{E5a}^2} DCB_{C1X-C5X}\right) \quad (11)$$

$$C5X^{q_E} = \rho^{*q_E} - c\left(\frac{f_{E1}^2}{f_{E1}^2 - f_{E5a}^2} DCB_{C1X-C5X}\right) \quad (12)$$

$$C5Q^{q_E} = \rho^{*q_E} - c\left(DCB_{C5X-C5Q} + \frac{f_{E1}^2}{f_{E1}^2 - f_{E5a}^2} DCB_{C1X-C5X}\right) \quad (13)$$

$$C7X^{q_E} = \rho^{*q_E} - c\left(DCB_{C1X-C7X} + \frac{f_{E5a}^2}{f_{E1}^2 - f_{E5a}^2} DCB_{C1X-C5X}\right) \quad (14)$$

$$C7Q^{q_E} = \rho^{*q_E} - c\left(DCB_{C1X-C7Q} + \frac{f_{E5a}^2}{f_{E1}^2 - f_{E5a}^2} DCB_{C1X-C5X}\right) \quad (15)$$

The impact of DCBs corrections on code point positioning in the aviation context is discussed in Deo and El-Mowafy (2016b).

Initial Fractional Phase Bias (IFPB) and Differential Phase Biases (DPB)

Initial fractional phase cycle bias exists in the satellite and receiver and is always less than 1 phase cycle. It is separate from the hardware phase bias and constant for each session which is reset each time the receiver is switched off and on. IFPB is different for each frequency, but at the receiver end it is assumed the same for signals on the same frequency for satellites on the same constellation. Thus it is eliminated by forming BSSD measurements from the same frequency and constellation.

Differential Phase bias (DPB) also exists when forming linear combinations, due to the phase hardware biases being different for each frequency. BSSD measurements from the same frequency and constellation will eliminate DPB at the receiver end. However, the satellite DPB remains in the PPP model. Satellite DPBs are stable like the IFPB, but they are difficult to separate from each other. Therefore they are usually combined in one term, i.e. the DPB. In PPP with float ambiguity estimation, these are usually lumped with the non-integer carrier phase ambiguity term. For PPP-AR, the estimation of DPB is the key to enable integer ambiguity resolution.

3.2 Multi-constellation Biases

Inter-System Time Bias (ISTB)
The ISTB is due to each constellation having the satellite clocks referenced to the constellation own timescale. The ISTBs are accounted for by either estimating a separate bias for each system, or by estimating the bias for one system and then estimating the differences from other systems with reference to this system.

Inter System Biases (ISB)
As discussed earlier, the signals from different frequencies and constellations will have different hardware biases for code and phase observations (Hegarty et al, 2004). When a common receiver clock offset is used, which include biases of a primary system, for all constellations, the differences between the receiver biases for different constellations form the ISB. Thus, additional parameters must be introduced in the PPP model to account for these differences are known as inter-system biases (ISB).

4. TRIPLE FREQUENCY PPP MODEL

In this section, the functional and stochastic models for a triple frequency multi-constellation PPP method are described. The constellations included in the modelling include GPS (G), Beidou (C) and Galileo (E). It is assumed that the MFMC biases have been applied to the observations as discussed in El-Mowafy et al. (2016).

4.1 Functional Model

In the subsequent modelling, the ISTB is merged with the ISB term, the DPB and IFPB are merged with the float ambiguity term, whereas DCBs are applied to code measurements as described earlier using MGEX published DCB values. A low noise triple frequency ionosphere-free combination developed in Deo and El-Mowafy (2016a) is used as the observations in the functional model. This linear combination has least noise propagation properties, is first order ionosphere-free; and preserves geometry. It is applied separately for the multi-constellation code and phase observations, which have the same coefficients for each measurement. Due to the minimisation of code noise propagation, the PPP solution can converge faster than when using standard dual-frequency ionosphere-free combination. The actual noise reduction was 14% for GPS, 3.1% for Galileo and 1.1% for Beidou; whereas the convergence time reduced by 11% for tests done for GPS only data (Deo and El-Mowafy, 2016a). The equations for functional models for GPS, Beidou and Galileo are:

For GPS:

$$P^{o_G} = \alpha_{1,G} \cdot P_{L1}^{q_G} + \alpha_{2,G} \cdot P_{L2}^{o_G} + \alpha_{3,G} \cdot P_{L5}^{o_G} = \rho^{o_G} + cdt_{\mathrm{G}} + T^{o_G} + \varepsilon_{\mathrm{P}}^{o_G} \quad (16)$$

$$\phi^{o_G} = \alpha_{1,G} \cdot \phi_{L1}^{q_G} + \alpha_{2,G} \cdot \phi_{L2}^{o_G} + \alpha_{3,G} \cdot \phi_{L5}^{o_G} = \rho^{o_G} + cdt_{\mathrm{G}} + T^{o_G} + \lambda N^{*o_G} + \varepsilon_{\phi}^{o_G} \quad (17)$$

with the coefficient values being $\alpha_{1,G} = 2.326\,944$, $\alpha_{2,G} = -0.359\,646$, and $\alpha_{3,G} = -0.967\,299$

For Beidou:

$$P^{p_C} = \alpha_{1,C} \cdot P_{B1}^{p_C} + \alpha_{2,C} \cdot P_{B2}^{p_C} + \alpha_{3,C} \cdot P_{B3}^{p_C} = \rho^{p_C} + cdt_G + T^{p_C} + ISB_{G-C} + \varepsilon_{P_j}^{p_C} \quad (18)$$

$$\phi^{p_C} = \alpha_{1,C} \cdot \phi_{B1}^{p_C} + \alpha_{2,C} \cdot \phi_{B2}^{p_C} + \alpha_{3,C} \cdot \phi_{B3}^{p_C} = \rho^{p_C} + cdt_G + T^{p_C} + ISB_{G-C} + \lambda N^{*p_C} + \varepsilon_{\phi}^{p_C} \quad (19)$$

with the coefficient values being $\alpha_{1,C} = 2.566\,439$, $\alpha_{2,C} = -1.228\,930$, and $\alpha_{3,C} = -0.337\,510$

For Galileo:

$$P^{q_E} = \alpha_{1,E} \cdot P_{E1}^{q_E} + \alpha_{2,E} \cdot P_{E5a}^{q_E} + \alpha_{3,E} \cdot P_{E5b}^{q_E} = \rho^{q_E} + cdt_G + T^{q_E} + ISB_{G-E} + \varepsilon_P^{q_E} \quad (20)$$

$$\phi^{q_E} = \alpha_{1,E} \cdot \phi_{E1}^{q_E} + \alpha_{2,E} \cdot \phi_{E5a}^{q_E} + \alpha_{3,E} \cdot \phi_{E5b}^{q_E} = \rho^{q_E} + cdt_G + T^{q_E} + ISB_{G-C} + \lambda N^{*q_E} + \varepsilon_{\phi}^{q_E} \quad (21)$$

with coefficient values being $\alpha_{1,E} = 2.314\,925$, $\alpha_{2,E} = -0.836\,269$, and $\alpha_{3,E} = -0.478\,656$.

If we consider the case of a GNSS receiver tracking $1 \ldots n$ GPS satellites, $1 \ldots m$ Beidou satellites, and $1 \ldots k$ Galileo satellites at an instant of time. The unknown parameters are

$$\boldsymbol{x} = [x \quad y \quad z \quad cdt_G \quad ZWD \quad ISB_{G-C} \quad ISB_{G-E} \quad \lambda N^*(G1, \ldots, Gn, C1, \ldots, Cm, E1, \ldots, Ek)] \quad (22)$$

Where x, y, z denotes the unknown receiver position; ZWD is the zenith wet delay after modelling the hydrostatic tropospheric delay using the Saastamoinen model and expressing the wet delay as a function of a wet mapping function (Tuka and El-Mowafy, 2013). The ambiguity terms for each satellite are float values due to the presence of DPB of the considered signals and DCBs of the base frequencies. The functional model in Eqs. 16-21 is non-linear, and thus the system is linearised around approximate values of the unknown parameters, $\boldsymbol{x_0}$. Small corrections, $\Delta\boldsymbol{x}$, are calculated using Kalman filter, which is applied to the approximations to get the parameter estimates as $\boldsymbol{x} = \boldsymbol{x_0} + \Delta\boldsymbol{x}$. The design matrix, A, for this system is:

$$A = \begin{bmatrix}
\frac{X^{G1}-x_0}{\rho_0} & \frac{Y^{G1}-y_0}{\rho_0} & \frac{Z^{G1}-z_0}{\rho_0} & 1 & m_w & 0 & 0 & 0 & 0 & 0 & 0 & 0 & 0 & 0 \\
\frac{X^{G1}-x_0}{\rho_0} & \frac{Y^{G1}-y_0}{\rho_0} & \frac{Z^{G1}-z_0}{\rho_0} & 1 & m_w & 0 & 0 & 1 & 0 & 0 & 0 & 0 & 0 & 0 \\
\vdots & \vdots & \vdots & \vdots & \vdots & \vdots & \vdots & \vdots & \vdots & \vdots & \vdots & \vdots & \vdots & \vdots \\
\frac{X^{Gn}-x_0}{\rho_0} & \frac{Y^{Gn}-y_0}{\rho_0} & \frac{Z^{Gn}-z_0}{\rho_0} & 1 & m_w & 0 & 0 & 0 & 0 & 0 & 0 & 0 & 0 & 0 \\
\frac{X^{Gn}-x_0}{\rho_0} & \frac{Y^{Gn}-y_0}{\rho_0} & \frac{Z^{Gn}-z_0}{\rho_0} & 1 & m_w & 0 & 0 & 0 & 0 & 1 & 0 & 0 & 0 & 0 \\
\frac{X^{C1}-x_0}{\rho_0} & \frac{Y^{C1}-y_0}{\rho_0} & \frac{Z^{C1}-z_0}{\rho_0} & 1 & m_w & 1 & 0 & 0 & 0 & 0 & 0 & 0 & 0 & 0 \\
\frac{X^{C1}-x_0}{\rho_0} & \frac{Y^{C1}-y_0}{\rho_0} & \frac{Z^{C1}-z_0}{\rho_0} & 1 & m_w & 1 & 0 & 0 & 0 & 0 & 1 & 0 & 0 & 0 \\
\vdots & \vdots & \vdots & \vdots & \vdots & \vdots & \vdots & \vdots & \vdots & \vdots & \vdots & \vdots & \vdots & \vdots \\
\frac{X^{Cm}-x_0}{\rho_0} & \frac{Y^{Cm}-y_0}{\rho_0} & \frac{Z^{Cm}-z_0}{\rho_0} & 1 & m_w & 1 & 0 & 0 & 0 & 0 & 0 & 0 & 0 & 0 \\
\frac{X^{Cm}-x_0}{\rho_0} & \frac{Y^{Cm}-y_0}{\rho_0} & \frac{Z^{Cm}-z_0}{\rho_0} & 1 & m_w & 1 & 0 & 0 & 0 & 0 & 0 & 1 & 0 & 0 \\
\frac{X^{E1}-x_0}{\rho_0} & \frac{Y^{E1}-y_0}{\rho_0} & \frac{Z^{E1}-z_0}{\rho_0} & 1 & m_w & 0 & 1 & 0 & 0 & 0 & 0 & 0 & 0 & 0 \\
\frac{X^{E1}-x_0}{\rho_0} & \frac{Y^{E1}-y_0}{\rho_0} & \frac{Z^{E1}-z_0}{\rho_0} & 1 & m_w & 0 & 1 & 0 & 0 & 0 & 0 & 0 & 1 & 0 \\
\vdots & \vdots & \vdots & \vdots & \vdots & \vdots & \vdots & \vdots & \vdots & \vdots & \vdots & \vdots & \vdots & \vdots \\
\frac{X^{Ek}-x_0}{\rho_0} & \frac{Y^{Ek}-y_0}{\rho_0} & \frac{Z^{Ek}-z_0}{\rho_0} & 1 & m_w & 0 & 1 & 0 & 0 & 0 & 0 & 0 & 0 & 0 \\
\frac{X^{Ek}-x_0}{\rho_0} & \frac{Y^{Ek}-y_0}{\rho_0} & \frac{Z^{Ek}-z_0}{\rho_0} & 1 & m_w & 0 & 1 & 0 & 0 & 0 & 0 & 0 & 0 & 1
\end{bmatrix} \tag{23}$$

where m_w is the wet mapping function. The parameter matrix and the design matrix must be dynamically updated when new satellites appear, or when a satellite disappears from view. The initial values of the float ambiguities must be recalculated for a new satellite, when a satellite reappears after loss of tracking, or when a cycle slips is detected that cannot be repaired.

4.2 Stochastic Model of Observations

For stochastic modelling of GPS observations, which is equally applicable for Beidou and Galileo, the raw measurements are assumed to be uncorrelated with code noise $\sigma_{P_1^G}$, $\sigma_{P_2^G}$ and $\sigma_{P_5^G}$, and carrier phase noise $\sigma_{\phi_1^G}$, $\sigma_{\phi_2^G}$ and $\sigma_{\phi_5^G}$. Thus, the noise in the triple frequency code and phase linear combinations is determined with error propagation law as:

$$\sigma_{P^G}^2 = \left(\alpha_{1,G} \cdot \sigma_{P_1^G}\right)^2 + \left(\alpha_{2,G} \cdot \sigma_{P_2^G}\right)^2 + \left(\alpha_{3,G} \cdot \sigma_{P_5^G}\right)^2 \tag{24}$$

$$\sigma_{\phi^G}^2 = \left(\alpha_{1,G} \cdot \sigma_{\phi_1^G}\right)^2 + \left(\alpha_{2,G} \cdot \sigma_{\phi_2^G}\right)^2 + \left(\alpha_{3,G} \cdot \sigma_{\phi_5^G}\right)^2 \tag{25}$$

The measurement weighting is based on elevation angle (E) of the satellites as $1/\sin(E)$. Since the code and phase observations on different frequencies are assumed uncorrelated, the measurement covariance matrix is diagonal, where the linear combinations used in the model are also uncorrelated.

5. VALIDATION OF MULTI-CONSTELLATION PPP MODEL

5.1 Test Description

Test data was simulated for one day at four sites at Hobart (HOB2), Alice Springs (ALIC), Yarragadee (YAR2) and Townsville (TOW2), which are distributed over the Australian continent. Simulated data was used due to issues in actual data such as the line bias variations in GPS Block IIF satellites (Montenbruck et al., 2012), insufficient number of GPS Block IIF satellites, and the unavailability of satellite antenna phase centre offsets for individual signals. The GPS satellite antenna offsets are available for the L1-L2 ionosphere-free combination only, whereas the offsets for Galileo and Beidou are based on satellite design diagrams rather than actual calibrations. Dilssner et al. (2014) calibrated these offsets for Beidou satellites and reported that these were vastly different from the IGS M-GEX recommended values, by as much as 3.9m (for IGSO). Hence simulated data is used to isolate these issues and focus on the performance of the PPP model. The epoch interval rate was 30 s, with measurement standard deviations of 0.01 cycles for carrier phase on all frequencies, and for code measurements: 0.37m, 0.48m and 0.36m for GPS P1, P2 & P5; 0.36m, 0.35m and 0.34m for Galileo E1, E5a & E5b codes and 0.51m, 0.37m and 0.34m for Beidou B1, B2 & B3. These values are based on a method for determining the standard deviations presented in El-Mowafy (2014 and 2015) using a single-receiver single-channel method. A satellite elevation cut-off of 10 degrees was used.

5.2 Analysis and Discussion of Results

The triple frequency MFMC PPP model was implemented applying Kalman filter processing using by an in-house software. The software is suitable for processing kinematic data, but was configured for static data. The performance of the MFMC PPP model was assessed based on comparing the convergence time and positional accuracy to the standard dual-frequency solutions, after a 3 dimensional (3D) precision of 5cm was reached and maintained. Accuracy is defined as the root mean squared errors (RMSE) in East, North and up directions with respect to the known station position, after convergence is achieved.

- The mean RMSE and convergence times for the four sites when processing hourly blocks of data are given in Table 1. The algorithms compared are the standard dual-frequency GPS only solution (L1-L2 G) and the triple frequency solutions for GPS only, GPS+Beidou (G+C) and GPS+Beidou+Galileo (G+C+E). Overall, when comparing the triple frequency solutions to the conventional dual-frequency solution, the triple frequency solution for G+C+E gave the best performance with a notable improvement 7.6 minutes in convergence time and improvements of 2mm in RMSE East. More specifically at the four sites. For ALIC, the triple frequency solution for G+C gave the best performance with an improvement of 5mm in RMSE East and 5.7 minutes in convergence time.
- For HOB2, triple frequency solution for G+C+E gave the best performance with improvement of 4mm in RMSE up and 7.4 minutes in convergence time.
- For TOW2, triple frequency solution for G+C+E gave the best performance with improvement of 4mm in RMSE up and 7.7 minutes in convergence time.
- For YAR2, triple frequency solution for G+C+E gave the best performance with a notable improvement 11.5 minutes in convergence time. There was no noticeable improvement in accuracy, whereas the triple frequency solution for G had a slightly higher convergence time than the dual-frequency results.

From Table 1, it is seen that the Northing RMSE is better than Easting by about a cm. Also, on average, the Easting RMSE is 2-3mm worse than the Up. This may be an artefact of the use of simulation signals together with the geometry of the satellites and location of sites.

Figure 1 shows, as an example, the PPP 3D positioning hourly solution errors at YAR2 for three triple frequency solutions using GPS only, GPS+Beidou and GPS+Beidou+Galileo as well as the conventional dual-frequency observations using GPS only observations. The improved performance of the MFMC PPP models, compared to the dual-frequency model is clearly visible with reduced convergence time and RMSE values.

Site	Solution	Mean RMSE East (m)	Mean RMSE North (m)	Mean RMSE Up (m)	Mean Convergence time (min)
ALIC	L1-L2 G	0.017	0.006	0.015	26.9
	Triple freq. G	0.018	0.006	0.014	24.9
	Triple freq. G+C	0.012	0.007	0.016	21.2
	Triple freq. G+C+E	0.012	0.007	0.018	22.1
HOB2	L1-L2 G	0.015	0.006	0.021	31.9
	Triple freq. G	0.012	0.007	0.017	25.8
	Triple freq. G+C	0.012	0.008	0.018	26.8
	Triple freq. G+C+E	0.014	0.007	0.017	24.5
TOW2	L1-L2 G	0.014	0.004	0.019	30.9
	Triple freq. G	0.012	0.005	0.015	26.3
	Triple freq. G+C	0.012	0.006	0.017	24.4
	Triple freq. G+C+E	0.014	0.007	0.015	23.2
YAR2	L1-L2 G	0.017	0.007	0.015	28.6
	Triple freq. G	0.016	0.006	0.019	30.0
	Triple freq. G+C	0.013	0.006	0.015	18.2
	Triple freq. G+C+E	0.017	0.005	0.015	17.1
Overall	L1-L2 G	0.016	0.006	0.018	29.6
	Triple freq. G	0.014	0.006	0.016	26.5
	Triple freq. G+C	0.012	0.007	0.016	23.0
	Triple freq. G+C+E	0.014	0.007	0.016	22.0

Table 1. Table of results showing mean RMSE and convergence times with hourly blocks of data for the conventional dual-frequency GPS only solution (L1-L2 G) and the triple frequency solutions for GPS only, GPS+Beidou (G+C) and GPS+Beidou+Galileo (G+C+E).

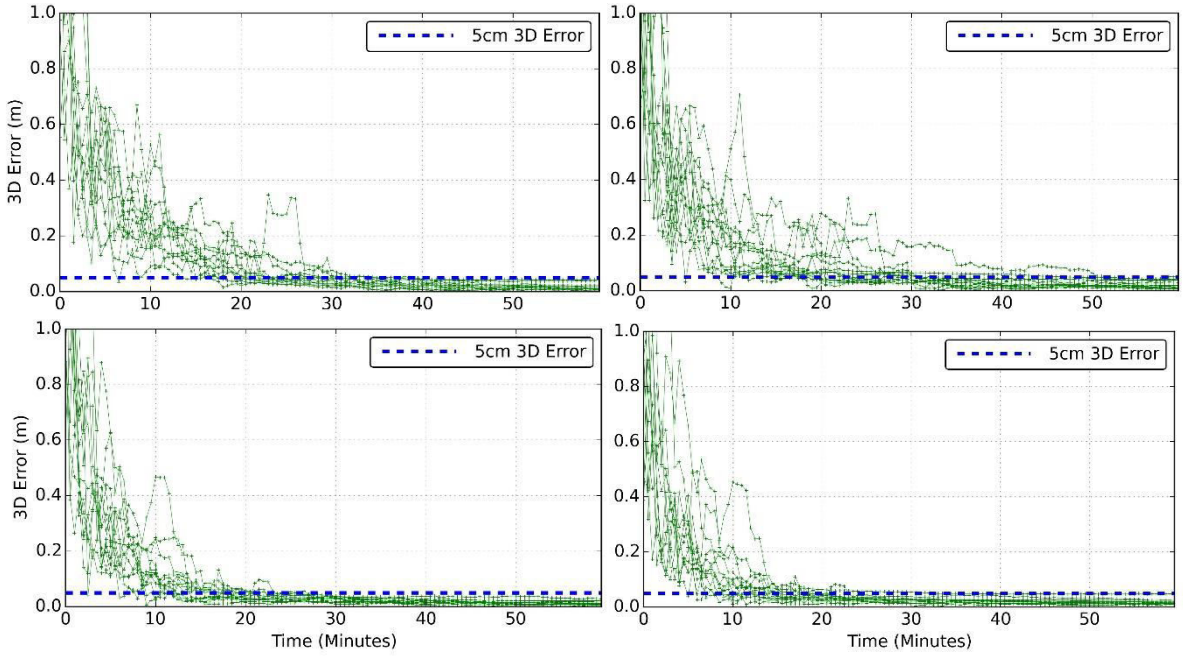

Figure 1. PPP 3-dimensional positioning errors for the hourly solutions at YAR2 for the standard dual-frequency GPS only solution (top-left) and the triple frequency solutions for GPS only (top-right), GPS+Beidou (bottom-left) and GPS+Beidou+Galileo (bottom-right).

6. CONCLUSIONS

An overview of the various biases that need to be considered when integrating MFMC data was given. A low-noise, ionosphere-free triple frequency PPP model proposed in Deo and El-Mowafy (2016a) was tested with hourly blocks of multi-constellation data from GPS, Beidou and Galileo at four sites covering the Australian continent. Improvements in both positioning accuracy by up to 5mm RMSE and convergence times by up to 11.5 minutes were noted at all four sites, when using the triple-frequency data compared to GPS-only dual-frequency PPP. Overall, the triple frequency solution for GPS+Beidou+Galileo gave the best performance with a notable overall improvement of 7.6 minutes in convergence time and improvements of 2mm in RMSE East and Up. This is a promising step for real-time PPP users who can potentially benefit from MFMC PPP.

REFERENCES

Cai C, Gao Y (2007) Precise Point Positioning Using Combined GPS and GLONASS Observations, *Journal of Global Positioning Systems*, 6(1): 13-22.

Cao W, Hauschild A, Steigenberger P, Langley RB, Urquhart L, Santos M and Montenbruck O (2010) Performance Evaluation of Integrated GPS/GIOVE Precise Point Positioning, *Proceedings of ITM 2009*, The Institute of Navigation International Technical Meeting, 25-27 January 2010, San Diego, California, pp. 540-552.

Deo MN, El-Mowafy (2016a) Triple Frequency GNSS Models for PPP with Float Ambiguity Estimation – Performance Comparison using GPS, *Survey Review*, published online 3 Dec 2016, http://dx.doi.org/10.1080/00396265.2016.1263179.

Deo MN, El-Mowafy (2016b) Evaluation of accuracy and availability of ARNS multi-constellation signals for aviation users in Australia, *IGNSS Conference 2016*, UNSW Australia, 6–8 December 2016.

Dilssner F, Springer T, Schönemann E, Enderle W (2014) Estimation of satellite antenna phase center corrections for BeiDou, *IGS Workshop*, Pasadena, California, USA (2014).

El-Mowafy A (2014). GNSS Multi-frequency Receiver Single-Satellite Measurement Validation Method, *GPS Solutions*, 18(4), 553-561.

El-Mowafy A (2015) Estimation of Multi-Constellation GNSS Observation Stochastic Properties Using a Single-Receiver Single-Satellite Data Validation Method, *Survey Review*, 47(341), 99-108.

El-Mowafy A, Deo M, Rizos C (2016) On biases in precise point positioning with multi-constellation and multi-frequency GNSS data, *Measurement Science and Technology*, 27 (2016), 10pp.

Gakstatter E (2016) ION GNSS+ a playground for high precision, *Geospatial Solutions*, September 22, 2016,< http://geospatial-solutions.com/ion-gnss-a-playground-for-high-precision-gnss/ >

Li W, Teunissen P, Zhang B and Verhagen S (2013) Precise Point Positioning Using GPS and Compass Observations, China Satellite Navigation Conference (CSNC) 2013 Proceedings, J. Sun et al. (eds.) , Springer-Verlag Berlin Heidelberg 2013.

Montenbruck O, Hauschild A and Steigenberger P (2014) Differential Code Bias Estimation using Multi-GNSS Observations and Global Ionosphere Maps, *Navigation*, 61(3): 191–201, Fall 2014.

Montenbruck O, Hugentobler U, Dach R, Steigenberger P, Hauschild A (2012) Apparent Clock Variations of the Block IIF-1 (SVN62) GPS Satellite, *GPS Solutions*, 16(3):303-313.

Prange L, Dach R, Lutz S, Schaer S, Jäggi A (2015) The CODE M-GEX Orbit and Clock Solution, *International Association of Geodesy Symposia*, Springer, Switzerland, 1-7.

Uhlemann M, Gendt G, Ramatschi M, Deng Z (2015) GFZ Global Multi-GNSS Network and Data Processing Results, *International Association of Geodesy Symposia*, Springer, Switzerland, 1-7.

Zumberge JF, Heflin MB, Jefferson DC, Watkins MM, Webb FH (1997) Precise Point Positioning for the Efficient and Robust Analysis of GPS Data from Large Networks, *Journal of Geophysical Research*, 102(B3): 5005-5017.

Hegarty C, Powers E, Fonville B (2004) Accounting For Timing Biases Between GPS, and GALILEO Signals", Proceedings of the 36th Annual Precise Time and Time Interval (PTTI) Systems and Applications Meeting, 7-9 December 2004, Washington, D.C., USA, pp. 307—318. Accessed online 23 March 2015, http://www.mitre.org/work/techpapers/techpapers05/050341/050341.pdf

Tuka A, El-Mowafy, A (2013). Performance Evaluation of Different Troposphere Delay Models and Mapping Functions, Measurement, Elsevier, 46(2) 928–937, doi http://dx.doi.org/10.1016/j.measurement.2012.10.015.

5 USE OF PRECISE IONOSPHERE CORRECTIONS FOR ACCELERATED PPP CONVERGENCE WITH MULTI-FREQUENCY AND MULTI-CONSTELLATION GNSS

Instead of forming ionosphere-free linear combinations as in conventional float PPP models, an alternative option is to constrain the ionospheric error with a RIM. This results in a significant reduction in the overall number of parameters to solve for in the PPP model, because the ionosphere error affects each receiver to satellite signal. This reduction of parameters improves the measurement geometry and may significantly reduce the convergence time. In this chapter, the float ambiguity estimation PPP model is analysed by constraining the ionosphere errors by using a high precision RIM that is determined from a ground network of GNSS stations in a regional area.

This paper is covered by the following publication:

- **Deo MN**, El-Mowafy A (2017) Ionosphere Augmentation for accelerated convergence in Precise Point Positioning with multi-frequency and multi-constellation GNSS, paper presented at ION Pacific PNT 2017 Conference, Honolulu, Hawaii, May 1-4, 2017.

Ionosphere Augmentation for accelerated convergence in Precise Point Positioning with triple-frequency GPS

Manoj Deo, *Dept of Spatial Sciences, Curtin University, Australia.*
Ahmed El-Mowafy, *Dept of Spatial Sciences, Curtin University, Australia.*

BIOGRAPHIES

Manoj Deo is currently a Ph.D. candidate at the Department of Spatial Science, Curtin University, Western Australia. He obtained his B.App.Sc and M.Sc degrees in 1998 and 2010, respectively. His current research focus is on precise point positioning with multi-constellation and multi-frequency GNSS.

Ahmed El-Mowafy is Associate Professor at the Department of Spatial Sciences, Curtin University, Western Australia. He has obtained his Ph.D. from the University of Calgary, Canada, in 1995. He has extensive publications in precise positioning and navigation using GNSS, quality control and integrity monitoring, estimation theory, and attitude determination.

ABSTRACT

A Precise Point Positioning (PPP) method is presented that uses raw triple-frequency GPS measurements augmented with a regional ionospheric model (RIM) for faster solution convergence. The proposed method has two characteristics. Firstly, there is no noise amplification since raw uncombined carrier phase and code measurements are used. This reduces the solution convergence time, contrary to the ionosphere-free linear combination with a noise amplification factor of 3 that is used in traditional dual-frequency model. Secondly, the ionosphere delay remaining in the uncombined equations is modelled using externally provided precise ionosphere corrections, hence reducing the number of parameters to be estimated.

Triple frequency simulated data was used to validate the model using a fully operational GPS constellation at four sites in Australia for one week duration. The performance of 2-hourly PPP solutions were compared for three cases including (1) the proposed triple frequency raw uncombined model with treatment of the ionosphere delay using an externally provided model (2) triple frequency raw uncombined model with estimation of ionosphere error (i.e. without RIM) and (3) traditional dual frequency PPP model. The three cases were compared in terms of solution convergence time taken to achieve and maintain 3-dimensional (3D), horizontal and vertical positional accuracies of 1 decimeter and 5cm. The tests for the first case considered the use of varying precisions of the externally provided ionosphere model with standard deviations (std) of 0.1, 0.25, 0.5 and 1.0 TECU. Results from the comparison show that the best improvement was achieved with the proposed raw model when using a high precision ionosphere model with std = 0.1 TECU, where the convergence time to achieve sub-decimeter was reduced by 37%, 86% and 33% in the 3D, horizontal and vertical components. The most significant improvement was in the horizontal component since the ionospheric error mostly affects the height. The second model also outperformed the standard dual frequency model, but had less improvement in convergence time by 13%, 3% and 21% in the three components.

INTRODUCTION

The precise point positioning (PPP) technique is used to get sub-decimeter accuracy position of a GNSS receiver without relying on measurements from a reference receiver, as is the case in relative positioning. It requires precise satellite orbit at few cm accuracy and satellite clock correction with few tenths of nanosecond accuracy, provided by the International GNSS Service (IGS) or other sources. Although PPP provides a few cm accuracy for static positioning and decimeter accuracy for kinematic positioning (Seeparsad and Bisnath, 2014), its main drawback is its need for lengthy convergence time of typically

30 minutes to achieve and maintain this accuracy. Whenever there is a loss of satellite tracking due to obstructions, the convergence process is repeated, thus costing users significant waiting time before carrying out actual PPP work. The lengthy convergence time is mainly due to the noise propagation of the code measurements due to use of the ionosphere-free linear combination in the standard dual frequency PPP. The availability of triple-frequency GPS data enables opportunities to reduce this convergence time.

Deo and El-Mowafy (2016) presented three PPP models that use triple frequency data to reduce solution convergence time for float ambiguities. These methods were validated using GPS data and demonstrated a 7-10% improvement compared to the standard dual frequency model. One of the models used raw uncombined triple frequency measurements to estimate the ionosphere as a parameter, rather than forming ionosphere free combinations. Guo et al. (2016) presented a similar approach for the Beidou constellation. Seeparsad and Bisnath (2014) applied another approach for code noise and multipath reduction to improve convergence, reporting a 34% improvement. Earlier, Gao and Shen (2002) introduced a single frequency code-phase combination in the PPP model that reduced the code noise by 50% and reported a slight improvement in convergence time.

This paper explores three approaches to reduce PPP convergence time through (1) reduction of code noise propagation in the functional model; (2) optimizing the use of triple frequency data; and (3) improving solution geometry by using a precise ionosphere model to account for ionosphere errors. An ideal approach to reduce code noise propagation in the PPP model is to avoid forming ionosphere-free linear combinations altogether and use measurements from the extra frequency to solve for the unknown parameters. Although this approach was attempted in Deo and El-Mowafy (2016), it did not result in a marked improvement in convergence time, mainly because significant time is taken to precisely estimate the extra ionosphere errors that must be solved for. In this situation, an accurate ionosphere model from an external source brings added advantage by modelling out the ionospheric error rather than estimating it.

The augmentation of precise ionospheric models has been studied for dual frequency PPP with integer ambiguity resolution (AR) in Juan et al. (2012); Rovira-Garcia et al. (2015); Rovira-Garcia et al. (2016); Collins et al. (2012) and Banville et al. (2014), or to improve accuracy for single frequency users in Van Der Marcel and De Bakker (2012). Rovira-Garcia et al. (2016) demonstrated a convergence time of few minutes to get sub-decimeter horizontal accuracy for PPP-AR with ionosphere corrections. The proposed system provided real-time precise satellite orbits, clock corrections and fractional phase biases along with an ionospheric model generated from a regional network with an accuracy of one Total Electron Content Unit (TECU). Tests with actual data showed that it took 8 minutes to attain sub-decimeter horizontal accuracy and 26 minutes for vertical accuracy, for a station at mid latitude (52° N) located less than 100km from a reference station that was used to generate the ionospheric correction. It was also shown that the accuracy of the regional ionospheric model was dependent on (i) the ionospheric activity, (ii) the distribution and inter-distance between reference stations, and (iii) the user latitude. It was possible to get an ionospheric model with accuracy of 0.25 TECU, with a mid-latitude network having less than 100km spacing (Rovira-Garcia et al., 2016). This study concluded that the GIM produced by IGS, with a nominal precision of 2.0 TECU, was not suitable for sub-decimeter PPP.

Recent research has also focused on using a local reference network infrastructure for generating ionospheric corrections for PPP real-time kinematic (PPP-RTK) systems. Harima et al. (2016) used dual frequency geometry-free measurements from a local network to estimate the ionosphere errors. This was used to interpolate ionospheric errors at a rover receiver and estimate wide lane and narrow lane ambiguities for integer ambiguity fixing. Li et al. (2014) also used dual frequency GPS measurements from a local network to estimate atmospheric errors for fast ambiguity resolution. Zhang et al. (2013) used the IGS GIM product and ionospheric errors from a local network to develop an ionospheric constrained PPP model.

The benefits of multi-constellation PPP has been studied in Cai & Gao (2007), Li et al. (2014) and El-Mowafy et al. (2016). Although multi-constellation PPP presents additional biases to deal with, studies have shown that the benefits outweigh these challenges by improving solution geometry and ultimately reducing convergence time.

In this paper, a PPP model with float ambiguity estimation is evaluated that uses raw uncombined triple frequency measurements from GPS with ionospheric augmentation from an external source for faster solution convergence. Whereas triple frequency data enables estimation of the ionospheric error as a parameter, availability of a precise ionospheric model improves the geometry of the solution, thus enabling faster solution convergence. No noise amplification occurs with this model, unlike the traditional ionosphere-free PPP model where the noise increases by a factor of 3. With the proposed method, users get a converged solution within a few minutes, and at a fraction of the time that is currently required in the traditional dual frequency PPP method. The model also compares well with the Fast PPP-AR model, which takes similar time to resolve integer ambiguity. Also, users may revert to using a float solution if AR is not successful within a few minutes and triple frequency data is available. Since the method avoids PPP-AR, user algorithms avoid dealing with fractional phase biases, and consequently the techniques that have been proposed in present literature to deal with them. In addition, the paper presents an

analysis of the required precision of the ionosphere model to achieve fast solution convergence to reach sub decimeter level accuracy. The next section presents the triple frequency observation model, analysis of the methodology, followed by validation of the proposed PPP model with ionospheric corrections having precisions of 0.1, 0.25, 0.5 and 1.0 TECU. The performance of the proposed model is compared to that from the standard dual frequency GPS-only model and the raw measurement model with ionospheric estimation.

TRIPLE FREQUENCY PPP MODEL

The first part of this section presents the triple frequency observation equations used in the proposed PPP model with and without the use of a regional ionospheric model (RIM). Both undifferenced and between-satellite single-differenced (BSSD) cases are considered. This is followed by a sub-section on stochastic modelling of observations.

Single Constellation Model

The raw carrier phase and code measurements are used in the proposed PPP model. Each triple-frequency GNSS satellite k has three code and phase measurements (scaled to distance units), to receiver r, can be modelled as:

$$P(i)_r^k = \rho_r^{\mathrm{k}} + c\left(dt_{\mathrm{r}} - dt^{\mathrm{k}} + d(i)_{\mathrm{r}} + d(i)^{\mathrm{k}}\right) + T^{\mathrm{k}} + \mu_i\, I^k + \varepsilon_{P(i)_r}^k \quad (1)$$

$$\phi(i)_r^{\mathrm{k}} = \rho_r^{\mathrm{k}} + c\left(dt_r - dt^{\mathrm{k}}\right) + T^{\mathrm{k}} - \mu_i\, I^{\mathrm{k}} + \lambda_i\left(N(i)_r^{\mathrm{k}} + \delta(i)_{\mathrm{r}} + \delta(i)^{\mathrm{k}}\right) + \varepsilon_{\phi(i)_r}^{\mathrm{k}} \quad (2)$$

where i is the frequency identifier, such that $i = 1, 2, 5$ for GPS L1, L2 and L5, respectively; $P(i)$ and $\phi(i)$ are the pseudorange and carrier-phase measurements whereas frequency is denoted as f_i. ρ is the satellite-to-receiver geometric range; c is the speed of light in vacuum; dt_r and dt^k are the receiver and satellite clock offsets, where the latter is eliminated in PPP by the use of precise clock corrections. T^k is the tropospheric path delay which may be separated into a Zenith Wet Delay (ZWD) and a Zenith Hydrostatic Delay (ZHD) as a function of respective wet and hydrostatic mapping functions (Tuka and El-Mowafy, 2013); λ_i denotes the wavelength for frequency i. $\mu_i = \frac{f_1^2}{f_i^2}$ is the dispersive coefficient and I^k is the ionosphere error for a reference frequency, e.g. L1 for GPS. $\varepsilon_{\phi(i)_r}^k$ includes measurement noise and multipath of the carrier-phase measurement whereas $\varepsilon_{P(i)_r}^k$ denotes code measurement noise and multipath. $d(i)_r$ is the receiver hardware bias for the code measurement and $d(i)^k$ is the satellite hardware bias. The satellite dependent code biases are corrected by using the Differential Code Bias (DCB) products, which are now available from IGS Multi-GNSS Experiment (MGEX) (Montenbruck et al., 2014). The receiver dependent code hardware delays remain in the equations due to the use of multiple frequencies and may be eliminated by applying BSSD of measurements or by estimating it as part of the inter-system biases (El-Mowafy et al., 2016). $N(i)_r^{\boldsymbol{k}}$ is the integer ambiguity term whereas $\delta(i)_r$ and $\delta(i)^k$ are the receiver and satellite hardware biases for the carrier-phase measurements, respectively, which make the ambiguity a non-integer term (Shi and Gao, 2014).

Since in this paper we restrict attention to solving float ambiguities, the different types of biases are lumped with the phase ambiguity terms and considered to be constant during the observation period, since biases are usually stable over several hours. These biases have the same coefficients in the solution design matrix, resulting in rank deficiency and inability to separate them and a preferred approach is to estimate them externally and provide them to users as known quantities (Deo and El-Mowafy, 2016).

Assuming availability of precise orbits and clock corrections, DCB's, precise satellite phase center offsets for individual frequencies, and modelling of the hydrostatic tropospheric delay and removing the receiver identifier (since we are dealing with a single receiver), the observation Eqs. 1 and 2 are simplified to:

$$\hat{P}(i)^k = \rho^k + cdt + \mathrm{ZWD} \cdot m_w^{\mathrm{k}} + \mu_i\, I^{\mathrm{k}} + \varepsilon_{P(i)}^k \quad (3)$$

$$\hat{\phi}(i)^k = \rho^{kG} + cdt + \mathrm{ZWD} \cdot m_w^{\mathrm{k}} - \mu_i\, I^{\mathrm{k}} + \lambda_{\mathrm{i}} N(i)^* + \varepsilon_{\phi(i)}^k \quad (4)$$

where $\hat{P}(i)^k$ and $\hat{\phi}(i)^k$ are the corrected pseudorange and carrier phase measurements; ZWD is the zenith wet delay common to all satellites measured; m_w^{k} is the wet tropospheric mapping function to map the ZWD to the slant receiver-satellite signal path; $N(i)^*$ is a float real number that includes the integer ambiguities and hardware biases. The unknown parameters in this model include three position components (i.e. X, Y, Z), a receiver clock offset, a tropospheric ZWD, and slant ionospheric errors as well as three phase ambiguities for each satellite when using the three frequencies. Thus, there are $6n$ observations and $5 + 4n$ unknowns for undifferenced measurements from n satellites. Availability of a regional ionospheric model (RIM) enables the ionospheric error to be modelled as known quantities; thus of Eqs. 3 and 4 are simplified as:

$$\tilde{P}(i)^k = \rho^k + cdt + \text{ZWD} \cdot m_w^{\text{k}} + \varepsilon_{P(i)}^k \quad (5)$$

$$\tilde{\phi}(i)^k = \rho^{k_G} + cdt + \text{ZWD} \cdot m_w^{\text{k}} + \lambda_{\text{i}} N(i)^* + \varepsilon_{\phi(i)}^k \quad (6)$$

where $\tilde{P}(i)^k = \hat{P}(i)^k - \mu_i \hat{I}^{\text{k}}$ and $\tilde{\phi}(i)^k = \hat{\phi}(i)^k + \mu_i \hat{I}^{\text{k}}$ are the reduced observations after applying the ionosphere corrections; $\hat{I}^{\text{k}}$ is the ionospheric correction determined from the ionospheric model, generally available as Vertical (V) TEC maps which contain the TEC values in the vertical direction. A mapping function is used to convert to slant (S) TEC values along the receiver-to-satellite signal path (Schaer, 1997). The RINEX V3 also enables the ionospheric delay to be recorded as pseudo observables (IGS, 2015) and present day efforts are underway to produce precise STEC maps with its incumbent standard deviation.

The number of unknown parameters are now reduced to $5 + 3n$. This increases the degrees of freedom (number of measurements minus number of unknown parameters) of the model, thus strengthening the geometry which could potentially reduce convergence time. Table 1 summarizes the number of measurements, unknowns and degrees of freedom for the undifferenced PPP model with and without use of RIM. As shown, the degrees of freedom increases by three with each additional satellite when using RIM and triple frequency observations, compared to an increase by two without RIM.

Users may employ between-satellite-single-differencing (BSSD) of measurements to eliminate receiver biases including the clock offset. This reduces the number of measurements to $6(n-1) = 6n-6$ and number of unknowns to three positions, a single differenced tropospheric ZWD, $n-1$ slant ionospheric error and $3(n-1)$ ambiguities; hence a total of $4 + 4(n-1) = 4n$ unknowns. If a RIM is used, the slant ionospheric error is eliminated, thus the number of unknowns is reduced to $4 + 3(n-1) = 1 + 3n$.

Table 1: Number of measurements, unknowns and degree of freedom for the single constellation undifferenced PPP model using triple frequency phase and code measurements with and without use of RIM.

No. of satellites (n)	No. of measurements	Undifferenced Model No RIM		Undifferenced Model with RIM	
		No. of unknown parameters	Degrees of freedom	No. of unknown parameters	Degrees of freedom
	6n	5+4n	2n-5	5+3n	3n-5
4	24	21	3	17	7
5	30	25	5	20	10
6	36	29	7	23	13
7	42	33	9	26	16
8	48	37	11	29	19

Stochastic Modelling of Observations

In this study, the raw carrier phase and code measurements are assumed to be uncorrelated. The standard deviations for carrier phase measurements are assumed as 0.01 cycles and for the code observations are derived from El-Mowafy (2014) as 0.37m, 0.48m and 0.36m for GPS P1, P2 & P5; 0.36m, 0.35m, 0.34m and 0.05m for Galileo E1, E5a, E5b and E6 codes and 0.51m, 0.37m and 0.34m for Beidou B1, B2 & B3. The precisions of the RIM are considered at various levels as 0.1, 0.25, 0.5, 1.0 and 2.0 TECU, where 1 TECU in electrons per m^2 is:

$$1\,TECU = 10^{16} electrons/m^2 \quad (7)$$

The first order ionospheric error for GNSS transmitting frequency f_i is:

$$I_i = \frac{40.3}{f_i^2} TEC \quad (8)$$

Considering GPS as an example, the ionospheric precision corresponding to $1\,TECU$ is 0.162m for L1, 0.267m for L2 and 0.291m for the L5 frequency. Table 2 shows the precisions of the tested ionospheric corrections for each signal of the GNSS constellations ($\sigma_{I_{P(i)}} = \sigma_{I_{\phi(i)}}$), as well as the expected overall precision of the corrected pseudoranges ($\sigma_{\tilde{P}(i)}$), with the code noise assumptions given in El-Mowafy (2014). As shown, the expected precision of the ionospheric corrections in the measurements range between 1-3cm (Std. RIM = 0.1 TECU), 4-7cm (Std. RIM = 0.25 TECU), 8-15cm (Std. RIM = 0.5 TECU), 16-29cm (Std. RIM = 1.0 TECU) and 32-58cm (Std. RIM = 2.0 TECU). If BSSD of measurements is performed, the overall noise increases by a factor of $\sqrt{2}$ due to error propagation law. The measurement weighting is simply based on elevation angle (E) of the satellites taken as $1/sin(E)$.

Table 2: Precisions of the ionospheric correction for the various pseudorange signals of each constellation, as well as the expected overall precision of the corrected pseudoranges with the assumed code noise.

System	$P(i)$	$\sigma_{P(i)}$ (m)	Std. RIM = 0.1 TECU		Std. RIM = 0.25 TECU		Std. RIM = 0.50 TECU		Std. RIM = 1.00 TECU		Std. RIM = 2.00 TECU	
			$\sigma_{I_{P(i)}}$ (m)	$\sigma_{\hat{P}(i)}$ (m)	$\sigma_{I_{P(i)}}$ (m)	$\sigma_{\hat{P}(i)}$ (m)	$\sigma_{I_{P(i)}}$ (m)	$\sigma_{\hat{P}(i)}$ (m)	$\sigma_{I_{P(i)}}$ (m)	$\sigma_{\hat{P}(i)}$ (m)	$\sigma_{I_{P(i)}}$ (m)	$\sigma_{\hat{P}(i)}$ (m)
G	P1	0.37	0.016	0.370	0.041	0.372	0.081	0.379	0.162	0.404	0.325	0.492
	P2	0.48	0.027	0.481	0.067	0.485	0.134	0.498	0.267	0.549	0.535	0.719
	P5	0.36	0.029	0.361	0.073	0.367	0.146	0.388	0.291	0.463	0.582	0.685
E	E1	0.36	0.016	0.360	0.041	0.362	0.081	0.369	0.162	0.395	0.325	0.485
	E5a	0.35	0.029	0.351	0.073	0.357	0.146	0.379	0.291	0.455	0.582	0.679
	E5b	0.34	0.028	0.341	0.069	0.347	0.138	0.367	0.277	0.438	0.553	0.649
	E6	0.05	0.025	0.056	0.062	0.079	0.123	0.133	0.246	0.251	0.493	0.495
C	B1	0.51	0.017	0.510	0.041	0.512	0.083	0.517	0.165	0.536	0.331	0.608
	B2	0.37	0.028	0.371	0.069	0.376	0.138	0.395	0.277	0.277	0.553	0.553
	B3	0.34	0.025	0.341	0.063	0.346	0.125	0.362	0.250	0.422	0.501	0.605

IONOSPHERIC CORRECTIONS IN THE CONTEXT OF AUSTRALIAN GNSS NETWORK

The Space Weather Services (SWS) unit of the Australian Bureau of Meteorology (BoM) is conducting a research project in collaboration with the Australian Cooperative Research Center for Spatial Information (CRCSI) to deliver a highly accurate real-time regional ionospheric model to support PPP-Real time kinematic (RTK) users for the National Positioning Infrastructure (NPI). The NPI is designed to deliver "instantaneous, reliable and fit-for-purpose access to positioning and timing information anytime and anywhere across the Australian landscape and its maritime jurisdictions" (Maher et al., 2016). GNSS data from a network of Continuously Operating Reference Stations (CORS) will be used to generate the regional ionospheric correction model, required with sub-TECU precision (Terkildsen, 2016). Since the RIM is not presently available for Australia, simulated data is used in this study to validate the proposed method.

VALIDATION OF THE PROPOSED MODEL

This section presents validation of the proposed PPP model with test data at four sites in Australia with the assumed precisions in terms of σ_I of RIM, as 0.1, 0.25, 0.5 and 1.0 TECU. These solutions are compared to the raw model without use of RIM, and the standard dual frequency model.

Test Description

Test data was simulated for one week at four stations namely Hobart (HOB2), Alice Springs (ALIC), Yarragadee (YAR2) and Townsville (TOW2), which are distributed over the Australian continent. Simulated data was used due to current insufficient number of GPS Block IIF satellites, the unavailability of satellite antenna phase center offsets for individual signals, and unavailability of precise ionospheric corrections from a regional network. We believe that these issues will be resolved in the near future. The data sample interval was 15 s, with measurement standard deviations given in the previous section. A satellite elevation cut-off angle of 10 degrees was used for measurement processing. The measurement modelling and simulation were carried out with the following approach to generate triple frequency measurements for a full GPS constellation (31 satellites):

- Use of the following IGS products: final precise ephemeris; IGS satellite clock correction for satellite clock offset, dt^k; IGS station ZTD and receiver clock products for the troposphere and receiver clock offset (produced for selected IGS stations using standard PPP); and the broadcast Klobuchar model for the ionospheric delay. This approach gives realistic errors in the simulated data.
- The satellite DCBs were ignored since these are available from IGS MGEX; whereas receiver DCBs may be eliminated when forming BSSD of measurements.
- The known station coordinates were obtained from the Asia Pacific Reference Frame (APREF) project records (Hu et al., 2011).

In order to simulate the RIM, a random error was added to the Klobuchar derived ionospheric error for each satellite observed. This random error had a normal distribution with zero mean and standard deviation equal to the assumed precision of the RIM; i.e. 0.1, 0.25, 0.5 and 1.0 TECU.

Analysis and Discussion of Results

The data was processed in 2-hour blocks, with the ambiguities re-initialized at the start of each block in order to analyze the convergence performance for a sufficient number of samples. The accuracy of PPP results was assessed by referencing them to the known station precise coordinates obtained from APREF. The three PPP models, including the raw model with use of RIM, raw model without RIM and the standard dual frequency model, were implemented using Kalman filter processing. Results are compared in terms of solution convergence time for the 3-dimensional (3D), horizontal (2D) and vertical position components, and precision of the estimated position. This will be of interest to the PPP users who require sub-decimeter accuracies in the 3D, 2D and vertical components. For example, cadastral surveyors may require only 2D positioning, engineering surveyors require vertical accuracy and precise navigation for unmanned aerial vehicles (UAVs) require 3D accuracy. The 3D convergence time is defined as the time when 3-dimentional (North – East – Up) positional accuracies of 0.1m and 0.05m is reached and maintained thereafter. Likewise, horizontal convergence time defines when a 2-dimensional accuracy is achieved and vertical convergence time defines when vertical positional accuracy is achieved. The accuracy is defined as the root mean squared errors (RMSE) of the estimated positions after convergence is achieved with respect to the known station position as mentioned above. The performance of the proposed PPP model is analyzed with ionospheric corrections having precisions of 0.1, 0.25, 0.5 and 1.0 TECU. In the software implementation, a randomly generated error (with a normal distribution, zero mean and the given standard deviation) is added to the known ionospheric error, estimated using Klobuchar model. The results from this analysis is compared the standard dual frequency GPS-only model and the raw measurement model, where the ionosphere is estimated as an unknown parameter.

For demonstration, the proposed model was firstly assessed for one site (YAR2) assuming a totally known ionospheric model (i.e., ionospheric error known with zero error). Although this is not feasible in practice, it demonstrates the ultimate benefits of the model. Figure 1 compares this case with the standard dual frequency PPP model. As shown, the proposed model achieved convergence within few minutes, with an average of 6.3, 1.0 and 5.6 minutes to reach sub-decimeter accuracy in 3D, horizontal and vertical directions, respectively, whereas the traditional model required much longer time to converge, with an average of 40.4, 27.8 and 21.3 minutes to achieve sub-decimeter accuracy in 3D, horizontal and vertical directions, respectively.

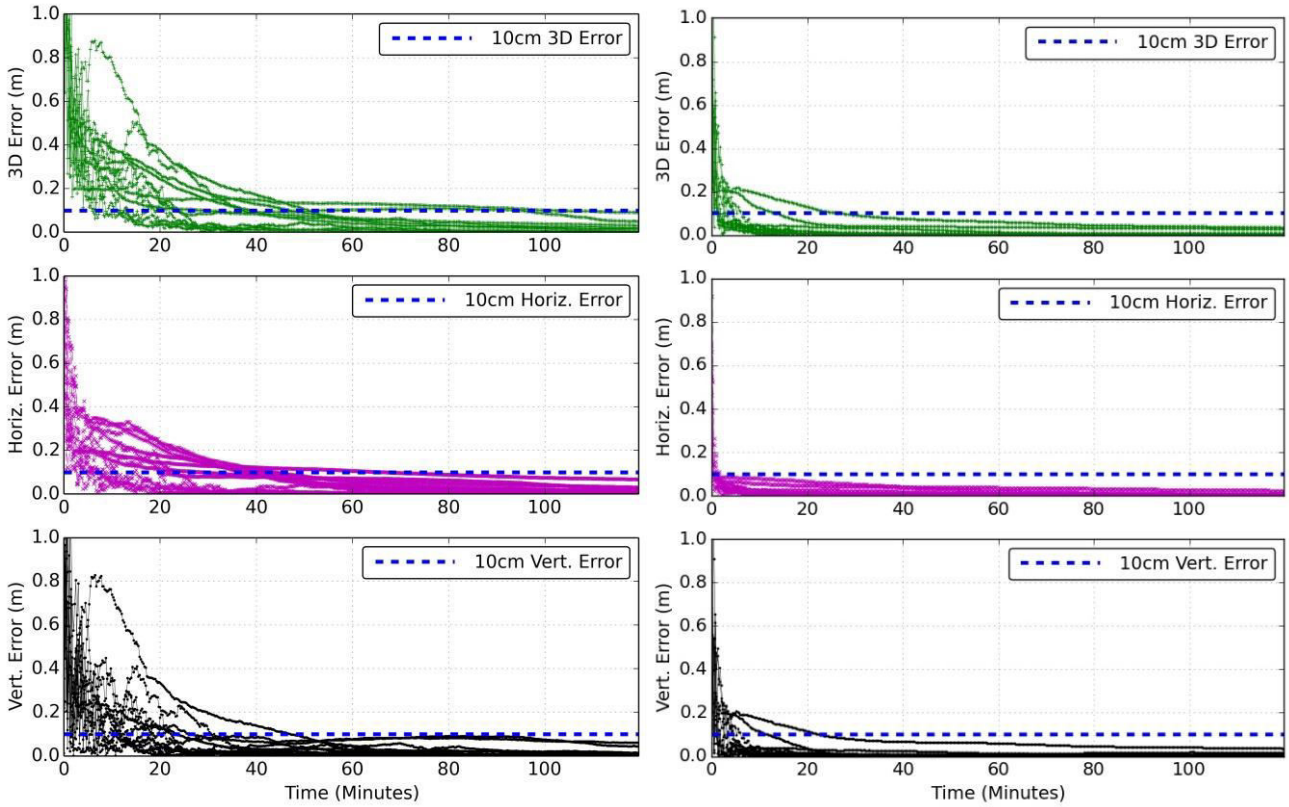

Figure 1: Comparison of the standard dual frequency PPP model (left) with the proposed model assuming totally known ionosphere error (right).

Table 3 shows the PPP convergence time taken to reach 0.1 and 0.05m positioning accuracy in the 3D, horizontal and vertical components within the 2-hour blocks. Table 4 shows the mean positional accuracy attained in the 3D, horizontal and vertical directions at 5, 10, 20 and 120 minutes after the filter reset, for each of the PPP models. Figure 2 compares results from the

triple frequency raw uncombined model without use of RIM to the standard dual frequency model that uses ionosphere free combination. This figure, supported by Table 1 show that the raw uncombined model had improved performance compared to the standard dual frequency model. After just 5 minutes of processing, the accuracy of the former model improved by 0.039m (13%), 0.010m (7%) and 0.037m (16%) in 3D, horizontal and vertical components, respectively. These improvements dissipate with time and after 2 hours of processing; both models provide 1-2cm level of accuracy.

Comparing the proposed triple frequency raw model with use of RIM to the standard dual frequency model, the following results were noted:

- When using a RIM precision of 0.1 TECU, the point positioning accuracy improved by 0.113m (40%), 0.096m (68%) and 0.063m (28%) after just 5 minutes of processing. After 10 minutes, the horizontal accuracy exceeds 5cm and after two hours, the performance is comparable to the standard dual frequency model.
- When using a RIM precision of 0.25 TECU, the improvements after 5 minutes are 0.056m (20%), 0.092m (65%) and 0.008m (3%); whereas with a RIM precision of 0.5 TECU, the improvements are 0.041m (14%), 0.093m (66%) and -0.011 (-4%); and with RIM precision of 1.0 TECU the improvements are 0.050 (17%), 0.089 (63%) and 0.003 (1%) in 3D, horizontal and vertical directions. Note that in all these cases, better than 5cm horizontal positioning accuracy is attained within 5 minutes.
- After 2 hours of processing, the precision attained with the raw model using 0.1 TECU RIM is at the same level as the standard dual frequency model, which is at the 1-2cm accuracy level. However, the raw model with lower RIM precisions of 0.25-1.0 TECUs give worse performance at 0.040–0.064m in 3D, 0.017–0.035m in horizontal and 0.034–0.470m in vertical components. This is expected since the precision of the ionosphere model directly affects the precision of the code and phase measurements, which manifest in the positioning error.

In terms of the convergence times, it took less than 2 minutes to attain 1 decimeter horizontal positioning accuracy for all cases where the RAW model with RIMs were used. To achieve 5cm horizontal positioning accuracy, it took less than 5 minutes with RIM precisions of 0.1-0.5 TECUs. Using the 1.0 TECU RIM, the solution actually converged within 5 minutes as well. However, the accuracy attainable was at the 5 cm level regardless of the processing time; hence the convergence time was higher using the criteria for assessment. It was also evident that better than 5cm 3D positioning accuracy performance is not attainable with RIM precisions of 0.5 and 1.0 TECUs.

Table 3: Time taken to reach 0.1m and 0.05m accuracy (3D, horizontal and vertical) and mean RMSE after convergence for the standard dual frequency, raw uncombined model without use of RIM, and raw uncombined models with RIMs of 0.1, 0.25, 0.5 and 1.0 TECU.

PPP Model	RIM Precision (TECU)	Convergence time for 0.1m accuracy (minutes)			Mean RMSE after 0.1m convergence (m)			Convergence time to reach 0.05m accuracy (minutes)			Mean RMSE after 0.05m convergence (m)		
		3D	Horiz.	Vert.	3D	Horiz.	Vert.	3D	Horiz.	Vert.	3D	Horiz.	Vert.
Standard Dual Freq	None	17.50	7.75	14.25	0.033	0.026	0.024	35.75	20.25	24.50	0.025	0.020	0.019
Raw	None	15.25	7.50	11.25	0.033	0.025	0.025	37.50	17.25	23.50	0.024	0.021	0.019
Raw	0.10	11.00	1.25	9.50	0.032	0.018	0.027	27.25	4.25	23.25	0.025	0.016	0.021
Raw	0.25	33.25	1.25	26.75	0.062	0.028	0.057	97.25	5.00	79.75	0.044	0.026	0.041
Raw	0.50	86.75	1.25	79.50	0.076	0.037	0.070	-	4.75	111.5	-	0.036	0.046
Raw	1.00	111.5	1.50	109.0	0.079	0.043	0.069	-	63.25	118.5	-	0.042	0.046

Table 4: The positional accuracy (3D, horizontal and Vertical) at 5, 10, 20 and 120 minutes after PPP filter reset for the standard dual frequency, raw uncombined model without use of RIM, and raw uncombined models with RIMs of 0.1, 0.25, 0.5 and 1.0 TECU.

PPP Model	RIM precision (TECU)	Accuracy after 5 min (m)			Accuracy after 10 min (m)			Accuracy after 20 min (m)			Accuracy after 120 min (m)		
		3D	Horz.	Vert.	3D	Horz.	Vert.	3D	Horz.	Vert.	3D	Horz.	Vert.
Standard Dual	None	0.283	0.140	0.221	0.172	0.083	0.135	0.088	0.050	0.064	0.013	0.008	0.009

Freq.													
Raw	None	0.244	0.130	0.184	0.144	0.078	0.110	0.079	0.046	0.058	0.012	0.008	0.008
Raw	0.10	0.170	0.044	0.158	0.104	0.035	0.091	0.068	0.026	0.058	0.015	0.007	0.012
Raw	0.25	0.224	0.048	0.213	0.184	0.040	0174	0.122	0.033	0.112	0.040	0.017	0.034
Raw	0.50	0.242	0.047	0.232	0.243	0.040	0.234	0.188	0.039	0.178	0.056	0.029	0.043
Raw	1.00	0.233	0.051	0.218	0.277	0.043	0.269	0.214	0.035	0.205	0.064	0.035	0.047

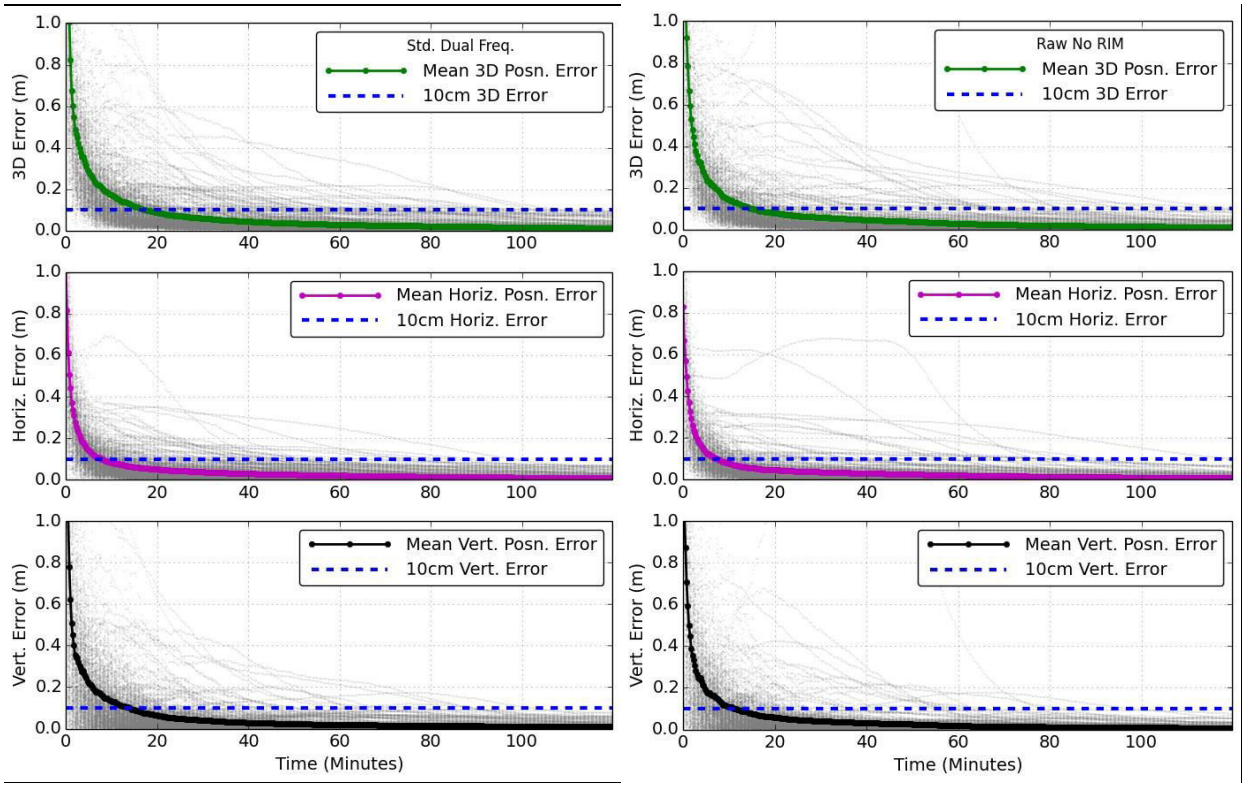

Figure 2: Position errors in 3D (top), Horizontal (middle) and vertical (bottom) for the standard dual frequency model (left) and the raw uncombined model without use of RIM (right). The thick lines represent the mean positional error whereas grey lines show the errors for individual 2-hour solutions.

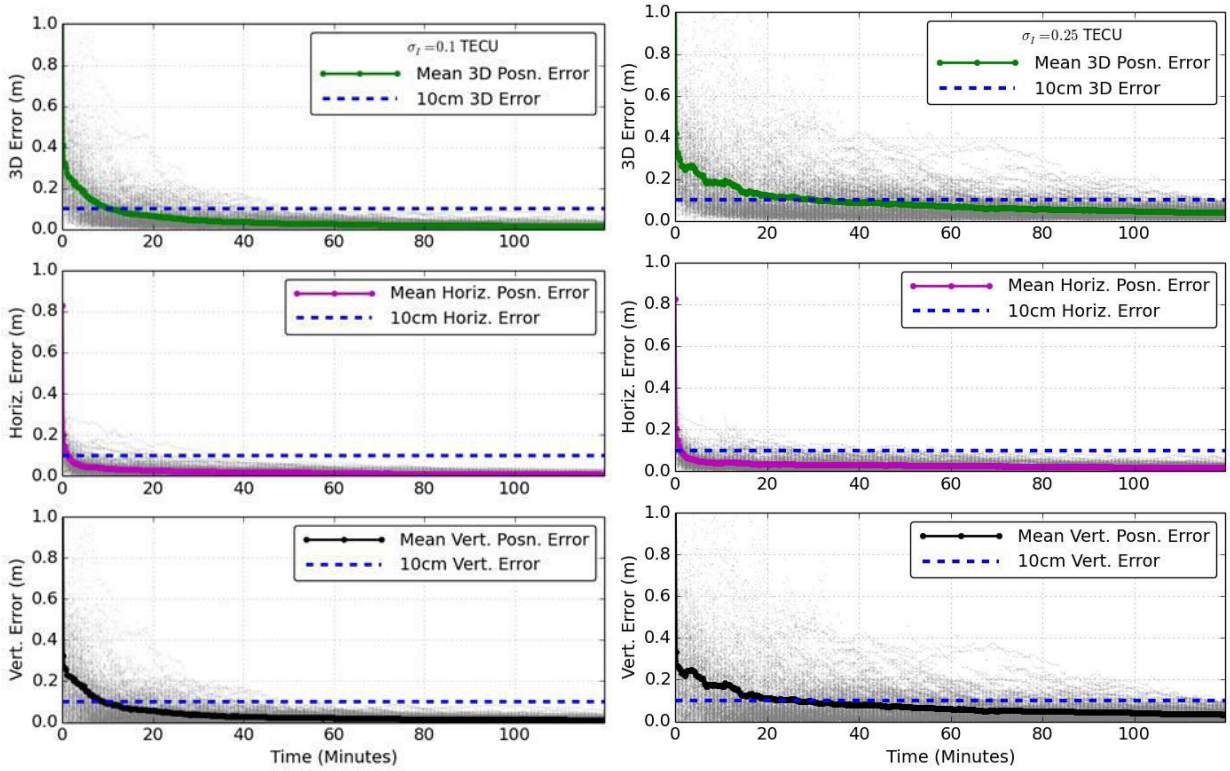

Figure 3: Position errors in 3D (top), Horizontal (middle) and vertical (bottom) for the raw uncombined model with use of RIM with an accuracy of 0.1 TECU (left) and 0.25 TECU (right). The thick lines represent the mean positional error whereas grey lines show the errors for individual 2-hour solutions.

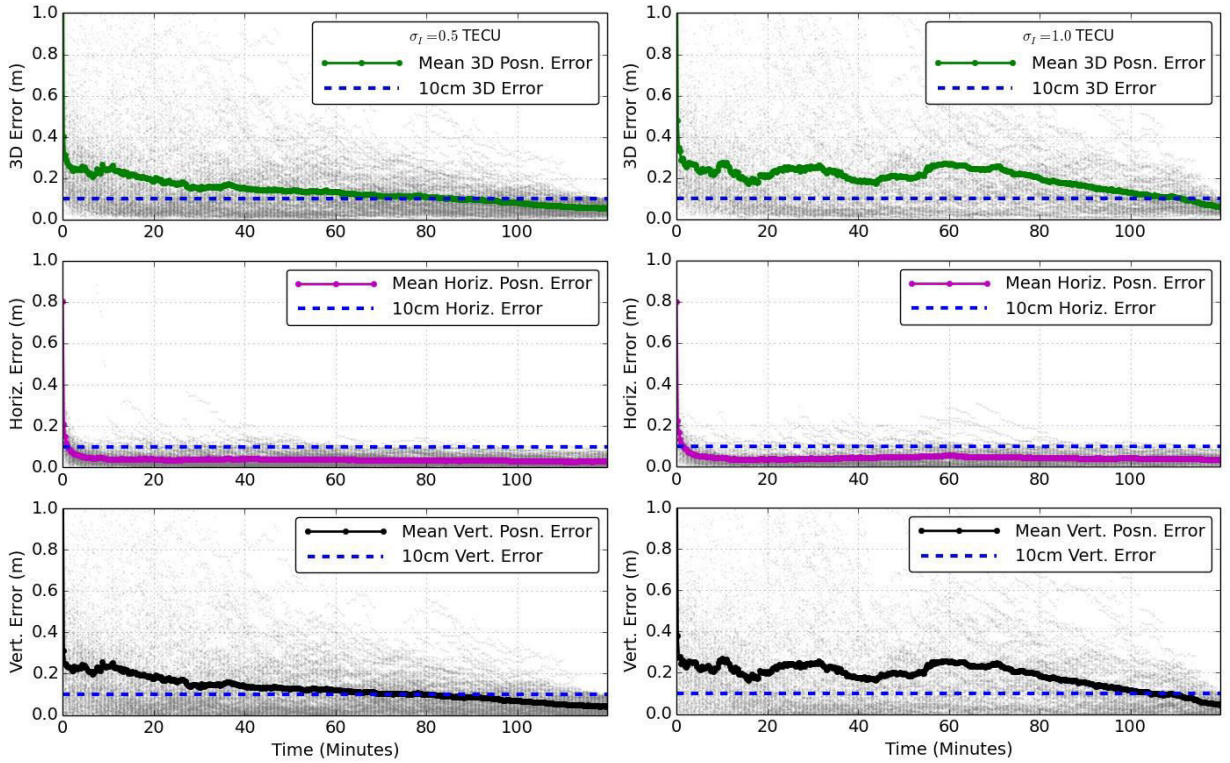

Figure 4: Position errors in 3D (top), Horizontal (middle) and vertical (bottom) for the raw uncombined model with use of RIM with an accuracy of 0.50 TECU (left) and 1.00 TECU (right). The thick lines represent the mean positional error whereas grey lines show the errors for individual 2-hour solutions.

CONCLUSIONS

This paper presented a PPP model with triple frequency raw uncombined measurements with the use of precise ionospheric corrections generated from a regional GNSS network. The model was validated using simulated data with RIM precisions of 0.1, 0.25, 0.5 and 1.0 TECU and results were compared to the raw model without the use of RIM, where the ionospheric error is estimated as an unknown parameter, and the standard dual frequency model. Although the raw model without RIM reduced the convergence time to achieve sub-decimeter accuracy by 13%, 3% and 21% in the 3D, horizontal and vertical components; the best performance was achieved with use of high precision RIM. An ionospheric model with 0.1 TECU precision gave sub-decimeter accuracy in under 2 minutes for horizontal and 11 minutes for 3D component; whereas to achieve sub 5cm accuracy required 4.25 minutes for horizontal and 27 minutes for 3D components. All the RIM precisions between 0.1 to 1.0 TECU that were tested are capable of providing horizontal positioning accuracy of 5cm within 5 minutes of convergence time. The 0.1 TECU RIM can provide better accuracy than the standard dual frequency model and the raw model without use of RIM throughout the convergence process. The RIMs with lower precisions provided improved accuracy in the horizontal component for the first 20 minutes of the convergence process for all cases. These performance indicators are promising for real-time PPP users of triple frequency GPS data who can achieve sub-decimeter horizontal accuracy within few minutes with float ambiguity estimation.

ACKNOWLEDGEMENT

Authors are thankful to Geoscience Australia for provision of the APREF solutions used in this paper.

REFERENCES

1. Banville S, Collins P, Zhang W and Langley R B. 2014. Global and Regional Ionospheric Corrections for Faster PPP Convergence, Navigation, 61(2): 115-124.
2. Cai C and Gao Y. 2007. Precise Point Positioning Using Combined GPS and GLONASS Observations, Journal of Global Positioning Systems, 6(1): 13-22.
3. Collins P, Lahaye F and Bisnath S. 2012. External Ionospheric Constraints for Improved PPP-AR Initialisation and a Generalised Local Augmentation Concept. Proceedings of the 25th International Technical Meeting of The Satellite Division of the Institute of Navigation (ION GNSS 2012), Nashville, TN, September 2012, pp. 3055-3065.
4. Deo M and El-Mowafy A. 2016. Triple Frequency GNSS Models for PPP with Float Ambiguity Estimation – Performance Comparison using GPS, Survey Review, published online 3 Dec 2016, http://dx.doi.org/10.1080/00396265.2016.1263179.
5. El-Mowafy A, Deo M and Rizos C. 2016. On biases in precise point positioning with multi-constellation and multi-frequency GNSS data, Measurement Science and Technology, 27(3), 035102.
6. El-Mowafy A. 2014. GNSS Multi-frequency Receiver Single-Satellite Measurement Validation Method, GPS Solutions, 18(4), 553-561.
7. Gao Y and Shen X 2002. A New Method for Carrier Phase Based Precise Point Positioning, Navigation, 40(2): 109-116.
8. Guo F, Zhang X, Wang J and Ren X. 2016. Modelling and assessment of triple-frequency BDS precise point positioning. J. Geod, 90:1223. doi:10.1007/s00190-016-0920-y.
9. Harima K, Choy S, Elneser L and Kogure S. 2016. Local augmentation to wide area PPP systems: a case study in Victoria, Australia, IGNSS Conference, UNSW, 6-8 December 2016.
10. Hu G, Dawson J, Jia M, Deo M, Ruddick R and Johnston G. 2011. Towards the Densification of the International Terrestrial Reference Frame in the Asia and Pacific Region – Asia Pacific Reference Frame (APREF), Advances in Geosciences, Vol 32: Solid Earth Sciences, Eds. Lo C-H et al. (2011), World Scientific Publishing Company.
11. IGS. 2015. The Receiver Independent Exchange Format Version 3.03. International GNSS Service (IGS), RINEX Working Group and Radio Technical Commission for Maritime Services Special Committee 104 (RTCM-SC104), <ftp://igs.org/pub/data/format/rinex303.pdf >, accessed 27 February, 2017.
12. Juan J M, Hernandez-Pajares M, Sanz J, Ramos-Bosch P, Aragon-Angel A, Orus R, Ochieng W, Feng S, Jofre M, Coutinho P, Samson J and Tossaint M. 2012. Enhanced Precise Point Positioning for GNSS Users. IEEE Transactions on Geoscience and Remote Sensing, doi 10.1109/TGRS.2012.2189888.
13. Li X, Ge M, Dousa J and Wickert J. 2014. Real-time precise point positioning regional augmentation for large GPS reference networks, GPS Solutions 18(1): 61-71.
14. Maher P, Terkildsen M, Kumar V, Bouya Z, Steward G, Lozbin V and Marshall R. 2016. Australian Bureau of Meteorology Space Weather Services: Recent Initiatives, SWPC Space Weather Workshop, 28 April 2016.
15. Montenbruck O, Hauschild A and Steigenberger P. 2014. Differential Code Bias Estimation using Multi-GNSS Observations and Global Ionosphere Maps, Navigation, 61(3): 191–201, Fall 2014.
16. Rovira-Garcia A, Juan J M, Sanz J, Gongáles-Casado G and Bertran E. 2016. Fast Precise Point Positioning: A System to Provide Corrections for Single and Multi-Frequency Navigation. Navigation, 63(3): 231-247, Fall 2016.

17. Rovira-Garcia A, Juan J, Sanz J and Gongåles-Casado G. 2015. A Worldwide Ionospheric Model for Fast Precise Point Positioning. IEEE Transactions on Geoscience and Remote Sensing, 53(8):4596-4604.
18. Schaer S. 1997. How to use CODE's Global Ionosphere Maps. Astronomical Institute, University of Berne.
19. Seepersad G and Bisnath S. 2014. Reduction of PPP convergence period through pseudorange multipath and noise mitigation, GPS Solut, 19(3): 369-379.
20. Shi J and Gao Y. 2014. A comparison of three PPP integer ambiguity resolution methods. GPS Solution, 18(4): 519-528.
21. Terkildsen M. 2016. Ionospheric Space Weather: Monitoring, modelling and mitigation, IGNSS Conference, 6–8 December 2016, UNSW Australia.
22. Van Der Marcel H and De Bakker P. 2012. Single versus Dual-Frequency Precise Point Positioning: What are the trade-offs between using L1-only and L1+L2 for PPP? Inside GNSS, July/August 2012.
23. Zhang H, Gao Z, Ge M, Niu X, Huang L, Tu R and Li X. 2013. On the Convergence of Ionospheric Constrained Precise Point Positioning (IC-PPP) Based on Undifferential Uncombined Raw GNSS Observations. Sensors 13(11), 15708-15725, doi:10.3390/s131115708
24. Tuka A, El-Mowafy, A. 2013. Performance Evaluation of Different Troposphere Delay Models and Mapping Functions, Measurement, Elsevier, 46(2) 928–937, doi http://dx.doi.org/10.1016/j.measurement.2012.10.015.

6 COMPARISON OF ADVANCED TROPOSPHERE MODELS FOR AIDING REDUCTION OF PPP CONVERGENCE TIME

The float ambiguity estimation PPP models must deal with the tropospheric error. This chapter investigates the application of high precision troposphere models derived from NWM data for constraining the troposphere error. The impact of applying externally obtained troposphere models to constrain the troposphere error is investigated. This is to answer the key question whether applying troposphere constraints improves the convergence time in float ambiguity estimation PPP models. For the first time, the NWM obtained from the Australian Bureau of Meteorology (BoM) is used in the analysis.

This chapter is covered by the following publication:

- **Deo MN**, El-Mowafy A (2018) Comparison of Advanced Troposphere Models for Aiding Reduction of PPP Convergence Time in Australia, Journal of Spatial Science, https://doi.org/10.1080/14498596.2018.1472046, first published online: 24 May 2018.

6.1 Errata

The following corrections apply to this published paper:

- Pg. 4 of article (sentence beneath Eqn. 2): P1, P2, P3 – first P should not be italicized
- Pg. 5 of article (sentence beneath Eqn. 4) line should read: "where G is a GPS satellite, ρ^G is the satellite-to-receiver geometric range, c is the speed of light in vacuum; dt_G is the receiver clock offset; N^{*G} is the non-integer phase ambiguity; ε_{Pi}^G and $\varepsilon_{\phi_i}^G$ comprises code and phase measurement combined noise and multipath, respectively."
- Pg. 8 of article (Section 3.2 first paragraph second last sentence): "studythe agreement between GDAS meteorological values". There should be a space between "study" and "the"
- Pg. 21 of article (Section 6 second paragraph first sentence): "The BoM NWM data was used to constraint the tropospheric". The word "constraint" should be replaced by "constrain".

- Pg. 22 of article (references). The following reference should be added to the reference list:
    - Dow JM, Neilan RE and Rizos C (2009) The International GNSS Service in a changing landscape of Global Navigation Satellite Systems. Journal of Geodesy 83(3–4):191–198, DOW:10.1007/s00190-008-0300-3

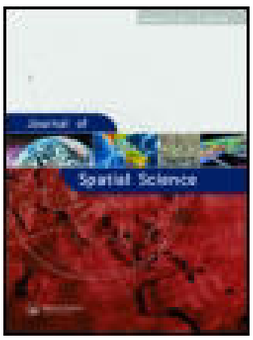

Journal of Spatial Science

ISSN: 1449-8596 (Print) 1836-5655 (Online) Journal homepage: http://www.tandfonline.com/loi/tjss20

Comparison of advanced troposphere models for aiding reduction of PPP convergence time in Australia

M. Deo & A. El-Mowafy

To cite this article: M. Deo & A. El-Mowafy (2018): Comparison of advanced troposphere models for aiding reduction of PPP convergence time in Australia, Journal of Spatial Science, DOI: 10.1080/14498596.2018.1472046

To link to this article: https://doi.org/10.1080/14498596.2018.1472046

Published online: 24 May 2018.

JOURNAL OF SPATIAL SCIENCE, 2018
https://doi.org/10.1080/14498596.2018.1472046

Taylor & Francis
Taylor & Francis Group

Comparison of advanced troposphere models for aiding reduction of PPP convergence time in Australia

M. Deo and A. El-Mowafy

Department of Spatial Sciences, Curtin University, Perth, Australia

ABSTRACT

This paper first analyses the precision of tropospheric zenith total delay (ZTD) values obtained from the empirical models GPT2 and GPT2w, and the numerical weather models (NWM) from Australian Bureau of Meteorology (BoM), and European Centre for Medium-Range Weather Forecasts (ECMWF). Comparison of these ZTD values with IGS ZTD product at four sites showed that the ZTDs from NWM datasets were more precise than the empirical models. The ZTD from BoM data gave the best results, with mean errors between -0.034 m to 0.029 m and standard deviations better than 0.045 m. Next, the PPP convergence time and achievable accuracy using the BoM NWM constrained ZTD by including them as pseudo-observations with a pre-set precision was compared to the case of estimating the troposphere. This resulted in a slight enhancement in convergence time, and improvements in vertical positioning accuracy was found at all the four tested sites at 0.036–0.058 m after 2 min, 0.023–0.038 m after 3 min and 0.013–0.020 m after 5 min of PPP initialisation.

KEYWORDS

Precise point positioning; troposphere constraint; numerical weather models; convergence; GNSS

1. Introduction

The troposphere is that part of the atmosphere between the Earth's surface up to an altitude of approximately 20–60 km (El-Mowafy and Lo 2014). It delays GNSS signals travelling through the same path equally, irrespective of their frequencies, and is thus usually referred to as the neutral atmosphere. The magnitude of total tropospheric delay depends on the signal path through the neutral atmosphere. It is typically lowest in the zenith direction and increases as the satellite elevation angle is reduced. It consists of a hydrostatic or dry component, which can be modelled accurately to an accuracy of 98% with an empirical model such as the Saastamoinen (Saastamoinen 1973) model, and a wet component which is more difficult to model precisely due to the temporal changes in water vapour pressure along the troposphere layer. The standard PPP model considers the troposphere to be isometric and estimates either the zenith total delay (ZTD), or computes the zenith hydrostatic delay (ZHD) with an empirical model and estimates the zenith wet delay (ZWD) as a parameter. Mapping functions, such as the Vienna Mapping Function (VMF), are then used to calculate the tropospheric delay at the observed satellite elevation angle, as discussed in Tuka and El-Mowafy

CONTACT M. Deo manoj.deo01@gmail.com

(2013) where several mapping functions were compared. However, the ZWD is highly correlated with the height parameter (Kjørsvik *et al*. 2006) and it requires a significant change in satellite geometry and longer observation time to reliably separate the correlation between these parameters. The commonly used random walk or first-order Gauss-Markov autocorrelation models often underestimate the temporal correlations in the ZWD, thus more complex dynamic models are required to depict the water vapour variability (El-Mowafy and Lo 2014). Ultimately, the troposphere is a nuisance parameter in PPP and if it is known apriori from an external model with inherent accuracy, appropriate constraints may be applied to improve the PPP model. This may result in a reduction in convergence time or improve the achieved accuracy, which is a key problem in PPP.

Several researchers have considered constraining the troposphere error by using empirical models or external data. Kjørsvik *et al*. (2006) compared PPP performance for the UNB3 empirical tropospheric model developed by Collins *et al*. (1996) with the traditional model that estimated the tropospheric error as a parameter. The nominal accuracy of the apriori ZWD model from UNB3 model was 0.035 m and when depending on this only, the study showed that horizontal accuracy of sub-0.2 m can be achieved. The vertical accuracy was much worse, which did not improve with longer observation periods. Shi *et al*. (2014) computed the precise tropospheric corrections generated from a local area network of GNSS receivers, which are next transmitted to users as a second-order polynomial function to improve PPP performance. Thus, users get improved PPP accuracy and convergence time when located within the GNSS network coverage area that is used to determine tropospheric corrections. The Trimble RTX service with tropospheric correction models the ZTD from a network of GNSS stations and reported providing sub-0.05 m level horizontal PPP accuracy within a few minutes (Talbot *et al*. 2015). Laurichesse and Privat (2015) used well-determined troposphere and ionosphere information from regional augmentation to reduce PPP convergence time to within minutes.

Zhang *et al*. (2016) compared three tropospheric models – IGGtrop, EGNOS and UNB3 m for PPP within China. The IGGtrop, which had an RMS error of 0.044 m compared to precise IGS final ZTD products, gave the best positioning accuracy in the vertical component with a mean positioning error of 0.15 m. The EGNOS and UNB3 m models gave slightly worse mean vertical errors of 0.21 m and 0.19 m, respectively. However, the IGGtropo, a 3-dimensional grid-based model, has been developed to provide tropospheric delay for the users of Chinese Beidou Navigation Satellite System and the area augmentation system based on BDS in China (Zhang *et al*. 2016). It uses a 3D grid to calculate ZTD to obtain more homogenous performances for different areas of China, hence giving superior performance in the BDS coverage area. It may also be applied on a global scale with a mean bias of −0.8 cm and RMS of 4.0 cm, which is comparable to the EGNOS and UNB3 m models (Li *et al*. 2012). Other empirical troposphere models that may be used in PPP include European Space Agency GAL-TROPO (Martellucci 2012), TropGrid (Krueger *et al*. 2004) and its update TopGrid2 (Schüler 2014). Zheng *et al*. (2017) developed a new troposphere correction model based on GPT2w to reduce PPP convergence time. The RMS of the ZTD with this model was 1.2 cm, compared to 3.6 cm for GPT2w. The improvement was due to a modified parameter of the ZWD exponential delay with respect to height. When the new model was applied to PPP, the convergence time reduced significantly by 20–50% for Beidou only PPP, due to the significant improvement in geometry for this constellation. Zhou *et al*. (2017) developed two site-specific troposphere models based on the Saastamoinen and Callaham models

using radiosonde data from 2005 to 2012. The Saastamoinen-based model had the best performance with a mean bias of 0.19 cm and RMS of 3.19 cm. The study also showed that troposphere models based on actual data perform better when recent meteorological data is used to build the model. This implies that tropospheric models require regular updates to remain valid. Lu *et al*. (2017) used multi-constellation GNSS data from the IGS Multi-GNSS Experiment (MGEX) network of 30 global stations to retrieve a real-time troposphere model using the PPP technique. The ZTD estimates from the GFZC2 IGS real-time service gave the best accuracy of 5.06 mm. With multi-constellation GNSS data, the accuracy of the real-time ZTD improved further by up to 22.2%, compared to the GPS only case. Vaclavovic *et al*. (2017) developed an augmented troposphere model for real-time kinematic PPP, using Numerical Weather Model (NWM) data which reflected the actual state of the atmosphere. When the ZTD was estimated as a parameter, the study found considerable correlation between the rover height and the ZTD, as also reported in Kjørsvik *et al*. (2006). When using the external tropospheric model, the PPP solution improved by shortened convergence time, better robustness in the case of degraded satellite geometry, and less parameters with lower correlation. The height accuracy of the PPP solution in kinematic model was 9–12 cm when using external troposphere model. Lu *et al*. (2016) developed a NWM constrained PPP model to improve the performance of multi-constellation GNSS PPP. The troposphere delay parameter from the European Centre for Medium-Range Weather Forecasts (ECMWF) was used in a four constellation (GPS, GLONASS, Beidou and Galileo) PPP model. The standard PPP results were compared to the NWM constrained results. In standard PPP, the tropospheric ZHD delay was corrected using GPT2, whereas ZWD was estimated as an unknown parameter along with receiver position, receiver clock, two horizontal tropospheric gradients (north-south and east-west components), ionosphere delays, code biases and carrier phase ambiguities. In the NWM constrained PPP, the ZWD from ECMWF was used as an *a priori* value, but a residual wet delay parameter was estimated to account for the imperfections in the ZWD derived from the NWM. Thus, the ZWD and two horizontal tropospheric gradients in the standard PPP model were replaced by a single residual wet delay parameter, hence reducing the number of unknown parameters by two. The improvements in convergence time in the NWM constrained PPP model was 20, 32 and 25% in the north, east and vertical components, whereas positioning accuracy improved by 2.5, 12.1 and 18.7% in the same components.

In this contribution, we study the feasibility of applying tropospheric models from four different sources to constrain the tropospheric ZTD parameter. These are the empirical models GPT2 and its revision GPT2w, the NWM from ECMWF gridded data product, and for the first time the Australian Bureau of Meteorology (BoM) GRIB version 2 data. The use of atmospheric profiles from radio occultation data from COSMIC/FORMOSAT-3 satellites was also considered, but this was not found to be feasible at present due to the limited number of satellites. This analysis was conducted for a period of one year. We next compare the performance of using the BoM model to constraint the troposphere error, which gave the best precision out of the four tested models, in terms of PPP convergence time and achievable accuracy, to the traditional case where the troposphere is estimated as an unknown parameter. We apply appropriate weighting to the troposphere correction model as determined from the long-term analysis to the constraint equations. While other researchers (e.g. Kjørsvik *et al*. 2006) have attempted constraining the troposphere with a dual-frequency model in PPP, our study focuses on use of triple frequency data from multi-constellation GNSS. The availability of triple frequency civil signals is a feature of the major GNSS constellations such

as GPS, Galileo, and Beidou. Therefore, we study the attainment of sub-decimetre PPP accuracy with multi-constellation and multi-frequency GNSS data with advanced NWM data from BoM to constrain the troposphere.

The next section briefly describes each of the tropospheric models that were studied, their data sources, and application. Next, we evaluate their accuracy by comparing them to the IGS final ZTD values at selected Australian sites over a one-year period. Finally, we analyse the impact of applying the BoM NWM constrained troposphere on PPP convergence time and accuracy.

2. PPP functional model

This section presents the PPP functional model for estimating the ZTD as a parameter, followed by constraining it by using external information. In this study, the triple frequency PPP model with code-only and phase-only triple-frequency ionosphere free code and phase combinations was used with simulated multi-constellation GNSS data from GPS, Beidou and Galileo constellations. The phase- and code-only ionosphere free, geometry preserving and least noise propagation linear combination was used in the PPP model, which leads to improved convergence performance (Deo and El-Mowafy 2016). This combination is expressed as:

$$P(IF) = \alpha_1 P1 + \alpha_2 P2 + \alpha_3 P3 \tag{1}$$

$$\phi(IF) = \alpha_1 \phi 1 + \alpha_2 \phi 2 + \alpha_3 \phi 3 \tag{2}$$

where $P(IF)$, $\phi(IF)$ are the triple frequency code and phase linear combinations, $P1$, P2, P3 and $\phi 1, \phi 2, \phi 3$ are the code and phase measurements on individual frequencies (e.g. L1, L2 and L5 for GPS) and $\alpha_1, \alpha_2, \alpha_3$ are the linear combinations coefficients.

2.1. Estimating the troposphere as a parameter

The equations for the functional models for GPS, Beidou and Galileo are given below, after application of satellite clock correction and differential hardware biases. In this model, the ZHD is computed with an empirical model and the ZWD is estimated as a parameter in the vertical component which is projected along the receiver-to-satellite line of sight using a wet mapping function (m_w).

For example, using the GPS co$\varepsilon^G_{\phi_i}$constellation, denoted as G we have:

$$P(IF)^G = \alpha_{1,G}\, P^G_{L1} + \alpha_{2,G}\, P^G_{L2} + \alpha_{3,G}\, P^G_{L5} = \rho^G + cdt_{\mathrm{G}} + m^G_w\, ZWD + \varepsilon^{\mathrm{G}}_{\mathrm{P}} \tag{3}$$

$$\phi(IF)^G = \alpha_{1,G}\, \phi^G_{L1} + \alpha_{2,G}\, \phi^G_{L2} + \alpha_{3,G}\, \phi^G_{L5} = \rho^G + cdt_{\mathrm{G}} + \lambda_G N^{*_G} + m^G_w\, ZWD + \varepsilon^{\mathrm{G}}_{\phi} \tag{4}$$

where G is a GPS satellite,$cdt_{\mathrm{G}}\alpha_{1,G} = 2.326944\, \rho^G$ is the satellite-to-receiver geometric range, is the speed of light in vacuum; is the receiver clock offset; N^{*_G} is the non-integer phase ambiguity; $\varepsilon^{\mathrm{G}}_{Pi}$ and comprises code and phase measurement combined noise and multipath,

respectively. The best coefficient values estimated for the above combination are :$\alpha_{2,G} = -0.359646$, and $\alpha_{3,G} = -0.967299$ (Li *et al*. 2014, Deo and El-Mowafy 2016).

For the Beidou constellation (denoted as *C*) the observation equations are:

$$P^C = \alpha_{1,C}\, P^C_{B1} + \alpha_{2,C}\, P^C_{B2} + \alpha_{3,C}\, P^C_{B3} = \rho^C + cdt_G + ISB_{G-C} + m^C_w\, ZWD + \varepsilon^C_{P_j} \tag{5}$$

$$\phi^C = \alpha_{1,C}\, \phi^C_{B1} + \alpha_{2,C}\, \phi^C_{B2} + \alpha_{3,C}\, \phi^C_{B3} = \rho^C + cdt_G + ISB_{G-C} + \lambda_C N^{*C} + m^C_w\, ZWD + \varepsilon^C_{\phi} \tag{6}$$

The terms are similar to the ones described for system *G* above, with the addition of $ISTB_{G\text{-}C'}$ which is the inter-system time bias between GPS and Beidou, combined for the receiver and the satellite. For Beidou, the coefficient values are found to be: $\alpha_{1,C} = 2.566439$, $\alpha_{2,C} = -1.228930$, and $\alpha_{3,C} = -0.337510$.

Similar ionosphere-free equations are derived for the Galileo constellation (denoted as *E*) such that :

$$P^E = \alpha_{1,E}\, P^E_{E1} + \alpha_{2,E}\, P^E_{E5a} + \alpha_{3,E}\, P^E_{E5b} = \rho^E + cdt_G + ISB_{G-E} + m^E_w\, ZWD + \varepsilon^E_P \tag{7}$$

$$\phi^E = \alpha_{1,E}\, \phi^E_{E1} + \alpha_{2,E}\, \phi^E_{E5a} + \alpha_{3,E}\, \phi^E_{E5b} = \rho^E + cdt_G + ISB_{G-C} + \lambda_E N^{*E} + m^E_w\, ZWD + \varepsilon^E_{\phi} \tag{8}$$

with coefficients $\alpha_{1,E} = 2.314925$, $\alpha_{2,E} = -0.836269$, and $\alpha_{3,E} = -0.478656$.

If we consider the case of a GNSS receiver tracking 1 to *n* GPS satellites, 1 to *m* Beidou satellites, and 1 to *k* Galileo satellites at an instant of time, the unknown parameters for a float PPP approach would be:

$$x = \left[\; x \quad y \quad z \quad cdt_G \quad ISB_{G-C} \quad ISB_{G-E} \quad m^{sys}_w \quad \lambda_{sys} N^*(G1, \ldots, Gn; C1, \ldots, Cm; E1, \ldots, Ek) \;\right] \tag{9}$$

where *x*, *y*, *z* denotes the unknown receiver position. The functional and stochastic models of the above combinations are discussed in (Deo and El-Mowafy 2016).

2.2. A modified PPP model constraining the troposphere

In this section, constraining of the ZTD obtained from external sources as additional 'quasi' observations in the PPP model is discussed. These ZTD values are estimated with associated uncertainties, for instance standard deviations. At the receiver, instead of treating the modelled ZTD as known values in the observation equations, they are added as 'quasi' observations with their uncertainty (precision). Thus, the observation vector of the code and phase observations and their covariance matrices (denoted as Q_p and Q_φ) are augmented to include an additional 'quasi' observation $\tilde{T}$ to constraint the vertical troposphere, which is computed from the troposphere models. The observation equation of this quasi-observation is expressed as:

$$\tilde{T} = T + \varepsilon_{\tilde{T}} \tag{10}$$

$\varepsilon_{\tilde{T}}$ is the noise in $\tilde{T}$. Using GPS as an example, the linearised fault-free measurement model using all satellites in view is given as:

$$y = H\,x + \varepsilon \tag{11}$$

where y and x are the vectors of observations and unknowns, respectively, H is the design matrix and ε denotes the noise. Combining the observation Equations (3), (4) and (11), the final system of observation equations for n GPS satellites as an example is expressed as:

$$\underbrace{\begin{pmatrix} P(IF)^G \\ \phi(IF)^G \\ \tilde{T} \end{pmatrix}}_{y} = \underbrace{\begin{pmatrix} G & u & m_w^G & 0 \\ G & u & m_w^G & \lambda_G \times \mathrm{I} \\ 0 & 0 & 1 & 0 \end{pmatrix}}_{H} \underbrace{\begin{pmatrix} X_u \\ c\,\bar{dt}(IF)_G \\ T \\ N^{*_G}(IF) \end{pmatrix}}_{x} + \varepsilon \quad \text{for } s = 1 \text{ to } n \tag{12}$$

The design matrix H is full rank, where G is the geometry (direction-cosine) matrix computed from precise ephemeris with dimension $n \times 3$, I is the identity matrix of dimension n, u is a unit vector of ones and m_w^G is a column vector representing the line-of-sight troposphere mapping function. The observation covariance matrix is expressed as $(Q_{P(IF)^G}, Q_{\phi(IF)^G}, Q_{\tilde{T}})$, for s =1 to n. The sub-covariance matrices $Q_{P(IF)^G}$ and $Q_{\phi(IF)^G}$ are typically assumed diagonal for the observed satellites, with a priori values as shown in El-Mowafy (2015) weighted using an arbitrary satellite elevation-angle-dependent model, and uncorrelated code and phase observations. $Q_{\tilde{T}}$ is uncorrelated with $Q_{P(IF)^G}$ and $Q_{\phi(IF)^G}$, and is assumed diagonal with the standard deviation of the quasi-observation ($Q_{\tilde{T}}$) either assumed or estimated from external source.

3. Troposphere modelling

The tropospheric delay, T, along a GNSS satellite elevation angle, E, is modelled as (Böhm *et al*. 2006a):

$$T(E) = m_h\,ZHD + m_w\,ZWD \tag{13}$$

where ZHD, ZWD are the hydrostatic and wet delay components in zenith direction, and m_h, m_w are the hydrostatic and wet mapping functions, respectively. The zenith hydrostatic delay (ZHD) can be adequately calculated with the empirical models such as the Saastamoinen's formula Saastamoinen (1972), given in Davis *et al*. (1985) as:

$$ZHD = P \times \frac{0.0022768}{1 - 0.00266cos(2\phi) - 0.28 \times 10^{-6}h} \tag{14}$$

where P is the surface atmospheric pressure in hPa, ϕ is the station latitude in radians, and h is the station orthometric or ellipsoid height in metres. The difference due to using either height system is negligible (IERS Conventions *et al*. 2010). The pressure can be computed from an empirical model, a numerical weather model (NWM) or with *in situ* measurements at the observing location.

The zenith wet delay (ZWD) can be approximately calculated if measurements of relative humidity (*RH*) and temperature are available at the observing station, for instance expressed as (Andrei and Chen 2009):

$$ZWD = 0.002277\left(\frac{1255}{t} + 0.05\right)e \tag{15}$$

where t is the temperature in Kelvin and e is the partial water vapour pressure, which can be calculated from the *RH* measurements as

$$e = 6.108\,\frac{RH}{100}\cdot e^{\left(\frac{17.15t\ -\ 4684}{t\ -\ 38.45}\right)} \tag{16}$$

Hence, the surface temperature and either the relative humidity or partial water vapour pressure measurements are required to calculate approximate ZWD. However, an accurate estimation of ZWD would require knowing the water vapour content along the whole length of the troposphere layer, using for instance water vapour radiometers. Since these expensive instruments are not available for normal users, the ZWD parameter is usually estimated as an unknown parameter in the standard PPP model, whereas the ZHD component is modelled with Equation. 14 with a hydrostatic mapping function.

The next sections describe some of the options for modelling the troposphere delay using empirical models and NWMs.

3.1. GPT model and its revisions

The Global Pressure Temperature (GPT) empirical model (Böhm *et al*. 2007) and its revisions GPT2 (Lagler *et al*. 2013) followed by GPT2w (Böhm *et al*. 2015) may be used to determine the required parameters for calculating the troposphere delay. Although GPT enables calculation of the pressure value in Equation. 14, it is inadequate for precise positioning applications where precise heights are required. Kouba (2009) reported height errors in the standard PPP solution of 0.10 m or more when satellites below 10^0 are included and only the ZHD is modelled. GPT2 was introduced as a refinement of GPT, which enables calculation of pressure, temperature, temperature lapse rate, partial water vapour, as well as the hydrostatic and wet coefficients, defined as and a_w, that are required by the Vienna Mapping Function (VMF1) (Böhm *et al*. 2006a). This enables users to apply the more precise VMF1, compared to other functions such as the Global Mapping Function (GMF) (Böhm *et al*. 2006b). Application of VMF1 requires use of the coefficients a_h and for calculating m_h and, respectively, which are subsequently used to calculate and *ZHD* values using Equation. 13.

The GPT2w model is an extension of GPT2, with improved capability to determine the ZWD empirically (Böhm *et al*. 2015). This was validated with the zenith total delay ($ZTD = ZHD + ZWD$) estimates from the IGS precise ZTD products at 341 GNSS sites over 110 days (Böhm *et al*. 2015). The difference between the GPT2w derived ZTD and the IGS determined delays ranged between -0.042 m and +0.073 m, with a mean difference of –0.0002 m and RMS of 0.036 m. The GPT2w requires gridded raw data with regular intervals of either 5^0 or the higher 1^0 resolution, along with the station location, height and date as input parameters. The model interpolates the pressure, temperature, temperature lapse rate, mean temperature of water vapour, water vapour pressure, water vapour lapse rate, geoid undulation and the coefficients for the hydrostatic and wet mapping functions for a given

location and date. The ZHD can be calculated using Equation. 14 whereas the ZWD is expressed as (Askne and Nordius 1987):

$$ZWD = 10^{-6}\left(k_2^{'} + k_3/t_m\right)\frac{R_d}{(\lambda+1)g}e_s \tag{17}$$

where $k_2^{'}$ and k_3 are empirically determined coefficients, R_d denotes the specific gas constant for the dry constituents and g is the gravity constant. The variable e_s is the water vapour pressure at the site, λ is the water vapour lapse rate, t_m is the mean temperature of the water vapour in degrees Kelvin. All these values can be computed from the GPT2w model (Böhm *et al*. 2015). The hydrostatic and wet mapping functions are calculated with VMF1 using the respective coefficients, a_h and a_w, and the total tropospheric delay is finally calculated by using Equation. 13.

3.2. Numerical weather models

To achieve mm accuracy in station height, ZHD must be known to better than 0.01 m accuracy. This requires pressure values with better than 5 hPa accuracy from *in situ* measurements at the station, or NWM data (Kouba 2009). Such accuracy is achievable from the Global Data Assimilation System (GDAS), produced at 1^0 x 1^0 grid in real time by the National Center for Environment Prediction (NCEP) of the US National Oceanic and Atmospheric Administration (NOAA). The ZWD may also be modelled using relative humidity or partial water pressure values from NWMs. Andrei and Chen (2009) used GDAS data for computing both the hydrostatic and wet zenith delay, which agreed to IGS total zenith delay to within 0.05 m. In their studythe agreement between GDAS meteorological values and *in situ* direct measurements at selected IGS stations was 1 mbar in pressure, 3 degrees Celsius for temperature and 13% for relative humidity. Most of the error was attributed to the poor quality of relative humidity and temperate values from GDAS, which resulted in less accurate estimation of ZWD.

Although NWMs can provide 0.05 m level ZTD estimates, their implementation requires additional time and resources by the users to acquire data from external sources. An advantage of this approach is that it can be adopted for real-time PPP, even when there is data outage since the weather models forecast data for several hours into the future. The next sub-sections describe two NWMs that have been used in this study.

3.2.1. ECMWF

The European Centre for Medium-Range Weather Forecasts (ECMWF) produces coefficients for calculation of ZWD and ZHD on a global grid of 2.0^0 interval in north-south and 2.5^0 in east-west. These coefficients are produced every 6 h at 00, 06, 12 and 18 UTC at http://ggosatm.hg.tuwien.ac.at. This website also provides the ZHD and ZWD values in metres, in these grid and time intervals. The ZHD and ZWD values are for ellipsoidal heights h_{DEM}, which is obtained from a digital elevation model (DEM), for instance available from the website http://ggosatm.hg.tuwien.ac.at/DELAY/GRID/orography_ell, with a grid resolution of 2.0^0 for latitude and 2.5^0 for longitude. The interpolation of a_h, a_w, ZHD, ZWD and h_{DEM} at the required station latitude and longitude (ϕ, λ) is performed using a bilinear model.

Provided that the difference between $h_{DEM}$and the station height h is within 1 km, the ZHD at the station, ZHD_h, can be extrapolated using the formula (Steigenberger *et al*. 2009):

$$ZHD_h = ZHD_{h_{DEM}} - 2.77 \times 10^{-3} \frac{g \cdot P(h_{DEM})}{R \cdot t(h_{DEM})} \left(h - h_{DEM}\right) \tag{18}$$

where $R = 8.3144621\ J \cdot K^{-1} \cdot mol^{-1}$ is the molar gas constant and the height difference is in km units. The pressure $P(h_{DEM})$ and temperature $t(h_{DEM})$ at the station with the h_{DEM} estimated at its location may be computed with the use of GPT2w model.

3.2.2. Australian bureau of meteorology access data

The Australian Community Climate and Earth-System Simulator (ACCESS) data are available from the Australian Bureau of Meteorology (BoM) as gridded binary (GRIB) edition 2 as well as Network Common Data Form-4 (NetCDF-4) formats. Further details of the different types of products and their accessibility are available at http://reg.bom.gov.au/nwp/doc/access/NWPData.shtml. The ACCESS-Regional (R) data contains meteorological data on three-dimensional grids in the greater Australian region, at a resolution of 12 km. There are various versions of the data files, containing different combinations of parameters which may be deduced from the filenames.

In this study, the ACCESS-R single-level surface data were used. This product is released every six hours at UTC base hours 00, 06, 12 and 18, and for each base time, there are three files issued with forecast validity times of 3, 6 and 9 h. These data were converted to netCDF-4 using the wgrib2 software (www.cpc.ncep.noaa.gov/products/wesley/wgrib2/) and decoded using an in-house software. The key useful fields in this file include the surface temperature in Kelvin, surface pressure in Pa and the relative humidity at 1.5 m above ground. Hence, the ZWD can be calculated using Equations. 15 and 16, and ZHD with Equation. 14, once the relative humidity, temperature and pressure values are interpolated at a given station location and time.

3.3. Radio occultation from COSMIC satellites

The Constellation Observing System for Meteorology, Ionosphere and Climate (COSMIC) / Formosa Satellite 3 (FORMOSAT-3) constellation of six satellites were launched into a low-Earth orbit (LEO) in April 2006. Since then, its data has been successfully used in a wide range of scientific applications such as weather forecasting, ionosphere and the Earth's gravity studies (Yue *et al*. 2010). The COSMIC/ FORMOSAT-3 Radio Occultation (RO) data are available to users from the COSMIC Data Analysis and Archive Centre (CDAAC) at the University Corporation for Atmospheric Research (UCAR) website http://cdaac-www.cosmic.ucar.edu/cdaac/products.html for authorised users. The RO processed data come in three types, namely (1) COSMIC2013: consisting of reprocessed data using enhanced processing strategies resulting in higher RO counts, (2) COSMIC post-processed data with a typical latency of six weeks and (3) COSMICRT containing real-time data with a latency of a few hours. These data sets are available in the netCDF-4 format.

The COSMIC2013 reprocessed data was considered in this study. Of the several versions of the available atmospheric profiles, the wetPrf product was used, which contains the profiles of temperature, water vapour pressure and refractivity at 0.1 km intervals up to an altitude of 40 km. These data are not regularly gridded in latitude and longitude, but is rather limited to where the RO point occurred in relation to the COSMIC and GPS satellite

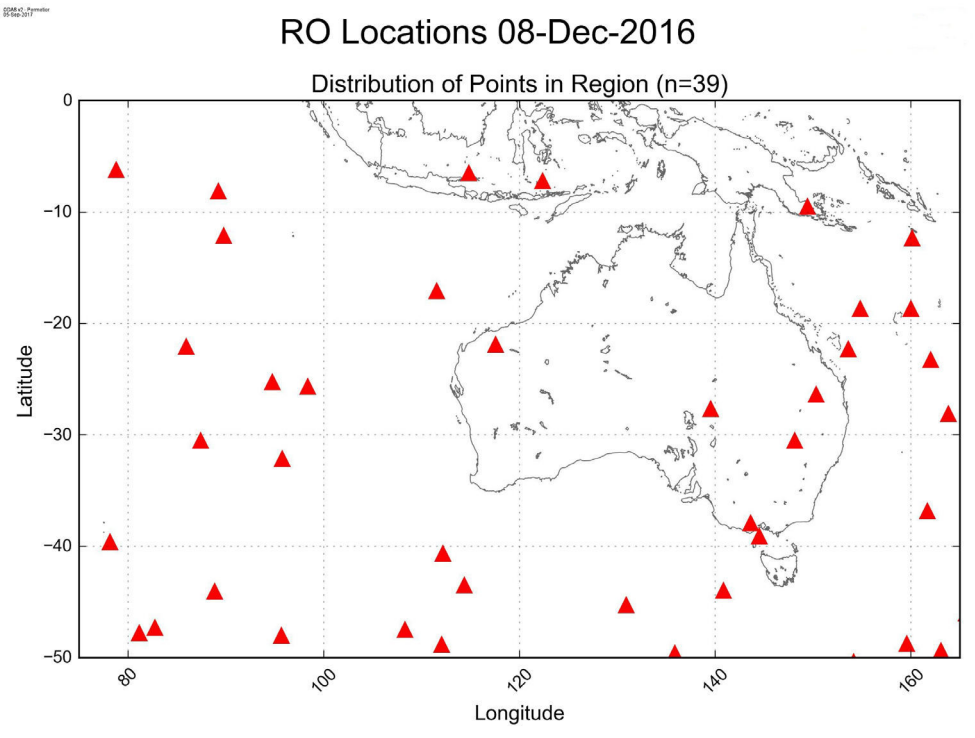

Figure 1. Radio Occultation locations for 39 RO points in the Australian region from COSMIC data on 8 December 2016.

line-of-sight. Once the water vapour pressure and temperature are interpolated at a given location and time, the ZWD may be calculated using Equation 15. One issue with the COSMIC RO data is that there is not enough spatial and temporal resolution to accurately interpolate the atmospheric variables at any given location and time, which makes the interpolation infeasible at some locations (Yue *et al*. 2010). Figure 1 shows the RO locations in the Australian region for one day of the COSMIC data on 8 December 2016, and Figure 2 shows the Pressure, water vapour pressure and temperature profiles for the 634 globally located RO points on the same day. As shown, only 39 RO points were observed in the Australian region during that day and there were less than ten points within the landmass. Thus this data could not be used in this study. However, this situation is likely to improve in the future as more COSMIC satellites are launched.

4. Analysis of ZTD models

In this section, we analyse the performance of each of the presented troposphere models by comparing the estimated ZTD from employing these models with the values obtained from the precise IGS ZTD product at selected stations in Australia. The stations analysed are distributed over the Australian continent and include Hobart (HOB2), Alice Springs (ALIC), Yarragadee (YAR2) and Townsville (TOW2). Table 1 shows the ITRF2008 geodetic coordinates (latitude, longitude and ellipsoid height) for these stations, extracted from the Asia Pacific Reference Frame (APREF) solution produced by Geoscience Australia for GPS week 1877.

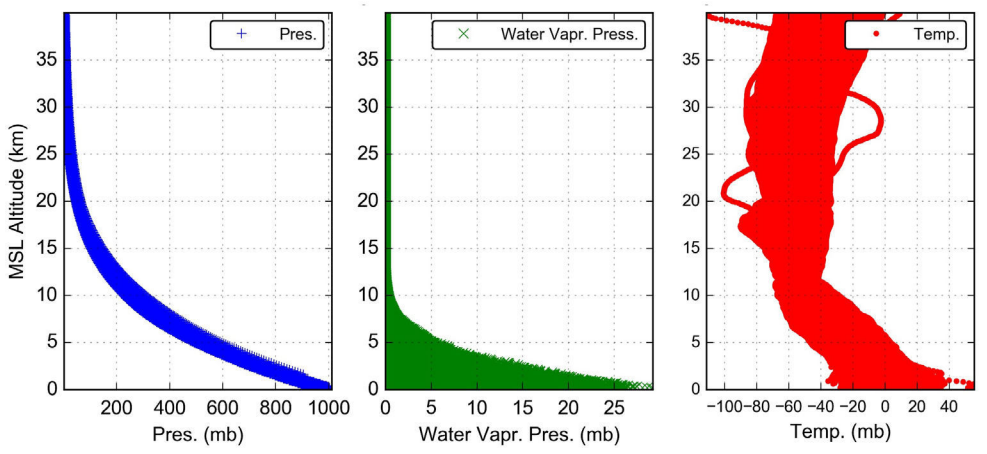

Figure 2. Pressure, water vapour pressure and temperature profiles for the 634 globally located RO data points from COSMIC data on 8 December 2016.

Table 1. ITRF08 Geographical coordinates of the test points from APREF solution for week 1877 and Orthometric height from the Australian national geodetic database.

Site	Latitude (degrees)	Longitude (degrees)	Ellipsoidal Height (h) (m)	Orthometric Height (H)	Difference *h*–*H* (m)
ALIC	S 23.670	E 133.886	603.245	587.643	15.602
HOB2	S 42.805	E 147.439	41.044	44.756	–3.712
TOW2	S 19.269	E 147.056	88.109	29.474	58.635
YAR2	S 29.047	E 115.347	241.289	266.528	25.239

The Orthometric heights are also given, which were obtained from the Australian national geodetic database (www.ga.gov.au/ngrs). Since these stations are IGS reference stations, they have precise ZTD estimates available as an IGS product. These were used as reference values for comparison with results from the tested models. The analysis pertains to the full year from 1 January to 31 December 2016. The GRIB2 data was only available for approximately seven months of this period, due to connection issues that result in data outages.

Figures 3-6 show the time series of the ZHD and ZWD values from the GPT2 and GPT2w empirical models, and the ECMWF and BoM NWM data at ALIC, HOB2, TOW2 and YAR2 respectively. As shown in the figures, the ZHD values from GPT2 and GPT2w have millimetre level agreement with each other at all four sites. However, the discrepancy between these and the ECMWF model was at the 0.02–0.04 m level at YAR2 and up to 0.10 m at TOW2. Note that the ECMWF ZHD values are based on ellipsoidal heights on a low resolution DEM. Thus this observed discrepancy may be attributed to the low resolution of DEM and the accuracy of geoid-ellipsoid undulation model at this location. The ZHD from BoM data is in agreement with the GPT2/ GPT2w models at the 0.01–0.02 m level. The IGS ZWD in these figures is calculated by subtracting the ZHD determined from GPT2w from the IGS ZTD. Overall, the mean and standard deviations (std) of the difference between the modelled ZWD and the IGS ZWD were mean = 0.031 m, std = 0.065 m, for BoM; mean = -0.061 m, std = 0.076 m for ECMWF; mean = -0.048 m, std = 0.115 m for GPT2; mean = -0.039 m, std = 0.105 m for GPT2w. Thus, the BoM derived ZWD was the most accurate and precise at these four tested sites.

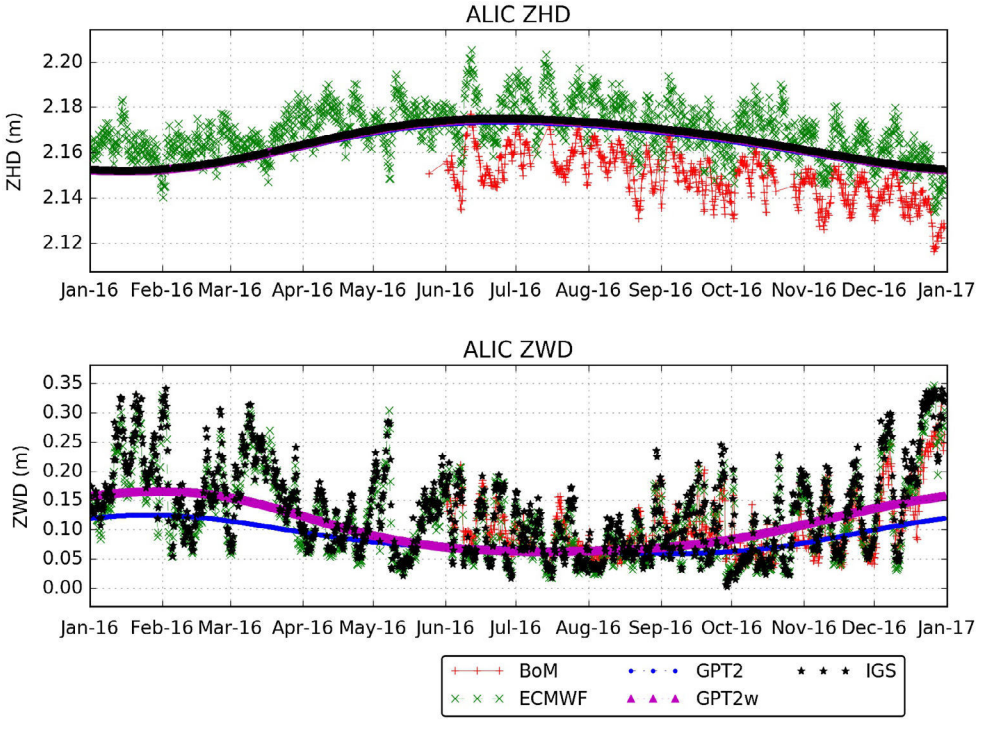

Figure 3. Time series of the ZHD and ZWD from the GPT2 and GPT2w empirical models, and ECMWF and BoM numerical weather model data for one year at ALIC site.

From Figures 3 to 6, it is apparent that there are seasonal patterns for the troposphere accuracy for the different models at the four selected sites. We extracted monthly mean relative humidity and rainfall data from the BoM website (http://www.bom.gov.au/climate/data/) to gain more insight into these patterns. The data was extracted from weather stations located at local airports close to the GNSS stations, where Miorawa Airport was the closest to YAR2, Alice Springs Airport was the closest to ALIC, Townsville Aero was closest to TOW2 and Hobart Airport was closest to HOB2. As shown in Figure 7, the rainfall and relative humidity profiles differ considerably at these four sites because of their geographic locations and unique weather patterns. It is known from a previous study by Zhou *et al*. (2017) that the accuracy of NWM decreases in some areas due complex weather changes.

For TOW2, the offset in ZTD determined from BoM and IGS is more visible in the ZWD component. The ZWD at this site is comparatively noisier with a range of 0.4 m, which indicates greater variability in the atmospheric moisture profiles. This may be because TOW2 is in a tropical zone close to the coast, where there is increased relative humidity throughout the year, as shown in Figure 7. At ALIC, the ZWD from BoM NWM is in good agreement with the IGS ZWD, but the overall standard deviation for ZTD is relatively higher at 0.043 m. The ZWD profile at ALIC shows more variation during the Northern Territory wet season, which spans from November until April, and is characterised by increased rain and storms. The impact of the wet season during this period is visible in Figure 3. Despite the higher rain during this period, the relative humidity is low due to the increased temperatures in the

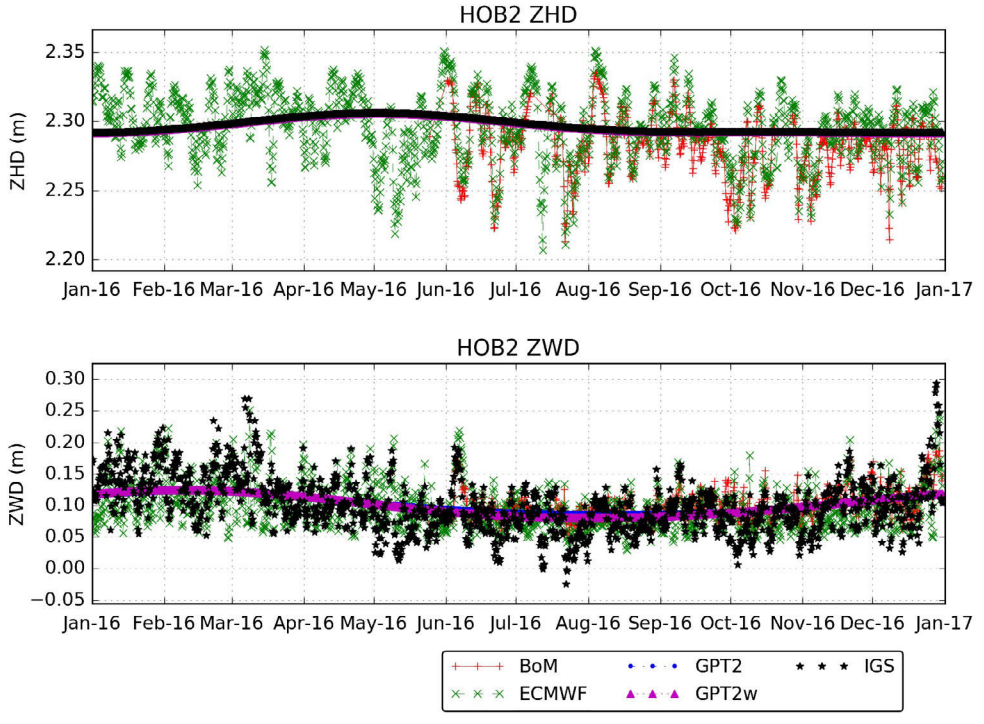

Figure 4. Time series of the ZHD and ZWD from the GPT2 and GPT2w empirical models, and ECMWF and BoM numerical weather model data for one year at HOB2 site.

warmer summer months. At HOB2, Figure 4 shows close agreement between the BoM NWM and IGS in the ZHD as well as ZWD components. This site has comparatively lesser variation in the ZWD profile, which may be due to the comparatively lesser variation in rainfall and relative humidity throughout the year. The YAR2 site also has lesser variation in the ZWD for most part of the year, except for Mar to May as shown in Figure 7. This site has higher rainfall from May to September, which correlates with the increased relative humidity. The increased ZWD variability may be due to the complex change from dry to wet season between Mar to May.

The ZTD from these models were compared to the IGS ZTD product available for these stations. Figures 8–11 show histograms of the difference between the ZTD obtained from IGS and those calculated as the sum of ZHD and ZWD from the GPT2 and GPT2w empirical models, and ECMWF and BoM NWM data. As shown, the agreement of ZTD between IGS and NWMs is better than the empirical models and 95% of the differences are within the range ± 0.2 m, with the majority within ± 0.1 m. The mean and standard deviations (std) of these differences are also summarised in Table 2 for the four sites. As shown, the precisions of the ZTD from NWM datasets, represented by the standard deviations, are consistently better than the GPT2 and GPT2w empirical models at the four sites. The GPT2w model gave more accurate ZTD values compared to GPT2, with a slight improvement in precision at the mm level. The ZTD from ECMWF model gave precise results at ALIC (mean = 0.007 m, std = 0.018 m) and HOB2 (mean = 0.006 m, std = 0.026 m), both of which have low discrepancy between ellipsoid and orthometric height. However, results were poor at TOW2 and YAR2

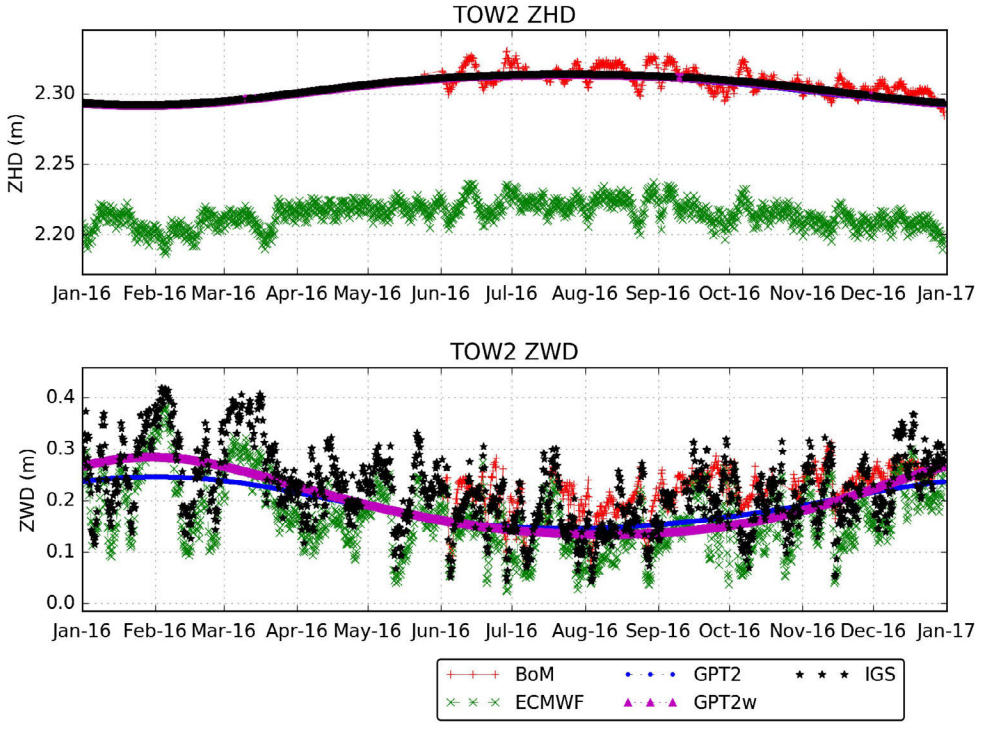

Figure 5. Time series of the ZHD and ZWD from the GPT2 and GPT2w empirical models, and ECMWF and BoM numerical weather model for one year data at TOW2 site.

due to the low resolution of DEM used in the ECMWF model, as discussed earlier. The ZTD from BoM data gave consistent results at all four sites with mean errors between -0.034 m and 0.029 m and standard deviations better than 0.045 m. Overall, use of BoM NWM data gave more precise and accurate ZTD values than any other of the tested models. The next section analyses the PPP performance when constraining the ZTD with the BoM NWM, the proven best model.

5. PPP performance analysis with the BOM NWM tropospheric model

This section analyses the performance of PPP in terms of the convergence time taken to achieve sub-decimetre positioning errors, and the accuracy after convergence is achieved. The PPP model with and without the ZTD aiding was implemented using Kalman filter; i.e. processing the data by constraining the ZTD from BoM NWM model and the stds given in the last column of Table 2, and next processing the same data in the conventional method by estimating ZTD as one of the parameters. In both cases, a satellite elevation cut-off angle of 10^0 was used. The triple frequency low noise and ionosphere-free linear combinations for carrier phase and code measurements were used when constraining the ZTD using the BoM NWM, and in the conventional case of estimating it as a parameter. In the conventional method, the ZHD was modelled with Equation. 14 with the Neill's hydrostatic mapping function (Neill 1996), whereas the ZWD was determined as an unknown parameter.

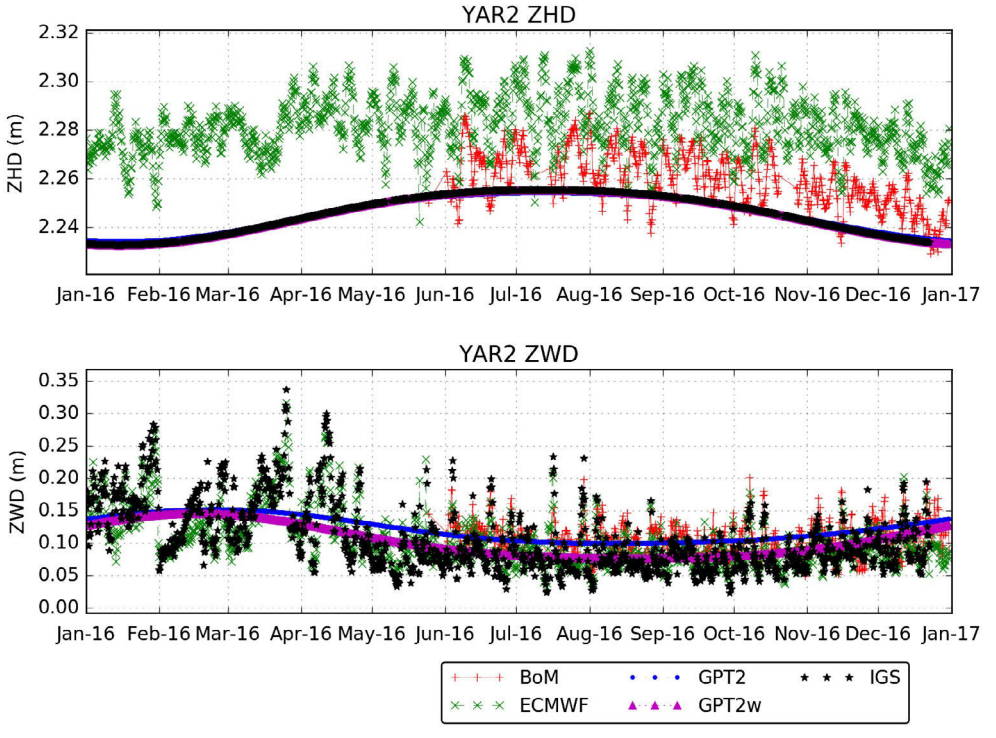

Figure 6. Time series of the ZHD and ZWD from the GPT2 and GPT2w empirical models, and ECMWF and BoM numerical weather model data for one year at YAR2 site.

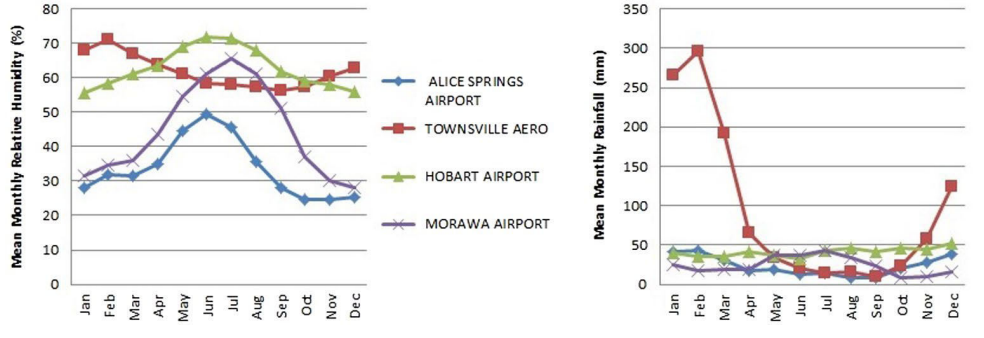

Figure 7. Mean monthly relative humidity (left) and rainfall (right) data at the four selected sites, extracted from the BoM website (http://www.bom.gov.au/climate/data/).

5.1. PPP results

Results are compared in terms of solution convergence time taken to achieve sub-decimetre accuracy in the horizontal dimension (2D), including North (N) and East (E) position components, as well as the vertical dimension. The 2D convergence time is defined as the time when horizontal positional accuracy of 0.10 m is reached and maintained thereafter, indicating stability of the float ambiguity solution. Likewise, the N, E and vertical convergence

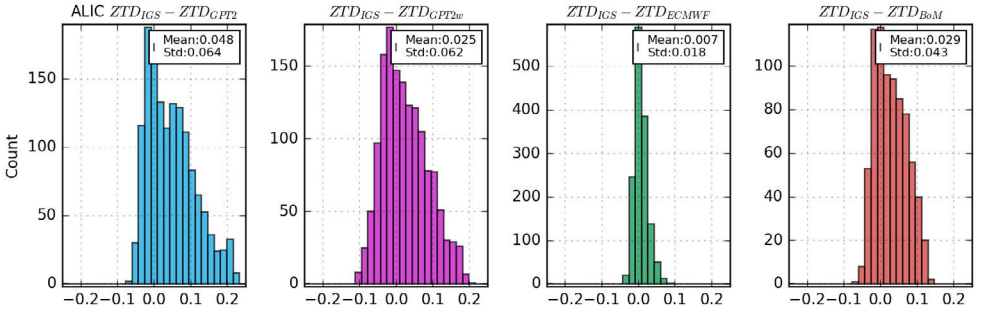

Figure 8. Histograms of the difference between IGS ZTD and model ZTDs from GPT2, GPT2w, ECMWF and BoM, from left to right, at station ALIC.

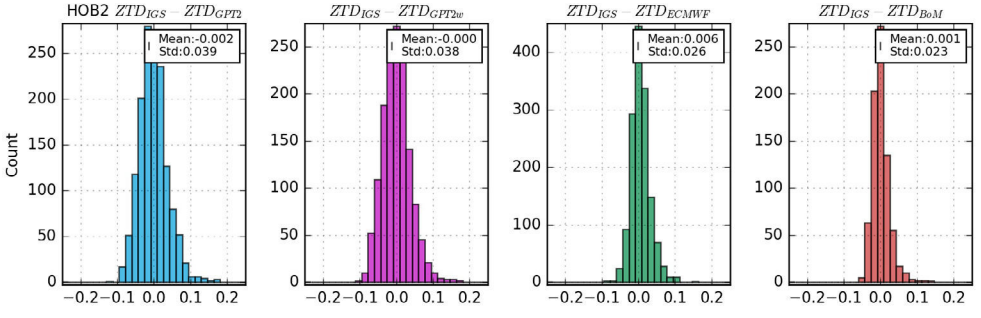

Figure 9. Histograms of the difference between IGS ZTD and model ZTDs from GPT2, GPT2w, ECMWF and BoM, from left to right, at station HOB2.

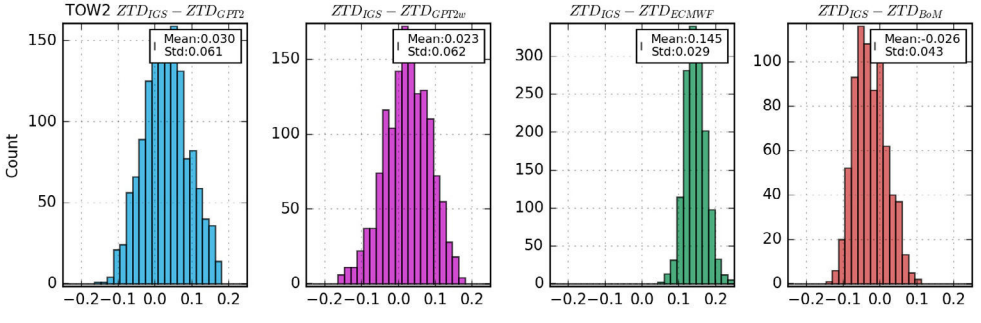

Figure 10. Histograms of the difference between IGS ZTD and model ZTDs from GPT2, GPT2w, ECMWF and BoM, from left to right, at station TOW2.

time defines when sub-decimetre accuracy is achieved in N, E and vertical components, respectively. The accuracy is defined in terms of the root mean squared error (RMSE) of the estimated positions after convergence is achieved with respect to the known station coordinates obtained from the APREF solution. The results from constraining the troposphere with the BoM NWM are compared to the case where the troposphere is estimated as an unknown parameter. Appropriate weighting was applied to the BoM NWM-derived ZTD

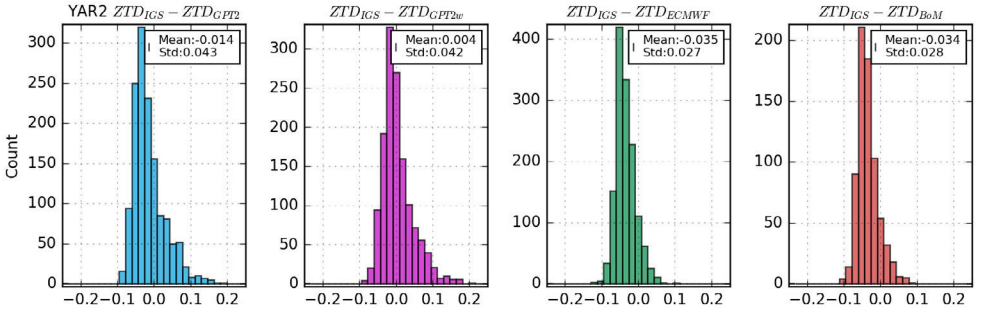

Figure 11. Histograms of the difference between IGS ZTD and model ZTDs from GPT2, GPT2w, ECMWF and BoM, from left to right, at station YAR2.

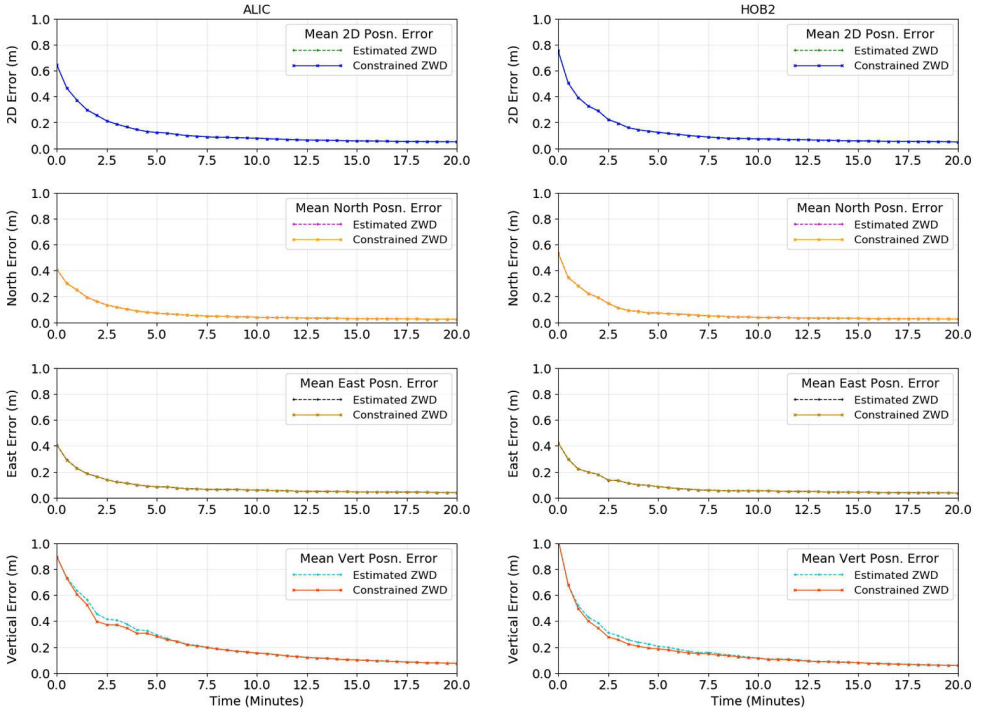

Figure 12. Comparison of PPP positioning errors in 2D and absolute values in North, East and Vertical components for the triple frequency PPP model when estimating the troposphere as a parameter and constraining the troposphere using BoM GRIB2 data at ALIC (left) and HOB2 (right).

values, based on the analysis in the previous section. In addition, we applied a constraint based on the real accuracy of the ZTD determined from the long-term analysis. This constrained PPP model accounts for the imperfections in the ZTD derived from the BoM NWM model, mainly due to limitations in accurately modelling complex weather changes. The study was conducted with simulated multi-constellation triple frequency GNSS data with 32 GPS, 17 Galileo and 14 Beidou satellites at the sites ALIC, HOB2, TOW2 and YAR2, with 30 s epoch interval and 5 day's of data from 3 to 7 June 2016.

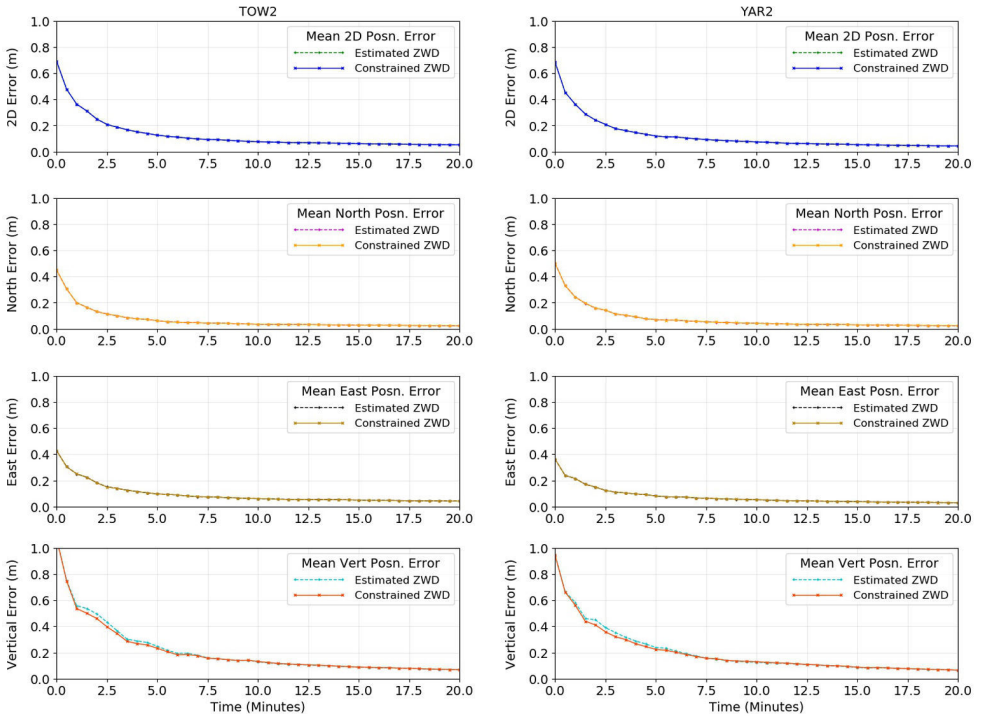

Figure 13. Comparison of PPP positioning errors in 2D and absolute values in North, East and Vertical components for the triple frequency PPP model when estimating the troposphere as a parameter and constraining the troposphere using BoM GRIB2 data at TOW2 (left) and YAR2 (right).

Table 2. Mean and standard deviation (std) of the difference between the IGS ZTD and modelled ZTDs from GPT2, GPT2w, ECMWF and BoM.

	$ZTD_{IGS} - ZTD_{GPT2}$		$ZTD_{IGS} - ZTD_{GPT2w}$		$ZTD_{IGS} - ZTD_{ECMWF}$		$ZTD_{IGS} - ZTD_{Bom}$	
Site	Mean(m)	Std. (m)	Mean(m)	Std. (m)	Mean(m)	Std. (m)	Mean(m)	Std. (m)
ALIC	0.048	0.064	0.025	0.062	0.007	0.018	0.029	0.043
HOB2	−0.002	0.039	0.000	0.038	0.006	0.026	0.001	0.023
TOW2	0.030	0.061	0.023	0.062	0.145	0.029	−0.026	0.043
YAR2	−0.014	0.043	0.004	0.042	−0.035	0.027	−0.034	0.028

For demonstration, the proposed model was firstly assessed for HOB2 assuming a totally known troposphere delay (i.e., troposphere with zero error). Although this is not feasible in practice, it demonstrates the ultimate benefits of modelling out the troposphere if it is accurately known. Estimating the troposphere as an unknown parameter in the PPP model resulted in a convergence time of 6.0 min to reach a 2D accuracy of 0.10 m, and a convergence time of 12.5 min to reach a 2D accuracy of 0.05 m. When the troposphere is exactly known from the IGS ZTD model, the convergence time to reach 2D accuracy of 0.10 m was 5.5 min, and a 2D accuracy of 0.05 m was reached after 11.5 min. A satellite elevation cut-off angle of 10 degrees was used in both cases. Therefore, modest improvements in convergence time of 0.5 and 1 min was achieved to reach 0.1 m and 0.05 m accuracy, respectively. These convergence times may appear over optimistic, noting that simulated data was used, which did

Table 3. Convergence time taken to reach accuracy of 0.1 m and 0.05 m (2D, North, East and Vertical) for the PPP model with troposphere estimation, and when using BoM NWM constrained troposphere.

Site	Troposphere Model	Average number of satellites	Convergence time to reach 0.1 m (min)				Convergence time to reach 0.05 m accuracy (min)			
			2D	N	E	Vert.	2D	N	E	Vert.
ALIC	ZTD Estimated	20	6.5	4.0	4.0	15.5	22.0	7.5	12.0	32.0
	BoM Constrained	20	6.5	4.0	4.0	15.5	22.0	7.5	12.0	32.0
HOB2	ZTD Estimated	18	6.5	3.5	4.0	12.5	20.0	8.0	11.5	24.0
	BoM Constrained	18	6.5	3.5	4.0	12.0	20.0	8.0	11.5	24.0
TOW2	ZTD Estimated	20	7.0	3.0	5.0	13.5	21.5	6.5	15.0	28.0
	BoM Constrained	20	7.0	3.0	5.0	13.5	21.5	6.5	15.0	27.5
YAR2	ZTD Estimated	21	7.0	4.0	4.0	13.5	16.5	8.5	11.0	26.5
	BoM Constrained	21	7.0	4.0	4.0	13.5	16.5	8.5	11.0	26.5

Table 4. RMSE after convergence to 0.1 m and 0.05 m accuracy (2D, North, East and Vertical) for the PPP model with troposphere estimation, and when using BoM NWM constrained troposphere.

Site	Troposphere Model	Mean RMSE after 0.1 m convergence (m)				Mean RMSE after 0.05 m convergence (m)			
		2D	N	E	Vert.	2D	N	E	Vert.
ALIC	ZTD Estimated	0.045	0.024	0.039	0.047	0.037	0.021	0.033	0.034
	BoM Constrained	0.045	0.023	0.038	0.046	0.037	0.020	0.033	0.034
HOB2	ZTD Estimated	0.045	0.025	0.036	0.043	0.038	0.021	0.032	0.035
	BoM Constrained	0.045	0.024	0.036	0.042	0.037	0.020	0.032	0.034
TOW2	ZTD Estimated	0.043	0.021	0.038	0.043	0.034	0.018	0.031	0.031
	BoM Constrained	0.043	0.021	0.038	0.043	0.034	0.018	0.031	0.031
YAR2	ZTD Estimated	0.040	0.024	0.032	0.044	0.034	0.021	0.027	0.034
	BoM Constrained	0.040	0.024	0.032	0.044	0.034	0.020	0.027	0.034

not include multipath. Moreover, the enhanced triple frequency model was implemented, which has significantly better performance than the traditional dual-frequency model (Deo and El-Mowafy 2016).

For the case of using the BoM NWM to constrain the ZTD, Table 3 shows the convergence time required to achieve 0.1 m and 0.05 m accuracy in 2D, N, E and vertical components compared with the case of estimating the troposphere as a parameter. As the table shows, the results practically did not change. There was however a slight improvement by 0.5 min in the BoM constrained model to reach 0.1 m vertical accuracy at HOB2 and at TOW2 to reach 0.05 m accuracy. In terms of the accuracy achieved after convergence, Table 4 compares the RMSE in the 2D, N, E and vertical components after convergence of the PPP solutions to reach 0.1 m and 0.05 m at the four sites. As the table shows, there are slight improvements found at the millimetre level at ALIC, HOB2 and YAR2, whereas the results are unchanged at TOW2.

The mean positioning errors of the hourly PPP solutions for the 5 days were computed after convergence periods of 2, 3, 5, 10 and 20 min after the PPP initialisation times. This was done for the 2D, N, E and vertical components at the four sites. Results are given in Table 5. One of the key findings from this table is that the accuracy of the BoM constrained troposphere model achieved faster convergence in the vertical component for the first few minutes of convergence, compared to the PPP model which estimated the troposphere as a parameter. The BoM constrained troposphere model PPP had better vertical accuracy than the former model by 0.036–0.058 m after 2 min, 0.023–0.038 m after 3 min and 0.013–0.020 m

Table 5. Mean positioning errors in 2D, North, East and Vertical components after PPP initialisation times of 2, 3, 5, 10 and 20 min for the PPP model with tropospheric estimation and the PPP model with BoM NWM constrained troposphere.

Troposphere Model		Estimated parameter					BoM Constrained (diff)				
Time since PPP initialisation		2 min	3 min	5 min	10 min	20 min	2 min	3 min	5 min	10 min	20 min
HOB2 Mean RMSE (m)	2D	0.289	0.194	0.124	0.073	0.049	0.289(0.000)	0.192(-0.002)	0.124(0.000)	0.074(+0.001)	0.049(0.000)
	N	0.193	0.112	0.073	0.038	0.025	0.195(+0.002)	0.112(0.000)	0.072(−0.001)	0.040(+0.002)	0.026(+0.001)
	E	0.179	0.133	0.085	0.052	0.035	0.179(0.000)	0.133(0.000)	0.085(0.000)	0.052(0.000)	0.036(+0.001)
	Vert.	0.386	0.289	0.205	0.115	0.059	0.346(−0.040)	0.255(−0.034)	0.185(−0.020)	0.114(−0.001)	0.058(−0.001)
YAR2 Mean RMSE (m)	2D	0.241	0.175	0.119	0.073	0.043	0.241(0.000)	0.176(+0.001)	0.119(0.000)	0.074(+0.001)	0.043(0.000)
	N	0.158	0.113	0.069	0.042	0.024	0.158(0.000)	0.114(+0.001)	0.070(+0.001)	0.042(0.000)	0.024(0.000)
	E	0.149	0.110	0.081	0.051	0.030	0.149(0.000)	0.110(0.000)	0.081(0.000)	0.052(+0.001)	0.030(0.000)
	Vert.	0.450	0.352	0.239	0.126	0.065	0.411(−0.039)	0.320(−0.032)	0.223(−0.016)	0.130(+0.004)	0.064(−0.001)
ALIC Mean RMSE (m)	2D	0.255	0.187	0.123	0.079	0.050	0.255(0.000)	0.186(−0.001)	0.123(0.000)	0.079(0.000)	0.050(0.000)
	N	0.162	0.118	0.072	0.040	0.025	0.162(0.000)	0.118(0.000)	0.072(0.000)	0.040(0.000)	0.025(0.000)
	E	0.164	0.122	0.084	0.060	0.040	0.164(0.000)	0.121(−0.001)	0.084(0.000)	0.059(−0.001)	0.040(0.000)
	Vert.	0.455	0.408	0.295	0.152	0.075	0.397(−0.058)	0.370(−0.038)	0.282(−0.013)	0.153(+0.001)	0.074(+0.001)
TOW2 Mean RMSE (m)	2D	0.250	0.187	0.126	0.076	0.051	0.249(−0.001)	0.186(−0.001)	0.125(−0.001)	0.075(−0.001)	0.051(0.000)
	N	0.131	0.099	0.062	0.034	0.023	0.131(0.000)	0.099(0.000)	0.061(−0.001)	0.034(0.000)	0.023(0.000)
	E	0.182	0.140	0.097	0.060	0.042	0.182(0.000)	0.139(−0.001)	0.097(0.000)	0.061(−0.001)	0.042(0.000)
	Vert.	0.496	0.368	0.247	0.128	0.067	0.460(−0.036)	0.345(−0.023)	0.232(−0.015)	0.131(+0.003)	0.068(+0.001)

after 5 min of PPP initialisation. After 6-7 min of convergence, both models performed at similar level of accuracy at all the four sites.

6. Conclusions

This paper first compared the tropospheric models obtained from (1) GPT2, (2) GPT2w, (3) ECMWF gridded data, and (4) BoM GRIB2. An inter-comparison of these models with the IGS ZTD product used as a reference showed that the precision of the ZTD from actual NWM datasets (BoM and ECMWF) were consistently better than the empirical models (GPT2 and GPT2w). The GPT2w model was more precise and accurate than its predecessor GPT2. The ZTD from ECMWF model at IGS station ALIC gave a mean error = 0.007 m and std = 0.018 m, and station HOB2 gave mean = 0.006 m and std = 0.026 m. However, results were poor at stations TOW2 and YAR2, which is likely to be due to the low resolution of DEM heights used in this model. The ZTD from BoM NWM data gave the best precision and accuracy at all four sites, with mean errors between -0.034 m to 0.029 m and standard deviations better than 0.045 m.

The BoM NWM data was used to constraint the tropospheric delay in PPP processing at the four sites with 5 days data with hourly PPP solutions. The performance of PPP convergence time and achievable accuracy with the BoM NWM constrained troposphere was compared to the traditional case where the troposphere is estimated as an unknown parameter. Improvements in vertical positioning accuracy was found at all the four sites during the first few minutes of initialisation. The BoM constrained troposphere model PPP had better vertical accuracy by 0.036–0.058 m after 2 min, 0.023–0.038 m after 3 min and 0.013–0.020 m after 5 min of PPP initialisation. This result suggests that constraining the troposphere with the BoM NWM data in PPP has some merit in improving the vertical convergence during the first few minutes of initialisation and is beneficial for applications where fast vertical convergence is required. This could be a cost-effective means of improving the PPP vertical convergence using existing NWM data, rather than the more expensive approach of using precise troposphere corrections provided by an external provider using a local GNSS network.

Acknowledgement

The BoM GRIB2 data were supplied courtesy of Air services Australia. The IGS (Dow et al., 2009) is acknowledged for provision of the precise orbit and clock products to enable simulation of RINEX data. The precise station coordinates were obtained from the weekly Asia Pacific Reference Frame (APREF) solution provided by Geoscience Australia.

Disclosure statement

No potential conflict of interest was reported by the authors.

ORCID

A. El-Mowafy http://orcid.org/0000-0001-7060-4123

References

Andrei, C.O. and Chen, R., 2009. Assessment of time-series of troposphere zenith delays derived from the Global Data Assimilation System numerical weather model. *GPS Solutions*, 13, 109–117. doi:https://doi.org/10.1007/s10291-008-0104-1.

Askne, J. and Nordius, H., 1987. Estimation of tropospheric delay for microwaves from surface weather data. *Radio Science*, 22 (3), 379–386.

Böhm, J., Heinkelmann, R., and Schuh, H., 2007. Short note: A global model of pressure and temperature for geodetic applications. *Journal of Geodesy*, 81 (10), 679–683. doi:https://doi.org/10.1007/s00190-007-0135-3.

Böhm, J., Werl, B., and Schuh, H., 2006a. Troposphere mapping functions for GPS and VLBI from ECMWF operational analysis data. *Journal of Geophysical Research*, 111 (B02406), 1–9. doi:https://doi.org/10.1029/2005JB003629.

Böhm, J., *et al*., 2006b. Global mapping function (GMF): a new empirical mapping function based on data from numerical weather model data. *Geophysical Research Letters*, 33 (L07304), 1–4. doi:https://doi.org/10.1029/2005GL025546.

Böhm, J., *et al*., 2015. Development of an improved empirical model for slant delays in the troposphere (GPT2w). *GPS Solutions*, 19, 433–441. doi:https://doi.org/10.1007/s1029-014-0403-7.

Collins, P., Langley, R.B., and LaMance, J. 1996. Limiting factors in tropospheric propagation delay error modelling for GPS airborne navigation. *In*: Proceedings ION-AM-1996, June 19–21, Cambridge, Massachusetts, Institute of Navigation, 519–528.

Davis, J.L., *et al*., 1985. Geodesy by radio interferometry: effects of atmospheric modelling errors on estimates of baseline length. *Radio Science*, 20 (6), 1593–1607.

Deo, M. and El-Mowafy, A. 2016. Triple-frequency GNSS models for PPP with float ambiguity estimation: performance comparison using GPS. Survey Review, 50, 249–261. https://doi.org/10.1080/00396265.2016.1263179.

El-Mowafy, A., 2015. Estimation of multi-constellation GNSS observation stochastic properties using a single-receiver single-satellite data validation method. *Survey Review*, 47 (341), 99–108.

El-Mowafy, A. and Lo, J., 2014. Dynamic modelling of GNSS troposphere wet delay for estimation of precipitable water vapour. *Journal of Applied Geodesy*, 8 (1), 31–42.

IERS Conventions, Petit, G, and Luzum, B., eds. 2010. IERS Technical Note 36, Frankfurt am Main: Verlag des Bundesamts für Kartographie und Geodäsie, 179 pp, ISBN 3-89888-989-6.

Kjørsvik, NS, Gjevestad JGO, and Øvstedal O. 2006. Handling of the tropospheric delay in kinematic precise point positioning. *In*: Proceedings of the 19th International Technical Meeting of the Satellite Division of the Institute of Navigation (ION GNSS 2006), September 2006 Fort Worth, TX, 2279–2281.

Kouba, J., 2009. Testing of global pressure/temperature (GPT) model and global mapping function (GMF) in GPS analyses. *Journal of Geodesy*, 83, 199–208.

Krueger E, *et al*. 2004. Galileo tropospheric correction approaches developed within GSTB-V1. In: Proceedings of ENC-GNSS 2004, Rotterdam, The Netherlands, May 16–19.

Lagler, K., *et al*., 2013. GPT2: Empirical slant delay model for radio space geodetic techniques. *Geophysical Research Letters*, 40, 1069–1073.

Laurichesse D and Privat A. 2015. An Open-source PPP Client Implementation for the CNES PPP-WIZARD Demonstrator, ION GNSS 2015, September 15-18, 2015, Tampa, Florida.

Li, W., *et al*., 2012. A new global zenith tropospheric delay model IGGtrop for GNSS applications. *Chinese Science Bulletin*, 57 (17), 2132–2139.

Li, T., Wang, J., and Laurichesse, D., 2014. Modeling and quality control for reliable precise point positioning integer ambiguity resolution with GNSS modernization. *GPS Solutions*, 18 (3), 429–442.

Lu, C., *et al*., 2016. Tropospheric delay parameters from numerical weather models for multi-GNSS precise positioning. *Atmospheric Measurement Techniques*, 9, 5965–5973. doi:https://doi.org/10.5194/amt-9-5965-2016.

Lu, C, *et al*. 2017. Real-time tropospheric delays retrieved from multi-GNSS observations and IGS real-time product streams. *Remote Sensing* 9(12), 1317. doi:https://doi.org/10.3390/rs9121317.

Martellucci, A. 2012. Galileo reference troposphere model for the user receiver. ESA-APPNG-REF/00621-AM v2.7.

Neill, A.E., 1996. Global mapping functions for the atmosphere delay at radio wavelengths. *Journal of Geophysical Research*, 101 (B2), 3227–3246.
Saastamoinen, J., 1972. Atmospheric correction for the troposphere and stratosphere in radio ranging satellites. Geophysical Monograph. *Henriksen (ed)*, 15, 247–251.
Saastamoinen, J., 1973. Contributions to the theory of atmospheric refraction. *Bullétin Géodésique* 107(1), 13–34. Part 3 of 3.
Schüler, T., 2014. The TropGrid2 standard tropospheric correction model. *GPS Solutions*, 18 (1), 123–131.
Shi, J., *et al*., 2014. Local troposphere augmentation for real-time precise point positioning. *Earth, Planets and Space*, 66 (30), 1–13. doi:https://doi.org/10.1186/1880-5981-66-30.
Steigenberger, P., Böhm, J., and Tesmer, V., 2009. Comparison of GMF/GPT with VMF1/ECMWF and implications for atmospheric loading. *Journal of Geodesy*, 83 (10), 943–951. doi:https://doi.org/10.1007/s00190-009-0311-8.
Talbot, N., *et al*. 2015. Trimble RTX orbit determination and user positioning performance with BeiDou satellites, IGNSS Conference, 6–8 December 2016, UNSW Australia.
Tuka, A. and El-Mowafy, A., 2013. Performance evaluation of different troposphere delay models and mapping functions. *Measurement*, 46 (2), 928–937. doi:https://doi.org/10.1016/j.measurement.2012.10.015.
Vaclavovic, P., *et al*., 2017. Using external tropospheric corrections to improve GNSS positioning of hot-air balloon. *GPS Solutions*, 21, 1479. doi:https://doi.org/10.1007/s10291-017-0628-3.
Yue, X., *et al*., 2010. Error analysis of Abel retrieved electron density profiles from radio occultation measurements. *Annales Geophysicae*, 28, 217–222. doi:https://doi.org/10.5194/angeo-28-217-2010.
Zhang, H., *et al*., 2016. Assessment of three tropospheric delay models (IGGtrop, EGNOS and UNB3 m) based on precise point positioning in the chinese region. *Sensors*, 16 (122), 1–12. doi:https://doi.org/10.3390/s16010122.
Zheng, F., *et al*. 2017. Modeling tropospheric wet delays with national GNSS reference network in China for BeiDou precise point positioning. Journal of Geodesy. published online 29 Oct 2017, 1–16, doi: https://doi.org/10.1007/s00190-017-1080-4.
Zhou, C, *et al.,* 2017. Establishment of a site-specific tropospheric model based on ground meteorological parameters over the China region. Sensors, 17(8), 1722. doi:https://doi.org/10.3390/s17081722.

7 MAINTAINING REAL-TIME PRECISE POINT POSITIONING DURING OUTAGES OF ORBIT AND CLOCK CORRECTIONS

During communication outages, the GPS satellite orbit and clock corrections are unavailable to the real-time PPP user. Such outages may last from a few minutes to several hours and during this time, the PPP solution is lost. Once the corrections are restored, the user has to wait for the PPP solution to re-converge within decimetre accuracy, which is a problematic exercise.

This chapter presents a method for maintaining real-time PPP with better than decimetre 3D accuracy during communication outage. The real-time service (RTS) products sourced from open-access IGS are used to predict the precise orbit and clock corrections as time series during the outage. For short outage periods of a few minutes, the IGS-RTS orbits are predicted using a high-order polynomial, and for longer outages up to 3 h, the most recent IGS ultra-rapid orbits are used. As for the precise clocks, IGS-RTS clock corrections are predicted using a second-order polynomial with sinusoidal terms.

This chapter is covered by the following publication:

- El-Mowafy A, **Deo MN**, Kubo N (2016) Maintaining real-time precise point positioning during outages of orbit and clock corrections. GPS Solutions, 21(3), 937-947. DOI:10.1007/s10291-016-0583-4.

7.1 Errata

The following corrections apply to this published paper:

- Pg. 1 of article (Introduction, 7th sentence): “where RT PPP relays on online streaming” should be replaced by “where RT PPP relies on online streaming”

Maintaining real-time precise point positioning during outages of orbit and clock corrections

Ahmed El-Mowafy, Manoj Deo & Nobuaki Kubo

GPS Solutions
The Journal of Global Navigation Satellite Systems

ISSN 1080-5370

GPS Solut
DOI 10.1007/s10291-016-0583-4

Springer

GPS Solut
DOI 10.1007/s10291-016-0583-4

ORIGINAL ARTICLE

Maintaining real-time precise point positioning during outages of orbit and clock corrections

Ahmed El-Mowafy[1] · **Manoj Deo**[1] · **Nobuaki Kubo**[2]

Received: 10 July 2016 / Accepted: 10 November 2016

Abstract The precise point positioning (PPP) is a popular positioning technique that is dependent on the use of precise orbits and clock corrections. One serious problem for real-time PPP applications such as natural hazard early warning systems and hydrographic surveying is when a sudden communication break takes place resulting in a discontinuity in receiving these orbit and clock corrections for a period that may extend from a few minutes to hours. A method is presented to maintain real-time PPP with 3D accuracy less than a decimeter when such a break takes place. We focus on the open-access International GNSS Service (IGS) real-time service (RTS) products and propose predicting the precise orbit and clock corrections as time series. For a short corrections outage of a few minutes, we predict the IGS-RTS orbits using a high-order polynomial, and for longer outages up to 3 h, the most recent IGS ultra-rapid orbits are used. The IGS-RTS clock corrections are predicted using a second-order polynomial and sinusoidal terms. The model parameters are estimated sequentially using a sliding time window such that they are available when needed. The prediction model of the clock correction is built based on the analysis of their properties, including their temporal behavior and stability. Evaluation of the proposed method in static and kinematic testing shows that positioning precision of less than 10 cm can be maintained for up to 2 h after the break. When PPP re-initialization is needed during the break, the solution convergence time increases; however, positioning precision remains less than a decimeter after convergence.

Keywords Real-time PPP · GPS · Prediction · IGS products

Introduction

Precise point positioning (PPP) can provide centimeter- to decimeter-level accuracy using a single receiver in undifferenced mode. In recent years, the advent of real-time precise orbit and clock correction streams allows users to shift from the traditional post-mission PPP processing to real-time PPP (RT PPP) solution anywhere in the world. RT PPP is currently used in natural hazard early warning systems, crustal deformation and landslide monitoring. One example is the Jet Propulsion Laboratory's GPS Real Time Earthquake and Tsunami Alert project (GREAT); (http://www.gdgps.net/products/great-alert.html). RT PPP can also be used for atmospheric water vapor measurement and remote sensing applications (Jin and Komjathy 2010), and it is becoming a popular approach in offshore hydrographic surveying. In addition, PPP-RTK represents a main component of Australia's National Positioning Infrastructure (NPI), where it is planned to be used for various applications including intelligent transport systems. In all these applications, where RT PPP relays on online streaming of orbit and clock corrections, an obvious concern is the possibility of a disruption in receiving these corrections that may occur, for instance, due to a temporary modem failure or network outage, which may take from a few minutes up to hours to be fixed. In such a case, severe decline of PPP accuracy may result to the meter level due to switching to the default single point positioning mode.

✉ Ahmed El-Mowafy
a.el-mowafy@curtin.edu.au

[1] Department of Spatial Sciences, Curtin University, Bentley, Australia

[2] Tokyo University of Marine Science and Technology, Tokyo, Japan

Published online: 19 November 2016

Solving this problem is the research question that is being addressed in this contribution. We propose to predict the real-time orbits and clock corrections as time series to enable RT PPP for a prolonged period of time until the break is fixed.

For prediction of satellite orbits, some previous studies discussed using numerical integration of the equations of motion in connection with a dynamic force modeling (Montenbruck and Gill 2000). This includes modeling earth, solar and lunar gravitation, solar radiation pressure, harmonic behavior and general relativity. Similarly, Seppänen et al. (2012) discussed solving the satellite equation of motion numerically and estimating the satellite's initial states by a nonlinear least squares fitting algorithm. Leandro et al. (2011) studied applying Kalman filtering for estimation and prediction of satellite orbits. Moreover, Hadas and Bosy (2015) proposed a short-term prediction of real-time International GNSS Service (IGS) precise GPS orbits with less than 10 cm accuracy for up to 10 min using polynomial fitting. For prediction of satellite clocks, the current United States Naval Observatory (USNO) algorithm uses a linear model, where it was found that a quadratic model degraded the accuracy of satellite clock predictions rather than improving it (Hackman 2012). To improve the model, Heo et al. (2010) proposed adding cyclic terms to overcome possible periodic variation. Likewise, Huang et al. (2014) used a model with multiple periodic terms and weighted the observations as a linear function of age of data when predicting IGS ultra-rapid (IGU) clock corrections.

In this study, we restrict attention to GPS RT precise orbits and clock corrections owing to their availability, whereas similar products for other systems are currently in the experimental phase. We limit our analysis and proposed methods to the use of two open-access RT products, the IGS-RTS, which is the IGC01 stream and thereafter denoted as IGC for brevity, and the predicted half of the IGU. We assume that before a break in communications takes place, an RT PPP user can obtain the latest update of the IGU and IGC streams online. We first study the accuracy of the precise orbits and the performance of their prediction as a time series. Next, we analyze the accuracy, stability, spectrum and autocorrelation of the clock corrections and then investigate their prediction as time series. The steps of building the prediction models are discussed, and the accuracy of prediction is analyzed. For quality control, a process for detection of outliers in the data used in creating the prediction model was applied before commencement of this process. We fit the orbit and clock data to polynomials and check that the difference between each data point and its corresponding value from the fitting model does not differ by more than three times the standard deviation (STD), corresponding to 99.7% confidence level. A first-order fitting polynomial was used for clock corrections, and fourth-order polynomials were used for the orbits. When an outlier is found, the data of this epoch are excluded.

We next assess the impact of the proposed method on PPP positioning results by conducting many tests in the static and kinematic modes and analyzing the resulting solution convergence time and precision. Since the quality of orbits and clock corrections may affect the initialization period of PPP, i.e., conversion of the solution, we tested initialization of PPP assuming that the break is taking place at different instances in time. Test results are presented and discussed, and finally concluding remarks are given.

Implementation of the RT orbit and clock corrections

In April 2013, the IGS launched an open-access real-time service (RTS). Currently, this service includes the IGS01/IGC01 stream, which is based on a single epoch GPS combination solution, IGS02 stream that is a Kalman filter GPS combination solution and IGS03 stream, which is a Kalman filter GPS + GLONASS combination solution (http://www.igs.org/rts/products). These streams are a combination of products from nine analysis centers (ACs) that process more than 160 stations located around the world. In addition to IGS-RTS, the IGS provides the ultra-rapid (IGU) products with less accurate clock corrections, which do not need to be streamed in RT. The IGU is released four times each day and contains 2 days of orbits; the first day is computed from observations, and the second day includes predicted orbits and clocks that can be used for RT applications. Table 1 summarizes the current STD of the orbits, clock corrections root mean square (RMS) and product latency for both IGS-RTS and IGU products (http://rts.igs.org and http://www.igs.org/products/data). In a following section, we check this information by comparing them with the IGS final products. In addition to the open-access products, a number of private commercial providers serve similar products such as Trimble RTX service (Leandro et al. 2011), Fugro G2 service (http://www.starfix.com/positioning-systems) and TERRASTAR (http://www.terrastar.net/about-terrastar.html).

Typically, a user can access the real-time products exploiting a wireless modem and employing the network

Table 1 IGS real-time products

Product	Orbit STD (cm)	Clock RMS (ns)	Latency
IGS-RTS	5	0.3	25 s
IGU	5	3	RT

transport of Radio Technical Commission for Maritime Services (RTCM) by the Internet Protocol (NTRIP) client application. The IGS-RTS products can be streamed using the RTCM-State Space Representation (SSR) format. The open-source application of Bundesamt für Kartographie und Geodäsie (BKG) Client (BNC) NTRIP and the RTKLIB software are two examples that allow NTRIP access to RT precise orbits and clock corrections.

The orbit corrections in RTCM-SSR are defined in terms of the radial, along-track and cross-track components, denoted here as $\delta\rho_r, \delta\rho_a$ and $\delta\rho_c$, respectively, along with their velocities ($\delta\dot{\rho}_r, \delta\dot{\rho}_a$ and $\delta\dot{\rho}_c$). Using a broadcast navigation message with a reference time t_o, the orbit corrections at time t can be computed as follows (Hadas and Bosy 2015):

$$\delta\rho = [\rho_r\, \delta\rho_a\, \delta\rho_c]^{\mathrm{T}} + [\delta\dot{\rho}_r\, \delta\dot{\rho}_a\, \delta\dot{\rho}_c]^{\mathrm{T}}(t - t_o) \quad (1)$$

These corrections are transformed to geocentric corrections by applying the radial, along-track and cross-track unit vectors (e_r, e_a and e_c) and adding them to the broadcast orbit x_{brdcst} to give the final precise orbit x_{precise}:

$$x_{\mathrm{precise}} = x_{\mathrm{brdcst}} + \mathrm{diag}(e_r e_a e_c)\delta\rho \quad (2)$$

The clock correction is given in terms of a quadratic polynomial with coefficients $(q0, q1, q2)$ as a range correction such that:

$$c\delta t = q0 + q1(t - t_o) + q2(t - t_o)^2 \quad (3)$$

where c is the speed of light. Hence, the corrected satellite clock offset t_{sat} is expressed as:

$$t_{\mathrm{sat}} = t_{\mathrm{brdcst}} + \delta t \quad (4)$$

where t_{brdcst} denotes the broadcast GPS satellite clock offset.

Dealing with the precise orbits during communication breaks

For prediction of the precise orbits, El-Mowafy (2006) studied several approaches and showed that prediction of the orbits as a time series can be successful for only a short period, up to 15 min, using Holt–Winters' method (Chatfield and Yar 1991). In the same way, Hadas and Bosy (2015) predicted the IGS-RTS precise orbits with less than 10 cm accuracy for up to 10 min by using polynomial fitting. In addition to these methods, we tested another approach that can potentially provide this accuracy over a longer prediction period. In this approach, the difference between the IGC and IGU orbits is predicted through a high-order polynomial, e.g., a fourth-order polynomial, and the predicted differences are added to the IGU orbits to resemble approximate IGC orbits. Figure 1 demonstrates the performance of this method through one representative example. The 3D difference between the predicted orbits and the IGS final orbits on August 28, 2015, is depicted for PRN 16, 29 and 30, which represent the current GPS blocks IIR, IIR-M and IIF, respectively. The model is built from the data of the previous 2 h before prediction, based on autocorrelation analysis of the orbits. As Fig. 1 shows, a prediction error less than 10 cm can only be achieved for up to the first 0.5 h of prediction, and thereafter, the error significantly grows with time.

In PPP, the precise orbits need to be accurate to less than 10 cm; hence, in case the orbit corrections outage is longer than 0.5 h, an approach other than prediction of the corrections as a time series will be needed. To this end, we first investigated the accuracy of the RT orbit streams considered in this study, i.e., the IGU and IGC. The statistics of their 3D differences from the IGS final orbits, defined here for brevity as IGS orbits, are given in Table 2 for all GPS satellites during August 2015. Since the IGU orbits are updated every 6 h, the IGU data included here are the first 6 h of the predicted part of the updated files. Figure 2 shows the histogram of the absolute 3D differences among IGU–IGS (top), IGC–IGS (middle) and IGU–IGC (bottom) for PRN 16, 29 and 30, as exemplar of the current three GPS satellite blocks and using a 15-min sampling rate over the whole month of August 2015.

Taking the IGS final products as ground truth, Table 2 and the sample histograms show that the differences between IGC and IGS were typically within ±7 cm (95% range) and the STDs were 0.023 m on average, which agree with the published values by the IGS-RTS monitoring facility (http://www.igs.org/rts/monitor). The differences between the IGU (predicted half) and IGS were in the same range, although at many epochs the IGU orbits had fewer errors than IGC. The differences between IGU and IGC orbits were mostly within ±6 cm. These results

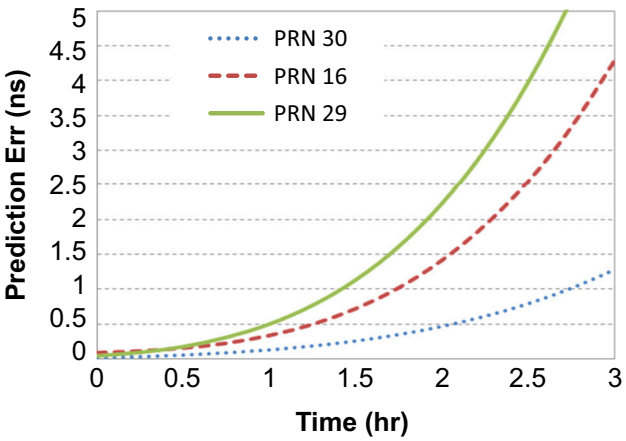

Fig. 1 3D error of orbit prediction using a fourth-order polynomial

Table 2 Statistics of the 3D differences among precise orbits for all GPS satellites during August 2015 (m)

Stats	IGU–IGS	IGC–IGS	IGU–IGC
Range (95%)	±0.07	±0.07	±0.06
Max (absolute)	0.101	0.130	0.101
Average	0.034	0.041	0.036
STD	0.018	0.023	0.018

show that the IGU orbits are numerically compatible with the IGC orbits within this level of accuracy. This compatibility is further validated statistically by examining the significance of the residuals between the two sets of data and the IGS final orbits, i.e., IGC–IGS and IGU–IGS. As illustrated from the sample histograms in Fig. 3, the distribution of the orbit residuals is not Gaussian; therefore, nonparametric statistical hypothesis tests were used. The Wilcoxon signed-rank test of the IGU–IGS and IGC–IGS daily residuals over August 2015 was applied to assess whether their population mean ranks differ. The test passed for almost all samples. In addition, testing of their variances was performed using Kruskal–Wallis H test (Kruskal and Wallis 1952), which was successful for 93% of the data with P values > 0.05.

Based on the above, upon a break of receiving the IGC stream, for a short period of a few minutes one can predict the IGC orbits using a fourth-order polynomial, and for a medium period of about 3 h one may use the most recent IGU orbits as a reasonable substitute for the IGC orbits. In this case, the IGU orbits will be used in place of x_{precise} in (2). In a following section, the impact of this approach on PPP positioning results is investigated.

Dealing with clock corrections during communication breaks

Currently, all operational GPS satellites from block IIR onward have rubidium clocks except for PRN 8 and 24 (block IIF), which have cesium clocks. Rubidium clocks have short-term noise performance, but their temperature sensitivity and inherent high-frequency drift uncertainty limit their long-term stability (Trigo and Slomovitz 2011). To develop the best prediction model of the IGC clock corrections, we first analyze the accuracy and stability of these clock corrections. Next, we present the model and discuss the process of building it.

Accuracy and stability of IGC clock corrections

The accuracy of the IGC clock corrections can be computed in terms of their differences from the IGS final clock corrections. As an example, the IGC–IGS differences for all satellites and different blocks are illustrated for GPS weeks 1859 and 1860 in Fig. 3 after removing the average of the differences at each epoch. This average, which was approximately 15 ns, represents an offset between the IGC and IGS clock corrections. This offset is due to the IGC products being a combination of solutions from several contributing ACs, which follow their inherent timescales. The IGS aligns all these solutions to a reference AC, which can change at any time, as not all solutions are available at each epoch. Hence, the average can change between epochs. For PPP processing, the common part of this offset, for instance the mean value, for all satellites can be absorbed in the estimated receiver clock offset that is determined every epoch; thus, the PPP performance remains unaffected. The remaining clock differences from

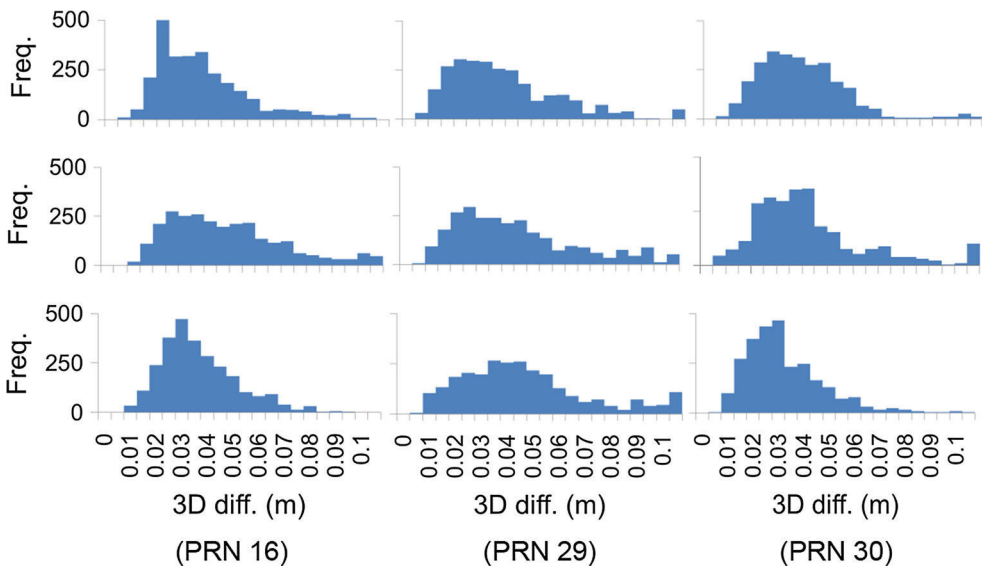

Fig. 2 Histograms of 3D differences among precise orbit products for PRN 16, 29 and 30 over 1 month. IGU–IGS (*top*), IGC–IGS (*middle*), IGU–IGC (*bottom*)

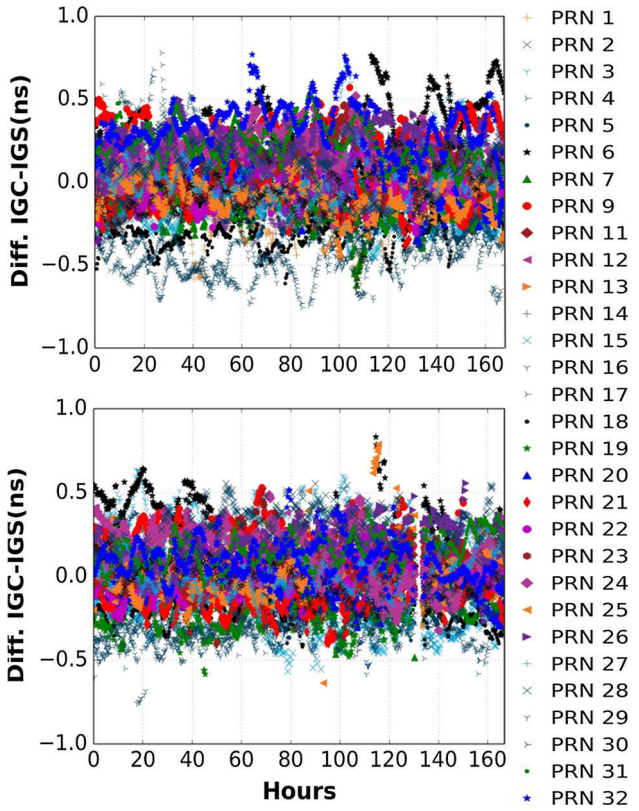

Fig. 3 IGC referenced to IGS final clock corrections. GPS week 1859 (*top*) and week 1860 (*bottom*)

the mean value, which vary among different satellites in general within ±0.5 ns, as depicted in Fig. 3 for the two example weeks, are absorbed in the individual ambiguities for phase observations. The statistics of the IGC–IGS clock correction differences are given in Table 3 for different blocks. The table shows that error dispersion in IGC clock corrections was less in block IIF than that of older blocks IIR-M and IIR. The STD of the differences ranged between 0.161 and 0.254 ns with an overall mean of 0.230 and 0.203 ns for the two example weeks.

We next characterize the stability of the IGC clock corrections by means of their Allan deviation, which is the IEEE standard for clock frequency stability analysis. The Allan deviation, denoted as $\sigma_{\mathrm{d}t}$, is (Allan 1987):

$$\sigma_{\mathrm{d}t}(\tau) = \sqrt{\frac{1}{2(n-2)\tau^2}\sum_{i=1}^{n-2}\left(\mathrm{d}t_{i+2} - 2\mathrm{d}t_{i+1} + \mathrm{d}t_i\right)^2} \quad (5)$$

where n is the number of dt, which is the difference between IGC and the final IGS clock corrections, and τ is the averaging time interval. Figure 4 shows Allan deviation for 1 week of data (GPS week 1859) for PRN 30 as an example. The plot shows the overlapping Allan STD (denoted as ADEV) and its lower and upper bounds, the modified Allan STD (denoted as MDEV) and the overlapping Hadamard STD (HDEV) (Snyder 1981; Ferre-Pikal et al. 1997). From the analysis of the data of all rubidium GPS satellites, one can conclude that the IGC clock corrections are reasonably stable with Allan deviations ranging between 10^{-11} and 10^{-14} s, which converges with the increase in the averaging time, and the clock corrections have mostly a white noise. Hence, we can proceed to the step of their prediction as a time series.

Building the clock prediction model

A possible prediction model of clock corrections is given as (Huang et al. 2014):

$$\delta t = a0 + a1\Delta t + \frac{a2\Delta t^2}{2} + \sum_{i=0}^{k} A_i \sin(\omega_i \Delta t_i + \phi_i) + \varepsilon_{\delta t} \quad (6)$$

where Δt is the time since start of prediction, a0, a1 and a2 are the polynomial parameters corresponding to the bias, drift and drift rate of the clock corrections, respectively, and $\varepsilon_{\delta t}$ denotes the noise. k is the number of sinusoidal periods considered, A_i is the amplitude of period i, Δt_i is the time since start of this period, ω_i denotes the frequency of the period, and ϕ_i is its phase. In the time domain, we rewrite (6) as follows:

$$\delta t = a0 + a1\Delta t + \frac{a2\Delta t^2}{2} + \sum_{i=0}^{k} A_i \sin\left(\frac{\Delta t_i}{\lambda_i} \times 2\pi + \frac{t_{\phi_i}}{\lambda_i} \times 2\pi\right) + \varepsilon_{\delta t} \quad (7)$$

where λ_i is the time length for the periodic term i and t_{ϕ_i} is its initial phase in time units. For a real-time user, the predicted clock correction δt is used whenever an outage of the IGC is experienced.

In our method, the parameters of (6) are determined using least squares except for λ_i, which is preselected as will be explained next. The outlier-free observations are weighted according to age of data, where the most recent

Table 3 Statistics of the IGC–IGS clock correction differences (in ns) for all GPS satellites during GPS weeks 1859 and 1860 after removing the mean of all satellites at each epoch

Stats	Week 1859			Week 1860		
	Block IIR	Block IIR-M	Block IIF	Block IIR	Block IIR-M	Block IIF
Max (absolute) all	0.779	0. 756	0.612	0.833	0.758	0.585
STD all	0.218	0. 254	0.161	0.176	0.208	0.170

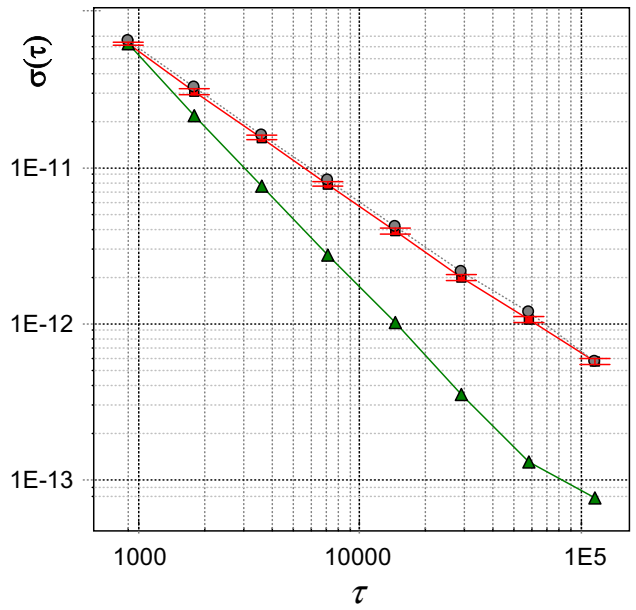

Fig. 4 Allan deviation (ADEV) with up and lower bounds. *Red color* (modified Allan deviation MDEV), *green color* (Hadamard deviation HDEV), *blue color* (RT clock correction of PRN 30) over week 1859 in seconds

observations are given more weights. The weight is assumed decaying gradually with time in the form:

$$W = \mathrm{diag}(w_j), \quad w_j = e^{-\Delta t/T} \times 1/\sigma_{\delta t}^2 \tag{8}$$

where W is the weight matrix, w_j is the individual weight for δt number j, taken during the regression period used for the development of the model. T is the correlation time length, which is determined from the autocorrelation analysis that will be discussed next. $\sigma_{\delta t}$ is set according to Allan deviation given in (5). Results of our study show that the IGC clock corrections for GPS satellites are mainly driven by the bias and drift. The drift rate was insignificant, and therefore, the difference between predictions using first-order or second-order polynomials in (6) is 0.1 ns over a prediction period of 2–3 h. Likewise, the contribution of the periodic terms is small, typically less than 0.2 ns, which slightly varies among satellites.

The time length λ_i can be estimated from the analysis of the data in the frequency domain using, for instance, fast Fourier transform (FFT). As an example, Fig. 5 (top) illustrates the IGC clock corrections for PRN 30 over week 1859 in the frequency domain using FFT. The periodic terms are clear in the frequency spectrum. The bottom panel shows the frequency spectrum of the differences between IGC and IGS clock corrections. The signature of the clock correction error is noise like for high frequencies, and some periodic terms appear with periods ranging between 15 min and 3 h. For the shown example, and considering a prediction period of 2 h, the two periods of

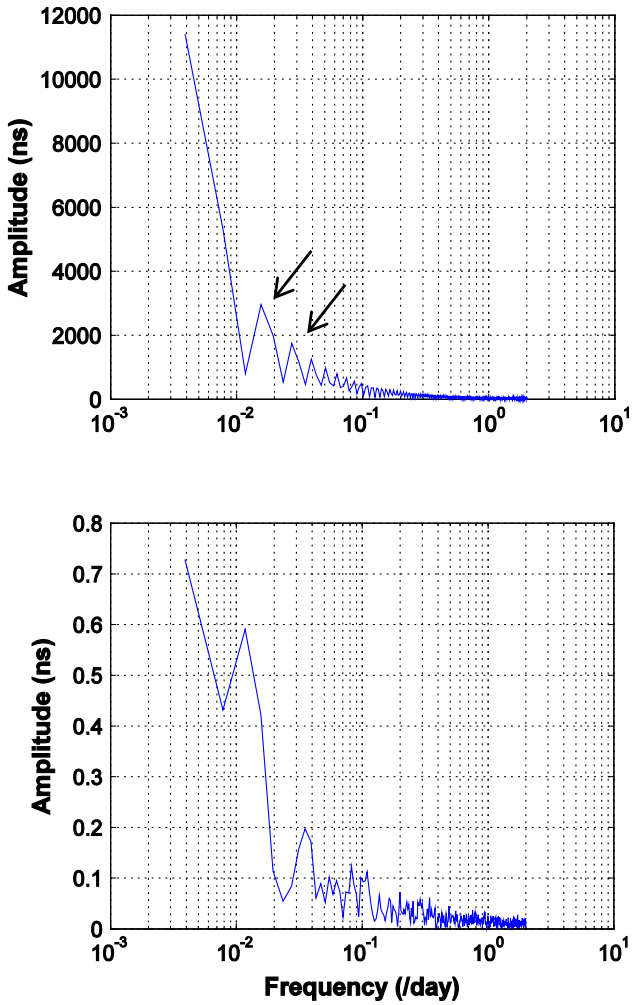

Fig. 5 Spectrum of IGC clock corrections (*top*) and IGC–IGS clock correction differences (*bottom*) for PRN 30 using 1 week of data

approximately 15 and 30 min are the most noticeable, and on a longer term, a 3-h period is noticeable.

It is expected that different sampling rates would be exploited by various PPP users; therefore, instead of defining a specific number of data points for estimating the prediction model parameters, we define an equivalent time window during which this process is performed. In time series analysis, the time lag corresponding to a significant autocorrelation is often estimated and the number of data points within this time is used for building the prediction model (Box et al. 1994). Figure 6 shows the autocorrelation plots of the IGC clock corrections of the selected exemplar satellites PRN 16, 29 and 30. From these plots, the significant correlation time length can be estimated by the intersection of the red dotted lines, which correspond to 95% confidence level, with the autocorrelation function. Alternatively, it can be empirically selected at an autocorrelation with an arbitrary value, e.g., 0.7. The plots show that the significant correlation time length for clock

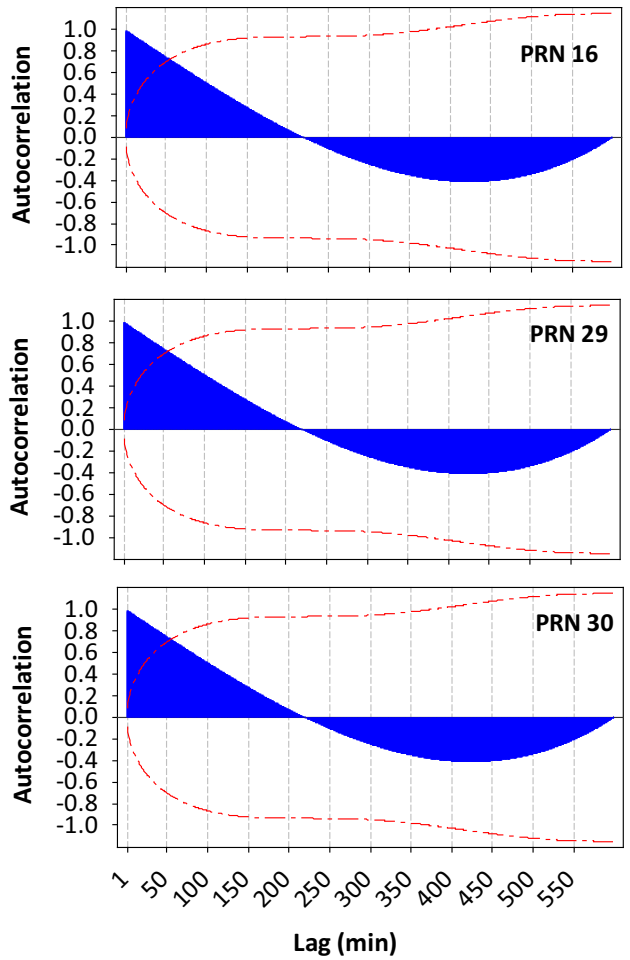

Fig. 6 Autocorrelation of IGC clock corrections (95 confidence level shown in *red*)

corrections is approximately 1 to 1.5 h. This result was consistent for all GPS satellites during the test period.

Accuracy of prediction of the clock corrections

The accuracy of prediction of IGC clock corrections using the presented model was evaluated by differencing the predicted values with their known IGC values at the prediction period. Table 4 summarizes the descriptive statistics of the prediction error of IGC clock corrections for the three GPS blocks over 1 week of data after an assumed break in receiving the RT products and for prediction periods of 1, 1.5 and 2.0 h. The table shows that the STD of different blocks ranges between 0.12 ns and 0.40 ns. As an example of the temporal change of the prediction errors, Fig. 7 shows the prediction errors for all satellites over 4 days (August 23–26, 2015) for up to 3 h of prediction. The figure clearly shows that the error increases with the increase in time for all satellites; it was typically within 0.5 ns during the first hour and 1 ns after 2 h. In addition, the satellites that have clock corrections causing most of the errors belong to the old generation of blocks IIR or IIR-M, such as PRN 20, 21, 05, 07 and 11. Moreover, the case of PRN 24 was an anomaly, where its prediction error was large even after a very short period. This satellite is the only satellite observed that has a cesium clock, whereas the rest of the satellites have rubidium clocks. Therefore, PRN 24 was excluded from computation of the statistics presented in Table 4. In general, our study shows that prediction of the clock corrections for the block IIF satellites was better than that of IIR-M satellites and those were better than IIR satellites. This clearly reflects the improvement in the stability of the newer generation of clocks, which allows for better prediction of their behavior.

Analysis of the impact of the proposed methods on PPP results

Although it would be desirable to use predicted clock and orbit corrections from the same solution, however, at present the prediction accuracy of the IGC orbits as a time series is good only for a few minutes. Nevertheless, the basic assumption in RT PPP is that the user employs IGC products as 'known' values. When a break in receiving this information occurs, we propose the use of the predicted orbits of IGU in place of predicted IGC orbits. The IGU and IGC orbits proved to be numerically and statistically compatible as discussed earlier. Thus, the IGU orbits are the best substitute currently available to the IGC orbits, which when used along with predicted IGC clock corrections provides a practical substitute to IGC corrections when they are not available.

The RT PPP algorithm, e.g., in early warning systems or hydrographic surveying, can use the precise IGU orbits as x_{precise} in (2) and apply the predicted clock corrections in (4). This will require the user to download the most recent

Table 4 Statistics of the prediction error of IGC clock corrections (in ns) for three GPS blocks over 1 week of data

Prediction period	1 h				1.5 h				2 h			
Block	IIR	IIRM	IIF	All	IIR	IIRM	IIF	All	IIR	IIRM	IIF	All
Mean	0.02	0.10	0.01	0.04	0.02	0.13	0.03	0.05	0.01	0.17	0.04	0.06
STD	0.27	0.20	0.12	0.23	0.33	0.23	0.17	0.28	0.40	0.29	0.22	0.35
Max (absolute)	1.01	0.64	0.45	1.01	1.19	0.89	0.57	1.19	1.48	1.25	0.73	1.48

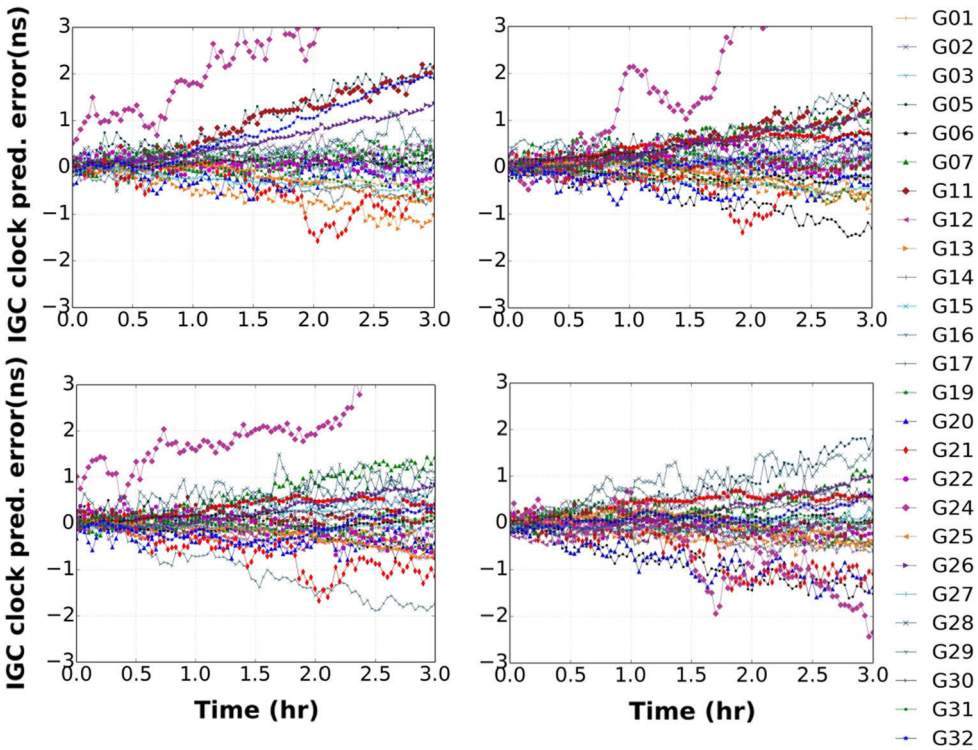

Fig. 7 Prediction error of IGC clock corrections for up to 3 h for four separate days of August 23–26, 2015

IGU orbits, which are contained in one small-size file that is being updated every 6 h. It is proposed that the user sequentially builds the prediction model with a sliding time window and uses predicted clock corrections whenever real-time corrections are unattainable. To reduce the computational load, the process can be performed at a suitable time interval depending on the application, e.g., every 10 min, and to use the predicted corrections for the following 2–3 h.

In this section, the practical application of the proposed method is presented. Its impact on PPP solution convergence and precision in static and kinematic modes is evaluated. The observations used comprised ionospheric-free combination of L1 and L2 dual-frequency GPS data, which were validated and weighted using the single-receiver single-satellite method presented in El-Mowafy (2014, 2015) and processed in a float ambiguity PPP scheme.

Description of the static and kinematic tests

The static test was performed at four IGS stations with a global distribution. The stations are GMSD (Japan), CUT0 (Australia), DLF1 (the Netherlands) and ABMF (the Caribbean). The data used span GPS week number 1859 with a 30-s sampling interval. We assumed as an example an early warning system situation. We investigate the communication break taking place at three instants, including at the start of PPP initialization, at 0.5 and 1 h from the start of initialization. In each case, the IGC clock corrections were predicted for up to 3 h using parameters estimated through a regression period of 1.5 h. For demonstration of results, we show the PPP solution for 3 h from start of its initialization. The PPP started at 3:00 UTC each day, which is the middle of the IGU predicted orbit period. The performance was evaluated by comparing the obtained results with the results of PPP processing the same observations when using the IGC orbit and clock corrections without prediction. Since the data were reprocessed at several instances, processing was performed in a post-mission mode. Hence, data latency was not included in this analysis. During the test period, the differences between the predicted IGU orbits and IGC orbits were within ±6 cm. The predicted IGC clock corrections when compared with their streamed values were within 0.5 ns during the first hour and 1 ns after 2 h as mentioned earlier.

Two kinematic tests were carried out. The first test was performed in a shipborne mode, in an open-sky environment, spanning a 2-h period using 10 Hz sampling rate. In this test, a Trimble SPS855 receiver was mounted on a ship sailing in Tokyo Bay, Japan, for a total distance of almost 27 km. The second test was conduct on land, with a Trimble R10 receiver mounted on a vehicle traveled for 1.74 h using 1 Hz sampling rate in an urban area in Perth, Western Australia. The observation environment in this test had somewhat a challenging sky visibility during some periods due to the presence of trees close to the vehicle's trajectory. For both tests, processing was performed in post-mission to compare the results between first using the

Table 5 Average statistics of PPP for the static tests during the prediction period of the corrections after solution convergence (m)

Start of break	Convergence (min)	(Average) after convergence		
		σ_E	σ_N	σ_U
At the init.	37	0.045	0.049	0.040
0.5 h After init.	34	0.044	0.048	0.040
1 h After init.	31	0.044	0.048	0.040
Without prediction	31	0.038	0.041	0.039

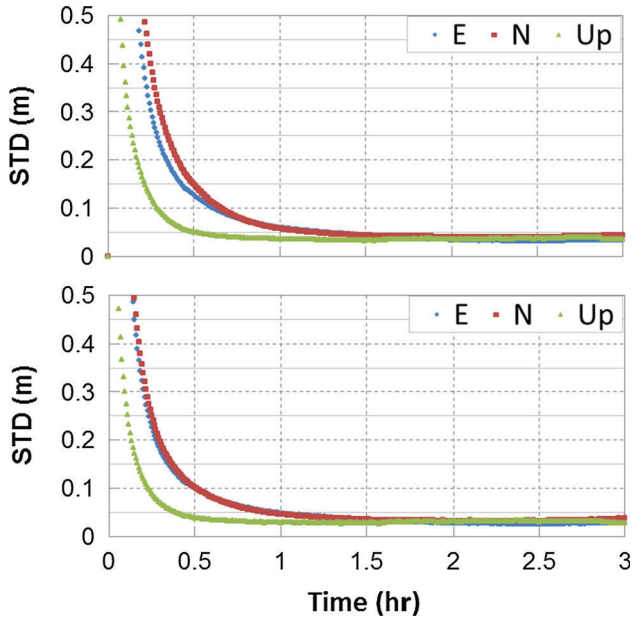

Fig. 8 PPP STD in Easting (*E*), Northing (*N*) and Up at GMSD. *Top* IGU orbits were used with predicted IGC clock corrections starting from PPP initialization. *Bottom* PPP using IGC without prediction

orbit and clock corrections without experiencing a break in communications and second when assuming a break taking place after 1 h from the start.

Results of the static tests

The average STD σ_E, σ_N and σ_U of the local grid Easting, Northing and Up (E, N and U) coordinates and convergence times of the static tests using the proposed approach are given in Table 5. The convergence time is defined as the first time that the STD reached 10 cm or less and maintained this level. In addition, the average results of PPP without prediction using only IGC products are given in the last row of the table as a reference to show the expected performance if no break was experienced. Figure 8 shows the solution precision for one test at station GMSD as an example. The top panel of the figure illustrates PPP results when the communication break is assumed at start of PPP initialization, which is the critical case among the three discussed outage cases. The bottom panel demonstrates PPP results without prediction.

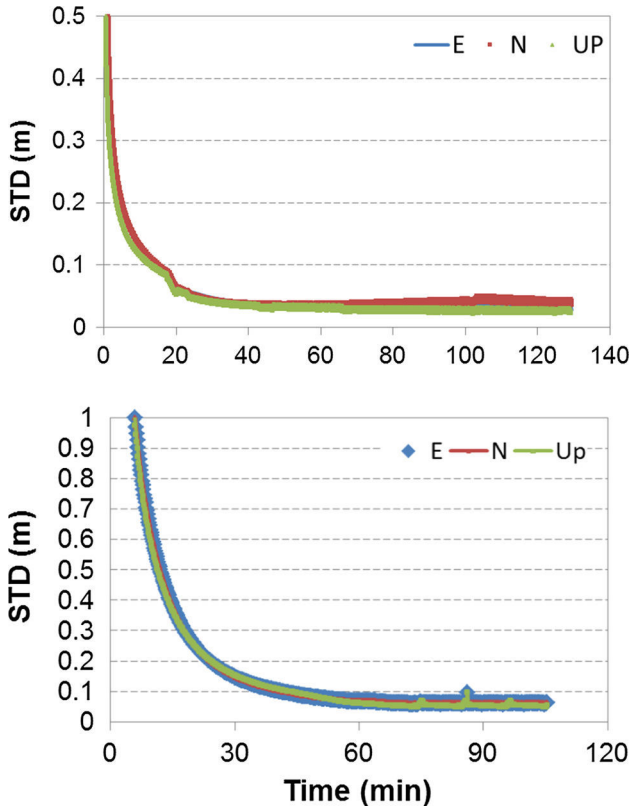

Fig. 9 PPP results of the kinematic tests; shipborne (*top*) and vehicle (*bottom*)

Results show that with the proposed method the achieved STDs after convergence were within 6 cm for a prediction period of 2 h. These results are slightly worse than PPP results without prediction that are given in the last row of Table 5. However, the convergence time needed to reduce noise of code observations over time increased with the use of the predicted orbit and clock corrections compared with the use of IGC corrections without prediction by almost 6 min.

Results of the kinematic tests

For the kinematic tests, processing was performed in post-mission to compare the results between two cases. In the first case, no outage of the IGC orbit and clock corrections was assumed, i.e., no prediction was applied. In the second

Table 6 Statistics of PPP for the kinematic tests after solution convergence with and without prediction–convergence time (min) and STD (m)

Kinematic test	With the prediction method				Without prediction			
	Conv. time	σ_E	σ_N	σ_U	Conv. time	σ_E	σ_N	σ_U
Test 1 (shipborne)	21	0.041	0.038	0.051	21	0.031	0.031	0.039
Test 2 (vehicle test)	38	0.073	0.073	0.080	38	0.068	0.067	0.075

case, a break in communications is assumed after PPP initialization, which is a more likely case in the kinematic mode. The break is assumed taking place after 1 h from the start of the test, and the proposed prediction method was used. During the two kinematic tests, the differences between the IGU and IGC orbits were within ±6 cm. The difference between the predicted IGC clock corrections using the proposed approach and their streamed values were within ±0.6 ns. Figure 9 shows results for the two kinematic tests, and Table 6 summarizes these results for the two compared cases, with and without prediction. For the first test in the shipborne mode, the solution converged after about 21 min and the average values of the E, N and Up STD were 0.035, 0.039 and 0.031 m, respectively, during which the number of satellites ranged between 8 and 10, which explained the good results obtained. The number of satellites and their geometry were not as good in the second test due to tree canopy, where five to nine satellites were observed, dropping to four at a few epochs. This resulted in the solution converged after about 38 min, and the average values of the E, N and Up STDs were 0.073, 0.073 and 0.084 m, respectively. The results of these tests are close to that of PPP without prediction of corrections as shown in Table 6 with a few millimeter increase in error when using the predicted corrections. The results of the static and kinematic tests demonstrate the practicality of the proposed method.

Conclusion

An effective and practical approach is presented to solve a major concern in real-time PPP for applications that operate for long periods. This approach can maintain decimeter-level positioning accuracy using GPS observations during outages of the precise orbit and clock corrections that may need from a few minutes to a few hours to be regained. Both IGU (predicted half) and IGS-RTS (IGC) precise orbits were found to be statistically and numerically compatible with accuracy typically within ±7 cm when referenced to the IGS final orbits and with an average difference of about 3.6 cm. Therefore, for a few minutes of corrections outage, IGC can be predicted using a high-order polynomial, and for longer outage periods it is sufficient to use the IGU predicted orbits in place of the IGC orbits. For clock corrections, we investigated prediction of IGC clock corrections as a time series. A prediction model consisting of a low-order polynomial and cyclic terms can give prediction accuracy typically within 0.5 ns during the first hour and 1 ns for the second hour with STD between 0.12 and 0.40 ns. In general, prediction of clock corrections for block IIF satellites was better than that of block IIR-M and IIR, respectively, which show the improved stability of satellite clocks of the newer generation of satellites. It is proposed that the user sequentially builds the prediction model, with a sliding time window. To reduce the computational load, the process can be performed at a suitable time interval depending on the application, e.g., every 10 min.

Validation of the proposed approach in the static and kinematic modes showed that when a break in communications is experienced, the use of the GPS–IGU orbits with IGC predicted clock corrections can achieve positioning precision less than a decimeter after the solution converged. This accuracy was maintained for up to 2 h after the break. The number of data points needed to reliably estimate the prediction parameters was chosen within a time length corresponding to a significant autocorrelation, where 1–1.5 h of data was deemed sufficient for building the prediction model. When the PPP was initialized using the predicted corrections, the convergence time increased; however, positioning precision remained less than a decimeter after solution convergence. These results can be used as an indication of performance for other data sets under similar conditions.

Acknowledgements The Institute for Geoscience Research (TIGeR), Curtin University, is acknowledged for partially funding this research.

References

Allan D (1987) Time and frequency (time-domain) characterization, estimation and prediction of precision clocks and oscillators. IEEE Trans Ultrason Ferroelectr Freq Control 34:647–654

Box G, Jenkins G, Reinsel G (1994) Time series analysis: forecasting and control, 3rd edn. Prentice-Hall, Upper Saddle River

Chatfield C, Yar M (1991) Prediction intervals for multiplicative holt-winters. Int J Forecast 7:31–37

El-Mowafy A (2006) On-the-fly prediction of orbit corrections for RTK positioning. J Navig 59(2):321–334

El-Mowafy A (2014) GNSS multi-frequency receiver single-satellite measurement validation method. GPS Solut 18(4):553–561

El-Mowafy A (2015) Estimation of multi-constellation GNSS observation stochastic properties using a single-receiver single-satellite data validation method. Surv Rev 47–341:99–108

Ferre-Pikal ES et al. (1997) Draft revision of IEEE STD 1139-1988 standard definitions of physical quantities for fundamental frequency and time metrology-random instabilities. IEEE International Frequency Control Symposium, Orlando 338–357
Hackman C (2012) Accuracy/precision of USNO predicted clock estimates for GPS satellites. 44th Annual PTTI Systems and Applications Meeting, Reston 43–52
Hadas T, Bosy J (2015) IGS RTS precise orbits and clocks verification and quality degradation over time. GPS Solut 19(1):93–105
Heo JH, Cho J, Heo MB (2010) Improving prediction accuracy of GPS satellite clocks with periodic variation behavior. Meas Sci Technol 21:1–8
Huang GW, Zhang Q, Xu GC (2014) Real-time clock offset prediction with an improved model. GPS Solut 18(1):95–104
Jin SG, Komjathy A (2010) GNSS reflectometry and remote sensing: new objectives and results. Adv Space Res 46(2):111–117
Kruskal WH, Wallis A (1952) Use of ranks in one-criterion variance analysis. J Am Stat Assoc 47(260):583–621
Montenbruck O, Gill E (2000) Satellite orbits: models, methods, and applications. Springer, Berlin Heidelberg
Leandro R et al. (2011) RTX positioning: the next generation of cm-accurate real-time GNSS positioning. In: Proc ION GNSS 2011, Institute of Navigation, Portland 1460–1475
Seppänen M et al (2012) Autonomous prediction of GPS and GLONASS satellite orbits. Navigation 59(2):119–134
Snyder JJ (1981) An ultra-high resolution frequency meter. In: Proceedings of 35th Ann, Freq. Control Symposium, Ft. Monmouth, NJ, 07703: 464–469
Trigo L, Slomovitz D (2011) Long term experimental results of a rubidium atomic clock with drift compensation. In: Proc SEMETRO 10, Natal, Brasil 1–3

Ahmed El-Mowafy is Associate Professor of Positioning and Navigation, Department of Spatial Sciences, Curtin University, Australia. He obtained his Ph.D. from the University of Calgary, Canada, in 1995. He has extensive publications in precise positioning and navigation using GNSS, quality control, integrity monitoring and estimation theory.

Manoj Deo is operational data analyst at Airservices Australia. He has a B.AppSc. (Hons Class 1A, RMIT 1998), a Master of Spatial Sc Tech (USQ, 2010), and currently pursuing a Ph.D. in the Department of Spatial Science, Curtin University, in the area of multi-constellation PPP.

Nobuaki Kubo is Associate Professor and Head of Laboratory of Communication Engineering, Faculty of Marine Technology, Tokyo University of Marine Science and Technology (TUMSAT). He has a Ph.D. from Tokyo University in 2005. His research spans precise positioning applications as well as integrations of GNSS with IMU and other sensors.

8 IMPROVED ALGORITHMS FOR PRECISE POINT POSITIONING WITH INTEGER AMBIGUITY RESOLUTION USING TRIPLE-FREQUENCY GNSS DATA

Triple frequency GNSS data presents the opportunity to improve the current methods for PPP with integer ambiguity resolution (PPP-AR). This paper proposes a novel PPP-AR method that uses triple frequency GNSS data. Firstly, an enhanced linear combination is developed for rapid fixing of the extra wide-lane (EWL) and wide lane (WL) ambiguities. This linear combination has improved performance compared to the currently used Melbourne-Wübbena (MW) linear combination. Following the correct fixing of the EWL/ WL ambiguities, a full rank triple frequency carrier phase only PPP-AR model is proposed with atmospheric constraints for rapid integer ambiguity resolution. The carrier phase equations in this model are formulated in terms of individual carrier phase ambiguities, which is estimated using the Least Squares Ambiguity Decorrelation Adjustment (LAMBDA) method (Teunissen, 1995).

This chapter is covered by the following publication:

- Deo MN, El-Mowafy A (2019) A method for Precise Point Positioning with Integer Ambiguity Resolution with Triple-frequency GNSS Data, Measurement Science and Technology, 30(6): 065009, https://doi.org/10.1088/1361-6501/ab0945.

8.1 Errata

The following corrections apply to this published paper:

- Pg. 2 of article (first column): "(3) Decoupled satellite clock (DSC) (Collins 2010)" should be replaced by "(3) Decoupled satellite clock (DSC) (Collins et al 2010)"
- Pg. 2 of article (second column, paragraph 2): "$\lambda_{IF,2-5} = 12.47cm$" should be replaced by "$\lambda_{IF,25} = 12.47cm$".
- Pg. 15 of article (References): The following reference should be removed from the reference list as it is not referenced in the main body of the paper:
    - Laurichesse D and Blot A 2016 Fast PPP convergence using multi-constellation and triple-frequency ambiguity resolution ION GNSS 2016 (Portland, Oregon, 12–16 September 2016).

PAPER

A method for precise point positioning with integer ambiguity resolution using triple-frequency GNSS data

IOP Publishing Measurement Science and Technology
Meas. Sci. Technol. **30** (2019) 065009 (16pp) https://doi.org/10.1088/1361-6501/ab0945

A method for precise point positioning with integer ambiguity resolution using triple-frequency GNSS data

Manoj Deo and Ahmed El-Mowafy

School of Earth and Planetary Sciences, Curtin University, Bentley, WA 6102, Australia

E-mail: manoj.deo01@gmail.com

Received 30 November 2018, revised 10 February 2019
Accepted for publication 21 February 2019
Published 10 May 2019

Abstract

This paper proposes a method for precise point positioning with integer ambiguity resolution (PPP-AR) using triple-frequency global navigation satellite systems (GNSS) data. Firstly, an enhanced linear combination is developed for rapid fixing of the extra wide-lane (EWL) and wide lane (WL) ambiguities. This combination has improved performance compared to the Melbourne–Wübbena linear combination, and has 6.7% lower measurement error for the GPS L1/L2 signals, 12.7% lower error for L1/L5, and 0.7% lower error for L2/L5. Comparable improvements were also determined for the Beidou and Galileo constellations.

After fixing the EWL/WL ambiguities, a full-rank, triple-frequency carrier-phase-only PPP model is proposed with ionosphere constraints. The probability of AR success rate (*P*s) is analysed with the LAMBDA method, using a range of carrier phase and regional ionospheric model (RIM) precisions. Results show that a *P*s of 99% is achieved within four epochs of data with carrier phase std = 0.002 m and RIM std = 0.1 total electron content unit (TECU); and within six epochs when RIM std = 0.5 TECU. When the carrier phase std was increased to 0.02 m (depicting high multipath conditions), and with use of a low-precision RIM (std = 0.5 TECU), the proposed method gave significantly improved performance over the method proposed by Li *et al* (2014 *GPS Solut.* **18** 429–42).

The direct estimation of the more challenging narrow-lane (NL) integer ambiguity is analysed by multi-epoch averaging of a proposed geometry-free and ionosphere-free triple-frequency linear combination. Tests with GPS data showed that 65.4% of the NL ambiguities were fixed within 10 min, 90.2% within 20 min, and 95.6% within 30 min.

Keywords: precise point positioning, ambiguity resolution, GNSS, ionosphere constraint, triple-frequency linear combination

(Some figures may appear in colour only in the online journal)

1. Introduction

Dual-frequency precise point positioning with integer ambiguity resolution (PPP-AR) is now offered as a real-time service by several commercial, scientific, and government providers such as the RTX service from Trimble (Leandro *et al* 2012), the Starfire service from Novatal (Dixon 2006, Morley and MacLeod 2015), and the PPP Wizard Project provided by CNES (Laurichesse and Privat 2015). However, the main drawback to the real-time dual-frequency PPP-AR methods is the time needed to start fixing integer ambiguities, typically around 20–30 min. This long time is attributed to the pseudo-range measurement noise, satellite geometry, multipath due to surrounding environment, and receiver and antenna quality (El-Mowafy 2014, Seepersad and Bisnath 2014).

In PPP-AR, satellite uncalibrated phase delay (UPD) is required to separate the float carrier phase ambiguities from their integer values and fix the latter. This improves the positioning accuracy from the decimetre level, achievable with standard float PPP, to the centimetre (cm) level (Laurichesse

and Privat 2015). In Cheng *et al* (2017), the three main PPP-AR methods are discussed that use ionosphere-free (IF) implementations. These are the following.

(1) Fractional cycle bias (FCB): Proposed firstly by Ge *et al* (2008) and further enhanced in Geng *et al* (2010). Here, the fractional part of the satellite wide-lane (WL) UPD is estimated using data from a network of reference stations to estimate integer WL ambiguities. These WL integer ambiguities are introduced into the IF phase combination to estimate the narrow-lane (NL) UPD. The biases are broadcast to real-time users, who apply these to the raw measurements and perform between satellite single differencing (BSSD). This eliminates the receiver biases and isolates the integer ambiguities. The integer WL ambiguity is firstly estimated by multi-epoch averaging of Melbourne–Wübbena (MW) measurements. This, along with the NL UPD, is introduced in a carrier-phase-only IF equation to fix the integer NL ambiguity. However, due to the short wavelength involved ($\lambda_{NL} = 10.7$ cm), it typically takes around 30 min to fix the NL ambiguity to get a precise solution (Geng and Bock 2013).
(2) Integer recovery clock (IRC) (Laurichesse *et al* 2009, Laurichesse and Privat 2015): This method aims to estimate common mode errors to fix integer ambiguities in undifferenced measurements. The satellite clock term is redefined to produce different clock terms for phase and code observations. The satellite-specific code and phase biases, and orbit and clock products, are estimated from a network of GNSS stations and transmitted to users. The modelling preserves the integer nature of ambiguities.
(3) Decoupled satellite clock (DSC) (Collins 2010): In this method, it was proven that the code biases also contribute to the fractional part of the carrier phase ambiguities. These were treated not as constants, but modelled as a unique signal that is functionally the same as the underlying oscillator, which is not synchronised to the phase observations. These synchronisation biases were modelled rigorously using a network of GNSS stations. By applying the decoupled clock corrections, the satellite clock term is redefined to preserve the integer nature of the ambiguity in undifferenced measurements.

Teunissen and Khodabandeh (2015) proposed PPP-RTK models based on S-System theory for a common clock and distinct clock parameterisation. The FCB, IRC, and DSC models were shown to be intrinsically the same and differ only due to the (a) choice of S-basis, (b) choice of parameterisation, and (c) choice of whether or not to eliminate the ionosphere (Teunissen and Khodabandeh 2015). However, PPP-RTK with S-basis requires sophisticated software, which is not available to a general user at present (Nadarajah *et al* 2018).

PPP-AR models with triple-frequency data follow the three carrier ambiguity resolution (TCAR) approach (Vollath *et al* 1998, Jung *et al* 2000). The extra wide lane (EWL) and WL integer ambiguities are firstly fixed using the MW geometry-free and ionosphere-free (GIF) linear combination, followed by fixing the shorter-wavelength NL ambiguity (Li 2018). In addition to the dual-frequency models, Geng and Bock (2013) presented a PPP-AR approach for the triple-frequency GPS case, where the L2/L5 EWL ambiguity was firstly resolved using the MW combination. This was then expressed in terms of L1/L2 WL carrier phase measurements to form a carrier-phase-only IF observable with $\lambda_{WL} = 3.4$ m. This was used with the L1/L2 dual-frequency IF pseudorange-only linear combination to fix the L1/L2 WL ambiguity that was used to fix the NL ambiguity. Li *et al* (2014) enhanced the step for estimating the WL ambiguity by introducing a low-noise, triple-frequency IF linear combination.

In PPP-AR, the geometry-based standard dual-frequency IF combination is not used because the noise is very high in proportion to the wavelength. For example, the GPS L1/L2, L1/L5, and L2/L5 IF combinations may be expressed in terms of the integer ambiguities $\lambda_{IF,12}\,(77N1 - 60N2)$, $\lambda_{IF,15}\,(154N1 - 115N5)$, and $\lambda_{IF,25}\,(24N2 - 23N5)$, respectively. The resulting ionosphere wavelengths for the L1/L2 and L1/L5 combinations are $\lambda_{IF,12} = 0.63$ cm, $\lambda_{IF,15} = 0.28$ cm, respectively, which are too short for meaningful integer AR. The L2/L5 combination has a larger wavelength of $\lambda_{IF,2-5} = 12.47$ cm, but the noise is about 30% of wavelength, which would make AR challenging amongst high multipath or other errors. Triple-frequency linear combination with integer coefficients has also been studied extensively. Cocard *et al* (2008) and Urquhart (2009) suggested the coefficients [4, 0, −3] for GPS L1, L2, and L5, respectively. This combination has a wavelength of 10.8 cm, with a low ionospheric factor relative to L1 of −0.01 and low noise of 5% wavelength cycle. Another combination [13, −7, −3] has almost zero ionospheric delay, but a short wavelength of only 3.6 cm and noise of 14% wavelength cycle. These integer options have very short wavelengths which are challenging to resolve in PPP-AR. Thus, these were more relevant to double-differenced models. A triple-frequency IF linear combination with measurement noise minimisation was proposed in Li *et al* (2014), whereas Deo and El-Mowafy (2016) proposed an IF mixed code-phase linear combination with noise minimisation for float-ambiguity estimation. These linear combinations include float coefficients, and thus do not enable integer AR.

Unlike relative positioning or PPP with float ambiguity estimation, PPP-AR models require use of GIF linear combinations that have a long wavelength relative to the measurement noise in cycles so as to enable easier fixing of integer ambiguities (Deng *et al* 2018, Li 2018).

In this contribution, we propose a method for PPP-AR with triple-frequency data. Firstly, an enhanced triple-frequency GIF linear combination is proposed for faster fixing of the EWL/WL ambiguities compared to the commonly used MW combination. This linear combination particularly improves the WL AR success rate, which, once resolved, may be applied to the method in Li *et al* (2014) to solve the NL ambiguity along with precise position parameters. Hence, the proposed combination enhances the approach of Li *et al* (2014). In an alternative proposed model, the EWL/WL ambiguities are used to formulate the carrier-phase-only measurements in terms of an individual ambiguity, e.g. the GPS N_2. The LAMBDA method (Teunissen 1995) may be used to fix this integer ambiguity,

along with position, troposphere, and slant ionosphere delay parameters. For rapid ambiguity fixing, a high-precision regional ionosphere model (RIM) and precise troposphere model is applied as atmospheric constraints. For cases where the N_2 integer ambiguity is not fixed, a method is proposed to directly estimate the NL integer ambiguity using a triple-frequency, carrier-phase-only GIF linear combination. This study is restricted to the GNSS constellations with triple-frequency code division multiple access (CDMA) signals. Thus, the GPS, Galileo, and Beidou constellations are included. GLONASS is excluded since it uses FDMA signals at present, although the future GLONASS K2 satellite will transmit CDMA signals. The Indian Regional Navigation Satellite System, with an operational name of NAVIC, is also excluded since it has frequency signals on the L5 (1176.45 MHz) and S band (2492.08 MHz).

The next section of this paper presents the GNSS observation equations, followed by a summary of the method proposed in Li *et al* (2014) in Section 3, and the development of improved linear combinations that enable enhanced fixing of the EWL and WL ambiguities in Section 4. Section 5 presents a detailed development of the proposed PPP-AR approach. Section 6 presents analysis and validation of the proposed method, and the finally the conclusions are presented.

2. The observation equations

The observation equations for the pseudorange and carrier phase measurements for frequency j and satellite k from a GNSS constellation, such as GPS (denoted here as G), for one receiver are

$$P_j^{k_G} = \rho^{k_G} + c\left(\mathrm{d}t_G - \mathrm{d}t^{k_G} + \mathrm{d}_{j_G} - \mathrm{d}_j^{k_G}\right) + T^{k_G} + \frac{f_1^2}{f_j^2} I^{k_G} + \varepsilon_{P_j}^{k_G} \tag{1}$$

$$\Phi_j^{k_G} = \rho^{k_G} + c\left(\mathrm{d}t_G - \mathrm{d}t^{k_G} + \delta_{j_G} - \delta_j^{k_G}\right) + T^{k_G} - \frac{f_1^2}{f_j^2} I^{k_G} + \lambda_j N_j^{*k_G} + \varepsilon_{\Phi_j}^{k_G} \tag{2}$$

where P_j is the pseudorange and Φ_j is the carrier phase measurement in distance units; f_j is the transmitting frequency; ρ^{k_G} is the satellite-to-receiver geometric range; c is the speed of light in vacuum; $\mathrm{d}t_G$ and $\mathrm{d}t^{k_G}$ are the receiver and satellite clock offsets, where the latter is eliminated in PPP by the use of precise clock corrections; T^{k_G} is the tropospheric delay; λ_j denotes the wavelength for frequency j; I^{k_G} is the ionosphere error for a reference frequency, e.g. $i = \mathrm{L1}$ for GPS; and $\varepsilon_{\Phi_j}^{k_G}$ and $\varepsilon_{P_j}^{k_G}$ include measurement noise and multipath of the phase and code measurements, respectively. d_{j_G} is the receiver hardware bias for code measurements on frequency j. Similarly, $\mathrm{d}_j^{k_G}$ is the satellite hardware bias, which also includes the satellite differential code biases (DCBs) of a reference IF combination (e.g. L1/L2 pseudoranges for GPS) that exists because of the use of satellite clock offsets determined from IF measurements with embedded DCBs. The DCB corrections are externally available for the GNSS satellites (including GPS, Galileo, and Beidou, for example) from the IGS multi-GNSS experiment (MGEX) website at http://mgex.igs.org (Montenbruck *et al* 2014, Guo *et al* 2015, Wang *et al* 2015). Likewise, δ_{j_G} and $\delta_j^{k_G}$ are the receiver and satellite hardware biases for the carrier phase measurements. $N_j^{*k_G}$ is the non-integer ambiguity term containing the fractional phase biases in the receiver and satellite hardware.

In this study, it is assumed that users have applied the satellite carrier phase and code biases, including UPD and DCB biases, available *a priori* from external sources, and performed BSSD of measurements to remove receiver hardware biases and clock error. Also, when integrating measurements from several constellations, additional biases such as inter-system biases and inter-system satellite time offsets must be considered (El-Mowafy *et al* 2016). In the following sections, for simplicity, we assume the same measurement precision denoted by standard deviations (std) for carrier phase and for code measurements for all available triple frequencies i,j, and k, noting that individual values can be applied. Thus, $\sigma_\Phi = \sigma_{\Phi_i} = \sigma_{\Phi_j} = \sigma_{\Phi_k}$ and $\sigma_P = \sigma_{P_i} = \sigma_{P_j} = \sigma_{P_k}$.

3. Summary of the approach in Li *et al* (2014)

This paper makes several comparisons to the approach presented in Li *et al* (2014). Therefore, this section briefly summarises this approach, hereafter referred to as Li's method.

Equation (7) in Li's paper was the MW linear combination for GPS L1-L2, which was recommended to be used with the WL UPD bias to estimate the WL ambiguity by multi-epoch averaging Geng and Bock (2013). Equation (8) was the carrier-phase-only IF combination, which was presented as a function of the N_1 and N_{WL} ambiguities. Equation (9) was the well-known dual-frequency pseudorange IF combination. Equation (10) was the MW linear combination for GPS L2–L5, which if used with the EWL UPD, can estimate N_{EWL} in just a few epochs. Equation (13) was a new triple-frequency carrier phase-only linear combination that was presented as a function of N_{WL} and N_{EWL}. This is a geometry-based model, and N_{WL} has a wavelength of 3.403 m. It was recommended to use this model to estimate N_{WL} along with position, and avoid using equation (7). Equation (14) was a triple-frequency pseudorange-only linear combination with noise minimisation, also proposed in Deo and El-Mowafy (2016). Li suggested replacing equation (9) with (14), since this was a more precise pseudorange, and use equations (14) with (8) to estimate N_1 along with cm-level precise position. Alternatively, if N_{WL} is known, equation (13) also becomes a precise pseudorange, which was represented as equation (16). Thus, equation (16) could also be used with equation (8) in the PPP-AR model to solve for the N_1 ambiguity along with precise position parameters.

The key focus of Li's method was to enhance the estimation of the WL ambiguity. However, the coefficients in equation (13) had large values (17.8854, −84.7059, 67.8205), and thus the overall measurement noise increases rapidly with increasing carrier-phase noise. Therefore, the next section of this paper proposes an improved linear combination

Table 1. Proposed combination coefficients for GPS, Beidou Phase II, and Galileo signals, with the measurement noise propagation compared to MW, and as a fraction of the WL wavelength (λ_{WL}). The std of measurement noise was computed using a carrier phase and pseudorange stds of 0.002 and 0.4 m, respectively.

GNSS	f_i	f_j	α	β	γ	λ_{WL}(m)	Std proposed comb (m)	Std MW (m)	Improvement in std over MW (%)	Proposed comb. Std as fraction of λ_{WL}
GPS/ QZSS	L2	L5	−0.012 11	−0.444 99	−0.5429	5.861	0.289	0.291	0.70	0.049
	L1	L5	−0.523 18	−0.267 34	−0.209 48	0.751	0.250	0.286	12.68	0.332
	L1	L2	−0.598 33	−0.241 22	−0.160 45	0.862	0.266	0.285	6.69	0.309
Beidou	B3	B2	−0.019 95	−0.552 58	−0.427 48	4.884	0.285	0.289	1.14	0.058
	B1	B3	−0.597 33	−0.148 65	−0.254 03	1.025	0.267	0.285	6.31	0.260
	B1	B2	−0.4972	−0.218 69	−0.284 11	0.847	0.245	0.285	13.99	0.290
Galileo	E5b	E5a	−0.004 35	−0.527 51	−0.468 14	9.768	0.303	0.303	0.23	0.031
	E1	E5b	−0.589 49	−0.182 14	−0.228 37	0.814	0.263	0.286	7.75	0.324
	E1	E5a	−0.544 48	−0.208 71	−0.246 81	0.751	0.253	0.286	11.37	0.337

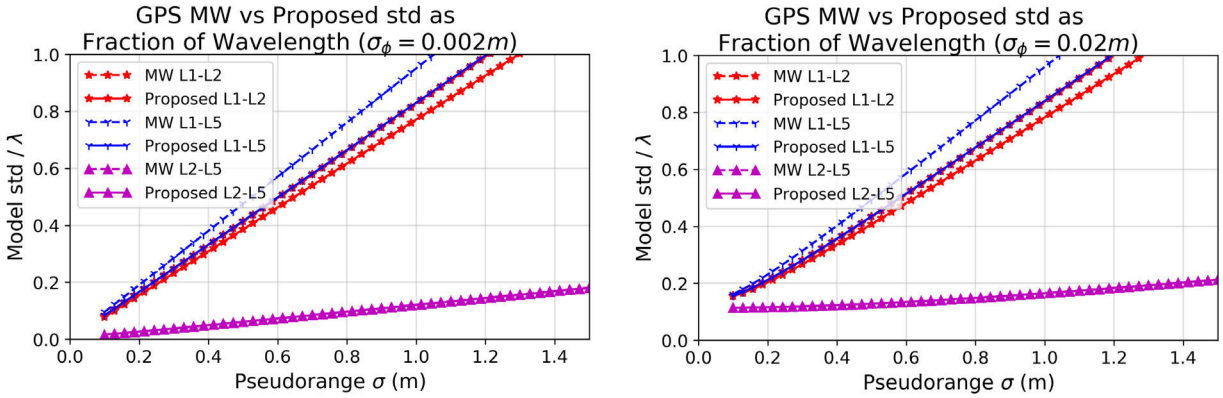

Figure 1. Comparison of the measurement std propagation in the proposed linear combination with the MW linear combination for *GPS* with pseudorange std between 0.1–1.5 m and carrier phase std of 0.002 m (left) and 0.02 m (right).

for estimating the N_{WL} and N_{EWL} ambiguities. This may be substituted into equations (13) to give (16) in Li's method, or used in an alternative PPP-AR strategy.

4. Improved linear combination for EWL and WL ambiguity estimation

The first part of this section presents the development of an enhanced code-carrier combination which preserves the EWL/WL ambiguity but has lower measurement noise than MW. Following this, the performance of this model is compared to the WL ambiguity-resolution method presented in Li *et al* (2014).

4.1. Formation of improved combination

For a user accessing triple-frequency carrier phase and code measurements, a linear combination is formed as follows:

$$\psi_{ij} = \frac{c}{f_i - f_j}(\phi_i - \phi_j) + \alpha_{ij}P_i + \beta_{ij}P_j + \gamma_{ij}P_k \qquad (3)$$

where ϕ_i and ϕ_j are the carrier phase measurements in cycle units for frequencies i and j, respectively; P_i, P_j, and P_k are the code measurements in distance units; α_{ij}, β_{ij}, and γ_{ij} are the combination coefficients associated with frequencies i and j, applied for code measurements; and f_i, f_j are the transmitting frequencies. The coefficient $\frac{c}{f_i - f_j}$ ensures that a WL ambiguity persists in this combination, whereas the pseudorange coefficients for the three frequencies enable reduction of the overall measurement noise. The satellite and receiver identifiers have been removed for simplicity since the equation is concerned with a single receiver and satellite. A similar equation may be formed for carrier frequencies i and k as

$$\psi_{ik} = \frac{c}{f_i - f_k}(\phi_i - \phi_k) + \alpha_{ik}P_i + \beta_{ik}P_j + \gamma_{ik}P_k \qquad (4)$$

where ϕ_k is the carrier phase measurement for frequency k on transmitting frequency f_k. The carrier phase coefficients in cycle units of $+1$ and -1 ensure that the WL phase ambiguity is preserved. When expressing phase measurements in distance units ($\Phi_i = \lambda_i\phi_i, \Phi_j = \lambda_j\phi_j$), equation (3) becomes

$$\Psi_{ij} = \frac{f_i}{f_i - f_j}\Phi_i - \frac{f_j}{f_i - f_j}\Phi_j + \alpha_{ij}P_i + \beta_{ij}P_j + \gamma_{ij}P_k. \qquad (5)$$

In determining the coefficients α_{ij}, β_{ij}, and γ_{ij}, three conditions are placed such that the resulting combination is geometry-free, first-order IF, and has least measurement noise propagation. The resulting combination replaces the MW combination with the advantage of lower measurement noise, hence enabling faster ambiguity resolution. The first-order IF

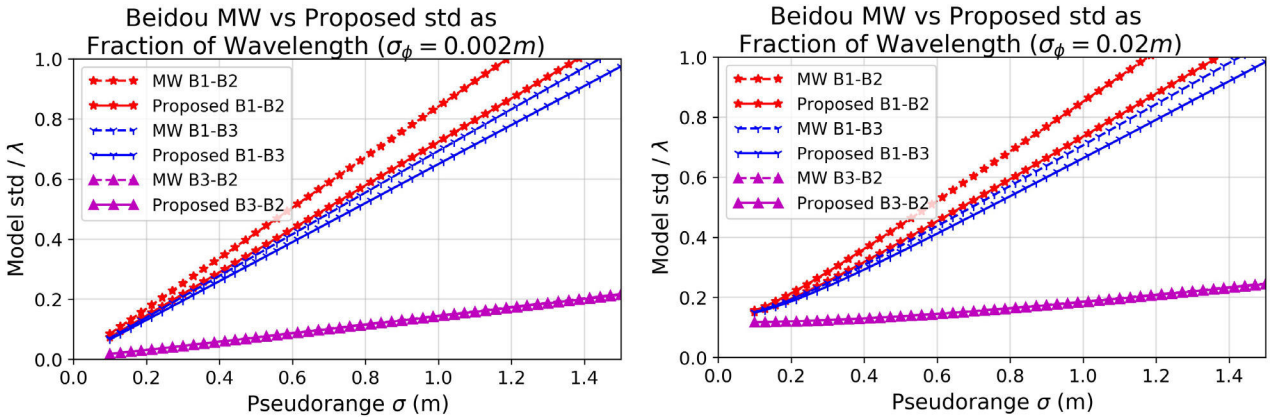

Figure 2. Comparison of the measurement std propagation in the proposed linear combination with the MW linear combination for *Beidou* with pseudorange std between 0.1–1.5 m and carrier phase std of 0.002 m (left) and 0.02 m (right).

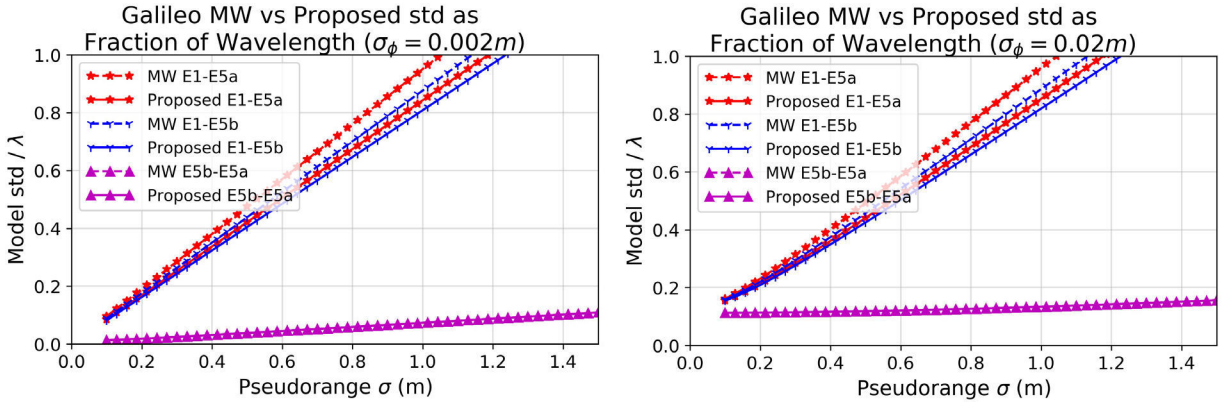

Figure 3. Comparison of the measurement std propagation in the proposed linear combination with the MW linear combination for *Galileo* with pseudorange std between 0.1–1.5 m and carrier phase std of 0.002 m (left) and 0.02 m (right).

condition is achieved by equating the sum of the ionospheric terms in equation (5) to zero as

$$\frac{f_i}{f_i - f_j}\frac{f_1^2}{f_i^2}I + \frac{f_j}{f_i - f_j}\frac{f_1^2}{f_j^2}I + \alpha_{ij} + \beta_{ij}\frac{f_1^2}{f_j^2}I + \gamma_{ij}\frac{f_1^2}{f_k^2}I = 0 \quad (6)$$

which is rearranged by placing the known terms to the right-hand side of the equation as follows:

$$\alpha_{ij} + \beta_{ij}\frac{f_1^2}{f_j^2} + \gamma_{ij}\frac{f_1^2}{f_k^2} = \frac{f_1^2}{f_i^2 - f_i f_j} - \frac{f_1^2}{f_i f_j - f_j^2}. \quad (7)$$

The geometry-free condition is achieved by equating the geometry terms in equation (5) to zero, expressed as

$$\frac{f_i}{f_i - f_j}\rho - \frac{f_j}{f_i - f_j}\rho + \alpha_{ij}\rho + \beta_{ij}\rho + \gamma_{ij}\rho = 0 \quad (8)$$

which results in

$$\alpha_{ij} + \beta_{ij} + \gamma_{ij} = \frac{f_j - f_i}{f_i - f_j}. \quad (9)$$

The carrier phase coefficients given in equation (4) are known constants due to preservation of the WL ambiguity. Therefore, the measurement noise minimisation is achieved by minimising the sum of the squares of the code coefficients as

$$\alpha_{ij}^2 + \beta_{ij}^2 + \gamma_{ij}^2 = \text{MIN}. \quad (10)$$

The conditions in equations (7), (9), and (10) are applied to solve for the code coefficients α_{ij}, β_{ij}, and γ_{ij}. The resulting GIF combination contains the integer WL ambiguity presented as

$$N_{ji} = N_i - N_j = \phi_i - \phi_j + \frac{f_i - f_j}{c}\left(\alpha_{ij}P_i + \beta_{ij}P_j + \gamma_{ij}P_k\right) + \varepsilon \quad (11)$$

where the ε term contains satellite and receiver fractional hardware biases and multipath. The N_{ji} WL ambiguity may now be fixed by averaging multiple epochs of data (Ge *et al* 2008, Laurichesse *et al* 2009, Geng *et al* 2010). The combination coefficients evaluated for different signal combinations for GPS (G), Beidou Phase II (C), and Galileo (E) signals are given in table 1. The future Beidou Phase III frequencies B1C, B2a, and B2b coincide with the Galileo E1, E5a, and E5b frequencies (Lu and Yao 2014). Also given is the measurement noise expressed by the std in the proposed and MW combinations as a fraction of λ_{WL}. The std values, in distance units, were computed using $\sigma_\Phi = 0.002$ m and $\sigma_P = 0.4$ m as

$$\sigma_{ij} = \sqrt{\sigma_\Phi^2\left(a_{ij} + b_{ij}\right) + \sigma_P^2\left(\alpha_{ij}^2 + \beta_{ij}^2 + \gamma_{ij}^2\right)} \quad (12)$$

where $a_{ij} = \frac{f_i^2}{(f_i - f_j)^2}$ and $b_{ij} = \frac{f_j^2}{(f_i - f_j)^2}$. Figure 1 compares the propagation of measurement noise in this proposed linear combination to the MW combination for GPS with

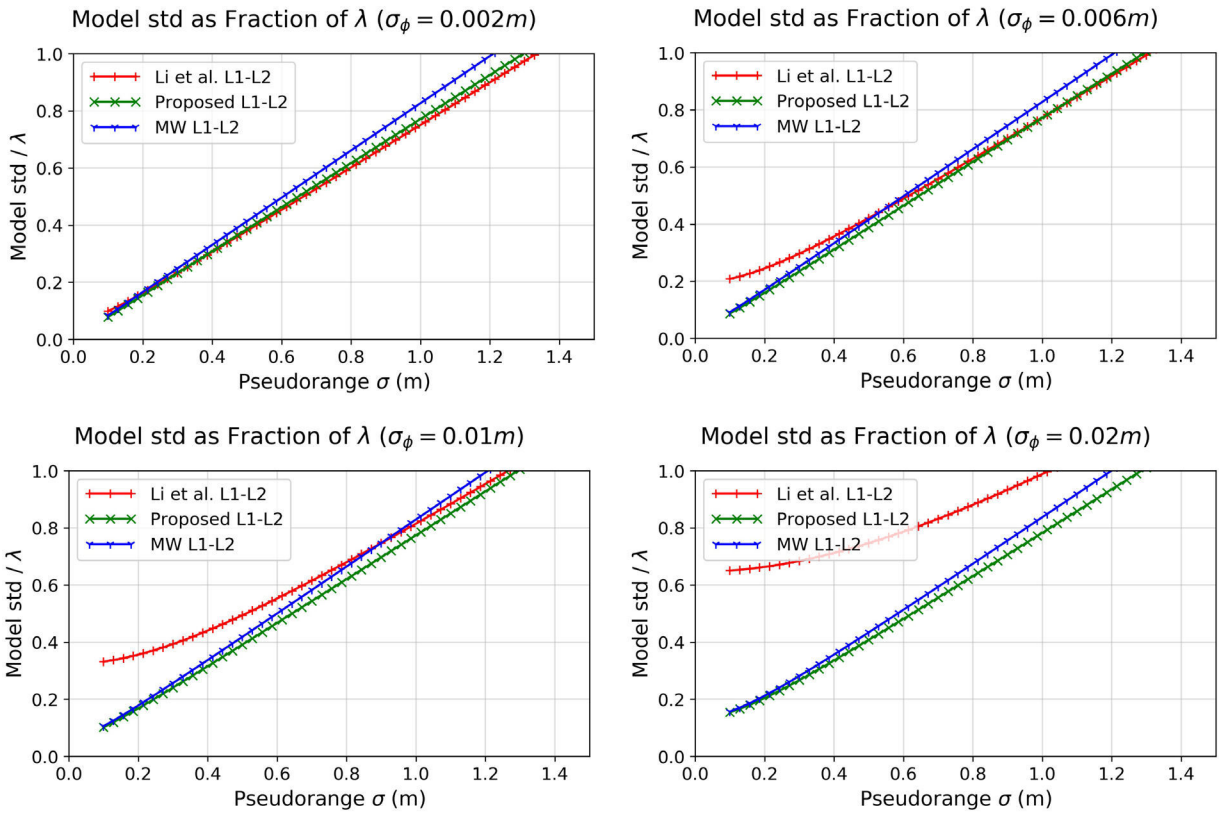

Figure 4. Comparison of measurement std propagation as a fraction of the wavelength for estimation of the GPS N_{21} WL ambiguity for the model presented in Li *et al* (2014), the MW model, and the proposed model with pseudorange std in the range 0.1–1.5 m and carrier phase std of 0.002 m (top left), 0.006 m (top right), 0.01 m (bottom left), and 0.02 m (bottom right).

$0.1\,\text{m} \leqslant \sigma_P \leqslant 1.5\,\text{m}$ and carrier phase std of 0.002 m (left) and 0.02 m (right). This range of std values depicts measurement quality during low- to high-multipath conditions as reported in Liu *et al* (2016) and Ray *et al* (1999). As shown in table 1 and figure 1, the improvements in std when using the proposed combination over MW are 6.7% for L1–L2, 12.7% for L1–L5 and 0.7% for L2–L5. There is a substantial improvement in measurement noise propagation for the L1–L5 combination that becomes apparent as the pseudorange std increases. At $\sigma_P = 1.0\,\text{m}$, the std of the measurement noise in the proposed combination is a factor of 0.8 of the wavelength, whereas this std is about the same as the wavelength for MW. The increase in carrier phase std has little impact when $\sigma_P > 0.2\,\text{m}$ for the WL combinations. The improvement for the L1–L2 proposed combination is also substantial, and these results are promising for the rapid estimation of the L1–L2 and L1–L5 ambiguities. The L2–L5 EWL ambiguity, with a measurement noise factor of less than 5% of the wavelength, is expected to be resolved instantly with both methods.

Figure 2 compares the measurement noise propagation in the proposed linear combination with MW for Beidou, whereas figure 3 compares the same for Galileo. Similar improvements in measurement noise propagation for the WL combinations are seen for these constellations. The difference in EWL measurement noise for GPS L2–L5, Beidou B3–B2, and Galileo E5b–E5a is practically the same (within 1.1%) for the proposed combination versus the MW combination. As a result, their noise profiles seem to overlap each other in figures 1–3.

4.2. Comparison of the improved model to Li's method

In Li's method, a model was presented for fixing the WL ambiguity, following the estimation of the EWL ambiguity. This required combining equations (13) and (14) in their paper to form a GIF linear combination, which has a long wavelength of 3.403 m. In doing so, users need to apply the WL and EWL UPD biases to equation (13) and the DCBs to equation (14) to get rid of hardware delays. Subtracting equations (14) from (13) results in elimination of the geometry, clock, and troposphere terms. Since N_{EWL} is known, the only unknown that remains is N_{WL}, which can be estimated by multi-epoch averaging. We compare the performance of our proposed method with Li's method for estimating the N_{21} WL ambiguity for the GPS case. Figure 4 shows the comparison of the measurement std as a fraction of wavelength in the proposed, MW, and Li's models using error propagation law. The pseudorange std is in the range 0.1–1.5 m, whereas the carrier phase std has values of 0.002, 0.006, 0.010, and 0.02 m. As the figure shows, with a carrier phase std of 0.002 m and pseudorange std less than 0.4 m, the proposed combination performs better than Li's model. As the pseudorange std increases above 0.4 m, the proposed model performs comparably at the same level, although there is a slight degradation. As the carrier phase std is increased to

Table 2. Suggested steps for PPP-AR procedure for GPS, Galileo, and Beidou triple-frequency signals.

Step No.	GPS	λ (m)	Galileo	λ (m)	Beidou	λ (m)
1	$N_{52} = N_2 - N_5$	5.861	$N_{5ab} = N_{5b} - N_{5a}$	9.768	$N_{B23} = N_{B3} - N_{B2}$	4.884
2	$N_{21} = N_1 - N_2$	0.862	$N_{5b1} = N_1 - N_{5b}$	0.814	$N_{B31} = N_{B1} - N_{B3}$	1.025
3	X, Y, Z, ZWD, I, N_2	0.244	X, Y, Z, ZWD, I, N_{5b}	0.248	X, Y, Z, ZWD, I, N_{B3}	0.236

0.006, 0.010, and then to 0.02 m, the measurement std in Li's model is higher than the proposed model, and is well above both the proposed and MW models in the case of carrier phase std = 0.02 m. This occurs despite a long wavelength of 3.4 m in Li's model due to the large values of carrier phase coefficients (17.8854, −84.7059, 67.8205). Such rapid increase in the overall measurement noise would make it challenging to fix the N_{21} WL ambiguity in high-multipath environments.

5. Proposed PPP-AR method

This section proposes PPP-AR methods that use the EWL and WL ambiguities estimated with the improved linear combination presented in the previous section. The first method uses triple-frequency carrier-phase-only measurements to fix the N_2 ambiguity using the LAMBDA method, along with other parameters. The second method attempts to fix the NL ambiguities directly using linear combinations in the measurement domain. Although GPS is given as an example, the proposed procedure can be applied to other GNSS constellations having triple-frequency data.

5.1. PPP-AR with carrier phase measurements

This method reformulates the triple-frequency carrier-phase-only measurements in terms of the N_2 integer ambiguity, the best candidate for which is estimated using ILS principles. The LAMBDA is used for searching for the most likely integer candidate for N_2, taking into account the correlations in the ambiguity variance matrix (Teunissen 1995). If all the N_2 ambiguities are not successfully fixed, a partial ambiguity resolution approach may be applied (Li 2018).

The $N_{52} = N_2 - N_5$ EWL integer ambiguity, with a wavelength of 5.861 m and measurement noise component of only 4.9%, is estimated by multi-epoch averaging of the equation

$$N_{52} = N_2 - N_5 = \phi_2 - \phi_5 + \frac{f_2 - f_5}{c}(\alpha_{25}P_1 + \beta_{25}P_2 + \gamma_{25}P_5) + \varepsilon. \tag{13}$$

Similarly, the $N_{21} = N_1 - N_2$ WL ambiguity, with a wavelength of 0.862 m and measurement noise component of 30.9%, is estimated with the equation

$$N_{21} = N_1 - N_2 = \phi_1 - \phi_2 + \frac{f_1 - f_2}{c}(\alpha_{12}P_1 + \beta_{12}P_2 + \gamma_{12}P_5) + \varepsilon. \tag{14}$$

Finally, the $N_{51} = N_1 - N_5$ WL ambiguity, with a wavelength of 0.751 m and measurement noise component of 33.2%, is estimated with the equation

$$N_{51} = N_1 - N_5 = \phi_1 - \phi_5 + \frac{f_1 - f_5}{c}(\alpha_{15}P_1 + \beta_{15}P_2 + \gamma_{15}P_5) + \varepsilon. \tag{15}$$

After fixing the integer EWL ambiguity N_{52} and the two WL ambiguities N_{21} and N_{51}, the following relationships exist:

$$\begin{aligned} N_1 &= N_2 + N_{21} \\ N_2 &= N_5 + N_{52} \\ N_5 &= N_1 - N_{51}. \end{aligned} \tag{16}$$

However, the N_{51} WL ambiguity is dependent on the other EWL/WL ambiguities and may be estimated from the relation

$$N_{51} = N_{21} + N_{52}. \tag{17}$$

This may be used to check the determined value for any of the EWL/WL ambiguities, or may be applied as a constraint. According to equation (16), both N_1 and N_5 ambiguities may be expressed in terms of the N_2 ambiguity. Inserting equations (16) into (2) results in the following equations:

$$\Phi_1 - N_{21}\lambda_1 = \rho^* + N_2\lambda_1 - I + \varepsilon_{\Phi_1} \tag{18}$$

$$\Phi_2 = \rho^* + N_2\lambda_2 - \frac{f_1^2}{f_2^2}I + \varepsilon_{\Phi_2} \tag{19}$$

$$\Phi_5 + N_{52}\lambda_5 = \rho^* + N_2\lambda_5 - \frac{f_1^2}{f_5^2}I + \varepsilon_{\Phi_5} \tag{20}$$

where the ρ^* term includes the geometry, troposphere delay, and receiver clock error if BSSD measurements are not used. The N_2 ambiguity can now be estimated from equations (18) to (20). The ionosphere delay may be estimated either as an unknown parameter or by using a precise RIM to apply a constraint. The former case would take significantly longer time to reliably fix the N_2 ambiguity due to additional unknown parameters. Since only the carrier phase measurements are used, users can expect cm-level PPP accuracy once the N_2 ambiguity is fixed.

In Li's method, the NL ambiguity is estimated using the L1/L2 dual-frequency IF carrier phase equations formulated in terms of the N_{21} WL and N_1 integer ambiguities. This combination is used together with a triple-frequency carrier-phase-only linear combination that is expressed in terms of the N_{52} EWL and N_{21} WL ambiguities. However, such formulations are avoided here, since there are sufficient carrier phase measurements to solve for the unknown parameters. By not using the noisier IF combinations used in conventional PPP-AR methods, measurement noise amplification is avoided. Also, since the N_2 wavelength ($\lambda_{L2} = 24.4$ cm) is more than twice the NL ambiguity, it becomes easier to estimate. Ultimately, the NL ambiguity-fixing problem is reduced to just N_2 ambiguity fixing. Equations (18)–(20) in carrier phase cycle units are

$$\phi_1 - N_{21} = \frac{\rho}{\lambda_1} + \frac{T}{\lambda_1} + N_2 - \frac{I}{\lambda_1} + \varepsilon_{\phi_1} \tag{21}$$

$$\phi_2 = \frac{\rho}{\lambda_2} + \frac{T}{\lambda_2} + N_2 - \frac{f_1^2}{f_2^2}\frac{I}{\lambda_2} + \varepsilon_{\phi_2} \tag{22}$$

$$\phi_5 + N_{52} = \frac{\rho}{\lambda_5} + \frac{T}{\lambda_5} + N_2 - \frac{f_1^2}{f_5^2}\frac{I}{\lambda_5} + \varepsilon_{\phi_5}. \tag{23}$$

For n tracked satellites with triple-frequency data and BSSD of measurements, there are $3(n-1) = 3n-3$ observations, $n-1$ ambiguities, $n-1$ slant ionosphere terms, three position parameters, and a common troposphere term per epoch; hence a total of $2(n-1)+4 = 2n+2$ unknown parameters. This system is solvable with a minimum of five tracked satellites, as is the case for other PPP models.

If using a RIM, its precision must be better than half the N_2 wavelength. Such precision was reported in Rovira-Garcia *et al* (2016), where a std of 0.25 total electron content unit (TECU) was achieved in a mid-latitude GNSS network with station inter-spacing of less than 100 km. This would have residual ionospheric errors of 4.1 cm for GPS L1, 6.7 cm for L2, and 7.3 cm for L5, which are well below the N_2 wavelength. By eliminating the ionospheric delay parameter for each line-of-sight measurement, the number of unknown parameters is reduced to just $n+3$, resulting in a significant gain in geometry. Deo and El-Mowafy (2017) reported significant reduction in float PPP convergence time when modelling out the ionosphere, resulting in sub-5 cm horizontal accuracy within a few minutes.

The suggested steps for the PPP-AR procedure is summarised in table 2 for GPS, Galileo, and Beidou. The EWL and WL ambiguities are resolved concurrently by multi-epoch averaging of equations (14) and (15). This is followed by estimation of a selected ambiguity (e.g. GPS N_2) using equations (21)–(23).

5.2. Direct estimation of NL integer ambiguity

This section proposes a method to estimate the NL ambiguity directly using linear combinations in the measurement domain, through sequential rounding over several epochs. Although this method is less optimal than integer least squares (ILS), it has an advantage in that the ambiguity estimation does not require a search, and can therefore be computed directly (Teunissen 1998). To get cm-level accuracy in PPP-AR, the NL ambiguity must be fixed to recover the individual carrier phase ambiguities (Li 2018). NL ambiguity resolution is comparatively more challenging than the EWL/WL ambiguities due to the short wavelength involved. This is true even in the context of relative positioning, where double differencing is applied using measurements from a reference receiver (Li *et al* 2010).

From equations (18) to (20), a GIF linear combination of triple-frequency phase-only measurements is formulated that has minimum measurement error propagation. This allows direct estimation of the NL ambiguity as

$$\begin{aligned}\Phi_{\mathrm{IF-GF},1,2,5} &= \alpha_1\tilde{\Phi}_1 + \alpha_2\Phi_2 + \alpha_3\tilde{\Phi}_5 \\ &= N_2(\lambda_1\alpha_1 + \lambda_2\alpha_2 + \lambda_5\alpha_5) + \varepsilon_{\mathrm{IF-GF}}\end{aligned} \tag{24}$$

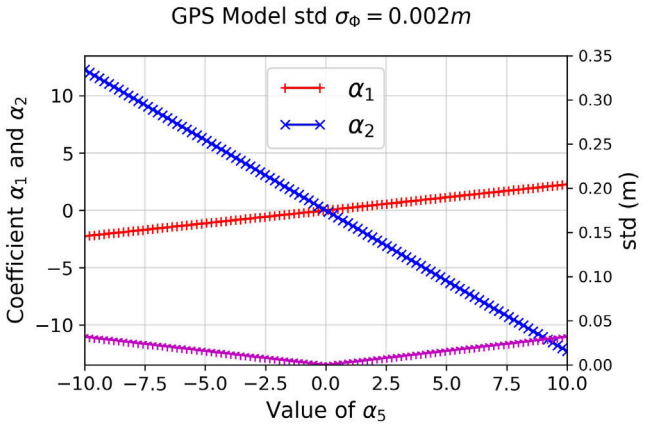

Figure 5. Coefficient values and overall measurement error for the triple-frequency, geometry-free, and IF linear combination of GPS carrier phase observations with standard deviation of 0.002 m.

where

$$N_2 = \frac{\Phi_{\mathrm{IF-GF},1,2,5}}{\lambda_1\alpha_1 + \lambda_2\alpha_2 + \lambda_5\alpha_5} + \varepsilon_{\mathrm{IF-GF}}. \tag{25}$$

The geometry-free condition is achieved by

$$\alpha_1 + \alpha_2 + \alpha_5 = 0. \tag{26}$$

The first-order IF condition is achieved by equating the sum of the ionospheric terms to zero (Deo and El-Mowafy 2016) as

$$\frac{\alpha_1}{f_1^2} + \frac{\alpha_2}{f_2^2} + \frac{\alpha_5}{f_5^2} = 0. \tag{27}$$

The measurement error minimisation is achieved by minimising the sum of the squares of the coefficients as

$$\alpha_1^2 + \alpha_2^2 + \alpha_5^2 = \mathrm{MIN}. \tag{28}$$

After some algebraic manipulation, we get the following equations for α_1 and α_2:

$$\alpha_1 = \alpha_5\frac{f_1^2f_2^2 - f_1^2f_5^2}{f_1^2f_5^2 - f_2^2f_5^2} \tag{29}$$

$$\alpha_2 = \alpha_5\frac{f_2^2f_5^2 - f_1^2f_2^2}{f_1^2f_5^2 - f_2^2f_5^2}. \tag{30}$$

Squaring equations (29) and (30) and substituting into equation (28), the following equality is obtained:

$$2\alpha_5^2\frac{f_1^4f_2^4 + f_2^4f_5^4 + f_1^4f_5^4 - f_1^4f_2^2f_5^2 - f_2^4f_5^2f_1^2 - f_5^4f_1^2f_2^2}{\left(f_1^2f_5^2 - f_2^2f_5^2\right)^2} = \mathrm{MIN}. \tag{31}$$

This is a quadratic equation of the form $A\alpha_5^2$ which is a minimum at $\alpha_5 = 0$, and thus $\alpha_2 = \alpha_1 = 0$. To get real-valued solutions, we selected suitable values for α_5 and calculated corresponding values for α_2 and α_1 using equations (29) and (30). Due to the quadratic nature of equation (31), it is known that the minimum measurement error propagation occurs when α_5 is zero. Therefore, we experimented with α_5 values in the range -10 to 10. Figure 5 shows the corresponding coefficient values for α_2 and α_1 with carrier phase std = 0.002 m.

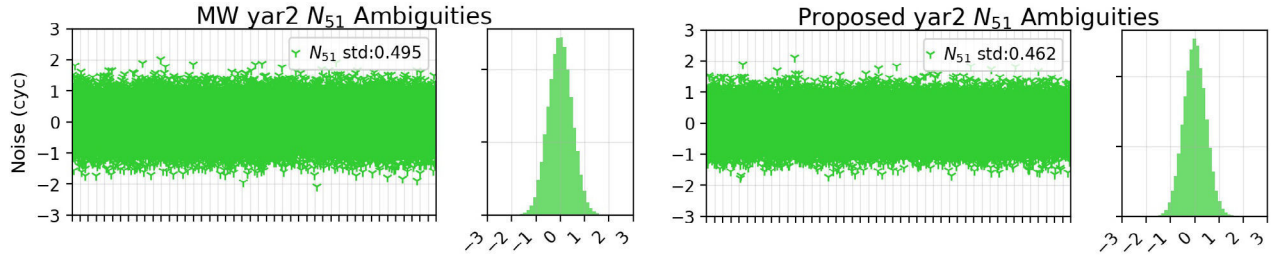

Figure 6. Time series and histogram of the single-differenced N_{51} WL ambiguities with the MW method (left) and proposed method (right) at site YAR2 for all observed satellite pairs.

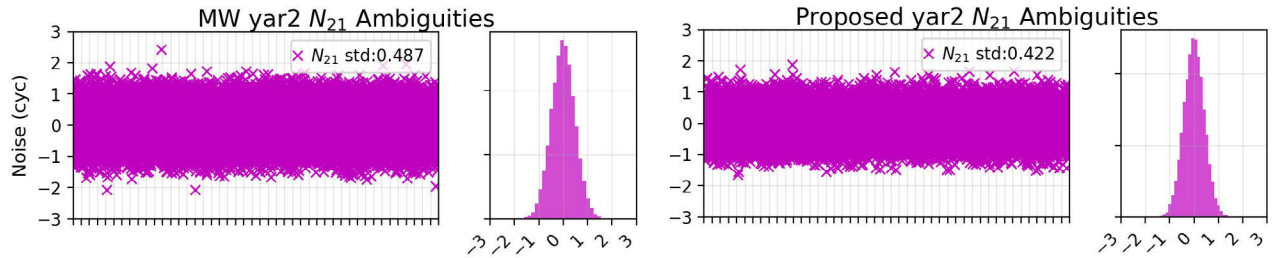

Figure 7. Time series and histogram of the single-differenced N_{21} WL ambiguities with the MW method (left) and proposed method (right) at site YAR2 for all observed satellite pairs.

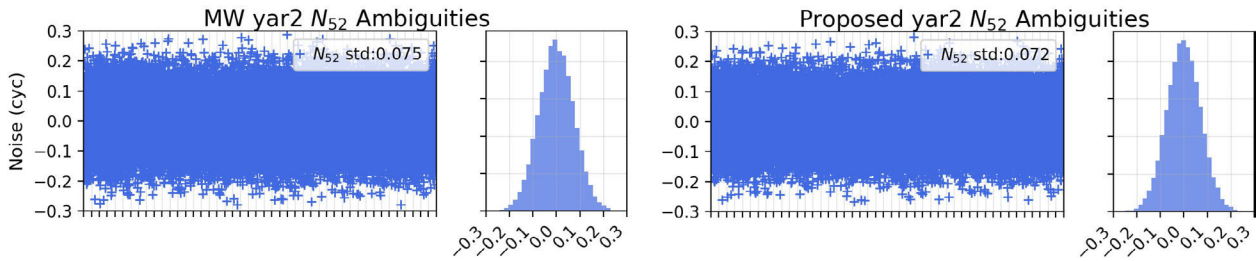

Figure 8. Time series and histogram of the single-differenced N_{52} WL ambiguities with the MW method (left) and proposed method (right) at site YAR2 for all observed satellite pairs.

As shown, the overall measurement error is minimal when all coefficients are equal to zero, and it increases as the α_5 value diverges away from zero. It was also verified that the overall measurement error increased by a factor of 10 when the carrier phase std increased from 0.002 to 0.020 m. When estimating N_2 with equation (24), users may select an arbitrary value for α_5 as long as α_2 and α_1 are calculated using equations (29) and (30), because the division by the wavelength scales it to a constant unit.

It is evident that the geometry term is common in equations (18)–(20). Thus, differencing equations (18) and (19), and equations (19) and (20) will result in two equations with the geometry term eliminated and only two remaining unknowns, namely the ionosphere and the N_2 ambiguity. Since there are two equations, the two unknowns may be directly estimated as follows:

$$I = \frac{\left(\tilde{\Phi}_1 - \tilde{\Phi}_5\right)(\lambda_1 - \lambda_2) - \left(\tilde{\Phi}_1 - \Phi_2\right)(\lambda_1 - \lambda_5)}{\lambda_2 - \lambda_5 - \frac{f_1^2}{f_2^2}(\lambda_1 - \lambda_5) + \frac{f_1^2}{f_5^2}(\lambda_1 - \lambda_2)} \tag{32}$$

$$N_2 = \frac{\tilde{\Phi}_1 - \Phi_2 + I - \frac{f_1^2}{f_2^2} I}{(\lambda_1 - \lambda_2)}. \tag{33}$$

Numerical analysis of this model showed that it is equivalent to the results obtained using equation (24).

6. Analysis

This section presents analysis of the proposed PPP-AR method using simulated test data at four Australian sites, namely Hobart (HOB2), Alice Springs (ALIC), Yarragadee (YAR2), and Townsville (TOW2). The data was for a 24 h period at an epoch rate of 15 s, and BSSD measurements were used in the analysis.

6.1. Analysis of the EWL and WL ambiguity resolution

Firstly, the performance of the improved linear combinations proposed in section 3 is compared with that of the standard MW approach for estimating the EWL/WL ambiguities. Figure 6 compares the time series and histogram for the N_{51} WL ambiguities at YAR2 for all the observed satellite pairs, where the mean value is subtracted to isolate the measurement noise in cycles. The left plots apply to the MW method whereas the right plots are for the proposed model. As shown, the std of the estimated N_{51} WL ambiguity in the proposed

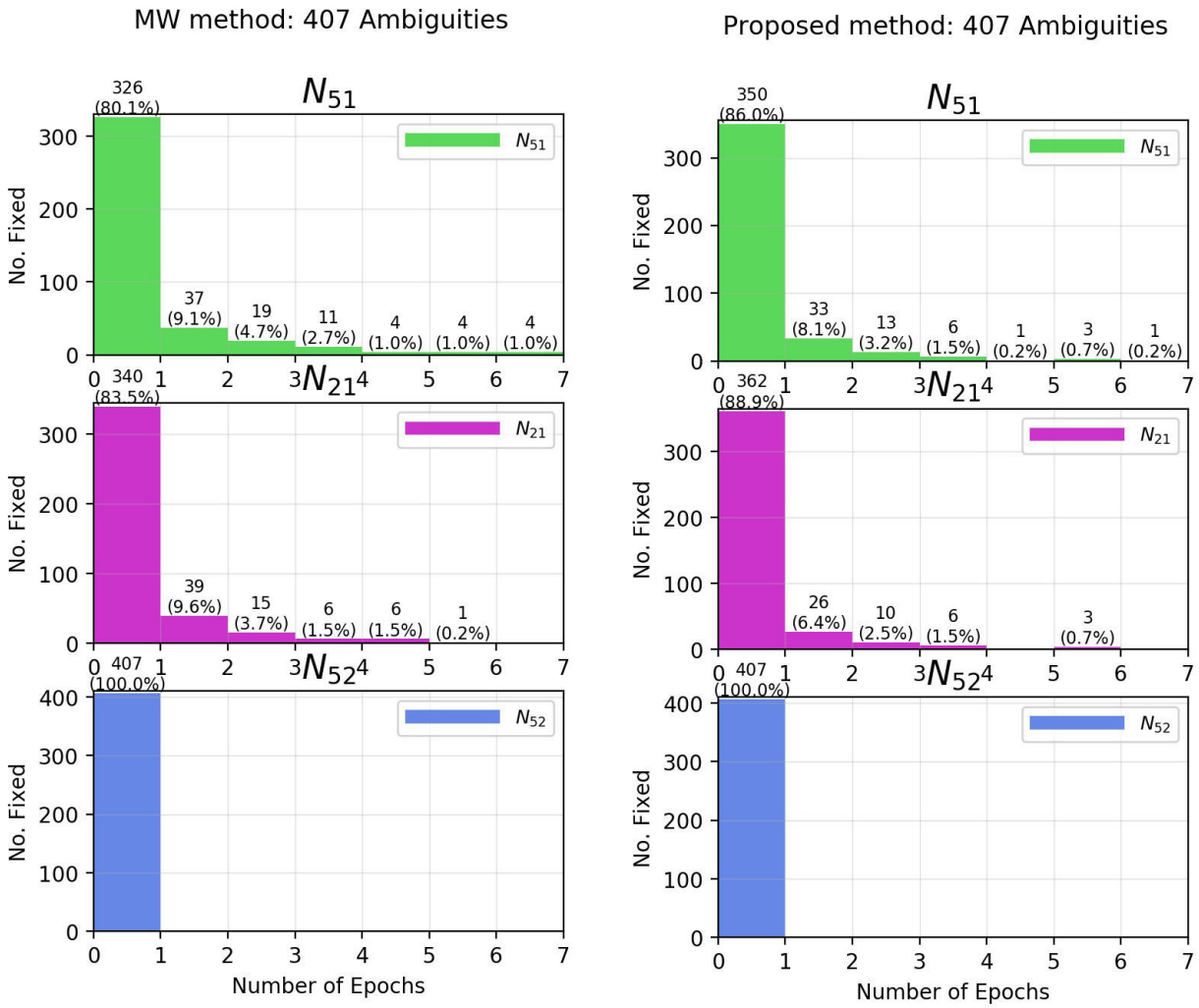

Figure 9. Histogram of the number of cases where the WL (top, middle) and EWL (bottom) ambiguities were correctly fixed using the MW method (left) and proposed method (right). The *x*-axis shows the number of epochs required to fix ambiguities, and the *y* axis shows the number of instances (percentage in brackets) of correct ambiguity fixing.

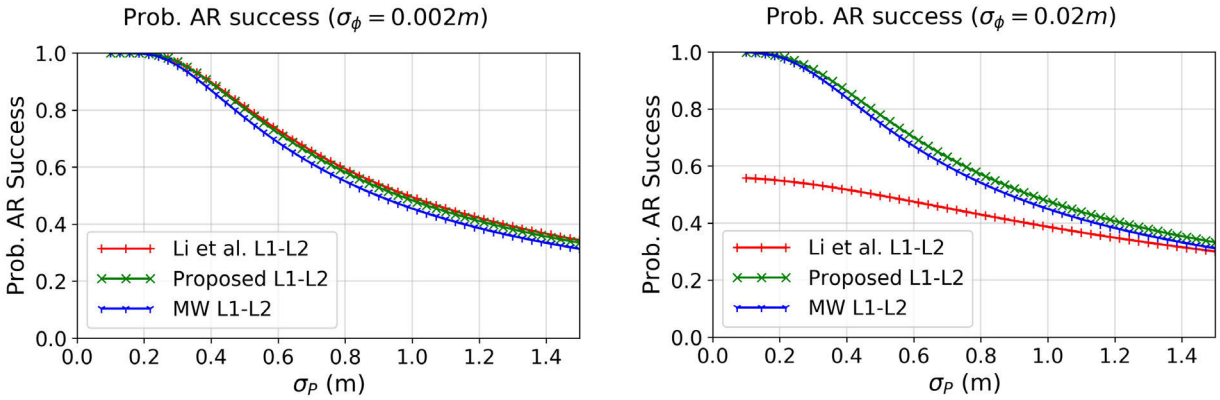

Figure 10. Probability of integer ambiguity resolution success with single-epoch data for the proposed model, MW model, and the model in Li *et al* (2014) with $\sigma_\Phi = 0.002$ m (left) and $\sigma_\Phi = 0.02$ m (right).

method improved by 6.7%. Figure 7 shows the same results for the N_{51} WL ambiguity, where the proposed model had an improvement of 13.3%. Figure 8 illustrates the results for the N_{52} ambiguity, which showed marginal improvement, as expected from table 1. Similar improvements were also found at the other sites, which have been excluded here for brevity.

Secondly, analysis of the time taken to fix the EWL/WL ambiguities was undertaken. This is defined as the elapsed time for the average integer rounded ambiguities to attain a constant value equal to the overall mean for the satellite pair. Figure 9 compares histograms of the number of epochs required to fix the EWL/WL ambiguities for the proposed and

Table 3. Number of epochs required for *P*s rate of 99.9% for the N_{21} WL ambiguity for models (13) and (14) of Li's method as well as the proposed and MW linear combinations.

		Number of epochs required for *P*s rate of 99.9%		
σ_Φ (m)	σ_P (m)	Li *et al* (2014) models 13 and 14	Proposed linear combination	MW linear combination
0.001	0.2	1	1	2
0.002	0.5	6	7	7
0.010	0.5	10	7	8
0.010	1.0	27	25	28
0.020	0.5	23	7	8
0.020	1.0	40	25	29
0.020	1.5	68	55	63

the MW method for all the satellite pairs that were observed at the four sites during the 24 h observation. As shown, the N_{52} EWL ambiguities were fixed to the correct integers within a single epoch for both methods. When using the proposed method, the N_{21} WL ambiguities were fixed correctly within a single epoch for 88.9% of cases, compared to 83.5% of cases for the MW method. The N_{51} WL ambiguities were fixed correctly within a single epoch for 86.0% of cases with the proposed approach, compared to 80.1% of cases for the MW method. For the proposed method, all the EWL/WL ambiguities were fixed with just seven epochs of data, which shows that the NL ambiguity estimation can proceed within less than 2 min.

6.2. Analysis of ambiguity resolution success rate

The EWL/WL ambiguity resolution is based on integer rounding of the average of float ambiguities estimated over several epochs. The lower bound for probability of AR success rate (*P*s) of uncorrelated WL and EWL integer ambiguity resolution by the proposed model, as well as the MW model, can be explicitly evaluated by the equation (Teunissen 1998):

$$P_{\mathrm{IR}(\breve{N}=N)} = 2\Phi\left(\frac{1}{2\sigma_{\hat{N}}}\right) - 1.0 \tag{34}$$

where $\breve{N}, \hat{N}$, and N are the integer rounded, float, and correct WL integer ambiguity, respectively, and Φ is the cumulative normal distribution function. The *P*s rate within a single epoch is assessed for the GPS N_{21} WL ambiguity for the proposed linear combination, the MW linear combination, and a GIF model that results from combining equations (13) and (14) in Li's paper. Results shown in figure 10(left) indicate that with $\sigma_\Phi = 0.002$ m, the proposed model performs slightly better than Li's model when $\sigma_P < 0.4$ m, whereas Li's model offers slightly better *P*s when $\sigma_P > 0.4$ m. However, the difference between these two models is practically negligible. To achieve a *P*s of 99.9% within a single epoch requires that $\sigma_P \leqslant 0.18$ m. This is possible with the modernised signals of the GNSS systems and advancements in receiver tracking technology. However, when $\sigma_\Phi = 0.02$ m, as shown in figure 10(right), the proposed model clearly outperforms the other two models. Li's model gives a significantly lower

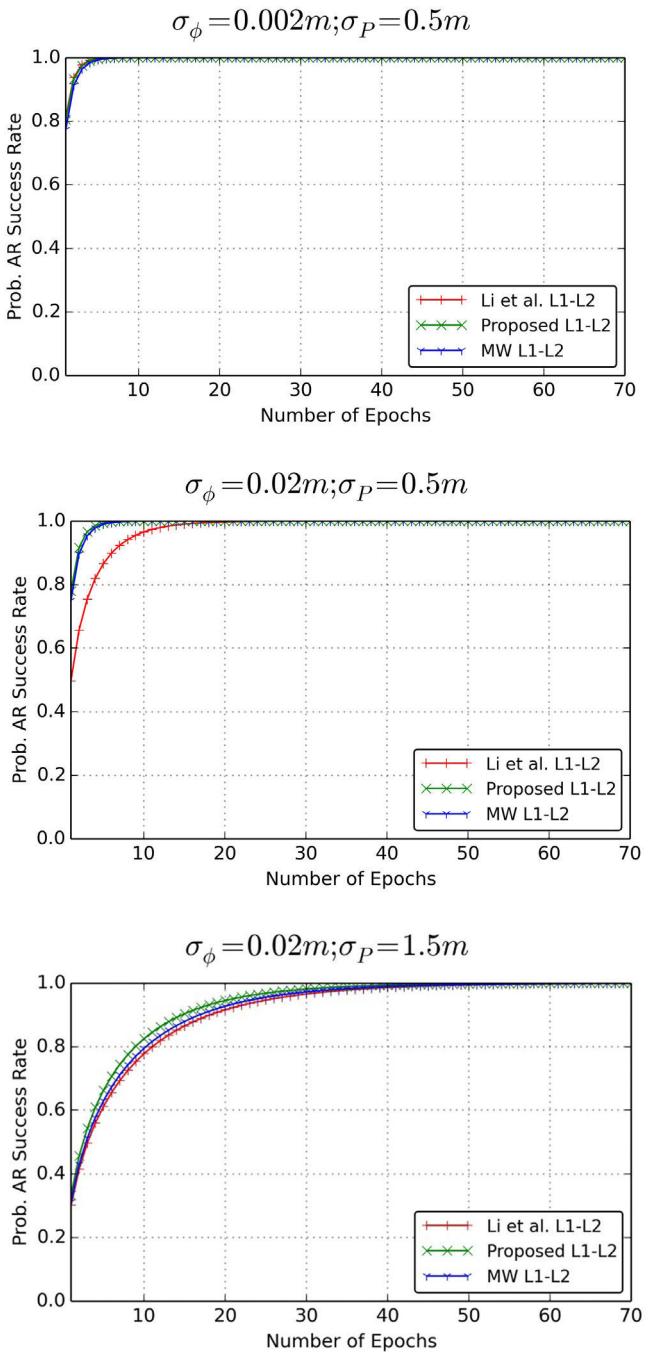

Figure 11. Probability of N_{21} WL ambiguity fixing success versus required number of epochs for models (13) and (14) of Li's method, as well as the proposed and MW linear combinations with $\sigma_\Phi = 0.002$ m, $\sigma_P = 0.5$ m (top); $\sigma_\Phi = 0.02$ m, $\sigma_P = 0.5$ m (middle); and $\sigma_\Phi = 0.02$ m, $\sigma_P = 1.5$ m (bottom).

*P*s rate, and even when $\sigma_P = 0.1$ m, *P*s is just 56%. The proposed model, on the other hand, can provide a *P*s of 99.9% with $\sigma_P = 0.1$ m. This shows that the key to resolving the WL ambiguities within a single epoch is the reduction of the pseudorange measurement noise.

Neglecting the correlation between the float EWL/WL ambiguities for the sake of simplicity, and based on error propagation law, the mean of the WL ambiguities has a std in cycles of $\sigma_{\hat{N}_{21}} = \sigma_{N_{21}}/\sqrt{n}$, where n is the number of epochs,

$\sigma_{N_{21}}$ is the std of the population of WL ambiguities, and $\sigma_{\hat{N}_{21}}$ is the std for WL sample ambiguities. This relationship was used to determine the number of epochs required to achieve a *P*s rate better than 99.9% for the N_{21} WL ambiguity. Table 3 shows the required number of epochs for models (13) and (14) of Li's method, and the proposed and MW linear combinations, for different combinations of σ_Φ and σ_P. Figure 11 plots the *P*s rate for the N_{21} WL versus required number of epochs for the three models, with $\sigma_\Phi = 0.002$ m, $\sigma_P = 0.5$ m (top); $\sigma_\Phi = 0.02$ m, $\sigma_P = 0.5$ m (middle); and $\sigma_\Phi = 0.02$ m, $\sigma_P = 1.5$ m (bottom). As shown in this table and figure, Li's models and the proposed model give similar performance when $\sigma_\Phi \leqslant 0.002$ m and $\sigma_P = 0.5$ m, slightly better than the MW model. As the carrier phase std increases, the proposed model gives substantial improvement since it requires the least number of epochs to fix the N_{21} WL ambiguity.

6.3. Analysis of N_2 ambiguity resolution success rates

This section analyses the *P*s rate for the N_2 ambiguity resolution with the LAMBDA method. The geometry-based equations (21)–(23), with ionosphere and troposphere constraints, are used in the primary PPP-AR model. The results are compared to models (8) and (16) in Li's method. The metric used to assess the performance of the models is the number of epochs required to achieve *P*s rates of 90%, 99%, and 99.9%. This metric is directly related to the time taken for cm-level positioning accuracy to be achieved, and was also used in Li *et al* (2014). The success rate metric evaluates the model strength and provides quality assurance for the resolved integer ambiguities, because it is risky to accept the resolved integer ambiguities when the success rate is low (Teunissen and Verhagen 2008, Verhagen *et al* 2013). The exact formula for the ambiguity fixing success rate for integer bootstrapping (IB) was used, since it is the best known lower bound for integer AR with ILS, given that the ILS lower bound is at or above the IB upper bound success rate (Verhagen *et al* 2013). This exact formula is given as (Teunissen 1998):

$$P_{\mathrm{ILS}} \geqslant P_{\mathrm{IB}(\breve{N}=N)} = \prod_{i=1}^{n} \left(2\Phi \frac{1}{2\sigma_{\hat{N}_{i|\xi}}} - 1.0 \right) \tag{35}$$

where $\hat{N}_{i|I}$ is the *i*th ambiguity calculated with the condition of the previous sequentially rounded ambiguities $\xi = \{i+1, i+2 \ldots i+n\}$. In using the geometry-based proposed model of equations (21)–(23), the troposphere was assumed to be known with $\sigma_T = 0.01$ m. This constraint was also used in Li's method. The RIM stds of 0.1 and 0.5 TECU were used for the ionosphere, and carrier phase stds were 0.002 and 0.02 m. The analysis included 1 h blocks of data over a 24 h period, with an epoch interval of 15 s at sites ALIC, HOB2, TOW2, and YAR2. Measurement weighting based on the satellite elevation angle (E) was applied as $1/\sin(E)$. Kalman filter was used with a static receiver configuration to estimate the variance–covariance matrix of the ambiguities and position parameters, which was used with the *P*s-Lambda software (Verhagen *et al* 2013) to compute the *P*s rate. Since actual measurements were not required for calculating the ambiguity variance–covariance matrix and the *P*s rate, the known receiver position and IGS satellite orbits were used to calculate the geometry term in the design matrix. The ambiguity variance–covariance matrix was propagated with multi-epoch data. The following six test cases were considered.

(1) Proposed method with $\sigma_\Phi = 0.002$ m and $\sigma_{\mathrm{RIM}} = 0.1$ TECU.
(2) Proposed method with $\sigma_\Phi = 0.02$ m and $\sigma_{\mathrm{RIM}} = 0.1$ TECU.
(3) Proposed method with $\sigma_\Phi = 0.002$ m and $\sigma_{\mathrm{RIM}} = 0.5$ TECU.
(4) Proposed method with $\sigma_\Phi = 0.02$ m and $\sigma_{\mathrm{RIM}} = 0.5$ TECU.
(5) Li's method with $\sigma_\Phi = 0.002$ m.
(6) Li's method with $\sigma_\Phi = 0.02$ m.

Table 4 presents the number of epochs required to attain *P*s rates of 90%, 99%, and 99.9% for these six cases. Figure 12 shows the *P*s rates for cases 1–4. As shown in this figure and table, the proposed method with case 1 gave *P*s $\geqslant$ 99% with less than four epochs of data. Case 2 gave *P*s $\geqslant$ 99% with less than six epochs of data. Cases 3 and 4 required up to 14 min to give *P*s $\geqslant$ 99%, both of which used $\sigma_{\mathrm{RIM}} = 0.5$ TECU. This shows that the precision of the RIM has a higher influence on

Table 4. Number of epochs required to attain *P*s rate of 90%, 99%,and 99.9% at the four sites for the six cases.

Case	Site	*P*s $\geqslant$ 90%	*P*s $\geqslant$ 99%	*P*s $\geqslant$ 99.9%
1	ALIC	2.0	3.4	4.5
	HOB2	1.7	2.8	3.8
	TOW2	2.2	3.7	5
	YAR2	2.2	3.6	4.6
	OVERALL	2	4	5
2	ALIC	3.2	5.2	7.0
	HOB2	2.7	4.6	6.2
	TOW2	3.3	5.8	7.9
	YAR2	3.2	5.6	7.2
	OVERALL	4	6	8
3	ALIC	28.2	47.1	61.0
	HOB2	24.9	42.1	55.9
	TOW2	29.0	47.2	62.0
	YAR2	28.9	53.0	66.4
	OVERALL	28	48	62
4	ALIC	29.0	48.8	62.8
	HOB2	25.8	43.5	57.3
	TOW2	30.3	48.7	63.8
	YAR2	29.9	54.1	68.8
	OVERALL	29	49	64
5	ALIC	6.7	11.5	15.1
	HOB2	6.3	10.7	14.0
	TOW2	7.2	12.3	15.9
	YAR2	6.8	11.5	14.8
	OVERALL	7	12	15
6	ALIC	120.7	167.8	191.9
	HOB2	107.7	151.7	176.1
	TOW2	111.5	157.3	180.7
	YAR2	112.0	167.8	187.9
	OVERALL	113	162	184

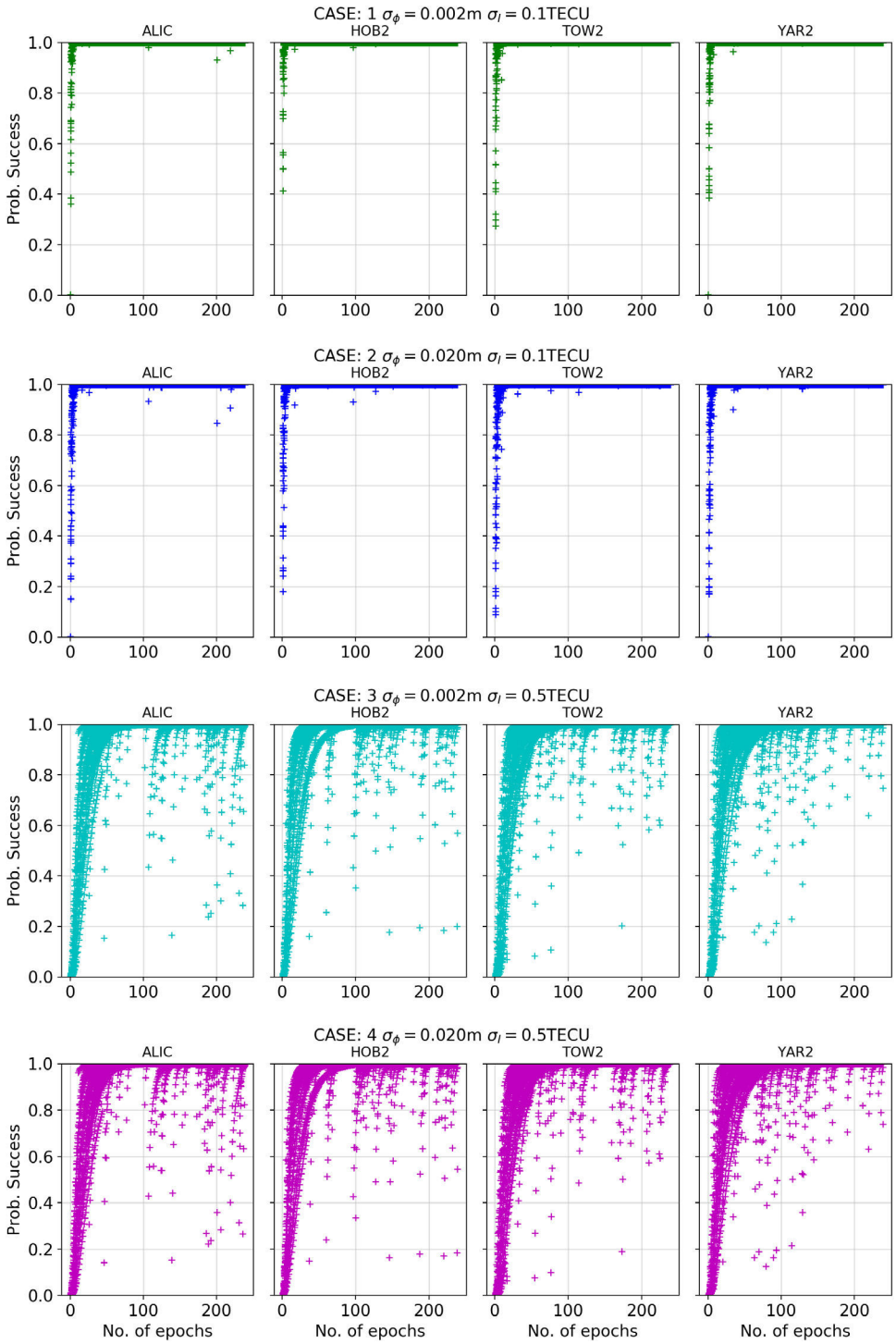

Figure 12. *P*s rates for the proposed method with the hourly dataset at sites ALIC, HOB2, TOW2, and YAR2 for cases 1 (top), 2 (upper middle), 3 (lower middle), and 4(bottom).

the PPP-AR solution than the carrier-phase std. The *P*s rate has fluctuations due to appearance or loss of satellites, which affects the geometry.

Figure 13 shows the *P*s rates for Li's method for cases 5 and 6. Compared to the proposed method with high-precision RIM ($\sigma_{\text{RIM}} = 0.1$ TECU), case 5 gives poorer performance. For example, achieving *P*s $\geqslant 99\%$ required up to 13 epochs of data in case 5, compared to 4 and 6 epochs for cases 1 and 2, respectively. With case 6 ($\sigma_\Phi = 0.02$ m), Li's method gave significantly poorer performance than case 4; i.e. the proposed method with a low-precision RIM ($\sigma_{\text{RIM}} = 0.5$ TECU). For case 6, a *P*s rate of 99% was not achieved for 14% of the hourly solutions, whereas a *P*s rate of 99.9% was not achieved for 35% of the hourly solutions. On the other hand, the proposed method gave a *P*s rate of 99.9% within the one-hour period for all datasets.

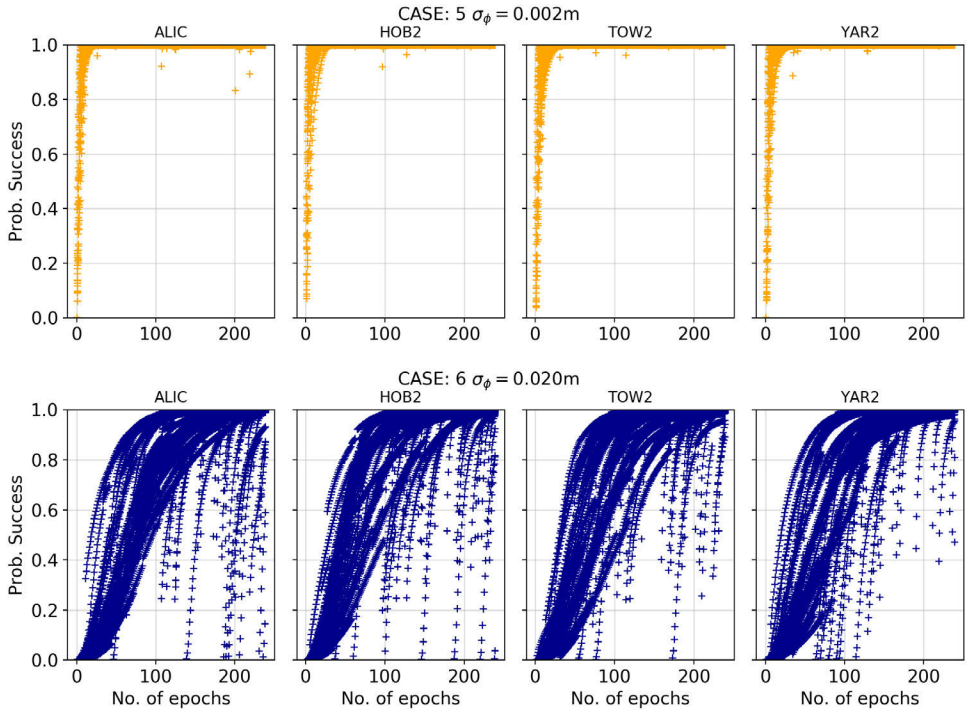

Figure 13. *P*s rates for the method of Li *et al* (2014) with hourly dataset at sites ALIC, HOB2, TOW2, and YAR2 for cases 5 (top) and 6 (bottom).

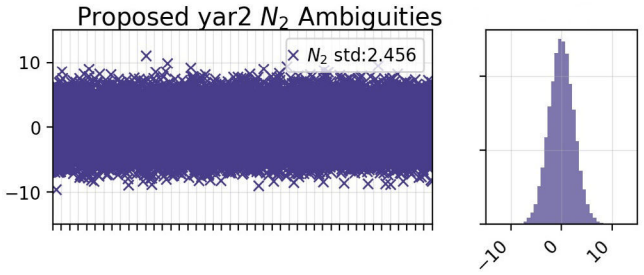

Figure 14. Time series and histogram of the single-differenced N_2 ambiguities, based on equation (24), at site YAR2 for all observed satellite pairs during 24 h of observation.

Table 5. Percentage of N_2 ambiguities that were fixed using the proposed triple-frequency GIF linear combination with measurement noise minimisation (equation (24)).

Time (min)	Num. Epochs	Percentage N_2 fixed
5	20	34.4%
10	40	65.4%
20	80	90.2%
30	120	95.6%

6.4. Direct estimation of NL ambiguity

This section analyses the direct estimation of the individual N_2 ambiguity, after fixing the EWL and WL integer ambiguities. The $\Phi_{\mathrm{IF},1,2,5}$ linear combination of equation (24) is used, which requires the N_{52} EWL and N_{21} WL ambiguities to be fixed.

Figure 14 shows the time series and histogram of the single-difference N_2 ambiguities calculated with this method at site YAR2, for all observed satellite pairs during the 24 h observation. The mean value has been subtracted to isolate the noise in cycles. As shown, the std of the estimated N_2 ambiguity is 2.5 cycles, after the measurement noise minimisation condition in equation (24). However, this std value is considerably higher than the effective N_2 wavelength. The probability of NL AR success rate with a single epoch is just 16%, which makes it challenging to fix the NL ambiguity even with multi-epoch averaging.

The time taken to fix the N_2 ambiguity was analysed. This is defined as the time needed for the average integer rounded ambiguity to attain a constant value, after which it is considered fixed. Table 5 shows the percentage of N_2 ambiguities that were fixed using the proposed method (equation (24)), within a duration of 5, 10, 20, and 30 min. As shown, 65.4% of the N_2 ambiguities were fixed within 10 min, 90.2% within 20 min, and 95.6% within 30 min.

The number of epochs required to resolve the NL ambiguity with a probability of success of 99.9% was analysed next. Figure 15(top) shows the probability of the NL ambiguity fixing success rate versus number of epoch measurements; whereas figure 15(bottom) shows the measurement noise in cycles versus the required number of epochs. As this figure shows, the noise in the estimated NL ambiguity is too high to fix with a high probability success rate using just a few epochs of data. It requires 244 epochs to fix the NL ambiguity with a *P*s of 99.9%, which amounts to more than an hour's data with 15 s epoch intervals. This result may be impractical, but this is to be expected since the NL AR is well known to be a challenging problem (Li *et al* 2014, Li 2018). For example, in Li *et al* (2014), the success rate for NL integer ambiguity resolution with their best performing model was 18.6% at 15 min, 48.6% at 25 min, and 84.9% at 30 min. However, once the N_2 ambiguity is fixed, the other individual ambiguities

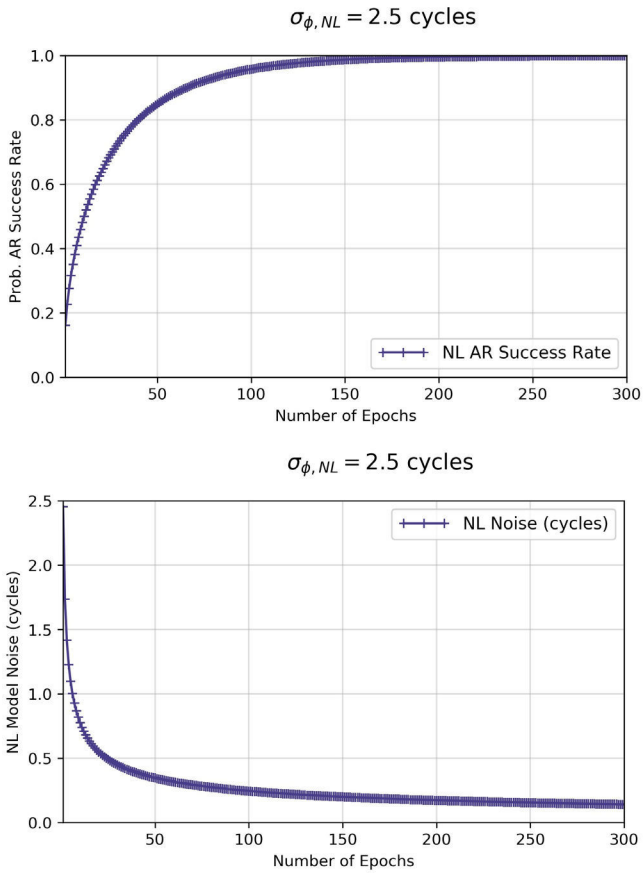

Figure 15. Probability of NL ambiguity fixing success (top) and measurement noise in cycles (bottom) versus the required number of epochs.

can be calculated using equation (16). Thus, the carrier phase measurements now become precise range measurements that enable cm-level PPP accuracy.

7. Conclusion

In this paper, we firstly developed improved linear combinations for estimation of the EWL/WL ambiguities. Compared to the MW linear combination for the GPS case, the measurement noise in the proposed combination was 6.7% lower for L1/L2, 12.7% lower for L1/L5, and a modest 0.7% lower for L2/L5. Data analysis at four sites showed that the N_{21} WL ambiguities were fixed correctly with a single epoch for 88.9% of cases, an improvement over the MW method by 5.4%. The N_{51} WL ambiguities were fixed correctly with one epoch for 86.0% of cases, an improvement over the MW method by 5.9%, whereas all EWL ambiguities were fixed with one epoch for both methods. For the proposed method, all the EWL and WL ambiguities were fixed in less than two minutes. The performance of the proposed linear combination for GPS N_{21} WL ambiguity resolution was compared to Li's method (Li *et al* 2014). Results showed that the proposed method gave slightly improved performance with $\sigma_\Phi = 0.002$ m, and substantially improved performance as the carrier phase std increased. To fix the N_{21} WL ambiguity with a single epoch with $Ps = 99.9\%$ requires that $\sigma_P \leqslant 0.18$ m, which is possible with the modernised signals of the GNSS systems. The proposed combination enhances the approach of Li *et al* (2014) by improving the WL AR success rate, which is the key for NL AR along with precise position estimation.

We proposed a triple-frequency carrier-phase-only PPP-AR model where the equations are formulated in terms of one ambiguity, e.g. the GPS N_2. The N_2 integer ambiguity is fixed with the LAMBDA method along with receiver position and atmospheric parameters. Here, the PPP-AR performance is greatly improved with precise models to constrain the ionosphere and troposphere. The results from the proposed model were compared to Li's method. It was shown that use of a precise troposphere model and RIM significantly improved the time to fix ambiguities. When using a RIM with std $= 0.1$ TECU and $\sigma_\Phi = 0.002$ m, a Ps rate better than 99% was achieved with less than four epochs of data. Decreasing the RIM precision to 0.5 TECU while retaining $\sigma_\Phi = 0.002$ m required up to six epochs of data to achieve $Ps \geqslant 99\%$. When using $\sigma_{\mathrm{RIM}} = 0.5$ TECU and $\sigma_\Phi = 0.02$ m, the proposed method required up to 14 min to give $Ps \geqslant 99\%$. A Ps rate of 99.9% was achieved within one hour for all the test cases using the proposed method. In comparison, Li's method with $\sigma_\Phi = 0.002$ m gave $Ps \geqslant 99\%$ with up to 13 epochs of data. When the carrier phase std was increased to 0.02 m, the performance of Li's method deteriorated drastically. These results demonstrate the improved performance of the proposed PPP-AR method when a high-precision RIM is used.

An approach for direct estimation of the NL ambiguity was also proposed using multi-epoch averaging of a phase-only GIF linear combination. The test results showed that 34.4% of the ambiguities were fixed in 5 min, 65.4% in 10 min, 90.2% in 20 min, and 95.6% in 30 min with the best of these approaches. AR with a probability success rate of 99.9% would require more than an hour of continuous carrier phase tracking.

ORCID iDs

Manoj Deo https://orcid.org/0000-0002-6325-5276

References

Cheng S, Wang J and Peng W 2017 Statistical analysis and quality control for GPS fractional cycle bias and integer recovery clock estimation with raw and combined observation models *Adv. Space Res.* **60** 2648–59

Cocard M, Bourgon S, Kamali O and Collins P 2008 A systematic investigation of optimal carrier-phase combinations for modernized triple-frequency GPS *J. Geod.* **82** 555–64

Collins P, Bisnath S, Lahaye F and Heroux P 2010 Undifferenced GPS ambiguity resolution using the decoupled clock model and ambiguity datum fixing *Navigation* **57** 123–35

Deng C, Tang W, Cui J, Shen M, Li Z, Zou X and Zhang Y 2018 Triple-frequency code-phase combination determination: a comparison with the Hatch–Melbourne–Wübbena combination using BDS signals *Remote Sens.* **10** 353

Deo M and El-Mowafy A 2016 Triple-frequency GNSS models for PPP with float ambiguity estimation: performance comparison using GPS *Surv. Rev.* **50** 249–61

Deo M and El-Mowafy A 2017 Ionosphere Augmentation for accelerated convergence in Precise Point Positioning with triple-frequency GPS *Proc. ION 2017 Pacific PNT Meeting (Marriott Waikiki Beach Resort & Spa Honolulu, Hawaii, 1–4 May 2017)* pp 687–97

Dixon K 2006 StarFire™: a global SBAS for sub-decimeter precise point positioning *ION GNSS 19th Int. Technical Meeting of the Satellite Division (Fort Worth, TX, 26–29 September 2006)*

El-Mowafy A 2014 GNSS multi-frequency receiver single-satellite measurement validation method *GPS Solut.* **18** 553–61

El-Mowafy A, Deo M and Rizos C 2016 On biases in precise point positioning with multi-constellation and multi-frequency GNSS data *Meas. Sci. Technol.* **27** 035102

Ge M, Gendt G, Rothacher M, Shi C and Liu J 2008 Resolution of GPS carrier-phase ambiguities in precise point positioning (PPP) with daily observations *J. Geod.* **82** 389–99

Geng J and Bock Y 2013 Triple-frequency GPS precise point positioning with rapid ambiguity resolution *J. Geod.* **87** 449–60

Geng J, Meng X, Dodson A H and Teferle F 2010 Integer ambiguity resolution in precise point positioning: method comparison *J. Geod.* **84** 569–81

Guo F, Zhang X and Wang J 2015 Timing group delay and differential code bias corrections for BeiDou positioning *J. Geod.* **89** 427–45

Jung J, Enge P and Pervan B 2000 Optimization of cascade integer resolution with three civil GPS frequencies *Proc. ION GPS 13th Int. Technical Meeting of the Satellite Division (Salt Lake City, UT)* pp 2191–200

Laurichesse D and Blot A 2016 Fast PPP convergence using multi-constellation and triple-frequency ambiguity resolution *ION GNSS 2016 (Portland, Oregon, 12–16 September 2016)*

Laurichesse D, Mercier F, Berthais J P, Broca P and Cerri L 2009 Integer ambiguity resolution on undifferenced GPS phase measurements and its application to PPP and satellite precise orbit determination *Navigation* **56** 135–49

Laurichesse D and Privat A 2015 An open-source PPP client implementation for the CNES PPP-WIZARD demonstrator *Proc. ION GNSS + 2015 (Tampa, Florida, September 2015)*

Leandro R, Gomez V, Stolz R, Landau H, Glocker M, Drescher R and Chen X 2012 Development on global centimeter-level GNSS positioning with Trimble CenterPoint RTX *Proc. 25th Int. Technical Meeting of the Satellite Division of the Institute of Navigation 2012 (Nashville, USA)* pp 3089–95

Li B 2018 Review of triple-frequency GNSS: ambiguity resolution, benefits and challenges *J. Glob. Positioning Syst.* **16** 1

Li B, Feng Y and Shen Y 2010 Three carrier ambiguity resolution: distance independent performance demonstrated using semi-generated triple frequency GPS signals *GPS Solut.* **14** 177–84

Li T, Wang J and Laurichesse D 2014 Modeling and quality control for reliable precise point positioning integer ambiguity resolution with GNSS modernization *GPS Solut.* **18** 429–42

Liu S, Zhang L and Li J 2016 A dual frequency carrier phase error difference checking algorithm for the GNSS compass *Sensors* **16** 1988

Lu M and Yao Z 2014 New signal structures for BeiDou navigation satellite system *Stanford's PNT Symp. (SLAC Stanford, CA 94305, 28–30 October 2014)*

Montenbruck O, Hauschild A and Steigenberger P 2014 Differential code bias estimation using multi-GNSS observations and global ionosphere maps *Navigation* **61** 191–201

Morley T and Macleod R 2015 Advances in NovAtel's precise point positioning (PPP) solution for high accuracy kinematic applications *IGNSS Symp. (Gold Coast, Australia, 14–16 July 2015)*

Nadarajah N, Khodabandeh A, Wang K, Choudhury M and Teunissen P J G 2018 Multi-GNSS PPP-RTK: from large- to small-scale networks *Sensors* **18** 1078

Ray J K and Cannon M E 1999 Characterization of GPS carrier phase multipath *ION NTM-99 (San Diego, 25–27 January 1999)*

Rovira-Garcia A, Juan J M, Sanz J, Gongales-Casado G and Bertran E 2016 Fast precise point positioning: a system to provide corrections for single and multi-frequency navigation *Navigation* **63** 231–47

Seepersad G and Bisnath S 2014 Reduction of PPP convergence period through pseudorange multipath and noise mitigation *GPS Solut.* **19** 369–79

Teunissen P J G 1995 The least-squares ambiguity decorrelation adjustment: a method for fast GPS integer ambiguity estimation *J. Geod.* **70** 65–82

Teunissen P J G 1998 Success probability of integer GPS ambiguity rounding and bootstrapping *J. Geod.* **72** 606–12

Teunissen P J G and Verhagen S 2008 GNSS ambiguity resolution: when and how to fix or not to fix? *VI Hotine-Marussi Symp. on Theoretical and Computational Geodesy: Challenge and Role of Modern Geodesy (Wuhan, China, 29 May–2 June 2006)* (Series: International Association of Geodesy Symposia) vol 132 pp 143–8

Teunissen P J G and Khodabandeh A 2015 Review and principles of PPP-RTK methods *J. Geod.* **89** 217–40

Urquhart L 2009 An analysis of multi-frequency carrier phase linear combinations for GNSS *Senior Technical Report* Department of Geodesy and Geomatics Engineering Technical Report No. 263, University of New Brunswick, Fredericton, New Brunswick, Canada, p 71

Verhagen S, Li B and Teunissen P 2013 *P*s-LAMBDA: ambiguity success rate evaluation software for interferometric applications *Comput. Geosci.* **54** 361–76

Vollath U, Birnbach S and Landau H 1998 Analysis of three carrier ambiguity resolution (TCAR) technique for precise relative positioning in GNSS-2 *ION GPS* **1998** 417–26

Wang N, Yuan Y, Li Z, Montenbruck O and Tan B 2015 Determination of differential code biases with multi-GNSS observations *J. Geod.* **90** 209–28

9 CONCLUSIONS AND FUTURE RESEARCH DIRECTIONS

9.1 Conclusions

This thesis comprised several contributions that aim to improve PPP performance by reducing the solution convergence time and improving positional accuracy. The approach taken was to identify some of the major challenges that hinder achievement of fast PPP solution convergence, and subsequently develop strategies to address these challenges. Considerable focus was given to the use of triple frequency data from multi-constellation GNSS to improve PPP models with both float ambiguity estimation and integer AR approaches. The use of precise atmospheric products for constraining the ionosphere and troposphere errors was also investigated. A method was proposed and validated for maintaining decimetre accuracy PPP during communication outages, when precise clock and orbit corrections are unavailable. Several key contributions were made in the development and validation of triple frequency PPP-AR models. The key contributions of this thesis are highlighted below.

Firstly, an efficient method was proposed in Chapter 2 for detection and repair of cycle slips and clock jumps with triple frequency data. This method was found to be effective in detecting and repairing cycle slips and clock jumps, which is an essential first step in preparing the MFMC data for PPP analysis. The third frequency improves reliable detection of cycle slips and enables an independent check to confirm the occurrence of a slip on an individual frequency. A method was developed and validated for detecting and repairing clock jumps when it appears in both pseudorange and carrier phase measurements. It was found that repairing clock jumps in this scenario makes the receiver clock error predictable and hence improves the dynamic model of the clock parameter in the Kalman filter for improved performance.

A thorough analysis of the biases that occur when integrating multi-frequency and multi-constellation was carried out in Chapter 3. This is one of the pioneering papers that provides a detailed review of all the biases that occur when integrating MFMC data and provides mathematical modelling of biases such as receiver hardware biases and inter-system time biases. This contribution addresses the complications faced by users of triple frequency GNSS data, who may use different measurements in the PPP model other than the reference signals used to generate the

precise orbit and clock products required for the PPP solution. In such cases where non-reference signals are used, the precise orbit and clock corrections and differential code biases require further adjustments in order to get the highest PPP accuracy. It is recommended that the satellite phase biases are treated as calibrated quantities obtained from external sources for improved convergence in float-PPP models as well PPP-AR. It was pointed out that the IGS can play a major role in supporting MFMC PPP users by producing precise orbits, clock corrections and phase centre offsets for each GNSS satellite and each individual frequency. This will enable PPP users to apply these corrections to raw measurements prior to forming any linear combination, thus avoiding further complications.

Chapter 4 thoroughly investigated the use of triple frequency data for PPP with float ambiguity estimation. This resulted in the development and testing of three algorithms, one of which included a novel mixed code-phase linear combination with ionosphere-free, geometry preserving and low noise propagation properties. In the second model, a code- and phase-only triple frequency ionosphere-free, geometry preserving and noise minimisation linear combination was developed for the major GNSS constellations. The full mathematical derivation of these combinations was presented for the first time, for easy implementation in navigation algorithms in the GNSS receiver. The third model used the additional frequency to estimate the ionosphere error, rather than forming combinations to eliminate it. The analysis of tested data for up to eight days at three sites in Australia revealed that all the three models had similar performance in terms of convergence time and achievable accuracy, and had significant improvements in convergence time compared to the dual-frequency case. When using the triple-frequency ionosphere-free model, the convergence time improved by 10%, the improvement was 9% when using the mixed code-phase model, whereas the individual uncombined model resulted in 8% improvement. In the second paper of this chapter, the PPP model with code- and phase-only triple frequency linear combination was extended to the multi-frequency case and validated with test data. It was revealed that use of multi-constellation data offered additional improvements in the PPP convergence time. Compared to the GPS-only case, the triple frequency solution for GPS+Beidou+Galileo constellations resulted in an overall improvement of 7.6 minutes in convergence time and an improvement of 2mm in RMSE East and Up. This is a promising step for real-time PPP users who can potentially benefit from MFMC PPP.

In Chapter 5, the PPP model with raw un-combined carrier phase and code measurements was augmented with precise RIM data to correct for the ionosphere error. This model was found to give significantly improved PPP convergence, particularly in the horizontal positioning component. Here, better than 5cm horizontal positioning accuracy was achieved within five minutes for all tested data with RIM precisions from std=0.1 to 1.0 TECU. Such rapid PPP convergence is promising for real-time PPP users who have access to triple frequency GNSS data and a high precision RIM.

Chapter 6 investigated the application of high precision troposphere models derived from NWM data for constraining the troposphere error. For the first time, NWM data from the Australian BoM was used to estimate the zenith tropospheric delay. When compared to IGS ZPD values and other empirical and NWM derived ZPD estimates, the BoM NWM data gave the best accuracy for the four Australian sites that were tested for a period of one year. The ZPD values derived from BoM NWM data was used as pseudo-observations with known precision to constrain the troposphere error. This was found to improve the PPP convergence performance, particularly in the vertical component during the first few minutes of initialisation. Improvements in vertical positioning accuracy was found at all the four tested sites at 0.036-0.058m after 2 minutes, 0.023-0.038m after 3 minutes and 0.013-0.020m after 5 minutes of PPP initialisation.

In Chapter 7, a method was proposed and validated for maintaining real-time PPP accuracy during a loss in data communication, when the precise clock and orbit corrections are not available to users. The clocks were predicted using a second-order polynomial with sinusoidal terms. The model parameters are estimated sequentially using a sliding time window with historical data of 2 hours, such that the clock error may be estimated when needed. The prediction model of the clock correction is built based on the analysis of their properties, including their temporal behaviour and stability. The prediction of the precise satellite orbit with the Holt Winter's method showed that this was possible only for short period of a few minutes. For longer outages up to 3 h, the most recent IGS ultra-rapid orbits are used which have prediction data for up to 24 hours and are available every 6 hours. For the clock prediction, the proposed method was found to give better than 0.5ns accuracy for up to an hour. Using the predicted clock corrections in testing static and kinematic data, it was shown that the PPP user can maintain decimetre level accuracy for up to two

hours after a communication loss. When the PPP re-initialisation is required during the communication break, it was found that the solution convergence time increases. However, the positioning precision remained less than a decimetre after convergence.

Since all GNSS constellations offer measurements on three frequencies (including GLONASS K2), a significant contribution was made in Chapter 8 in developing an improved triple frequency PPP-AR model. Firstly, a new triple frequency GIF linear combination was developed for estimating the WL and EWL integer ambiguities. This linear combination takes advantage of the availability of pseudorange measurements on a third frequency and offers improved performance over the widely used MW combination for estimating the WL and EWL ambiguities. Compared to the MW combinations, the proposed linear combination has 6.7% lower measurement error for the GPS L1/L2 signals, 12.7% for L1/L5 and 0.7% for L2/L5. Substantial improvements were also made for Beidou and Galileo constellations. This linear combination particularly improves the WL AR success rate, which once resolved, may be applied to the method in Li et al. (2014) to solve the NL ambiguity along with precise position parameters. Hence, the proposed combination enhances the approach of Li et al. (2014).

A full rank triple frequency carrier phase only PPP model was proposed where the carrier phase equations were formulated in terms of an individual carrier phase ambiguity (e.g. GPS N2) rather than a NL ambiguity used in present PPP-AR models. Analysis of the probability of AR success rate with the LAMBDA method showed that PPP-AR performance of the proposed model is greatly improved when using a precise RIM. Results show that a probability success rate of 99% is achieved within four epochs of data with carrier phase std=0.002m and RIM std=0.1TECU; and within six epochs when RIM std=0.5TECU. When the carrier phase std was increased to 0.02m, depicting high multipath conditions, and with use of a low precision RIM (std=0.5TECU), the proposed method gave significantly improved performance than the method proposed by Li et al (2014).

A method was also proposed for the direct estimation of the NL integer ambiguity by multi-epoch averaging of the newly proposed triple frequency linear combinations, given that EWL and WL ambiguities are resolved with the proposed linear combinations. This gave comparable performance to existing PPP-AR methods.

9.2 Overall Concluding Remarks

In the eight-year duration of this research, several contributions were made by other researchers in improving the performance of PPP with use of MFMC data (e.g. Geng and Bock 2013; Li et al, 2014; Guo et al, 2016). It was challenging to keep track and remain abreast of the developments that were taking place in this broad research area for such a long period of time. Maintaining a research direction that was relevant in this fast-paced environment was vital. The proposed methods in this research were developed to offer an advantage over other methods, or complement them. Overall, this research primarily concerns a PPP user of MFMC data in contract to a provider of PPP services. Moreover, the research was focused on a PPP user in Australia. The algorithms and methods developed were aimed at improving the PPP convergence time while maintaining or improving accuracy. The research assumed that along with access to triple frequency data from a sufficient number of GNSS satellites, the PPP user is provided with the necessary infrastructure required to compute an enhanced PPP solution. Such infrastructure includes the following:

- Accurate satellite antenna offsets for the individual satellites and frequencies of each GNSS constellation
- Calibrated satellite phase delays to isolate integer ambiguities in the PPP-AR model that are suitable in the raw uncombined model
- Accurate troposphere ZPD values determined from a dense network of GNSS receivers
- Accurate ionospheric corrections, also determined from a dense network of GNSS receivers

It is interesting to note that some of the ideas developed in this research are also being developed by contemporary researchers. For example, Choy and Harima (2019) propose communication options for transmitting local ionospheric corrections to PPP users in Australia. Such delivery of precise ionospheric corrections is vital for the PPP methods proposed in Chapters 5 and 8 of this thesis. In Chapter 5, the precise ionospheric corrections are applied to the raw uncombined float ambiguity estimation model whereas in in Chapter 8, the precise ionosphere is applied as a constraint to the PPP-AR model for fixing the ambiguity on an individual signal rather than a NL formulation. Aggrey and Bisnath (2019) have recently shown that constraining the ionosphere and troposphere parameters through precise RIMs and

ZPD products improves PPP initialisation in the first few minutes of processing. Wilgan et al (2017) also applied precise troposphere constraints in the float PPP model to shorten convergence time by several minutes. This reaffirms the conclusions from Chapters 4, 5 and 8 where atmospheric constraints were applied to improve the PPP convergence.

During the early stages of the research, it was decided to perform a simulation study to validate the proposed methods. This approach was sufficient to compare the performance of the enhanced algorithms to the present-day dual frequency models in a controlled experiment where the results are not distorted by biases such as the GPS L5 line bias reported in Montenbruck et al (2011). Other reasons for a simulation approach were:

- insufficient number of GNSS satellites from different constellations (GPS, Galileo, Beidou) with triple frequency CDMA signals.
- unavailability of satellite antenna phase centre offsets for individual signals to apply in the PPP model. The GPS satellite antenna offsets were available for the L1-L2 ionosphere-free combination only, whereas the offsets for Galileo and Beidou were based on satellite design diagrams rather than actual calibrated values.
- unavailability of precise ionospheric and tropospheric corrections generated from a regional network.
- unavailability of satellite carrier phase biases for isolating integer ambiguities in triple frequency PPP models

However, the number of GNSS satellites delivering triple frequency CDMA signals has grown significantly for the GPS, Galileo and Beidou constellations. The IGS has established an antenna working group to study the calibration of satellite antennas, which are now available for Galileo, Beidou, IRNSS, QZSS and GLONASS satellites. Previously these offsets were available for GPS satellites only. Further work is required to determine these offsets for individual frequencies rather than the reference ionosphere-free signals (i.e. L1-L2 for GPS as an example) for the benefit of triple frequency PPP users. This calibration would become possible as the number of satellites transmitting triple frequencies increases in number (Schmid et al, 2016). The generation of precise ionospheric model using a regional GNSS network has been studied in Rovira-Garcia et al. (2016) and the accuracy depends on the density of the network. Such precise ionospheric modelling has not been a

possibility in the Australian context yet (Choy and Harima, 2019), although there were plans to develop such a model to support real-time PPP users in Australia. This was part of a 2.5-year collaboration project between the Corporative Research Centre (CRC) and the BoM – Space Weather Services for the National Positioning Infrastructure (Maher et al. 2016). However, there is no real-time ionospheric model available in Australia as yet (Choy and Harima, 2019). The availability of real-time ionosphere and troposphere models would greatly benefit real-time PPP users of triple frequency GNSS data in Australia and this can leverage off the dense GNSS network that is now available as part of the NPI. Much work has been done in providing satellite phase biases for triple frequency PPP-AR users (e.g. Laurichesse, 2015). However, such biases are suitable for triple frequency PPP-AR users who use the exact same method as proposed by the author. Further work is required to either convert these biases, or produce unified modelling of satellite biases that may be benefit users of alternate PPP-AR methods. Fortunately, this area is lately being actively researched (e.g. Seepersad and Bisnath, 2016; Xiao et al, 2019).

9.3 Future Research Directions

Future research direction, in the context of this research, is to validate the proposed methods with real data, once the required infrastructure becomes available. This is highly dependent on the availability of the precise atmospheric corrections, satellite phase centre offsets for individual frequencies and satellite hardware biases that are suitable for the proposed triple frequency PPP methods. Availability of the number of satellites transmitting triple frequency signals is no longer a limiting factor.

During the research, a bias was identified in the simulated software implementation that resulted in PPP east error being at the same level as the height error. However, the results gave the expected level of accuracy and effectively demonstrated improvements due to application of the proposed enhanced PPP models when compared to existing dual-frequency models. Validating the proposed methods with real data may identify the cause of this inconsistency.

10 REFERENCES

This Chapter presents the references for Chapters 1 and 9 only. The additional references for Chapters 2-8 are listed at the end of the enclosed papers.

1. Aggrey J and Bisnath S (2019) Improving GNSS PPP Convergence: The Case of Atmospheric-Constrained, Multi-GNSS PPP-AR, Sensors (Basel). 19(3), pii: E587, DOI: 10.3390/s19030587.
2. Abdel-salam MA (2005) Precise Point Positioning Using Un-differenced Code and Carrier Phase Observations, PhD Dissertation, University of Calgary, Alberta, Canada.
3. Aydin C, Uygur SÖ, Çetin S, Özdemir A and Dogan U (2017) Ability of GPS PPP in 2D deformation analysis with respect to GPS network solution, Survey Review, DOI: 10.1080/00396265.2017.1415664.
4. Banville S, Bavaro M, Carcanague S, Cole A, Dade K, Grgich P, Kleeman A and Segal B (2018) Network Modelling Considerations for Widearea Ionospheric Corrections, Proceedings of the ION GNSS+ 2018, 24-28 September 2018, Miami Florida.
5. Bawden GW, Melbourne TI, Bock Y. et al. (2016) Development of a GNSS-Enhanced Tsunami Early Warning System 11th Meeting of the International Committee on GNSS – Sochi, Russia, 07 – November, 2016, 1-36.
6. Bellone T, Dabove P, Manzino AM and Taglioretti C (2016) Real-time monitoring for fast deformations using GNSS low-cost receivers. Geomatics, Natural Hazards and Risk, 7(2):458-470, https://doi.org/10.1080/19475705.2014.966867.
7. Bertiger W, Desai S, Haines B, Harvey N, Moore A, Owen S, Weiss J (2010) Single receiver phase ambiguity resolution with GPS data, Journal of Geodesy 84(5): 327-337, DOI: 10.1007/s00190-010-0371-9
8. Bisnath S and Gao Y (2009) Precise Point Positioning: A powerful Technique with a Promising Future, GPS World, April 2009, Accessed online 21 March 2012, <http://www.gpsworld.com/gnss-system/algorithms-methods/innovation-precise-point-positioning-7040>
9. Cai C and Gao Y (2007) Precise Point Positioning Using Combined GPS and GLONASS Observations, Journal of Global Positioning Systems, 6(1): 13-22.

10. Cai C, Gao Y, Pan L and Jian-Jun Z (2015) Precise point positioning with quad-constellations: GPS, BeiDou, GLONASS and Galileo, Advances in Space Research, 56(1): 133-143, http://dx.doi.org/10.1016/j.asr.2015.04.001
11. Cao W, Hauschild A, Steigenberger P, Langley RB, Urquhart L, Santos M and Montenbruck O (2010) Performance Evaluation of Integrated GPS/GIOVE Precise Point Positioning, Proceedings of ITM 2010, The Institute of Navigation International Technical Meeting, 25-27 January 2010, San Diego, California, pp. 540-552.
12. Chen W, Hu C, Li Z, Chen Y, Ding X, Gao S and Ji S (2005) Kinematic GPS precise point positioning for sea level monitoring with GPS buoy, Journal of Global Positioning System, 3(1-2): 302-307.
13. Choy S and Harima K (2019) Satellite delivery of high-accuracy GNSS precise point positioning service: an overview for Australia, Journal of Spatial Science, 64(2): 197-208, DOI: 10.1080/14498596.2018.1427155.
14. Collins P, Bisnath S, Lahaye F and Heroux P (2010) Undifferenced GPS Ambiguity Resolution Using the Decoupled Clock Model and Ambiguity Datum Fixing, Navigation, Journal of the institute of Navigation, 57(2): 123-135.
15. Colombo OL, Sutter AW and Evans AG (2004) Evaluation of Precise, Kinematic GPS Point Positioning, Proceeding of ION-GNSS 2004, Long Beach California, USA, 21-24 September 2004.
16. de Bakker PF and Tiberius CCJM (2017) Real-time multi-GNSS single-frequency precise point positioning, GPS Solutions (2017) 21 (4): 1791-1803, https://doi.org/10.1007/s10291-017-0653-2.
17. Dow JM, Neilan RE and Rizos C (2009) The International GNSS Service in a changing landscape of Global Navigation Satellite Systems, Journal of Geodesy 83(3-4):191-198 (2009). DOI: 10.1007/s00190-008-0300-3.
18. Ebner R and Featherstone WE (2008) How well can online GPS PPP post-processing services be used to establish geodetic survey control networks? Journal of Applied Geodesy, September 2008, 2(3): 149–157, DOI: 10.1515/JAG.2008.017.
19. European Union (2010) European GNSS (Galileo) Open Service: Signal In Space Interface Control Document, Issue 1.1, European Union, September 2010.
20. Gao Y and Shen X (2002) A New Method for Carrier-Phase – Based Precise Point Positioning, Navigation, 40(2): 109-116, Summer 2002.

21. Ge M, Gendt G, Rothacher M, Shi C and Liu J (2008) Resolution of GPS carrier-phase ambiguities in Precise Point Positioning (PPP) with daily observations, Journal of Geodesy, 82(7): 389-399.
22. Geng J and Bock Y (2013) Triple-frequency GPS precise point positioning with rapid ambiguity resolution, Journal of Geodesy, 87: 449-460.
23. Geng J, Teferle FN, Meng X and Dodson AH (2010) Kinematic precise point positioning at remote marine platforms, GPS Solutions, 14(4): 343–350, https://doi.org/10.1007/s10291-009-0157-9.
24. Geng J, Teferle FN, Shi C, Meng X, Dodson AH and Liu J (2009) Ambiguity Resolution in precise point positioning with hourly data, GPS Solutions, 13(4): 263-270 DOI: 10.1007/s10291-009-0119-2.
25. Giovanni BP (2012) Capabilities of the GNSS Precise Point Positioning Technique for Landslide Monitoring, Disaster Advances, 5(4):509-513.
26. Guo F, Zhang X, Wang J and Ren X (2016) Modelling and assessment of triple-frequency BDS precise point positioning, Journal of geodesy, 90 (11), 1223–1235, DOI: 10.1007/s00190-016-0920-y.
27. Guo A, Li X, Li Z, Hu L, Yang G, Zhao C, Fairbairn D, Watson D and Ge M (2018) Multi-GNSS precise point positioning for precision agriculture, Precision Agriculture, 19(5): 895-911, https://doi.org/10.1007/s11119-018-9563-8.
28. Hauschild A, Steigenberger P and Rodriguez-Solano C (2012) Signal, orbit and attitude analysis of Japan's first QZSS satellite Michibiki, GPS Solutions, 16(1): 127–133, DOI 10.1007/s10291-011-0245-5.
29. Hegarty C, Powers E and Fonville B (2005) Accounting for Timing Biases Between GPS, and GALILEO Signals, Proceedings of the 36th Annual Precise Time and Time Interval (PTTI) Systems and Applications Meeting, 7-9 December 2004, Washington, D.C., USA, pp. 307—318. Accessed online 23 March 2012, <http://www.mitre.org/work/techpapers/techpapers05/050341/050341.pdf>
30. Heroux, P and Kouba, J (2001) GPS precise point positioning using IGS orbit products. Physics and Chemistry of the Earth, Part A: Solid Earth and Geodesy, 26(6-8): 573-578.
31. IERS Conventions (2010) IERS Technical Note 36, Petit, G and Luzum, B (eds), Frankfurt am Main: Verlag des Bundesamts für Kartographie und Geodäsie, 179 pp, ISBN 3-89888-989-6.

32. JAXA (2011) Quasi-Zenith Satellite System Navigation Service: Interface Specification for QZSS (IS-QZSS), v1.2, Japan Aerospace Exploration Agency, February 2011.
33. Kim BC and Tinim MV (2011) Potentialities of multifrequency ionospheric correction in Global Navigation Satellite Systems, Journal of Geodesy, 85(3): 159-169.
34. Knoop VL, de Bakker PF, Tiberius CCJM, and van Arem B (2017) Lane determination with GPS Precise Point Positioning, IEEE TRANSACTIONS ON INTELLIGENT TRANSPORTATION SYSTEMS, http://www.victorknoop.eu/research/papers/2017_IEEE_transactions_PPP.pdf
35. Kuo CY, Chiu KW, Chiang KW, Cheng KC, Lin LC, Tseng HZ, Chu FY, Lan WH and Lin HT (2012) High-frequency sea level variations observed by GPS buoys using precise point positioning technique, Terr. Atmos. Ocean. Sci. 2012, 23: 209–218.
36. Laurichesse D (2015) Handling the Biases for Improved Triple-Frequency PPP Convergence, GPS World, Innovation column, April 3 2015, Accessed online 6 August 2019, < https://www.gpsworld.com/innovation-carrier-phase-ambiguity-resolution/ >
37. Laurichesse D, Mercier F, Berthias JP, Broca P and Cerri L (2009) Integer Ambiguity Resolution on Undifferenced GPS Phase Measurements and its Application to PPP and Satellite Precise Orbit Determination, Navigation, Journal of the Institute of Navigation, 56(2): 135-146.
38. Leandro R, Landau H, Nitschke M, Glocker M, Seeger S, Chen X, Deking A, BenTahar M, Zhang F, Ferguson K, Stolz R, Talbot N, Lu G, Allison T, Brandl M, Gomez V, Cao A and Kipka A (2011) RTX Positioning: The Next Generation of cm-accurate Real-Time GNSS Positioning, Proceedings of the 24th International Technical Meeting of ION GNSS, Portland OR, September 19-23, 2011, pp. 1460-1475.
39. Lee S-W, Yun S-H, Kim DH, Lee D, Lee YJ, Schutz BE (2015) Real-time volcano monitoring using GNSS single-frequency receivers, Journal of Geophysical Research: Solid Earth, 120(12):8551-8569.
40. Li T, Wang J and Laurichesse D (2014) Modeling and quality control for reliable precise point positioning integer ambiguity resolution with GNSS modernization, GPS Solutions (2014) 18:429–442, DOI 10.1007/s10291-013-0342-8.

41. Li X, Zhang X, Ren, X, Fritsche M, Wickert Jens and Schuh H (2015) Precise positioning with current multi-constellation Global Navigation Satellite Systems: GPS, GLONASS, Galileo and BeiDou, Scientific Reports, 5(8328), doi:10.1038/srep08328.
42. Lu C, Chen X, Liu G, Dick G, Wickert J, Jiang X, Zheng K and Schuh H (2017) Real-time tropospheric delays retrieved from multi-GNSS observations and IGS realtime product streams. Remote Sensing 9(12) 1317, doi: https://doi.org/10.3390/rs9121317.
43. Lu M and Yao Z (2014) New Signal Structures for BeiDou Navigation Satellite System, Stanford's PNT Symposium, SLAC Stanford, CA 94305, 28-30 October 2014.
44. Maher P, Terkildsen M, Kumar V, Bouya Z, Steward G, Lozbin V and Marshall R (2016) Australian Bureau of Meteorology Space Weather Services: Recent Initiatives, SWPC Space Weather Workshop, 26-29 April 2016, Broomfield, Colorado, USA, Accessed online 6 August, 2019 < https://www.swpc.noaa.gov/sites/default/files/images/u33/Maher20SWW2016_AUS_BOM_SWS_P-Maher_v1.4.pdf>.
45. Montenbruck O, Hugentobler U, Dach R, Steigenberger P and Hauschild A (2011) Apparent clock variations of the Block IIF-1 (SVN62) GPS satellite, GPS Solutions, 16(3): 303-313. https://doi.org/10.1007/s10291-011-0232-x.
46. Phelts RE (2007) Range Biases on Modernized GNSS Codes, Proceedings of European Navigation Conference GNSS/TimeNav, 29 May 29 – 1 June 2007, Geneva, Switzerland, Accessed online 23 March 2012, <http://waas.stanford.edu/wwu/papers/gps/PDF/PheltsENC07.pdf>.
47. Pratt M, Burke B and Misra P (1998) Single-epoch integer ambiguity resolution with GPS-GLONASS L1-L2 Data, Proceedings of ION GPS-98, pp. 389–398.
48. Rabbou M and El-Rabbany A (2017) Performance analysis of precise point positioning using multi-constellation GNSS: GPS, GLONASS, Galileo and BeiDou, Survey Review, 49(352):39-50, doi: 10.1080/00396265.2015.1108068
49. Revnivykh S (2011) GLONASS Status and Modernisation, 6th International Committee on GNSS, September 2011, Accessed online 23 March 2012, http://www.unoosa.org/pdf/icg/2011/icg-6/3.pdf

50. Robach U (2000) Positioning and Navigation Using the Russian Satellite System GLONASS, PhD Dissertation, Universität der Bundeswehr München, Werner-Heisenberg-Weg 39, D-85577 Neubiberg eingereicht.
51. Rovira-Garcia A, Juan J M, Sanz J, Gongåles-Casado G and Bertran E. 2016. Fast Precise Point Positioning: A System to Provide Corrections for Single and Multi-Frequency Navigation. Navigation, 63(3): 231-247, Fall 2016.
52. Saastamoinen J (1972) Atmospheric correction for the troposphere and stratosphere in radio ranging satellites. Geophysical Monograph, Henriksen (ed), 15: 247 – 251.
53. Schmid R, Dach R, Collilieux X, Jaeggi A, Schmitz M and Dilssner F (2016) Absolute IGS antenna phase center model igs08.atx: status and potential improvements, Journal of Geodesy 90(4): 343-364, DOI: 10.1007/s00190-015-0876-3.
54. Seepersad G and Bisnath S (2016) Examining the interoperability of precise point positioning products, GPS World, Innovation column, March 8 2016, Accessed online 6 August 2019, < https://www.gpsworld.com/clarifying-the-ambiguities/>
55. Teunissen PJG (1995) The least-squares ambiguity decorrelation adjustment: a method for fast GPS integer ambiguity estimation, Journal of Geodesy, 70(1-2):65-82.
56. Victor LK, de Bakker PF, Tiberius CCJM, and van Arem B (2017) Lane determination with GPS Precise Point Positioning, IEEE Transactions On Intelligent Transportation Systems, http://www.victorknoop.eu/research/papers/2017_IEEE_transactions_PPP.pdf
57. Wanninger L (2012) Carrier-phase inter-frequency biases of GLONASS receivers, Journal of Geodesy, 86(2): 139–148, DOI 10.1007/s00190-011-0502-y.
58. Wilgan K, Hadas T, Hordyniec P and Bosy J (2017) Real-time precise point positioning augmented with high-resolution numerical weather prediction model, GPS Solutions, 21: 1341 – 1353, DOI 10.1007/s10291-017-0617-6.
59. Xiao G, Li P, Gao Y and Heck B (2019) A Unified Model for Multi-Frequency PPP Ambiguity Resolution and Test Results with Galileo and BeiDou Triple-Frequency Observations, Remote Sensing, 11(2), 116, DOI: https://doi.org/10.3390/rs11020116.

60. Yigit CO and Gurlek E (2017) Experimental testing of high-rate GNSS precise point positioning (PPP) method for detecting dynamic vertical displacement response of engineering structures, Geomatics, Natural Hazards and Risk, 8(2):893-904, https://doi.org/10.1080/19475705.2017.1284160.
61. Zheng F, Lou Y, Gu S, Gong X and Shi C (2017) Modelling tropospheric wet delays with national GNSS reference network in China for BeiDou precise point positioning. Journal of Geodesy, 92(5):545-560, doi: https://doi.org/10.1007/s00190-017-1080-4.
62. Zumberge JF, Heflin MB, Jefferson DC, Watkins MM and Webb FH (1997) Precise Point Positioning for the Efficient and Robust Analysis of GPS Data from Large Networks, Journal of Geophysical Research, 102(B3): 5005-5017.

APPENDIX A: COPYRIGHT PERMISSION STATEMENTS

I warrant that I have obtained, where necessary, permission from the copyright owners to use any third-party copyright material reproduced in this thesis, or to use any of my own published work (e.g. journal articles) in which the copyright is held by another party (e.g. publisher, co-author). These permissions are all attached below.

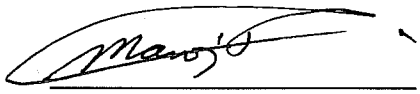

Manoj Nilesh Deo

Permission for the following '**The Institute of Navigation**' publication is attached below:

1. Deo MN, El-Mowafy A (2017) Ionosphere Augmentation for accelerated convergence in Precise Point Positioning with multi-frequency and multi-constellation GNSS, paper presented at ION Pacific PNT 2017 Conference, Honolulu, Hawaii, May 1-4, 2017.

THE INSTITUTE OF NAVIGATION
COPYRIGHT RELEASE FORM
ION PROCEEDINGS

Signing of "Statement A" or "Statement B" is required except that employees of governments other than the U.S. Government may submit equivalent statements. It is essential that the Institute of Navigation (ION) and its agents or assignees have the right of publication and reproduction.

Proceedings to Appear in: **ION Pacific PNT 2017 Meeting**

Session Number & Title: Session C3: High Precision GNSS Correction and Monitoring Networks

Paper Title *(exactly as it appears on the paper)*: Ionosphere Augmentation for Accelerated Convergence in Precise Point Positioning with Triple-frequency GPS

Author(s) & Affiliation(s) *(in the exact order they appear on the paper)*: Manoj Deo & Ahmed El-Mowafy
Department of Spatial Sciences, Curtin University, Perth, Western Australia

Primary Author Address: 7 Puddy Street, Bonython ACT 2905, Australia

Phone/Fax/E-Mail: +61 2 62932420/ +61 2 62685554/ manoj.deo01@gmail.com

STATEMENT A:
The undersigned "Copyright Owner," desiring to publish a paper (the "Paper") in ION Proceedings and/or through other publications of The Institute of Navigation ("ION"), hereby grants to ION the following rights in exchange for good and valuable consideration:

1.) The exclusive, royalty-free right of first publication in the conference proceedings and any other ION publications (including NAVIGATION: The Journal of the Institute of Navigation) for six months from date of presentation of the Paper. If the Paper is selected for publication in NAVIGATION: The Journal of the Institute of Navigation, a separate copyright agreement shall be requested and the copyright for the Paper shall be permanently owned by the ION.
2.) Royalty-free right of publication and distribution of the Paper throughout the world as part of the proceedings named above.
3.) A non-exclusive, perpetual, royalty-free, worldwide license to reprint and/or provide in electronic format the above Paper, either in excerpt, in summary, or in completed form, for free or in exchange for a fee after the six month exclusive period has expired.

Copyright Owner reserves all rights not specifically granted to ION herein and has the right after the Paper has been published, to reprint the Work in any publication six months after presentation, provided that the terms of such republication do not conflict with this license or other copyright agreements. Copyright Owner agrees to include the proper credit to ION for prior publication of the Paper in any reprint of the Paper in a publication, including date (month and year) and location (city and state) of the meeting at which the paper was presented.

Copyright Owner warrants that the Paper is original with him/her, that its publication will not infringe the rights of others, that the Paper is factually accurate and contains no defamatory or otherwise unlawful material, and that Copyright Owner has full power to make this agreement. Copyright Owner further warrants that the Paper has not been published elsewhere in whole or in part (except as set out in a rider attached thereto if applicable) and that no agreement to publish the Paper or any part or version thereof is outstanding. Should the Paper contain any material which requires permission for inclusion in the Paper, Copyright Owner agrees to obtain such permission in writing and provide a copy of such permission to ION.

1. Manoj Deo — PRIMARY AUTHOR'S SIGNATURE
Curtin University — EMPLOYER FOR WHOM WORK WAS PERFORMED
Manoj Deo — AUTHORIZED SIGNATURE
27-Feb-2017 — DATE FORM SIGNED

STATEMENT B:
This will certify that all authors of the above Paper are employees of the U.S. Government and that the authors created the Paper as part of their employment and that the Paper is therefore not subject to U.S. Copyright protection.

2. _____ PRIMARY AUTHOR'S SIGNATURE
_____ EMPLOYER FOR WHOM WORK WAS PERFORMED
_____ AUTHORIZED SIGNATURE
_____ DATE FORM SIGNED

Crown Copyright Certification (where applicable)

This will certify that all authors of the Work are employees of the British or applicable Commonwealth Government and prepared the Work in connection with their official duties. As such, the Work is subject to Crown Copyright and is not assigned to the ION as set forth above. The Undersigned acknowledges, however, that the ION has the right to publish, distribute and reprint the Work in all forms and media.

3. _____ AUTHORIZED SIGNATURE
_____ DATE FORM SIGNED
(Authors who are British or applicable Commonwealth Government employees should also sign line (1) above to indicate their acceptance of all terms other than the copyright transfer.)

Permission for the following '**Taylor & Francis**' publication may be found at the website https://authorservices.taylorandfrancis.com/copyright-and-you/#, and is attached in the following pages:

1. **Deo MN**, El-Mowafy A (2018) Comparison of Advanced Troposphere Models for Aiding Reduction of PPP Convergence Time in Australia, Journal of Spatial Science, https://doi.org/10.1080/14498596.2018.1472046, first published online: 24 May 2018.

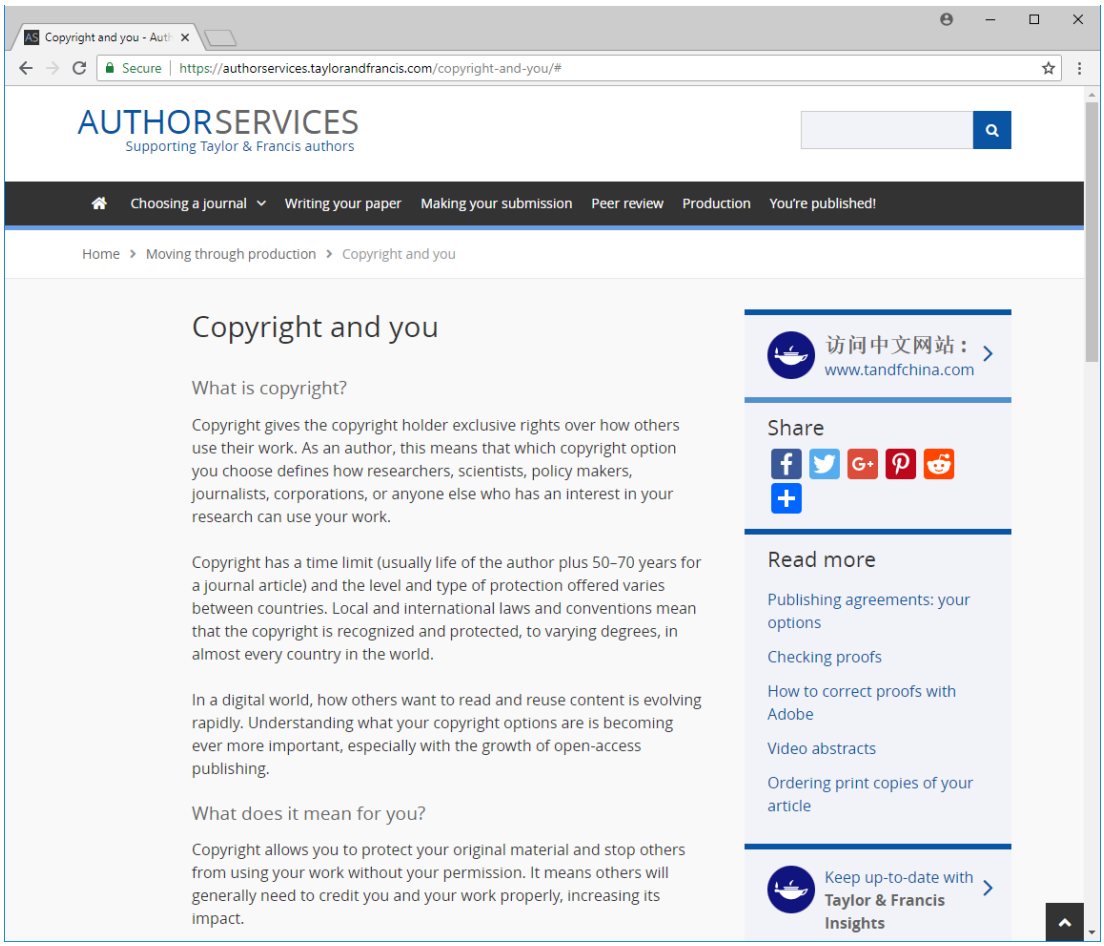

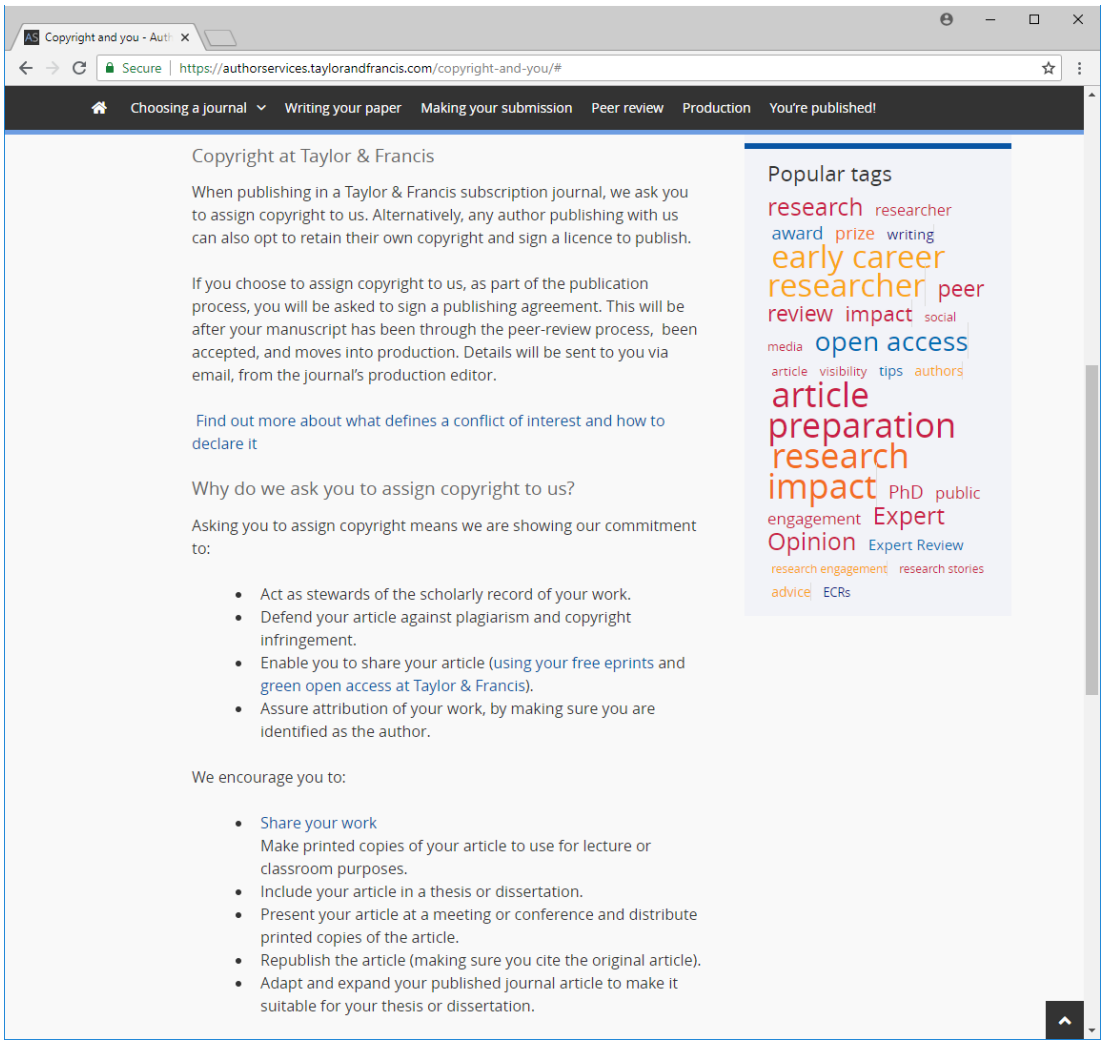
Copyright and you - Auth
Secure | https://authorservices.taylorandfrancis.com/copyright-and-you/#
Choosing a journal
Writing your paper
Making your submission
Peer review
Production
You're published!
Copyright at Taylor & Francis
When publishing in a Taylor & Francis subscription journal, we ask you to assign copyright to us. Alternatively, any author publishing with us can also opt to retain their own copyright and sign a licence to publish.
If you choose to assign copyright to us, as part of the publication process, you will be asked to sign a publishing agreement. This will be after your manuscript has been through the peer-review process, been accepted, and moves into production. Details will be sent to you via email, from the journal's production editor.
Find out more about what defines a conflict of interest and how to declare it
Why do we ask you to assign copyright to us?
Asking you to assign copyright means we are showing our commitment to:
Act as stewards of the scholarly record of your work.
Defend your article against plagiarism and copyright infringement.
Enable you to share your article (using your free eprints and green open access at Taylor & Francis).
Assure attribution of your work, by making sure you are identified as the author.
We encourage you to:
Share your work
Make printed copies of your article to use for lecture or classroom purposes.
Include your article in a thesis or dissertation.
Present your article at a meeting or conference and distribute printed copies of the article.
Republish the article (making sure you cite the original article).
Adapt and expand your published journal article to make it suitable for your thesis or dissertation.
Popular tags
research researcher award prize writing early career researcher peer review impact social media open access article visibility tips authors article preparation research impact PhD public engagement Expert Opinion Expert Review research engagement research stories advice ECRs

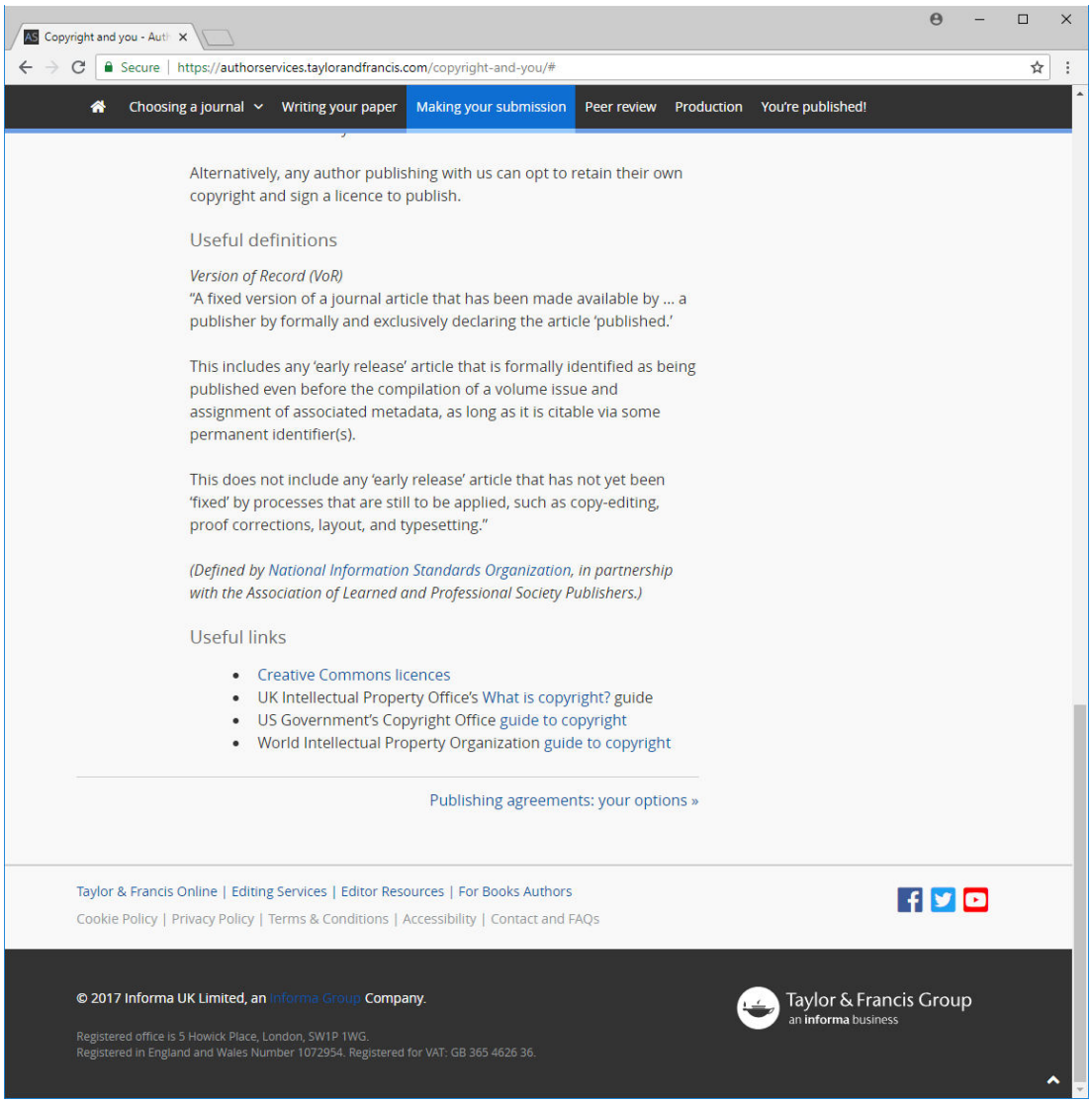
Copyright and you - Auth
Secure | https://authorservices.taylorandfrancis.com/copyright-and-you/#
Choosing a journal
Writing your paper
Making your submission
Peer review
Production
You're published!
Alternatively, any author publishing with us can opt to retain their own copyright and sign a licence to publish.
Useful definitions
Version of Record (VoR)
"A fixed version of a journal article that has been made available by ... a publisher by formally and exclusively declaring the article 'published.'
This includes any 'early release' article that is formally identified as being published even before the compilation of a volume issue and assignment of associated metadata, as long as it is citable via some permanent identifier(s).
This does not include any 'early release' article that has not yet been 'fixed' by processes that are still to be applied, such as copy-editing, proof corrections, layout, and typesetting."
(Defined by National Information Standards Organization, in partnership with the Association of Learned and Professional Society Publishers.)
Useful links
Creative Commons licences
UK Intellectual Property Office's What is copyright? guide
US Government's Copyright Office guide to copyright
World Intellectual Property Organization guide to copyright
Publishing agreements: your options »
Taylor & Francis Online | Editing Services | Editor Resources | For Books Authors
Cookie Policy | Privacy Policy | Terms & Conditions | Accessibility | Contact and FAQs
© 2017 Informa UK Limited, an Informa Group Company.
Registered office is 5 Howick Place, London, SW1P 1WG.
Registered in England and Wales Number 1072954. Registered for VAT: GB 365 4626 36.
Taylor & Francis Group
an informa business

Permission for the following '**Measurement Science Technology**' publication is attached below:

- **Deo MN**, El-Mowafy A (2019) A method for Precise Point Positioning with Integer Ambiguity Resolution with Triple-frequency GNSS Data, Measurement Science and Technology, https://iopscience.iop.org/article/10.1088/1361-6501/ab0945, accepted online 21 February 2019.

Assignment of copyright and publication agreement

IOP Publishing Limited ("IOP") agrees to publish:

Manuscript Title: A method for Precise Point Positioning with Integer Ambiguity Resolution with Triple-frequency GNSS Data (the "Article") written by

Names of all authors: Deo, Manoj; El-Mowafy, Ahmed ("the Named Authors") in the following journal Measurement Science and Technology ("the Journal")

Name of copyright owner(s) (if not the Named Author(s) – see Important Information above): ("the Copyright Owner")

IOP Ref: MST-108295.R1

Part 1 - Publication on a Subscription basis

1.1 In consideration for acceptance and publication of the Article, the Named Authors of the Article and/or the Copyright Owner hereby assign, where necessary by present assignment of future copyright, to IOP with full title guarantee the entire copyright in all original material published as part of the Article (which expression includes but is not limited to the text, abstract, tables, figures and graphs, related corrigenda or "comments" and multimedia content but excludes any other item referred to as supplementary material and/or any video abstract) throughout the world for the full term of copyright (including any extensions or renewals thereof) for all media and formats, whether known or unknown. Such assignment shall be effective only if the Article (or any resubmission of the Article) is accepted for publication. For the avoidance of doubt, copyright does not subsist in any fundamental data underlying the Article and nothing in this agreement is intended to limit access to or use of such data.

1.2 If the Article, or any part of it, is protected by Crown copyright, in consideration for acceptance and publication of the Article, the relevant Named Authors and the relevant originating department or agency hereby grant IOP a non-exclusive royalty-free worldwide freely-transferrable licence for the full term of copyright (including any extensions or renewals thereof) for all media and formats, whether known or unknown, to do in relation to the Article all acts restricted by copyright worldwide including, but not limited to, the right of action under section 101A of the Copyright Designs and Patents Act 1988. Such licence shall be effective only if the Article is accepted for publication.

1.3 If all the Named Authors are employees of the US Government, they represent and warrant to IOP that the Article was prepared as part of their official duties. In such circumstances, or where the Article was created as part of a work for hire, none of the original content within the Article is subject to copyright protection as it is in the public domain.

1.4 In consideration for acceptance and publication of the Article, the Named Authors and/or the Copyright Owner hereby grant IOP a royalty-free non-exclusive worldwide freely transferrable licence for the full term of copyright (including any extensions or renewals thereof) to do in relation to any supplementary material not deemed to be part of the Article and/or any video abstract all acts restricted by copyright worldwide. This shall include, but not be limited to, making the material available under any licence that IOP deems appropriate for purposes including, but not limited to, the maximisation of visibility and the long term preservation of the content.

1.5 Each of the Named Authors consents to all publication and processing of their personal data by IOP, as that data is displayed on the Article, including, but not limited to, the names and email addresses of the Named Authors. Accordingly, the Named Authors shall not object on data protection grounds to the use of their personal data on the Article wherever IOP chooses to display it, whether itself or via a third party.

Representations and warranties

2.1 The Copyright Owner and/or the Submitting Author on behalf of the Named Authors (as appropriate) represent and warrant that:

2.1.1 the Article is the original work of the Named Authors;

2.1.2 the Article has not been published previously in any form, other than in accordance with our Preprint pre-publication policy;

2.1.3 each of the Named Authors has made a material contribution to the conception and/or writing of the Article, has received the final version of the Article, has agreed to its submission on the terms contained herein and takes responsibility for it and submission has been approved as necessary by the authorities at the establishment where the research was carried out;

2.1.4 the Submitting Author completes and returns this agreement as authorised agent for and on behalf of all the Named Authors and the Copyright Owner (as applicable) and has the full power to enter into this agreement and to make the grants and assignments it contains;

2.1.5 the Article has not been and shall not be submitted to another publisher prior to withdrawal or rejection by IOP;

2.1.6 the Article does not infringe any third party rights, it contains nothing libellous or unlawful, all factual statements are to the best of the Named Authors' knowledge true or based on valid research conducted according to accepted norms and all required permissions have been obtained in writing;

2.1.7 the Article expressly acknowledges any third party funding and/or potential conflicts of interest; and

2.1.8 any supplementary material or video abstract is the original work of the Named Authors, or is the property of the Copyright Owner, or permission has been obtained from its owner(s) for its publication by IOP and permission has been obtained for the inclusion of any third party content.

2.2 The Named Authors and/or the Copyright Owner (as appropriate) indemnify and will keep indemnified IOP against all costs and expenses suffered or incurred by IOP as a result of and/or arising out of any breach of the representations and/or warranties in this section 2.

The Named Authors' rights

3.1 IOP grants the Named Authors the rights specified in paragraphs 3.2 and 3.3. All such rights must be exercised solely for non-commercial purposes. Where possible, any use should display citation information and IOP's copyright notice, and, for electronic use, best efforts must be made to include a link to the online abstract in the Journal.

Exercise of the rights in paragraph 3.2 may use the peer reviewed, edited, formatted and typeset version of the Article including any tagging, indexing and other enhancements published by IOP and/or its licensors ("Final Published Version").

Exercise of the rights referred to in paragraph 3.3 must not use the Final Published Version and extend only to the version of the Article accepted for publication including all changes made as a result of the peer review process, and which may also include the addition to the article by IOP of a header, an article ID, a cover sheet and/or an 'Accepted Manuscript' watermark, but excluding any other editing, typesetting or other changes made by IOP and/or its licensors (the "Accepted Manuscript") and must be accompanied by the following statement of provenance:

'This is the Accepted Manuscript version of an article accepted for publication in Measurement Science and Technology.

IOP Publishing Ltd is not responsible for any errors or omissions in this version of the manuscript or any version derived from it. The Version of Record is available online at [insert DOI].'

3.2 The rights are:

3.2.1 To make copies of the Final Published Version of the Article (all or part) for teaching purposes;

3.2.2 To include the Final Published Version of the Article (all or part) in a research thesis or dissertation provided it is not then published commercially;

3.2.3 To make oral presentation of the Final Published Version of the Article (all or part) and to include a summary and/or highlights of it in papers distributed at such presentations or in conference proceedings; and

3.2.4 To use original figures and text from the Final Published Version of the Article falling within the quota outlined in and subject to the STM Permissions Guidelines (http://www.stm-assoc.org/permissions-guidelines/) at the relevant time in force.

For the avoidance of doubt, the Named Authors retain all proprietary rights in the Article other than copyright.

3.3 Additional rights of the Named Authors are to:

3.3.1 Use the Accepted Manuscript (all or part) without modification in personal compilations of the Named Authors' own works (provided not created by a third party publisher); and

3.3.2 Include the Accepted Manuscript (all or part) on the Named Authors' own Personal Website(s), institutional website(s), repositories, Scientific Social Networks and third party websites provided that this is fully in accordance with the Author Rights set out at the following url legal.ioppublishing.org/author-rights on the date of submission of the agreement.

Miscellaneous

4. To the extent that there are moral rights in the Article, all the Named Authors expressly reserve and assert their moral rights to be identified as the authors of the Article.

5. The Named Authors and/or the Copyright Owner shall execute such further documents, and take such actions and do such things, as may be requested by IOP at IOP's reasonable expense to give full effect to the terms of the agreement.

6. For the avoidance of doubt, the grants and assignment envisaged herein shall become effective only upon acceptance of the Article for publication. In the event that the Article is withdrawn prior to acceptance, or is rejected, this agreement shall have no effect and no party shall be bound by it.

7. The agreement shall be governed by English Law and subject to the non-exclusive jurisdiction of the English courts.

Confirmation

8. By selecting to publish on a subscription basis, the Submitting Author is responsible for ensuring that, where relevant all Named Authors, who are affiliated to a university/institution which has an open access policy which is incompatible with IOP's green open access policy, obtain a waiver for the Article from their institution or university's open access policy and retain such waiver as evidence of compliance. These Named Authors agree that they shall obtain such waivers and provide them to IOP promptly on request.

9. By typing the Submitting Author's name into the box at Part 3 below and clicking "Submit", the Named Authors agree to these terms. The Authorised Signatories of any third party Copyright Owner(s) and/or the Submitting Author agree, on behalf of such Copyright Owner(s), to these terms by typing the Copyright Owner's name into the "Copyright Owner" box at the top of the page.

Part 2 - Publication on a Gold Open Access basis

1.1 In consideration for acceptance and publication of the Article, the Named Authors of the Article and/or the Copyright Owner hereby assign, where necessary by present assignment of future copyright, to IOP with full title guarantee the entire copyright in all original material published as part of the Article (which expression includes but is not limited to the text, abstract, tables, figures and graphs, related corrigenda or "comments" and multimedia content but excludes any other item referred to as supplementary material and/or any video abstract) throughout the world for the full term of copyright (including any extensions or renewals thereof) for all media and formats, whether known or unknown. Such assignment shall be effective only if the Article (or any resubmission of the Article) is accepted for publication. For the avoidance of doubt, copyright does not subsist in any fundamental data underlying the Article and nothing in the agreement is intended to limit access to or use of such data.

1.2 If the Article, or any part of it, is protected by Crown copyright, in consideration for acceptance and publication of the Article, the relevant Named Authors and/or the relevant originating department or agency hereby grant IOP a non-exclusive royalty-free worldwide licence for the full term of copyright (including any extensions or renewals thereof) for all media and formats, whether known or unknown, to do in relation to the Article all acts restricted by copyright worldwide.

1.3 If all the Named Authors are employees of the US Government, they represent and warrant to IOP that the Article was prepared as part of their official duties. In such circumstances, or where the Article was created as part of a work for hire, none of the original content within the Article is subject to copyright protection as it is in the public domain.

1.4 In consideration for acceptance and publication of the Article, the Named Authors and/or the Copyright Owner hereby grant IOP a royalty-free non-exclusive worldwide freely transferrable licence for the full term of copyright (including any extensions or renewals thereof) to do in relation to any supplementary material not deemed to be part of the Article and/or any video abstract all acts restricted by copyright worldwide. This shall include, but not be limited to, making the material available under any licence that IOP deems appropriate for purposes including, but not limited to, the maximisation of visibility and the long term preservation of the content.

1.5 Each of the Named Authors consents to all publication and processing of their personal data by IOP, as that data is displayed on the Article, including, but not limited to, the names and email addresses of the Named Authors. Accordingly, the Named Authors shall not object on data protection grounds to the use of their personal data on the Article wherever IOP chooses to display it, whether itself or via a third party.

1.6 Each of the Named Authors and, where relevant, the Copyright Owner consents to the publication of the Article under the Creative Commons Attribution 3.0 Unported licence (CC BY 3.0) (https://creativecommons.org/licenses/by/3.0/) or any successor to that licence.

Representations and warranties

2.1 The Copyright Owner and/or the Submitting Author, on behalf of the Named Authors (as appropriate) represent and warrant that:

2.1.1 the Article is the original work of the Named Authors;

2.1.2 the Article has not been published previously in any form, other than in accordance with our Preprint pre-publication policy;

2.1.3 each of the Named Authors has made a material contribution to the conception and/or writing of the Article, has received the final version of the Article, has agreed to its submission on the terms contained herein and takes responsibility for it and submission has been approved as necessary by the authorities at the establishment where the research was carried out;

2.1.4 the Submitting Author completes and returns the agreement as authorised agent for and on behalf of all the Named Authors and Copyright Owner (as applicable) and has the full power to enter into the agreement and to make the grants and assignments it contains;

2.1.5 the Article has not been and shall not be submitted to another publisher prior to withdrawal or rejection by IOP;

2.1.6 the Article does not infringe any third party rights, it contains nothing libellous or unlawful, all factual statements are to the best of the Named Authors' knowledge true or based on valid research conducted according to accepted norms and all required permissions have been obtained in writing;

2.1.7 the Article explicitly acknowledges any third party funding and/or potential conflicts of interest; and

2.1.8 any supplementary material or video abstract is the original work of the Named Authors, or is the property of the Copyright Owner, or permission has been obtained from its owner(s) for its publication by IOP and permission has been obtained for the inclusion of any third party content.

2.2 The Named Authors and/or the Copyright Owner indemnify and will keep indemnified IOP against all costs and expenses suffered or incurred by IOP as a result of and/or arising out of any breach of the representations and/or warranties in this section 2.

The Named Authors' rights

3.1 The Named Authors and all third parties will have the rights to use the Article as described in the licence applied to the Article pursuant to paragraph 1.6, above, which shall include the right to copy, distribute and display the published version of the Article and create derivative works, subject to appropriate attribution.

3.2 Where the Article is used in accordance with paragraph 3.1 above, the following attribution shall be included subject to any additional terms of the licence under which the Article was published:
Article title
Named Author(s)
DOI
Journal citation
Name of the licence with a link to that licence
Indication if any changes were made

Miscellaneous

4. To the extent that there are moral rights in the Article, all the Named Authors expressly reserve and assert their moral rights to be identified as the authors of the Article.

5. The Named Authors and/or the Copyright Owner shall execute such further documents, and take such actions and do such things, as may be requested by IOP at IOP's reasonable expense to give full effect to the terms of the agreement.

6. For the avoidance of doubt, the grants and assignment envisaged herein shall become effective only upon acceptance of the Article for publication. In the event that the Article is withdrawn prior to acceptance, or is rejected, the agreement shall have no effect and no party shall be bound by it.

7. The agreement shall be governed by English Law and subject to the non-exclusive jurisdiction of the

English courts.

Confirmation

8. By selecting to publish Gold Open Access, the Submitting Author is responsible for ensuring that the Article Publication Charge of the Journal is paid in full to IOP, pursuant to IOP's payment terms, unless otherwise agreed in writing with IOP.

9. By typing the Submitting Author's name into the box at Part 3 below and clicking "Submit", the Named Authors agree to all these terms. Authorised Signatories of any third party Copyright Owner(s) and/or the Submitting Author agree, on behalf of such Copyright Owner(s), to these terms by typing the Copyright Owner's name into the "Copyright Owner" box at the top of the page.

Part 3 – Confirmation and Execution
Please tick the appropriate boxes in section A, section B and section C below.

eq **Section A - Please tick one of the boxes below to confirm how you would like the Article published (if it is accepted):**

Subscription – Part 1 Applies

eq **Section B - Please tick one of the boxes below to confirm the following:**

For Subscription. Please tick this box to confirm that each Named Author, who is affiliated to a university/institution which has an open access policy which is incompatible with IOP's green open access policy, has obtained a waiver for the Article from their institution or university's open access policy. For more information refer to this page.

eq **Section C - Please ALSO tick one of the boxes below to confirm the basis upon which you are granting IOP the right to publish the article (if it is accepted):**

Standard transfer of copyright (assignment) – please select this box unless one of the exceptions below applies to the Article.

eq Type your name here:

Manoj Deo (the "Submitting Author")

eq Date:

11-Jan-2019

By clicking "Submit" and typing your name above, you shall be assumed to have read and understood all of the terms and conditions of the relevant part of the agreement and you will be agreeing to all of the terms and conditions and assignment (as the case may be) detailed above.

LAST UPDATED September 2017

APPENDIX B: STATEMENT OF CONTRIBUTIONS BY OTHERS

This Appendix states the contributions for the author's and co-author's, accompanied by signatures from all parties concerned. All the papers in this thesis were published in peer reviewed journals or conference proceedings.

To Whom it may concern

I, Manoj Nilesh Deo, wrote the manuscripts, developed the methodology and performed the numerical analysis using multi-frequency and multi-frequency GNSS data. The data simulation and analysis were performed using my own software written in the Python programming language. Associate Professor Ahmed El-Mowafy provided comments and suggestions to improve the quality of the manuscript so as to be accepted for publication. This statement holds for the following publications:

1. **Deo MN**, El-Mowafy A (2019) A method for Precise Point Positioning with Integer Ambiguity Resolution with Triple-frequency GNSS Data, Measurement Science and Technology, 30(6): 065009, https://doi.org/10.1088/1361-6501/ab0945.
2. **Deo MN**, El-Mowafy A (2018) Comparison of Advanced Troposphere Models for Aiding Reduction of PPP Convergence Time in Australia, Journal of Spatial Science, https://doi.org/10.1080/14498596.2018.1472046, first published online: 24 May 2018.
3. **Deo MN**, El-Mowafy A (2018) Triple Frequency GNSS Models for PPP with Float Ambiguity Estimation – Performance Comparison using GPS, Survey Review, 50(360): 249-261, doi: 10.1080/00396265.2016.1263179, first published online: 2 Dec 2016.
4. **Deo MN**, El-Mowafy A (2017) Ionosphere Augmentation for accelerated convergence in Precise Point Positioning with multi-frequency and multi-constellation GNSS, paper presented at ION Pacific PNT 2017 Conference, Honolulu, Hawaii, May 1-4, 2017.
5. **Deo MN**, El-Mowafy A (2016) Triple Frequency precise point positioning with multi-constellation GNSS, IGNSS Conference, UNSW Australia, 6–8 December 2016.

6. **Deo MN**, El-Mowafy A (2015) Cycle Slip and Clock Jump Repair with Multi-Frequency Multi-Constellation GNSS data for Precise Point Positioning, IGNSS Conference, Surfers Paradise, Qld, Australia, 14-16 July 2015.

Manoj Nilesh Deo 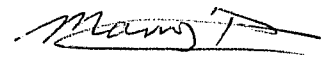

I, as a co-author, endorse that the level of contribution indicated by the candidate above is appropriate.

Ahmed El-Mowafy 

I, Manoj Nilesh Deo, wrote an initial version of the manuscript, contributed towards the methodology and performed the computer programming and numerical analysis for the following publication. Associate Professor Ahmed El-Mowafy re-wrote the manuscript and Professor Chris Rizos provided comments and suggestions to improve the quality of the manuscript.

1. El-Mowafy A, **Deo M**, Rizos C (2016) On Biases in Precise Point Positioning with Multi-Constellation and Multi-Frequency GNSS Data. Measurement Science and Technology, 27(3), 035102. DOI:/10.1088/0957-0233/27/3/035102.

I, Manoj Nilesh Deo, contributed significantly towards the computer programming and numerical analysis for the following publication. Associate Professor Ahmed El-Mowafy wrote the manuscript and performed some numerical analysis. Professor Nobuaki Kubo, along with me, provided comments and suggestions for improvement:

1. El-Mowafy A, **Deo MN**, Kubo N (2017) Maintaining real-time precise point positioning during outages of orbit and clock corrections. GPS Solutions, 21(3), 937-947. DOI:10.1007/s10291-016-0583-4.

Manoj Nilesh Deo 

I, as a co-author, endorse that the level of contribution indicated by the candidate above is appropriate.

Ahmed El-Mowafy 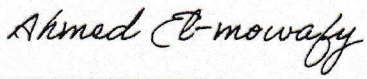

Chris Rizos 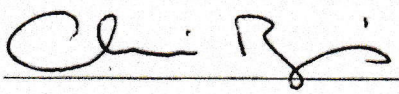

Nobuaki Kubo 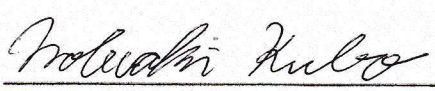

APPENDIX C: PROOF OF PEER-REVIEW AND ACCEPTANCE FOR CONFERENCE PROCEEDINGS

The following correspondence provides proof that the conference publications were published in peer-reviewed conference proceedings and accepted respectively:

1. **Deo MN**, El-Mowafy A (2017) Ionosphere Augmentation for accelerated convergence in Precise Point Positioning with multi-frequency and multi-constellation GNSS, paper presented at ION Pacific PNT 2017 Conference, Honolulu, Hawaii, May 1-4, 2017.
2. **Deo MN**, El-Mowafy A (2016) Triple Frequency precise point positioning with multi-constellation GNSS, IGNSS Conference, UNSW Australia, 6–8 December 2016.
3. **Deo MN**, El-Mowafy A (2015) Cycle Slip and Clock Jump Repair with Multi-Frequency Multi-Constellation GNSS data for Precise Point Positioning, IGNSS Conference, Surfers Paradise, Qld, Australia, 14-16 July 2015.

On Fri, Mar 24, 2017 at 4:48 AM <meetings@ion.org> wrote:
Dear Manoj Deo:

Your paper, titled Ionosphere Augmentation for Accelerated Convergence in Precise Point Positioning with Multi-frequency and Multi-constellation GNSS, has been accepted for presentation at the Pacific PNT 2017 Conference, taking place May 1-4, 2017, at the Marriott Waikiki Beach, Honolulu, Hawaii.

Your paper has been assigned to Session C3: High Precision GNSS Correction and Monitoring Networks, scheduled for Wednesday, May 3, 2017. You can view the full program online at: https://www.ion.org/pnt/program.cfm

Please confirm that you have been notified of the acceptance of your paper. Click here to confirm that you have received this acceptance notice:
https://www.ion.org/abstracts/confirmNotification.cfm?abstractkey=1E2E03C2D690861FCD55C3E4EDF384E0

Please carefully read the session chairs peer review comments for your paper. If you submitted your manuscript by the deadline of March 1 and your paper is missing the reviews, please check again in a few days, as some reviewers have not yet completed the peer review forms. If your paper did not pass the peer review, and the recommendation is "Endorse paper subject to satisfactory revision," make sure you upload a revised version of the paper addressing all the reviewers recommendations by April 20, 2017.

Revised papers not received by April 20 will not be given a second review. However, you may upload revisions at any time until the final deadline of May 11, 2017, but only those papers uploaded by April 20 will have the opportunity of a second review if they did not pass the first one.

Other Reminders:

All authors (primary and alternates) are required to attend a speakers' breakfast on the morning of their presentation(s) in the Waikiki Ballroom, 8:00 am. 8:45 a.m. If you are not in attendance, the Session Chairs will allocate your presentation time to another presenter.
Papers must be presented in order to be included in the conference proceedings. Only authors listed on a paper may present.
Alternate papers will be included in the proceedings if the author attends the speakers' breakfast, attend the session and is ready to present if needed.
Best Regards,
Miriam Lewis
ION Author Liaison
Phone: 703-366-2723
E-mail: meetings@ion.org


Dr. Xiaochun Lu,
Chinese Academy of Science, Timing Center, China


Dr. Xingqun Zhan,
Shanghai Jiaotong University, China

Session A3: BDS, 9:00 a.m. - 1:00 p.m.
Room: Kona Moku A

9:05 Keynote: Analysis on BDS Global System Performance: Yuanxi Yang, China National Administration of GNSS and Applications, China

9:35 BDS Space Service Volume Characteristics: Hui Yang and Xinuo Chang, China Academy of Space Technology, China

10:05 Analysis of Inner-consistency of BDS Broadcast Ephemeris Parameters and their Performance Improvement: Junping Chen, Qian Chen, Sainan Yang, Shanghai Astronomical Observatory and Chinese Academy of Sciences University, China; Bin Wang, Yize Zhang, Shanghai Astronomical Observatory, China; Jungang Wang, Technical University of Berlin, Germany

Break: 10:35 a.m. - 10:55 a.m.

11:00 Real-time Estimation of BDS High-rate Satellite Clock Offsets with Prior Troposphere Constraints: Ying Liu, Beijing Institute of Tracking and Telecommunications Technology, China; Wenju Fu, Guanwen Huang, Qin Zhang, Chang'an University, Xi'an, China

11:30 BDS Autonomous Orbit Determination using Inter-satellite Tracking and Onboard Accelerometers: Jing Qiao, Wu Chen, Zhizhao Liu, The Hong Kong Polytechnic University, Hong Kong

12:00 Research on Distortion of Space Signal of BDS Satellite Navigation System and the Influence of Civil Aviation Ranging Performance: Ruihua Liu, Yanan Zhao, Jian Wang, Civil Aviation University of China, China

12:30 Parameter Validity Period Estimation of Processing BDS Precise Orbit in BERN SRP Model: Tongyu Che, Wei Zhou, Zhuoxi Ma, Xian Division of Surveying and Mapping, China


Dr. Kevin Ang,
National University of Singapore, Singapore


Dr. Kevin Brink, Air Force Research Laboratory, USA

Session B3: Unmanned Aerial Systems 1, 9:00 a.m. - 12:30 p.m.
Room: Kona Moku B

9:05 Keynote: Design of Local Area DGNSS Architecture to Support UAV Networks: Optimal Integrity/Continuity Allocations and Fault Monitoring: Minchan Kim, Jinsil Lee, Dongwoo Kim, and Jiyun Lee, Korea Advanced Institute of Science and Technology, South Korea

9:35 Test and Evaluation of Mitigating Technologies for Unmanned Aircraft Systems in GPS Degraded and Denied Environments: Timothy Pitt, Greg Reynolds, US Army, AMRDEC; Will Barnwell, US Army, PM UAS; Laura McCrain and Jonathan Jones, NTA

10:05 UWB Odometry for Relative Navigation in GPS and Compass-denied Environment: Geng Qin, Kevin Z. Y. Ang, Xiangxu Dong, Wenqi Liu, Feng Lin, Temasek Laboratory, National University of Singapore, Singapore

Break: 10:35 a.m. - 10:55 a.m.

11:00 PHKD: Parallel Hierarchical Keyframe Decimation of UAV Captured Video for 3D Reconstruction: Zhen Xie, Jianhua Zhang, Qing Bu, Zhejiang University of Technology, China; MingJie Lao, Temasek Laboratories, National University of Singapore, Singapore; Shengyong Chen, Zhejiang University of Technology, China

11:30 New Vector Calibration Method for Magnetometer and its Impact on Integrated Navigation System for Low-cost UAV: Heekwon No, O-Jong Kim, Deokhwa Han, Junesol Song and Changdon Kee, Seoul National University, South Korea

12:00 Small Fixed-wing Aerial Positioning Using Inter-vehicle Ranging Combined With Visual Odometry: Benjamin M. Fain and John F. Raquet, Air Force Institute of Technology

Alternates

1. **Lowest Noise 6 DoF Single Chip MEMS IMU:** Mark Boysel, Louis Ross, Robert Zegarelli, Motion Engine, Inc.
2. **A Novel Approach to Characterize the Airborne Antenna Group Delay Variations as a Function of Arrival Angle using a MultiCopter:** Anurag Raghuvanshi and Frank van Graas, Ohio University


Dr. Todd Walter,
Stanford University, USA


Dr. Hui Liu,
Wuhan University,China

Session C3: High Precision GNSS Correction and Monitoring Networks, 9:00 a.m. - 12:30 p.m.
Room: Kona Moku C

9:05 Keynote: Analysis of the Extended Orbit and Clock Corrections for Real-Time PPP: Hongzhou Yang, Yang Gao, University of Calgary, Canada; Chaoqian Xu , Wuhan University, China; Zhixi Nie, China University of Petroleum, China

9:35 A Study on GPS/GLONASS Compact Network RTK and Analysis on Temporal Variations of Carrier Phase Corrections for Reducing Broadcast Bandwidth: Junesol Song, Seoul National University, South Korea; Byungwoon Park, Sejong University, South Korea; Changdon Kee, Seoul National University, South Korea

10:05 A New Algorithm for Ionosphere STEC Modeling through Combining Empirical Ionosphere Model with GNSS Observation Data: Li Wen, Yuan Hong, Ouyang Guangzhou, Li Zishen, Wang Ningbo, Zhoukai, Academy of Opto-Electronics, CAS, China

Break: 10:35 a.m. - 10:55 a.m.

11:00 Ionosphere Augmentation for Accelerated Convergence in Precise Point Positioning with Multi-frequency and Multi-constellation GNSS: Manoj Deo and Ahmed El-Mowafy, Curtin University, Australia

11:30 Potential of Locally Enhanced MADOCA PPP as a Positioning Infrastructure for the Asia-Pacific Region: Ken Harima, Suelynn Choy, RMIT University, Australia; Kazutoshi Sato, Japan Aerospace Exploration Agency, Japan

12:00 WAAS Signal Deformation Monitor Performance: Beyond the ICAO Threat Model: R. Eric Phelts, Stanford University; Karl Shallberg, Zeta Associates Incorporated; Todd Walter and Per Enge, Stanford University

Alternate

1. **Update of iGMAS:** Shuli Song, Wenhai Jiao, Hanrong Sun, Xiaolin Jia, China Satellite Navigation Project Center, China

Informal Luncheon, 12:30 p.m. - 1:30 p.m., Waikiki Ballroom

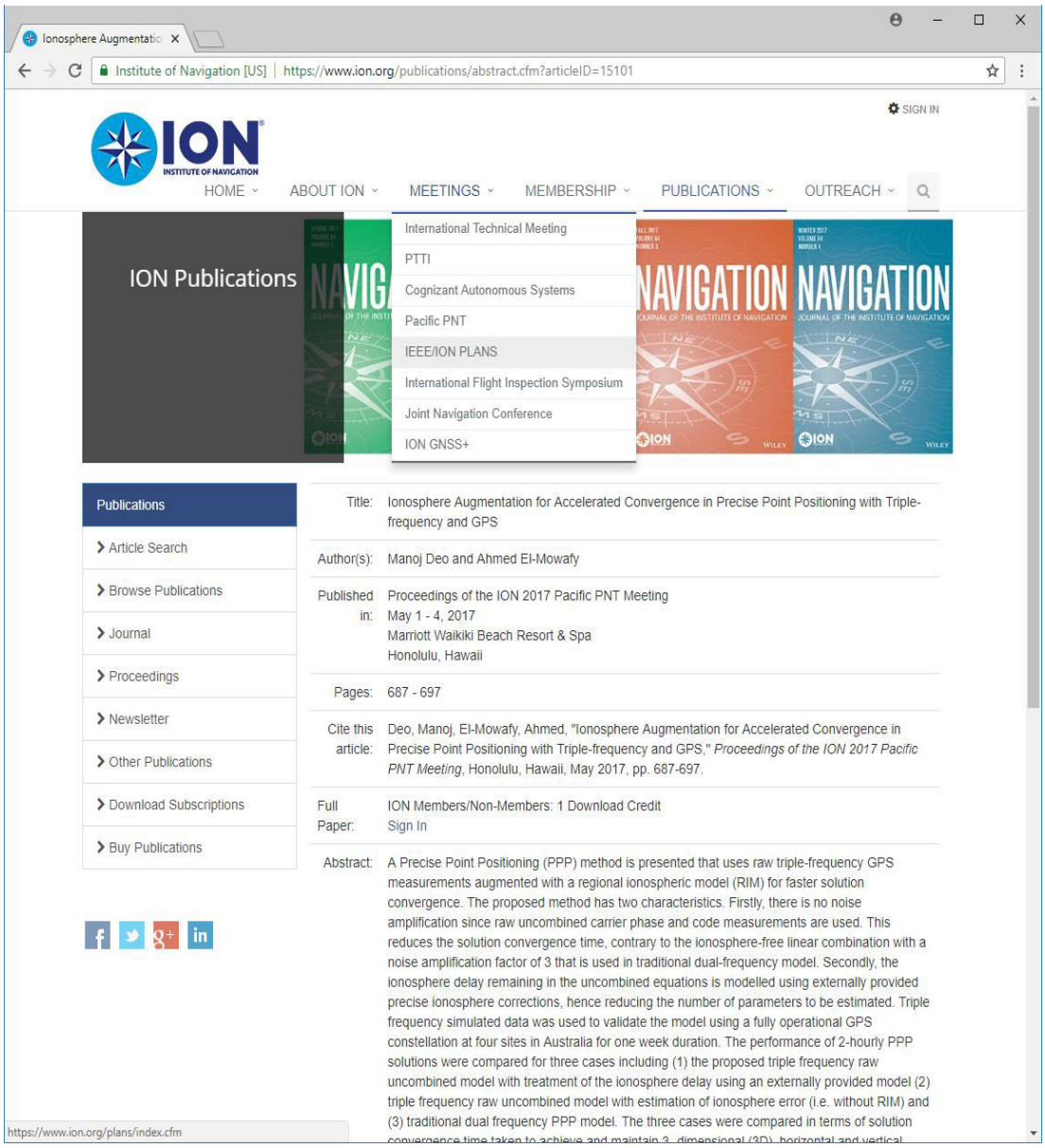
Ionosphere Augmentatio
Institute of Navigation [US] | https://www.ion.org/publications/abstract.cfm?articleID=15101
SIGN IN
ION
INSTITUTE OF NAVIGATION
HOME
ABOUT ION
MEETINGS
MEMBERSHIP
PUBLICATIONS
OUTREACH
ION Publications
International Technical Meeting
PTTI
Cognizant Autonomous Systems
Pacific PNT
IEEE/ION PLANS
International Flight Inspection Symposium
Joint Navigation Conference
ION GNSS+
NAVIGATION
JOURNAL OF THE INSTITUTE OF NAVIGATION
Publications
Article Search
Browse Publications
Journal
Proceedings
Newsletter
Other Publications
Download Subscriptions
Buy Publications
Title: Ionosphere Augmentation for Accelerated Convergence in Precise Point Positioning with Triple-frequency and GPS
Author(s): Manoj Deo and Ahmed El-Mowafy
Published in: Proceedings of the ION 2017 Pacific PNT Meeting
May 1 - 4, 2017
Marriott Waikiki Beach Resort & Spa
Honolulu, Hawaii
Pages: 687 - 697
Cite this article: Deo, Manoj, El-Mowafy, Ahmed, "Ionosphere Augmentation for Accelerated Convergence in Precise Point Positioning with Triple-frequency and GPS," Proceedings of the ION 2017 Pacific PNT Meeting, Honolulu, Hawaii, May 2017, pp. 687-697.
Full Paper: ION Members/Non-Members: 1 Download Credit
Sign In
Abstract: A Precise Point Positioning (PPP) method is presented that uses raw triple-frequency GPS measurements augmented with a regional ionospheric model (RIM) for faster solution convergence. The proposed method has two characteristics. Firstly, there is no noise amplification since raw uncombined carrier phase and code measurements are used. This reduces the solution convergence time, contrary to the ionosphere-free linear combination with a noise amplification factor of 3 that is used in traditional dual-frequency model. Secondly, the ionosphere delay remaining in the uncombined equations is modelled using externally provided precise ionosphere corrections, hence reducing the number of parameters to be estimated. Triple frequency simulated data was used to validate the model using a fully operational GPS constellation at four sites in Australia for one week duration. The performance of 2-hourly PPP solutions were compared for three cases including (1) the proposed triple frequency raw uncombined model with treatment of the ionosphere delay using an externally provided model (2) triple frequency raw uncombined model with estimation of ionosphere error (i.e. without RIM) and (3) traditional dual frequency PPP model. The three cases were compared in terms of solution
https://www.ion.org/plans/index.cfm

Your abstract has been accepted to IGNSS 2016! View this email in your browser

Dear Mr Manoj Nilesh Deo,

We are pleased to inform you that your abstract/s:
"Evaluation of accuracy and availability of ARNS multi-constellation signals for aviation users in Australia" AND "Biases in Multi-Constellation Triple-frequency PPP Models with a Float Ambiguity Solution"
have been accepted for oral presentation at IGNSS 2016.

We ask that you kindly register by clicking on the link below. Payment is by credit card only. Please select the "Speaker" rate or "Student" rate as appropriate.

The deadline for paper submission for peer review has been extended to Tuesday 4th October 2016.

Please contact the IGNSS secretariat at ignss@unsw.edu.au if you have further questions.

Best wishes from the 2016 IGNSS Program Committee!

REGISTER NOW!

Early-bird prices available until
Monday, 10 October 2016

Click here to register now!

Wednesday, 7th December

IGNSS2016

	Colombo Theatre A		Colombo Theatre B		Colombo Theatre C	
	Keynotes *Chair: Chris Rizos*					
9:00	**Joseph Winter** Head of AIS Innovation, R&D, Australian Institute of Sport **"Testbed for Wearable Electronic Sensors"**					
9:30	**Mike Terkildsen** Ionospheric Prediction Service, Australian Bureau of Meteorology **"Ionospheric Space Weather: Monitoring, modelling and mitigation"**					
10:00	**Greg Gutt** Chief Technical Officer, Satelles **"A New Robust System for Assured PNT - Satellite Time and Location - Hosted on Iridium"**					
10:30	**Morning Tea**					
	Australia's Next Generation Multi-GNSS Analysis Capability *Chair: Allison Kealy*		**Alternatives to GNSS** *Chair: Salil Goel*		**Algorithms and Methods II** *Chair: Joon Wayn Cheong*	
11:00	Multi-GNSS PPP-RTK network processing; achieving the accuracy	Peter Teunissen, CRCSI	Locata: Serving those Positioning, Navigation & Timing (PNT) Applications that GNSS can not	Chris Rizos, School of Civil & Environmental Engineering, UNSW	Seamless Train Localization Based on Beidou/INS/Odometer Multi-Sensor Navigation System	Wei Jiang, Beijing Jiaotong University
11:20	Development of the Multi-GNSS Analysis Centre Software	Stavros Melachroinos, Geoscience Australia	GNSS-based Positioning Schemes & Applications in Safety-critical Systems of Rail Transport	Chengming Jin, Beijing Jiaotong University/ University of Melbourne	Systematic Errors in UAS Aerial Photogrammetry	Yincai Zhou, University of New South Wales
11:40	BeiDou solar radiation pressure and attitude modelling	Stavros Melachroinos, Geoscience Australia	Inter-Pseudolite Range Augmented GNSS PPP Navigation for Airborne Pseudolite Systems	Panpan Huang, UNSW Australia	Dual GNSS / INS / Odometer post-processing	Michael Reichman, Advanced Navigation
12:00	**Lunch**					
	Construction, Mining and Structural Monitoring *Chair: Nick Talbot*		**SBAS/PPP I** *Chair: Suelynn Choy*		**Algorithms and Methods III** *Chair: Yanming Feng*	
13:00	BELS: GNSS Bridges between Europe and South East Asia	La The Vinh, Hanoi University of Science and Technology	A LEX-only QZSS LEX Signal Demodulation Scheme for LEX-PPP services	Huiben Zhang, Queensland University of Technology	Quantifying Mis-Modelling Effects in the GNSS Yaw-Attitude Determination	Thomas Papanikolaou & Stavros Melachroinos, CRCSI, Geoscience Australia
13:20	Developing an Integrated Wi-Fi-Based Positioning System and GIS for Improving Productivity Analysis of Construction Projects	Samad Sepasgozar & Sara Shirowzhan, Faculty of Built Environment, UNSW Australia	Biases in Multi-Constellation Triple-frequency PPP Models with a Float Ambiguity Solution	Manoj Deo, Curtin University	A Geometry-Free Approach for Estimation of Uncalibrated Signal Delays in GPS Triple Frequency Signals	Yanming Feng & Yongchao Wang, Queensland University of Technology
13:40	Third Generation of Positioning Systems for Underground Mine Environments, the Latest Progress	Binghao Li, University of New South Wales	Local Augmentation to Wide Area PPP Systems: a Case Study in Victoria, Australia	Suelynn Choy, RMIT University	Efficient Processing of Long Duration GNSS Signal Observations	Md Sohrab Mahmud, University of New South Wales, Canberra
14:00	Accuracy of stockpile volume determination using UAS photogrammetry	Luke Chidzey, Yincai Zhou, Craig Roberts, UNSW Australia	The Performance of Precise Point Positioning (PPP) using Triple-frequency GPS Measurements	Viet Tuan Duong, RMIT University	Influence of Individual GPS Antenna Calibrations on High Precision Geodetic Positioning, Case Study: Northern Surat Basin Queensland 2015 GPS Campaign	Guorong Hu & Michael Moore, Geoscience Australia
14:20	AeroPoints: Low-cost, Automated Ground Control Points for Aerial Surveying	Propeller	GPS/BDS Real-Time Precise Point Positioning using RCTM-SSR for Kinematic Maritime Applications	Fuxin Yang & Li Liang, Harbin Engineering University	IRNSS/NavIC L5 Attitude Determination	Safoora Zaminpardaz, Curtin University
14:40			Comparison of Different Precise Point Positioning Ambiguity Resolution (PPP-AR) Methods	Shuyang Cheng, UNSW Australia	Assessment of the Variation of Covariance Matrices of Triple-Frequency GNSS Measurements and its Impact on Positioning Results	Yongchao Wang & Yanming Feng, Queensland University of Technology

From: Manoj Deo <manoj.deo01@gmail.com>
Date: Mon, Dec 12, 2016 at 1:40 PM
Subject: Re: IGNSS2016 notification for paper 25
To: IGNSS2016 <ignss2016@easychair.org>, ENG ACSER IGNSS <IGNSS@unsw.edu.au>

Hi Cheryl,

Attached is our paper 25, updated according to reviewer comments.

I have also attached a response to review comments in case these are required by the reviewers (could not figure out a way to upload these using EasyChair).

Please feel free to let me know if there are any further issues.

Regards,

Manoj Deo

On Sun, Dec 4, 2016 at 11:50 PM, IGNSS2016 <ignss2016@easychair.org> wrote:
Dear Manoj Deo,

Your paper Triple Frequency precise point positioning with multi-constellation GNSS has been accepted for publication as a peer reviewed paper in the IGNSS 2016 conference publication.

Please revise your paper according to any comments suggested and resubmit by COB 12 December 2016.

Thanks and I look forward to seeing you next week.

Regards
Allison

---------- REVIEW 1 ----------
PAPER: 25
TITLE: Triple Frequency precise point positioning with multi-constellation GNSS
AUTHORS: Manoj Deo and Ahmed El-Mowafy

OVERALL EVALUATION: 2

---------- OVERALL EVALUATION ----------
The paper is acceptable for a conference paper, subject to clarification for the results: whether they are kinematic or static PPP results. From the models(22) and (23).

---------- REVIEW 2 ----------
PAPER: 25
TITLE: Triple Frequency precise point positioning with multi-constellation GNSS
AUTHORS: Manoj Deo and Ahmed El-Mowafy

OVERALL EVALUATION: 2

---------- OVERALL EVALUATION ----------
Title: Triple Frequency precise point positioning with multi-constellation GNSS

The paper provides an overview of triple-frequency PPP with multi-constellation GNSS. The paper is well written and is easy to follow.
Here are some comments for the authors to consider:
* Section 4.1: Should reference Li et al (2013)'s work "Modeling and quality control for reliable PPP integer ambiguity resolution with GNSS modernisation"
* Section 4.1: Could the authors present briefly why these are the best (optimal) model to help with readers' understanding, as Deo and El-Mowafy (2016a) is not published yet?
* Section 4.2: "For stochastic modeling of GPS observations, which is equally applicable for BeiDou...". Is it really equally applicable and realistic?
* Section 4.2: Can the authors explain, which satellite elevation angle method were use?
* Section 5.1: Why were simulated data used? What do the authors mean by simulated data?
* Section 5.1: "....by as much as 3.9m." Can the author confirm this value and provide more details?
* Section 6: "A proposed low noise, ionosphere-free triple frequency PPP model....". Did the author develop and propose this method? As far as aware, the method was published by Li et al (2013).

Minor comments:
* Page 4 " .....several constellations (Montenbruck et al., 2014). Since"
* Page 6 ".....form the ISB. Thus, ..."

* Page 6 ".....at the four sites."

From: Krys Henshaw - IGNSS Society <krys@ignss.org>
Date: Fri, Apr 24, 2015 at 4:47 PM
Subject: IGNSS 2015 - Registration Confirmation
To: Manoj Deo <manoj.deo01@gmail.com>

24 April 2015

Ref: 1298

Mr Manoj Deo
PHD Student - Part Time
Curtin University
GPO Box U 1987
PERTH WA 6845
AUSTRALIA

Dear Manoj

Thank you for registering for the International Global Navigation Satellite Systems Society, IGNSS 2015 Symposium being held at Outrigger Surfers Paradise, Gold Coast, Qld, Australia from 14 - 16 July, 2015.

Please check your registration details carefully and do not hesitate to contact us by phoning +61 7 5599 5007 if you have any questions. All changes will need to be made in writing and can be faxed to +61 7 5536 6366 or emailed to krys@ignss.org.

I have attached your GST Tax Invoice (if it has not already been sent to you) and request that you keep this for your own records or, if payment has been made by another source, it will be necessary for you to forward this to your relevant Accounts Department for use to obtain Tax Credits. No further GST Tax Invoice will be supplied.

Your registration details and queries regarding your registration are below. Please respond to any queries by return email:

Conference Cancellation Policy: It is highly recommended that Travel, Accommodation and Registration Cancellation Insurance is taken out to cover cancellation costs for registration, travel and accommodation. Cancellation fees for accommodation and registration are listed in the registration brochure and IGNSS website.

Any cancellations made to your registration must be advised in writing to krys@ignss.org. Cancellations made prior to Friday 15 May, 2015 will be refunded less a $125 administration fee. No registration refunds will be made after this date. As an alternative to cancellation, your registration may be transferred to another person without incurring any penalty. The IGNSS Society must be advised of this transfer in writing.

Please do not hesitate to contact me if you have any queries.

Kind Regards

Krys Henshaw
IGNSS Society
Ph: +61 7 5599 5007
Fax: +61 7 5536 6366
krys@ignss.org

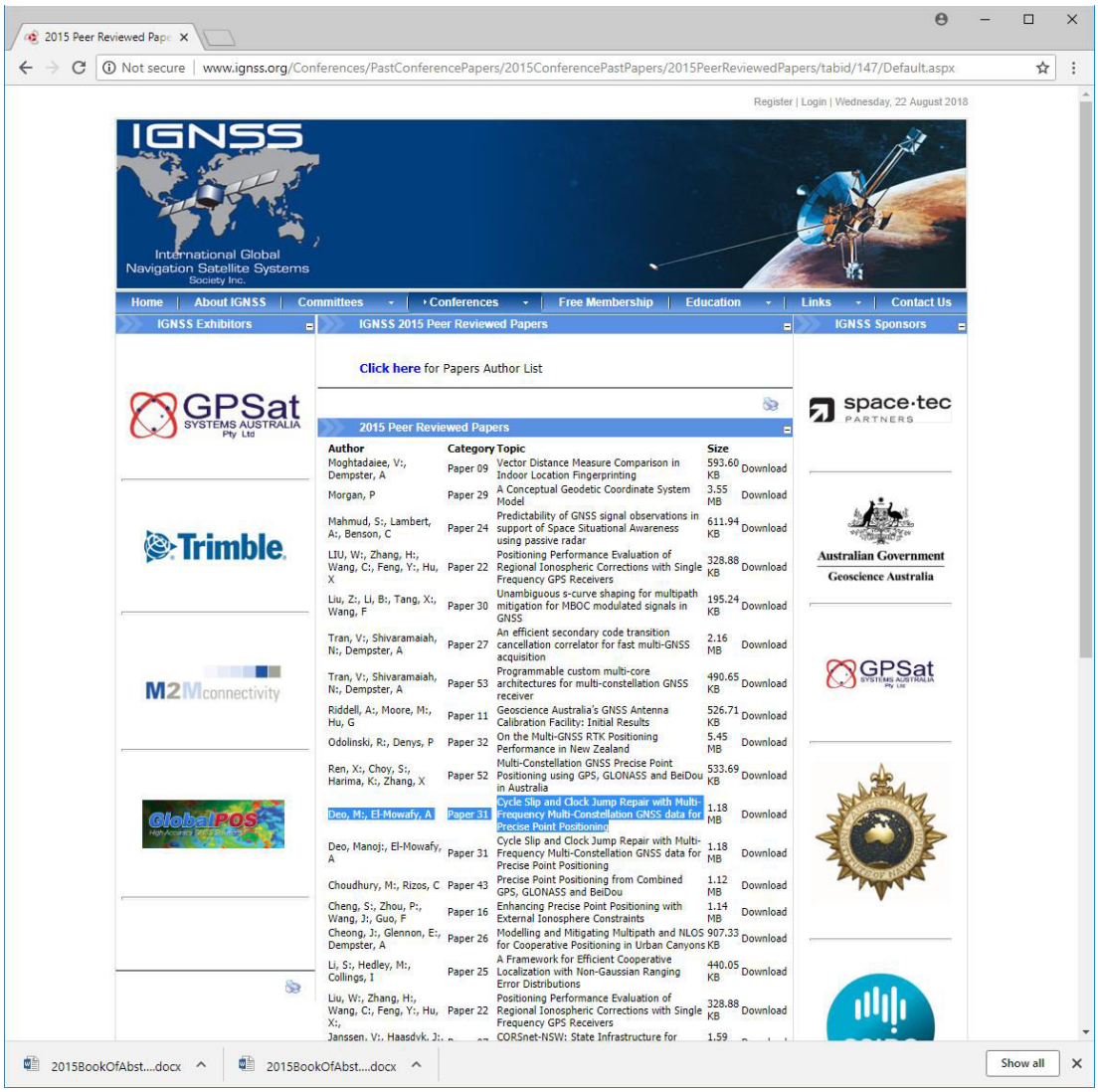

15:50-16:10	*Vector Distance Measure Comparison in Indoor Location Fingerprinting (p9)* **Professor Andrew Dempster,** University of New South Wales, SYDNEY, AUSTRALIA	*Advances in NovAtel's Precise Point Positioning (PPP) Solution for High Accuracy Kinematic Applications. (p56)* **Mr Rod MacLeod,** NovAtel, SYDNEY, AUSTRALIA and **Mr Thomas Morley,** NovAtel, CALGARY, CANADA	*Space Situational Awareness – A New Horizon of Australian Space Research (p59)* **Professor Kefei Zhang,** RMIT University, MELBOURNE, AUSTRALIA
16:10-16:30	*Enhanced Indoor Positioning Method Using RSSI Log Model Based on IEEE 802.11s Mesh Network (p38)* **Mr Jun Gyu Hwang,** Kyungpook National University, DAEGU, REPUBLIC OF KOREA	*Cycle Slip and Clock Jump Repair with Multi-Frequency GNSS data for improved Precise Point Positioning (p31)* **Mr Manoj Deo and Dr Ahmed El-Mowafy,** Curtin University, PERTH, AUSTRALIA	*Performance of GNSS Speed Measurement for Evidentiary Purposes (p13)* **Mr Andriy Dyukov and Mr Ivan Enierga,** Transport Certification Australia, MELBOURNE, AUSTRALIA
16:30-16:50	*Range Error Analysis of TDOA Based UWB-IR Indoor Positioning System (p34)* **Ms Lian Zhang,** Nanyang Technological University, SINGAPORE	*Enhancing Precise Point Positioning with External Ionosphere Constraint (p16)* **Mr Shuyang Cheng,** University of New South Wales, SYDNEY, AUSTRALIA	*Predictability of GNSS Signal Observations in Support of Space Situational Awareness using Passive Radar (p24)* **Dr Craig Benson,** University of New South Wales, CANBERRA, AUSTRALIA
		Precise Point Positioning from Combined GPS, GLONASS and BeiDou (p43) **Dr Mazher Choudhury,** University of New South Wales, SYDNEY, AUSTRALIA	*New Role of GNSS in Search-And-Rescue: Past, Present and Future of MEOSAR (p65)* **Mr Jack Scott,** Thales Australia, SYDNEY, AUSTRALIA
	Close of Sessions		

POSTER PRESENTATIONS

RTK and NRTK: Observational Accuracy vs Time (p5) **Mr Simon Conway,** Land Information New Zealand, WELLINGTON, NEW ZEALAND
Performance Analysis of AoA-based Localization with Software Defined Radio (p36) **Mr Donggu Kim,** Korea Advanced Institute of Science and Technology, DAEJEON, REPUBLIC OF KOREA
A Golden Reviver Used for GNSS Satellite Simulator Time Delay Calibration (p40) **Dr ZengJun Liu,** National University of Defense Technology, CHANGSHA, CHINA
Linear Combination Ionospheric Delay Model of GPS and Galileo (p49) **Dr Jungmin Joo,** Korea Aerospace Research Institute, DAEJEON, REPUBLIC OF KOREA
GNSS Signal Paths Traversing a Tropospheric Storm Event (p57) **Professor Kefei Zhang,** RMIT University, MELBOURNE, AUSTRALIA
Interference Monitoring Using Low Cost Software Defined Radios and GNSS Receivers (p62) **Mr Ryan Thompson,** University of New South Wales, SYDNEY, AUSTRALIA